University of Oxford

D.Phil. Thesis

Mathematical modelling of ice-sheet surface melt

Tilly Woods

Supervisor: Prof. I. J. Hewitt



A thesis submitted for the degree of Doctor of Philosophy

Mathematical Institute

New College

Michaelmas Term 2024

Declaration of Authorship

I, Tilly Woods, declare that the work presented in this thesis is my own, performed under the supervision of Professor Ian J. Hewitt. I hereby certify that all material obtained from published or unpublished sources of any type have been fully acknowledged at the proper point in the text and included in the list of references or in this declaration.

The following figures have been reproduced from other sources: Figure 1.2 from Ian Stevens, Figure 1.4 from Williamson et al. [2020], Figure 1.5(a) and Figure 1.6(a,b) from Eva Doting, Figure 1.6(c,d) from Giacomo Traversa, Figure 1.7 from Liston et al. [1999], Figure 6.1(a) from Fausto et al. [2021], and Figure 6.1(b) from Nanna Karlsson. Permission for reuse has been granted in each case.

Data from the Programme for Monitoring of the Greenland Ice Sheet (PROMICE) are provided by the Geological Survey of Denmark and Greenland (GEUS) at http://www.promice.dk. They include sites financially supported by the Glaciobasis programme as part of Greenland Ecosystem Monitoring (https://g-e-m.dk/), maintained by GEUS (ZAK, LYN) and by Asiaq Greenland Survey (NUK_K). The WEG stations are paid for and maintained by the University of Graz.

Much of the work in Chapters 2 and 4 is adapted from our work published in *The Cryosphere* in the manuscript *'A model of the weathering crust and microbial activity on an ice–sheet surface'* [Woods and Hewitt, 2023]. The work in Chapter 3 is adapted from work published in the *IMA Journal of Applied Mathematics* in the manuscript *'Modelling the evolution of an ice sheet's weathering crust'* [Woods and Hewitt, 2024].

Signed: Tilly Woods

Date: 04/10/2024

Abstract

Shortwave radiation penetrating beneath an ice–sheet surface can cause internal melting and the formation of a near-surface porous layer known as the weathering crust. The weathering crust is a dynamic hydrological system that provides home to impurities and microbial life. It grows and decays in response to changing weather and climate conditions, affecting the albedo, the melt rate, and the transport of meltwater and nutrients across the ice–sheet surface. We develop a mathematical model, incorporating thermodynamics, water flow and population dynamics, for the evolution of such layers. The model accounts for conservation of mass and energy, for internal and surface-absorbed radiation, for water flow governed by Darcy's law, and for logistic growth of a microbial species mediated by nutrients that are sourced from the melting ice. Existing models have accounted for only one or two of these processes, so our model is valuable in providing a more complete picture. In this thesis, we use a one-dimensional reduction of the model to explore (1) the effect of the weathering crust on near-surface melt, (2) the response of the weathering crust to changing weather conditions, and (3) the potential of microbes to enhance melting via a feedback between the weathering crust, albedo and melting. Idealised steadily-melting and time-dependent solutions both with and without meltwater flow provide physical insight into the evolution of the weathering crust, the effect of microbes, and the conditions that favour growth and decay. Our model demonstrates the importance of accounting for the weathering crust and subsurface melt processes, and agrees well with observations of surface lowering, porosity and temperature when forced with weather data from the Greenland ice sheet. The model therefore provides a useful tool for exploring the response of the weathering crust to climate change, and hence the resulting consequences for surface albedo, melting and runoff.

Acknowledgements

I am extremely grateful to Ian for being an absolutely fantastic supervisor and for making the past four years such a great experience. Discussing science with you has been a highlight of my PhD, and your endless source of ideas has been invaluable. Thank you for always giving me time and support when I've needed it, and for inspiring me to keep doing science.

A massive thank you to everyone in icy maths — past and present — for providing a supportive community full of ice-based enthusiasm, and for so willingly taking part in the Teddy Hall Relays! I would also like to thank the friends I have made in the wider glaciological community, particularly at the Karthaus summer school, for providing friendly faces at every conference. Thank you also to the people of OCIAM and the Mathematical Institute for making it a great place to work. Thanks especially to my office buddies for being in it together. Thanks must also go to the Engineering and Physical Sciences Research Council (EPSRC) for providing the funding for this work.

Thank you to all my friends in Oxford for making my eight years here so enjoyable. In particular, thank you to the runners — OUCCC, OUOC, and especially the Headington Road Runners I've got to know over the past two years — for providing (often mud-based) adventures and friendship.

Thank you to my loving, supportive family, especially Mum, Dad and Lottie, for providing a safe, happy home to retreat to, and for always supporting me to achieve anything I put my mind to. Mum and Dad — thank you for your countless drives to Oxford, and for looking after me so well during the final stages of thesis writing. Lottie — thank you for all our chats and sister adventures. Without our scientific investigations in the garage, this PhD might never have happened.

Finally, thank you to Olly for always being there for me, and for helping me believe I could do it. :)

Contents

Declaration of Authorship i

Abstract ii

Acknowledgements iii

Contents iv

1 Introduction 1
- 1.1 Motivation . . . 1
- 1.2 Background glaciological concepts . . . 2
  - 1.2.1 Glaciers and ice sheets . . . 2
  - 1.2.2 Ice–sheet mass balance . . . 2
  - 1.2.3 Surface hydrology . . . 3
  - 1.2.4 Albedo . . . 4
- 1.3 Weathering crust . . . 4
  - 1.3.1 What is the weathering crust? . . . 5
  - 1.3.2 Microbes in the weathering crust . . . 6
  - 1.3.3 Meltwater and microbe transport . . . 7
  - 1.3.4 Albedo and biological darkening . . . 8
  - 1.3.5 Interactions between the weathering crust and microbes . . . 9
  - 1.3.6 The variable weathering crust . . . 10
- 1.4 Thesis overview . . . 12
- 1.5 Thesis structure . . . 13
- 1.6 Surface energy balance and internal radiation . . . 14
  - 1.6.1 Radiation . . . 14
  - 1.6.2 Surface and subsurface radiation . . . 15
  - 1.6.3 Two-stream approximation . . . 16
  - 1.6.4 Surface energy balance . . . 17
    - 1.6.4.1 Shortwave radiation . . . 18
    - 1.6.4.2 Longwave radiation . . . 19

1.6.4.3 Turbulent heat fluxes . . . 20
1.6.5 Linking to weather conditions . . . 20

2 Model development and steadily melting solutions 21
2.1 Existing models . . . 21
2.2 Outline . . . 23
2.3 Weathering crust model . . . 24
2.3.1 Mass conservation . . . 25
2.3.2 Darcy's law . . . 25
2.3.2.1 Permeability . . . 26
2.3.2.2 Relative permeability . . . 26
2.3.2.3 Capillary pressure . . . 27
2.3.3 Energy equation . . . 28
2.3.4 Radiation model . . . 29
2.3.5 Kinematic conditions . . . 30
2.3.6 Surface energy balance . . . 30
2.3.7 Model summary . . . 31
2.3.8 Simplifications . . . 32
2.4 Steadily melting states . . . 33
2.5 Results . . . 36
2.5.1 Steadily melting solutions . . . 36
2.5.2 Comparison to observations . . . 41
2.5.3 Steady solution (non-melting) . . . 42
2.6 Discussion and summary . . . 44

3 Weathering crust evolution without flow 46
3.1 Time-dependent model . . . 47
3.1.1 Mass conservation . . . 49
3.1.2 Energy equation . . . 50
3.1.3 Internal shortwave radiation . . . 50
3.1.4 Kinematic condition . . . 51
3.1.5 Surface energy balance . . . 51
3.1.6 Far-field boundary conditions . . . 51
3.2 Enthalpy method . . . 52
3.3 'Switching' forcing - growth and decay of the weathering crust . . . 54
3.3.1 Setup . . . 54
3.3.2 Growth of a weathering crust . . . 55
3.3.3 Removal via surface melting . . . 56
3.3.4 Removal via surface freezing . . . 58
3.3.5 Dependence on the value of Q_0^{new} . . . 59
3.3.6 Dependence on the value of $Q_{\text{si}}^{\text{new}}$ . . . 62
3.4 Periodic forcing . . . 63
3.4.1 Periodic growth and complete removal . . . 63
3.4.2 Diurnal vs. annual forcing . . . 65

3.4.3 Superimposed diurnal and annual forcing . . . 66
3.5 Discussion . . . 68
3.5.1 Growth and decay behaviour and timescales . . . 68
3.5.2 Actual vs. potential surface lowering . . . 69
3.6 Summary . . . 70

4 Microbes and feedbacks **72**
4.1 Introduction . . . 72
4.2 Microbes and nutrients model . . . 73
4.3 Steadily melting solutions . . . 76
4.3.1 Effect of microbe growth rate . . . 78
4.3.2 Effect of nutrient parameters . . . 79
4.3.3 Total microbial abundance . . . 80
4.3.4 Residence times . . . 83
4.3.5 Summary . . . 85
4.4 Time-dependent solutions . . . 85
4.4.1 Time-dependent model . . . 85
4.4.2 Microbial growth . . . 87
4.4.2.1 Growth in a steadily melting weathering crust . . . 87
4.4.2.2 Combined microbial and crust growth . . . 89
4.4.3 Freezing of microbes . . . 91
4.5 Feedbacks between microbe growth, albedo, and melting . . . 92
4.5.1 Model . . . 93
4.5.2 Results . . . 94
4.6 Discussion and conclusion . . . 97

5 Weathering crust evolution with flow **100**
5.1 Introduction . . . 100
5.2 Model . . . 102
5.2.1 Darcy's law . . . 102
5.2.2 Lateral flow . . . 102
5.2.3 One-dimensional model equations . . . 103
5.2.4 Enthalpy formulation . . . 104
5.2.5 Non-dimensionalisation . . . 106
5.3 Numerical method . . . 110
5.3.1 Calculating water pressure and flux . . . 110
5.4 Isothermal water transport . . . 111
5.4.1 Qualitative solution . . . 112
5.4.2 Approximate solution neglecting capillary pressure . . . 112
5.4.2.1 Wetting fronts — before saturation occurs . . . 114
5.4.2.2 Saturation fronts — after saturation first occurs . . . 116
5.4.2.3 Semi-analytical solution without lateral drainage . . . 117
5.4.3 Comparison of drainage and no drainage . . . 118
5.5 Steady melting with lateral drainage . . . 120

5.5.1 Semi-analytical solution . . . 121
5.5.2 Numerical solution . . . 122
5.5.3 Conservation of water . . . 124
5.5.4 Inferring the value of $\mathcal{K}_\mathrm{d}$ . . . 124
5.6 Idealised periodic forcings . . . 125
5.7 Switching experiments . . . 127
5.8 Summary . . . 131

6 Comparison with observations from Greenland 132
6.1 Introduction . . . 132
6.2 Data . . . 132
6.2.1 PROMICE Automatic Weather Station (AWS) data . . . 132
6.2.2 Surface energy balance . . . 133
6.2.3 Calculating model forcings from observations . . . 136
6.2.3.1 Surface energy balance components . . . 136
6.2.3.2 Internal shortwave radiation . . . 137
6.2.3.3 Filling gaps in the PROMICE data . . . 139
6.2.3.4 Temperature at depth . . . 139
6.2.3.5 Fitting χ . . . 140
6.3 Time-dependent model solution . . . 141
6.3.1 Overall model behaviour . . . 142
6.3.2 Porosity . . . 145
6.3.3 Temperature . . . 147
6.3.4 Surface lowering . . . 148
6.3.5 Meltwater production and removal . . . 149
6.4 Discussion . . . 150
6.4.1 Shortwave radiation partitioning χ . . . 150
6.4.2 Lateral drainage . . . 152
6.5 Summary . . . 153

7 Summary and conclusions 155
7.1 Summary . . . 155
7.1.1 How does the weathering crust affect the production and transport of meltwater on an ice-sheet surface? . . . 156
7.1.2 How does the weathering crust respond to changing weather conditions? . . . 156
7.1.3 How do the weathering crust and microbes within it interact, and how does this interaction influence albedo, melting and runoff? . . . 157
7.2 Future work . . . 158
7.2.1 Higher dimensions . . . 158
7.2.2 Surface microbes . . . 159
7.2.3 Accumulation of snow . . . 159
7.2.4 Liquid water on Mars . . . 160
7.3 Concluding remark . . . 160

A Non-dimensionalisation **161**
A.1 Weathering crust . . . 161
A.1.1 Non-dimensionalisation . . . 161
A.1.2 Saturated model . . . 162
A.1.3 Steadily melting solutions . . . 163
A.2 Microbes and nutrients . . . 164
A.2.1 Non-dimensionalisation . . . 164
A.2.2 Model . . . 164

B Details of numerical method **166**
B.1 Saturated problem without flow (Chapter 3) . . . 167
B.1.1 Enthalpy flag . . . 168
B.1.2 Melt flag . . . 169
B.1.3 Implementing boundary conditions . . . 170
B.2 Unsaturated problem with flow (Chapter 5) . . . 171
B.2.1 Internal radiation . . . 171
B.2.2 Solving for q and p_w . . . 172
B.2.3 Discretised equations . . . 174
B.2.4 Unsaturated flag . . . 175
B.2.5 Implementing boundary conditions . . . 175
B.2.6 Iterations . . . 177

C Approximating the microbial growth rate **178**

References **180**

Chapter 1

Introduction

1.1 Motivation

Mass loss from ice sheets and glaciers provides a significant contribution to sea-level rise [WCRP Global Sea Level Budget Group, 2018, Meredith et al., 2019, Smith et al., 2020]. Over recent decades, the Greenland and Antarctic ice sheets have been losing mass [The IMBIE Team, 2018, 2020], and this contribution to sea-level rise is projected to continue into the future [DeConto and Pollard, 2016, DeConto et al., 2021, Edwards et al., 2021, Goelzer et al., 2020, Meredith et al., 2019]. Between 2006 and 2015, the average rates of mass loss from Greenland and Antarctica were 278 Gt yr^{-1} and 155 Gt yr^{-1}, respectively [Meredith et al., 2019], with Greenland contributing 10.8 mm to mean sea level rise between 1992 and 2018 [The IMBIE Team, 2020], and Antarctica contributing 7.6 mm between 1992 and 2017 [The IMBIE Team, 2018].

A key component of ice–sheet mass loss is the runoff of surface meltwater. This dominates mass loss from the Greenland ice sheet (accounting for 61% of Greenland's mass loss from 2007-2011 [Andersen et al., 2015] and 68% from 2009-2012 [Enderlin et al., 2014]). There have been dramatic increases in surface melt and runoff from Greenland over recent decades [Trusel et al., 2018], with 2012 being a year of notably extreme melt [Nghiem et al., 2012]. Surface melting and runoff is also increasingly thought to play a key role in the ice–sheet dynamics and mass loss from Antarctica [Kingslake et al., 2017]. Therefore, understanding the factors that control (1) how much surface melting occurs, and (2) where that meltwater ends up, is key to quantifying the future contribution of the ice sheets to sea level rise.

The work in this thesis focusses on an ice–sheet surface structure, known as the *weathering crust*, that plays a major role in surface melting and the transport of surface meltwater. In the rest of this chapter, I will give some background on the processes affecting ice–sheet mass loss, introduce the weathering crust, present an outline for the rest of the thesis, and provide some useful preliminaries for our modelling work.

1.2 Background glaciological concepts

1.2.1 Glaciers and ice sheets

A glacier is a body of ice that sits on land and was formed by snow accumulating and being compacted down into ice under its own weight over many years [Cuffey and Paterson, 2010]. An ice sheet is a roughly dome-shaped continental-scale body of glacial ice (see Figure 1.1). The Greenland and Antarctic ice sheets are the only ice sheets currently on Earth. They are up to 3–4 km thick and thousands of kilometres in extent. Mass loss from ice sheets and glaciers combined accounts for around half of the increase in sea level since 1993 [WCRP Global Sea Level Budget Group, 2018].

1.2.2 Ice–sheet mass balance

There are two main processes through which ice sheets and glaciers lose mass, demonstrated in Figure 1.1: (1) ice dynamics, and (2) surface melting and runoff (the surface mass balance). Basal melting can also contribute to mass loss. Ice dynamics refers to the ice flowing under its own weight, with typical flow speeds ranging from ~ 10 m yr^{-1} (small mountain glaciers) to kilometres per year (some outlet glaciers from ice sheets) [Cuffey and Paterson, 2010]. This results in the ice thinning and being discharged into the oceans. The surface mass balance (SMB) is the net gain (or loss) of mass from the ice surface. Mass is gained by the accumulation of snow, and lost by surface melting and the meltwater being removed as runoff [Cuffey and Paterson, 2010].

As a result of ice sheets being dome-shaped, most of the surface mass loss (melting) occurs near the edges (margins) of the ice sheet where the elevation is lower and air temperature is warmer. This region, where there is net surface mass loss throughout the year, is called the *ablation zone*. The higher elevation zone where there is net

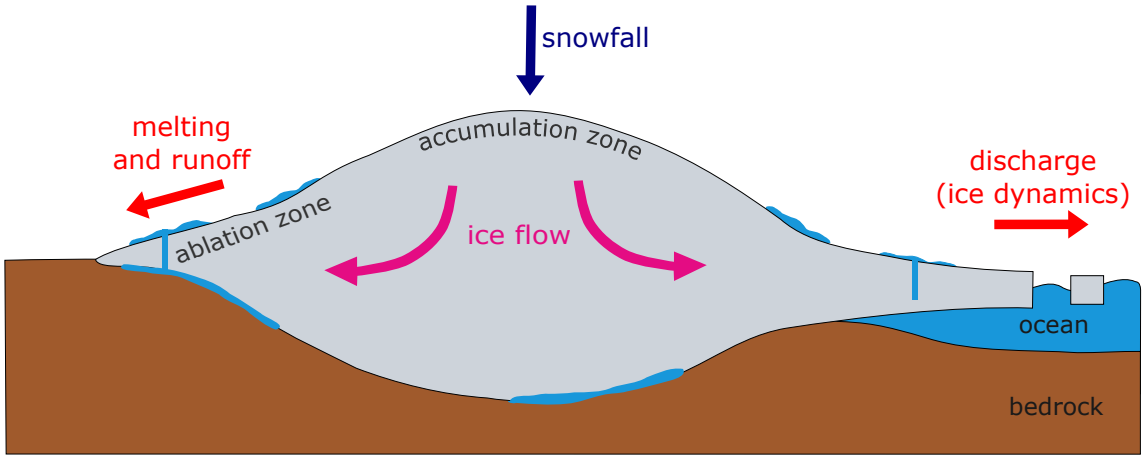


Figure 1.1: Schematic of an ice sheet. The ice sheet sits on land and flows under its own weight. The ice sheet gains mass from snowfall, and loses mass by (1) melting and runoff and (2) the discharge of ice into the ocean as a result of the ice dynamics. Net mass loss occurs in the lower elevation *ablation zone* and net mass gain occurs in the higher elevation *accumulation zone*. Weathering crusts — the focus of this thesis — occur in the ablation zone. Note that the thickness of the ice sheet (typically a few kilometres) is significantly exaggerated compared to its length (typically thousands of kilometres).

gain of mass at the surface (via snowfall) is called the *accumulation zone* [Cuffey and Paterson, 2010]. Both regions can experience both melting and snowfall at points throughout the year. The term *melt season* refers to the summer months during which melting occurs. This thesis focusses on melting processes occurring in the ablation zone, where all snow is removed from the surface at the beginning of the melt season, leaving exposed 'bare' ice.

1.2.3 Surface hydrology

As mentioned previously, a crucial part of quantifying ice–sheet mass loss is understanding the routing and final destination of surface meltwater. Surface meltwater can run off directly into the ocean through a network of surface streams, or it can be routed from surface streams or lakes to the ice sheet bed via moulins (vertical channels) or crevasses [Chu, 2014], where it affects the ice motion and mass loss via ice dynamics [Bell, 2008, van de Wal et al., 2008].

Surface meltwater can also be transiently stored or refrozen on the ice sheet for multiple years, for example in partially compacted snow (called *firn*). This delays its sea-level contribution [Harper et al., 2012]. Over time, the storage capacity of the firn can be reduced by (1) filling up with meltwater, and (2) impermeable *ice layers* of refrozen meltwater (sometimes referred to as *ice lenses*) forming in the firn,

preventing meltwater from percolating deeper into the firn [Clerx et al., 2022]. This can lead to increased lateral runoff and extreme runoff events can occur [e.g. Noël et al., 2017, Mikkelsen et al., 2016], with these phenomena becoming increasingly prevalent as Greenland melt increases [Culberg et al., 2021].

In addition, the area of Greenland over which melting occurs has been growing in recent decades [Mernild et al., 2011], making it increasingly important to understand the transport of surface meltwater.

1.2.4 Albedo

As well as understanding the transport of meltwater, it is also crucial to quantify how much meltwater is produced at and near the surface. A key quantity determining this is the *albedo*, a measure of how reflective a surface is to shortwave (solar) radiation. The albedo a is defined as

$$a = \frac{Q_{\mathrm{so}}}{Q_{\mathrm{si}}}, \tag{1.1}$$

the ratio between the outgoing shortwave radiation Q_{so} and the incoming shortwave radiation Q_{si}. Of the total incoming shortwave radiation Q_{si}, an amount $(1-a)Q_{\mathrm{si}}$ is absorbed by the ice and the rest aQ_{si} is reflected back out. Therefore, a lower albedo means that more radiation is absorbed and hence more energy is available for melting. Darker coloured surfaces have a lower albedo and absorb more radiation than lighter coloured surfaces.

There are three key factors affecting the albedo of an ice sheet: (1) the surface structure, (2) the presence of meltwater, and (3) biological and non-biological impurities. For example, snow has a higher albedo compared to bare (snow-free) ice and the albedo of snow depends on its grain size [Tedesco et al., 2016]. The presence of meltwater also lowers the albedo. Moreover, light-absorbing impurities, such as mineral dust, black carbon, and microbes (e.g. algae), can cause darkening, producing dirty-looking ice [Tedesco et al., 2016, Ryan et al., 2018]. I will discuss the darkening effect of biological and non-biological impurities further in Section 1.3.4.

1.3 Weathering crust

The weathering crust (as shown in Figure 1.2) is a structure on an ice sheet or glacier surface that affects the transport and storage of meltwater and microbes, as well as



Figure 1.2: A weathering crust on the Greenland Ice Sheet. Photo credit: Ian Stevens.

the albedo of the ice sheet [Müller and Keeler, 1969, Cooper et al., 2018, Irvine-Fynn et al., 2021]. Studying the weathering crust is the main focus of this thesis.

1.3.1 What is the weathering crust?

The weathering crust is a layer of porous ice, around a metre thick, that forms at the surface of ice sheets and glaciers, with impermeable ice below [Müller and Keeler, 1969, Cooper et al., 2018]. It is a transient structure that grows and decays over hours and days in response to rapidly changing weather conditions [e.g. Schuster, 2001, Tedstone et al., 2020]. The porous structure is formed by shortwave radiation from the sun penetrating below the surface of the ice, where it acts as a heat source, causing internal melting [Brandt and Warren, 1993, Cooper et al., 2021]. Most of the thickness of the weathering crust is saturated with meltwater [Cooper et al., 2018, Cook et al., 2016, Irvine-Fynn et al., 2021]. The porosity of the weathering crust decreases with depth. A typical structure is shown in Figure 1.3. There are a few centimetres of highly porous, unsaturated ice at the surface, below which there is a less porous layer that it saturated with meltwater. The saturated layer is known as the *weathering crust aquifer* [e.g. Christner et al., 2018] and can contain alternating thin solid ice layers, analogous to the ice lenses seen in firn [Cooper et al., 2018].

Weathering crusts form during the summer melt season on the bare (snow-free) ice of the ablation zone. Many studies of weathering crusts have focussed on those occurring on south-western Greenland [e.g. Cooper et al., 2018, Chandler et al., 2015, Irvine-Fynn et al., 2021, Tedstone et al., 2020]. However, weathering crusts have also been found elsewhere in the Arctic (e.g. Alaska [Schuster, 2001], Canadian Arctic

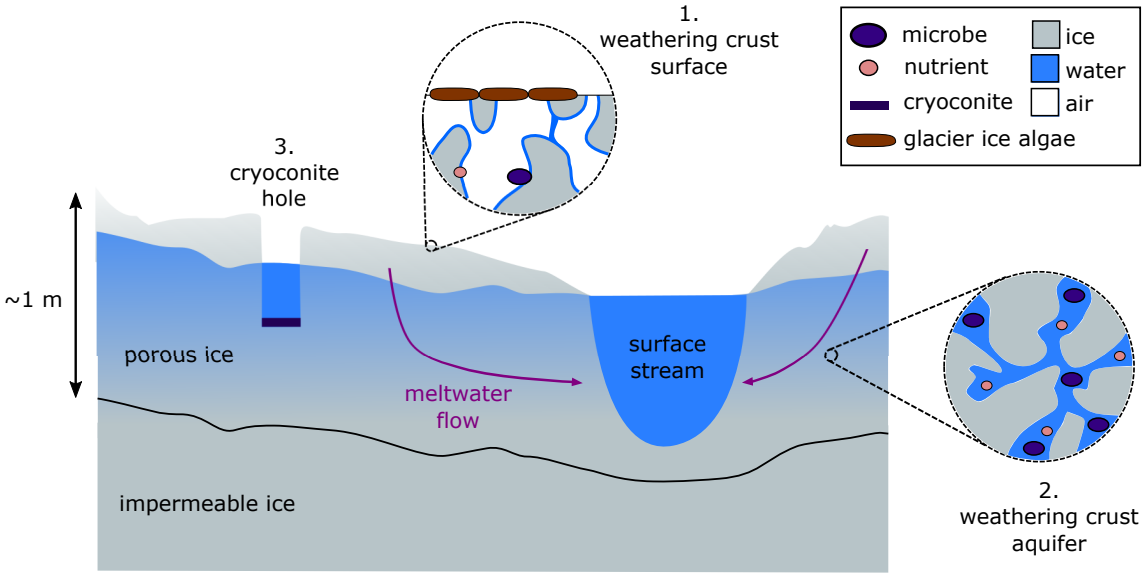


Figure 1.3: Schematic of a weathering crust — a near-surface layer of porous ice (above the solid black line), below which the ice is impermeable (though the "solid" ice shown here may contain small, closed-off air bubbles). The porosity of the weathering crust decreases with depth. Much of it is saturated with meltwater, with a thin unsaturated layer at the surface. Meltwater flows laterally through the saturated layer — known as the "weathering crust aquifer" — into nearby surface streams. The weathering crust is also home to microbes, with three different microbial environments shown: (1) the weathering crust surface, to which glacier ice algae 'stick', (2) the weathering crust aquifer, in which microbes live and are transported by the meltwater, and (3) cryoconite holes. Schematic based on Cooper et al. [2018], Stevens et al. [2022].

Archipelago [Müller and Keeler, 1969], Svalbard [Cook et al., 2016]), on mountain glaciers elsewhere (e.g. in Europe [Stevens et al., 2022]), and in Antarctica (e.g. the Antarctic Dry Valleys [Hoffman et al., 2014] and on Antarctic ice shelves [Traversa and Di Mauro, 2024]).

1.3.2 Microbes in the weathering crust

The weathering crust is home to many microorganisms [Irvine-Fynn and Edwards, 2014, Irvine-Fynn et al., 2021]. The presence of microbes has a significant impact on the albedo [e.g. Benning et al., 2014, Ryan et al., 2018, Tedstone et al., 2020]. Moreover, the growth and transport of microbes affects the cycling of nutrients such as carbon [e.g. Stibal et al., 2012] and nitrogen [e.g. Telling et al., 2012]. For example, microbial activity affects whether an ice–sheet surface is a source or a sink of CO_2 [Stibal et al., 2012]. Microbes and nutrients can also be transported by the flow of meltwater, impacting downstream habitats such as oceans and soils [Stibal et al., 2012].

Microbes are found in the *photic zone* — the top $\sim$ 2 m of ice where there is sufficient radiation (required for photosynthesis), water, air and nutrients for the microbes to survive [Irvine-Fynn and Edwards, 2014]. There are a few different microbial environments in the weathering crust. This is presented nicely by Stevens et al. [2022], and a simplified representation is shown in Figure 1.3. (1) Dark-coloured *glacier ice algae* [Cook et al., 2019, Hotaling et al., 2021] are found 'stuck' to the surface. (2) A range of algae and bacteria that are carried by the water in the saturated layer of the weathering crust [Irvine-Fynn and Edwards, 2014, Irvine-Fynn et al., 2021]. (3) Concentrated pockets of microbes can also be found in *cryoconite holes* [Wharton Jr. et al., 1985] — cylindrical, partially water-filled holes in the surface, with diameter and depth of a few centimetres. At the bottom of the hole sits a layer of *cryoconite* — a dark-coloured aggregate of inorganic and organic matter, including microbes. Cryoconite holes are formed by the cryoconite melting its way down into the ice from the surface due to its locally low albedo, and can have a significant impact on the overall surface albedo [Wharton Jr. et al., 1985].

1.3.3 Meltwater and microbe transport

The weathering crust is of interest for multiple reasons. Firstly, it affects the transport of meltwater and microbes across the surface of the ice sheet [Cooper et al., 2018, Irvine-Fynn et al., 2021]. Meltwater typically flows laterally through the weathering crust for up to about 10 metres before it reaches the nearest (faster flowing) surface stream [Irvine-Fynn et al., 2021, Chandler et al., 2015] (see stream through the crust in Figures 1.3, 1.5(a)). Typical flow speeds through the weathering crust are less than 0.13 m/day [Irvine-Fynn et al., 2021]. Surface meltwater can also be transiently stored or refrozen in the weathering crust [Smith et al., 2017, Cooper et al., 2018].

Moreover, microbial biomass is transported in the surface meltwater [Cook et al., 2016, Irvine-Fynn et al., 2021], affecting the provision of nutrients to downstream environments [Stibal et al., 2012], the carbon fluxes between the ice sheet and the atmosphere [Cook et al., 2012], and the local distribution of microbes and hence the spatial and temporal variability in albedo [Tedstone et al., 2020, Cook et al., 2016]. For example, microbes that are locally concentrated in cryoconite holes can be distributed across the surface by weathering crust water flow [Cook et al., 2016, Chandler et al., 2015]. However, it remains relatively unknown what controls the retention of microbes (particularly glacier ice algae) on the ice surface versus the transport of microbes through the weathering crust [Halbach et al., 2022].

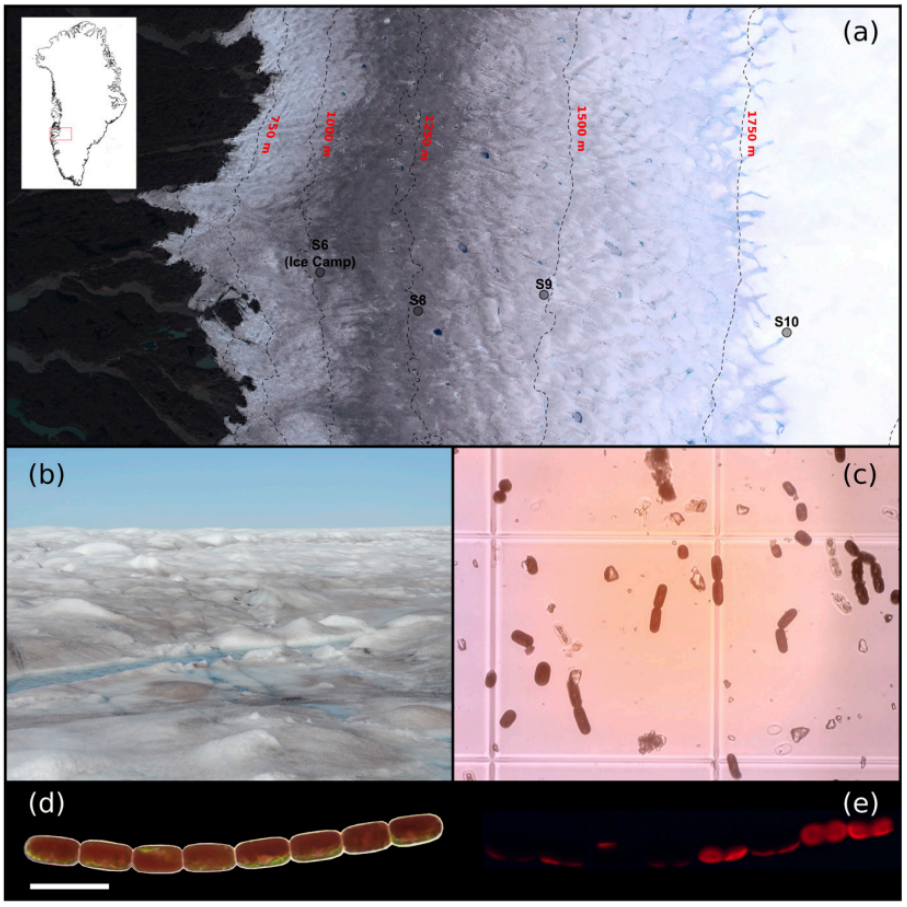


Figure 1.4: The 'dark zone' and glacier ice algae on the Greenland ice sheet, reproduced from Williamson et al. [2020] (with permission). (a) The south-western margin of the Greenland ice sheet near Kangerlussuaq, showing the 'dark zone' (the dark-coloured strip visible in the image). (b) The ice surface at 'ice camp' (shown in panel (a)), dominated by a glacier ice algal bloom during the 2016 melt season. (c)–(e) Glacier ice algae: (c) a sample of glacier ice algae taken from surface of the Greenland ice sheet, (d,e) *Ancylonema nordenskiöldii* filament — one of the two dominant taxa found by Williamson et al. [2020] in glacier ice algal blooms (the other being *Mesotaenium berggrenii*). Chloroplasts are highlighted in panel (e). The scale bar in panels (d,e) is 50 μm.

1.3.4 Albedo and biological darkening

Since 1996, the Greenland ice sheet has been darkening in colour, resulting in a lowering of the albedo and increased melting [Tedesco et al., 2016]. This is due to all of the main factors discussed in Section 1.2.4: changes to the ice–sheet surface structure, the presence of meltwater, and biological and non-biological light-absorbing impurities.

The weathering crust affects all three of these factors. For example, the weathering crust reflects more radiation than the glazed, bare ice left behind when the crust is removed [Tedstone et al., 2020]. The weathering crust also provides a home for

microbes (e.g. glacier ice algae) and non-biological impurities, which interact with the ice structure [Tedstone et al., 2020, McCutcheon et al., 2021] and act to lower the albedo [Benning et al., 2014, Tedesco et al., 2016, Hotaling et al., 2021]. Impurities can either be blown onto the ice from nearby land or exposed by melting ice [Hotaling et al., 2021].

Cook et al. [2020] estimated that 10-13% of the total runoff from south-western Greenland in summer 2017 could be attributed to algae growth. These glacier ice algae, shown in Figure 1.4, have a special dark-coloured pigmentation to protect them from high levels of UV radiation and photosynthetically active radiation (PAR), which makes them visibly dark in colour [Williamson et al., 2019]. Biological darkening is particularly prevalent in a strip called the 'dark zone' in the south-western Greenland ablation zone, where algal blooms are visible in satellite images [Ryan et al., 2018, Wientjes and Oerlemans, 2010] (Figure 1.4(a)).

1.3.5 Interactions between the weathering crust and microbes

The weathering crust and the microbes (such as glacier ice algae) that live within it are intrinsically linked, making it difficult to isolate and quantify the individual effect of the weathering crust or microbes on the albedo and melting without considering the other [Tedesco et al., 2016, Cook et al., 2017, Tedstone et al., 2020]. It has been highlighted by Halbach et al. [2022] that understanding the weathering crust, how it transports microbes, and how the microbes impact the weathering crust, is key to understanding the biological impact on Greenland's albedo. For example, the transport of microbes in the water of the weathering crust changes the local distribution of microbes across the surface, affecting the spatial variability in albedo [Tedstone et al., 2020, Cook et al., 2016]. Moreover, in addition to directly affecting the albedo via shortwave radiation absorption, glacier ice algae can also indirectly affect the albedo by causing melting that changes the weathering crust structure [Williamson et al., 2019].

A particular demonstration of the intrinsic link between the weathering crust and the microbes is the potential positive feedback loop associated with glacier ice algae and melting, whereby increased melting enables more algal growth (Figure 1.5) [Tedstone et al., 2020, McCutcheon et al., 2021]. The algae require nutrients to grow, which they get from mineral dust that is frozen within the ice [McCutcheon et al., 2021]. The ice must be melted to release the nutrients and make them available to the

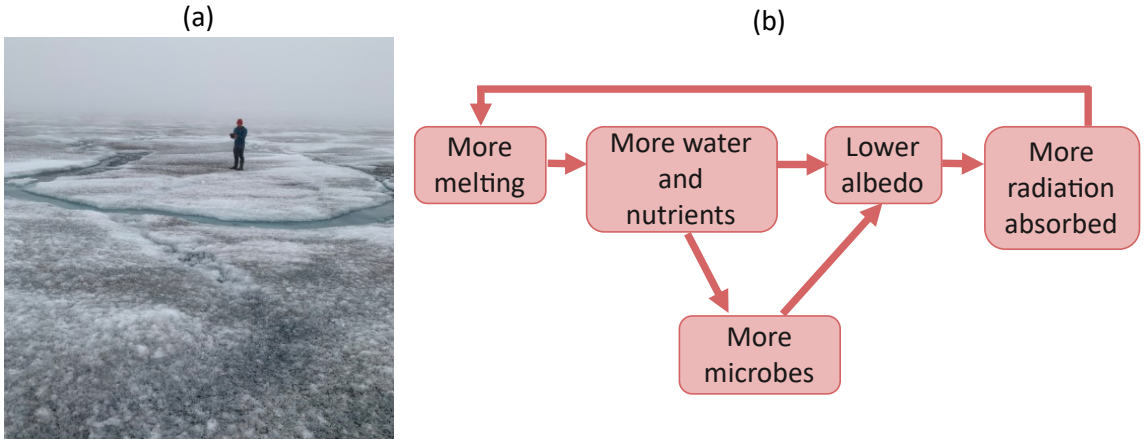


Figure 1.5: (a) Photo of a weathering crust on Greenland with significant biological darkening due to the presence of microbes (credit: Eva Doting). (b) The potential positive feedback between microbes (in particular glacier ice algae) and the weathering crust that could lead to enhanced melting.

algae. (A potential secondary purpose of the algae's dark pigment is to convert light energy to heat energy to melt the ice around them, releasing nutrients [Williamson et al., 2019]). The more algae there are, the darker the ice surface is and the lower the albedo. Hence more melting occurs, releasing more nutrients, enabling more algal growth. This leads to a potential positive feedback that could enhance melt.

A natural way to explore the coupled behaviour of the weathering crust and microbes, and their combined impact on melting and runoff, is by using a mathematical model, as we do in this thesis.

1.3.6 The variable weathering crust

The weathering crust is a naturally transient structure. It only forms in the summer months when there is enough shortwave radiation to cause internal (subsurface) melting [e.g. Cook et al., 2016]. On a shorter timescale, the weathering crust responds to rapidly changing weather conditions, growing and decaying on the order of hours and days [e.g. Schuster, 2001, Tedstone et al., 2020]. Clear, sunny conditions favour formation of the crust, whereas warm, windy, cloudy conditions favour removal [Müller and Keeler, 1969, Schuster, 2001]. Examples of weathering crusts in different weather conditions are shown in Figure 1.6.

The variations in the weathering crust that result from changing weathering conditions affects both the meltwater (and microbe) transport and the albedo [Tedstone et al., 2020, Chandler et al., 2015]. I will now demonstrate this using an example

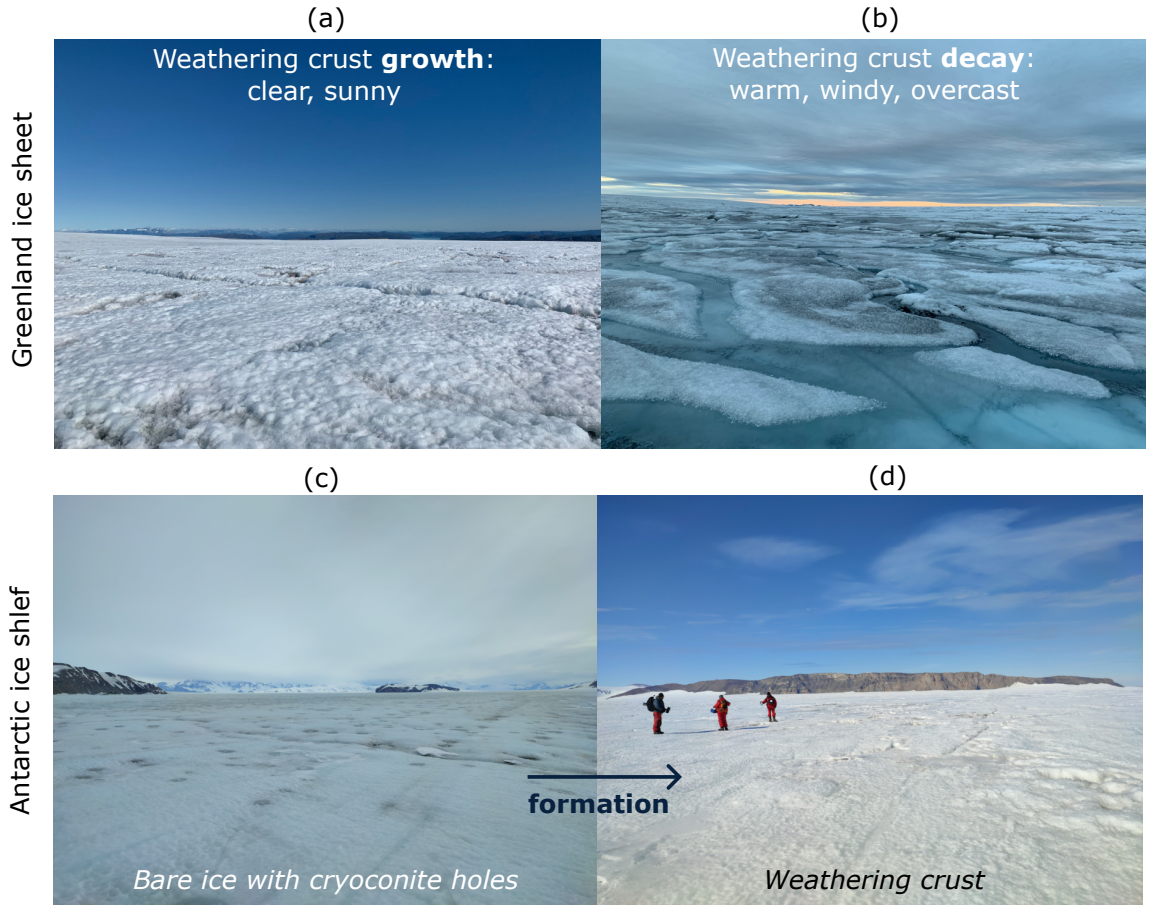


Figure 1.6: Photos of weathering crusts in different weather condition. Photos (a) and (b) show weathering crusts on Greenland in (a) clear, sunny conditions that favour weathering crust growth, and (b) warm, windy, cloudy conditions that promote weathering crust decay and removal (credit: Eva Doting). The weathering crust in (a) appears clean and white with a high albedo. In photo (b), there is more meltwater on the surface as the crust melts away, resulting in a lower albedo. Panels (c) and (d) show the formation of (d) a weathering crust from (c) bare ice with frozen cryoconite holes from one day to the next on Hells Gate Ice Shelf, Antarctica in December 2022 (credit: Giacomo Traversa). The clean, white weathering crust in (d) has a higher albedo than the bare ice in (c).

scenario based on observations from Greenland presented by Tedstone et al. [2020], Chandler et al. [2015], and guided by the photos from Greenland in Figure 1.6(a),(b). Suppose we start with a snow-covered surface at the start of the melt season. This has a high albedo. The snow then melts away, resulting in wet, bare ice, possibly with melt ponds present. This has a lower albedo (meaning it absorbs more radiation). Dirty ice from the previous year that had been buried under frozen meltwater and snow can also be exposed. A clear sunny period (with high levels of shortwave radiation) can result in the formation of a weathering crust via subsurface melting. The water from the surface drains away through the porous weathering crust, resulting in a drier, white-looking crust with a higher albedo (Figure 1.6(a)). Suppose the weather now turns warm, windy and cloudy for a few days. This results in the

weathering crust being melted away from the surface, possibly releasing debris and microbes from cryoconite holes and distributing them across the surface. The result is a wetter, dirtier-looking weathering crust with a lower albedo (Figure 1.6(b)). Continued warm, windy, cloudy conditions result in complete weathering crust removal and a return to wet, bare ice. The growth and removal of the weathering crust from bare-ice can happen many times in a melt season.

In order to understand the behaviour of the weathering crust and what impact it has on melting and the transport of meltwater, we need to understand its transient response to changing weather and climate conditions. Exploring this response is another focus of this thesis.

1.4 Thesis overview

In this chapter, I have highlighted the importance of the weathering crust in determining the amount of surface melting and runoff from an ice–sheet surface, via its affect on the surface albedo and meltwater transport. I have also pointed out that microbes that live within the weathering crust play an important role in determining the albedo and are intrinsically connected to the weathering crust structure. The key questions that have been raised, and which this thesis aims to address, are as follows:

1. How does the weathering crust affect the production and transport of meltwater on an ice–sheet surface?
2. How does the weathering crust respond to changing weather conditions?
3. How do the weathering crust and microbes within it interact, and how does this interaction influence albedo, melting and runoff?

A natural way to explore these questions is through the use of a mathematical model. However, there have been limited attempts to model the weathering crust [Schuster, 2001, Hoffman et al., 2008, 2014], and none of these have incorporated microbes or explicitly modelled meltwater flow. Similarly, a combination of observations and modelling have been used to assess and quantify the contribution of glacier algae to albedo and surface runoff [e.g. Cook et al., 2017, 2020, Tedstone et al., 2020, Chevrollier et al., 2023], but none of these studies have modelled microbial growth processes or accounted for interactions with the weathering crust.

This thesis acts to bridge these gaps and address the above questions by developing and using a continuum mathematical model for the evolution of the weathering crust and the microbes and nutrients that live within it.

1.5 Thesis structure

The structure of this thesis is as follows.

In Chapter 2, we begin by presenting the model for the weathering crust and meltwater flow. The model is presented in three dimensions, but this thesis uses only the one-dimensional simplification. For the rest of Chapter 2, we neglect meltwater flow, restrict to a fully saturated weathering crust, and seek so-called 'steadily melting' solutions in which constant weather conditions cause the surface to lower at a constant rate. We investigate how the structure of the weathering crust is affected by different forcing conditions.

In Chapter 3, we extend the work of Chapter 2 to seek time-dependent solutions to the one-dimensional weathering crust model with no water flow. The problem is solved numerically using an enthalpy method. We explore the mechanisms of weathering crust growth and decay in different idealised weather conditions.

In Chapter 4, we present a model for microbes and nutrients within the weathering crust, couple this to the weathering crust model, and seek both steadily melting and time-dependent solutions. We explore the effect of weather conditions on the microbial abundance and distribution, the effect of microbes on the albedo, and the potential feedbacks between the weathering crust and microbes that could enhance melt.

In Chapter 5, we introduce meltwater flow into the one-dimensional model, including a parametrisation for the lateral flow of meltwater through the weathering crust. We investigate the effect of lateral drainage efficiency on the weathering crust structure, hydrology and surface lowering. We do this using both steadily melting solutions and idealised time-dependent solutions.

In Chapter 6, we use weather data from the Greenland ice sheet to provide forcings for our model, and compare our model results to observations of surface lowering and porosity. We compare solutions from our model both with and without lateral drainage of meltwater.

In Chapter 7, we conclude and discuss areas for future work.

In the rest of this chapter, I present some background on radiation and the energy balance of an ice sheet, which are a key part of weathering crust evolution and will be helpful for the rest of the thesis.

1.6 Surface energy balance and internal radiation

The growth and decay of the weathering crust is controlled by the weather conditions. These conditions can be represented in a model via the *surface energy balance* and *internal shortwave radiation*, both of which are introduced below, and which determine how much melting occurs at the surface and internally (below the surface). It is the balance between internal and surface melting which controls the growth and decay of the weathering crust [e.g. Schuster, 2001, Tedstone et al., 2020].

1.6.1 Radiation

All matter emits electromagnetic radiation to its surroundings. The emitted radiation is distributed over a band of wavelengths from a continuous spectrum, including ultraviolet radiation, visible light and infrared radiation. The spectrum of emitted radiation depends on the temperature T of the body, with the wavelength of the peak radiative flux being inversely proportional to T.

The spectra of radiation emitted by the sun ($T \sim 6000$ K) and the Earth's surface ($T \sim 300$ K) barely overlap, and define two bands of radiation: *shortwave radiation* emitted by the sun, and *longwave radiation* emitted by the Earth's surface. Shortwave radiation (wavelengths from 0.15 to 4 μm) consists of mainly visible light and ultraviolet radiation. Longwave radiation (4 to 120 μm) is infrared (thermal) radiation.

The intensity E of the emitted radiation also depends on the temperature T. A material that absorbs all the radiation incident on it is referred to as a 'black body', and emits the maximum possible radiation for any body of the same temperature. The sun and the Earth's surface are both approximately black bodies. For a black body, the Stefan-Boltzmann law gives the emitted radiation as

$$E = \sigma T^4, \tag{1.2}$$

where $\sigma = 5.67 \times 10^{-8}$ W m^{-2} K^{-4} is the Stefan-Boltzmann constant. For a material that is not a perfect black body, the emitted radiation is lower, given by $\epsilon\sigma T^4$, where $\epsilon \in (0, 1)$ is the surface emissivity. For further details, see Cuffey and Paterson [2010].

1.6.2 Surface and subsurface radiation

Radiation incident on an ice–sheet surface provides a key heat source both at the surface and in the ice below. Longwave radiation is completely absorbed at the surface, whereas shortwave radiation can penetrate some depth below the surface, with shorter wavelengths penetrating deeper. Some of the radiation that penetrates is absorbed by the ice, acting as a heat source. The rest is scattered back to the surface, becoming the 'reflected' shortwave radiation referred to in the definition of the albedo [Cuffey and Paterson, 2010]. In general, a proportion R_0 of the incident shortwave radiation is immediately reflected without penetrating or being absorbed. However, the Fresnel reflection coefficient R_0 is small for ice [e.g. 0.05 Perovich, 1990], so for simplicity we neglect it in this thesis, assuming that all incident radiation enters the ice.

The net downward subsurface shortwave radiation flux F_λ for a given wavelength λ decreases approximately exponentially with the depth Z below the surface,

$$F_\lambda \approx F_\lambda|_{Z=0} e^{-\kappa_\lambda Z}, \tag{1.3}$$

where κ_λ is the *extinction coefficient* for wavelength λ [Brandt and Warren, 1993]. The extinction coefficient depends on the absorption and scattering of the given wavelength, which depend on properties of the ice including the grain size and water content [Brandt and Warren, 1993, Cuffey and Paterson, 2010].

The wavelength dependence means that, even within the shortwave radiation band, longer wavelengths are absorbed more quickly (nearer the surface) than shorter ones. To avoid having to track each wavelength separately, this fact can be accounted for by treating some proportion χ of the absorbed shortwave radiation $(1 - a)Q_{\mathrm{si}}$ as being absorbed 'at' the surface, representing the longer wavelengths that are absorbed very quickly in a thin layer near the surface [Hoffman et al., 2014, Law et al., 2020]. For example, around 34% of incident shortwave radiation is absorbed in the top 10 cm below the ice surface [Cooper et al., 2021]. The attenuation of the remaining shortwave radiation that penetrates through this layer can be described

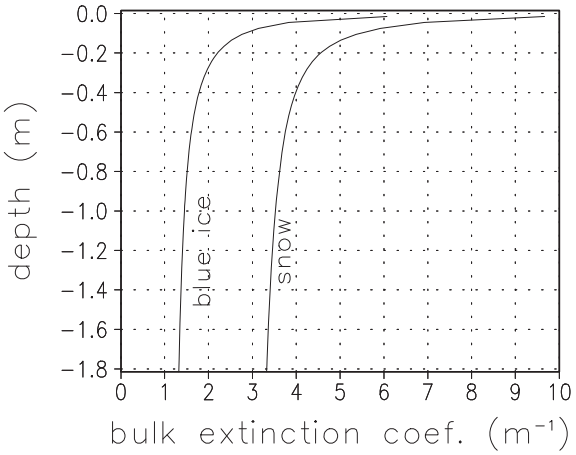


Figure 1.7: Bulk extinction coefficient κ as a function of depth for snow and blue ice (glacial ice with all the air bubbles squeezed out). Below a surface layer, κ is approximately constant. Figure reproduced from Liston et al. [1999] (with permission from Glen E. Liston and the publisher).

using a 'bulk' (wavelength-independent) extinction coefficient κ, as

$$F = F|_{Z=0} e^{-\kappa Z}, \tag{1.4}$$

where F is the net downward internal shortwave radiation. The extinction coefficient κ varies with depth and depends on the ice properties (as discussed above). Figure 1.7 demonstrates that (within a homogeneous material) κ is approximately constant below a surface layer of rapid radiation absorption. The rapid near-surface absorption that is accounted for separately by χ, so it is reasonable to treat κ as uniform with depth when modelling the internal shortwave radiation [e.g. Bintanja and Van Den Broeke, 1995, Taylor and Feltham, 2005].

The exponential decay of radiation (1.4) is referred to as Beer's law, and has previously been used to model radiation attenuation in sea ice [e.g. Maykut and Untersteiner, 1971] and glaciers [e.g. Kelliher et al., 1996]. However, in this thesis, we use an alternative, more sophisticated approach to modelling the attenuation of internal shortwave radiation, called the *two-stream approximation* [e.g. Schlatter, 1972, Perovich, 1990, Liston et al., 1999, Taylor and Feltham, 2004, 2005].

1.6.3 Two-stream approximation

The *two-stream approximation* [e.g. Schlatter, 1972, Perovich, 1990, Liston et al., 1999, Taylor and Feltham, 2004, 2005] has been used to model radiation attenuation in sea ice [Perovich, 1990, Taylor and Feltham, 2004], glacial ice [Liston et al., 1999],

snow on ice–sheet surfaces [Schlatter, 1972, Liston et al., 1999], surface melt lakes [e.g. Law et al., 2020], and weathering crusts [Hoffman et al., 2008, 2014]. One advantage of the two-stream approximation — and the reason that we choose to use it here — is that it allows for absorption and scattering coefficients α and r, respectively, to vary with depth and evolving ice properties (such as porosity, water content and microbe distributions).

The two-stream approximation decomposes the net (downward) internal radiation flux F into downward F_- and upward F_+ travelling components, satisfying

$$\frac{\partial F_-}{\partial Z} = -(\alpha + r)F_- + rF_+, \tag{1.5}$$

$$\frac{\partial F_+}{\partial Z} = (\alpha + r)F_+ - rF_-, \tag{1.6}$$

with $\alpha, r > 0$. These equations tell us that, as we move through the ice, F_- is decreased by some of this radiation being absorbed and reflected, but increased by some of F_+ being reflected (and so changing from a downward to an upward flux). A similar argument applies for F_+.

In an infinite domain with uniform absorption and scattering coefficients, the solution of the two-stream equations reduces to Beer's law (1.4), with $F = F_- - F_+$.

Although we use 'bulk' absorption and scattering coefficients in this thesis, it is also possible to use the two-stream approximation with spectrally dependent F_λ, α_λ and r_λ [e.g. Liston et al., 1999, Hoffman et al., 2014].

1.6.4 Surface energy balance

Ice sheets and glaciers receive energy fluxes that contribute to heating and melting in the form of shortwave radiation from the sun, longwave radiation, and heat fluxes from the atmosphere. They also emit longwave radiation. Most of the energy fluxes incident on the ice sheet are absorbed in a thin surface layer. We treat all of this absorption as happening **at** the surface. The *surface energy balance* (demonstrated illustratively in Figure 1.8) tells us that the energy fluxes into the ice surface must balance or, if not, any excess energy must be used to melt the surface at rate m_{surf}. This can be represented mathematically as

$$-k\frac{\partial T}{\partial z} + \chi(1-a)Q_{\text{si}} + Q_{\text{li}} + Q_{\text{lo}} + \text{SHF} + \text{LHF} + E_{\text{p}} = \rho_{\text{w}}\mathcal{L}m_{\text{surf}} \tag{1.7}$$

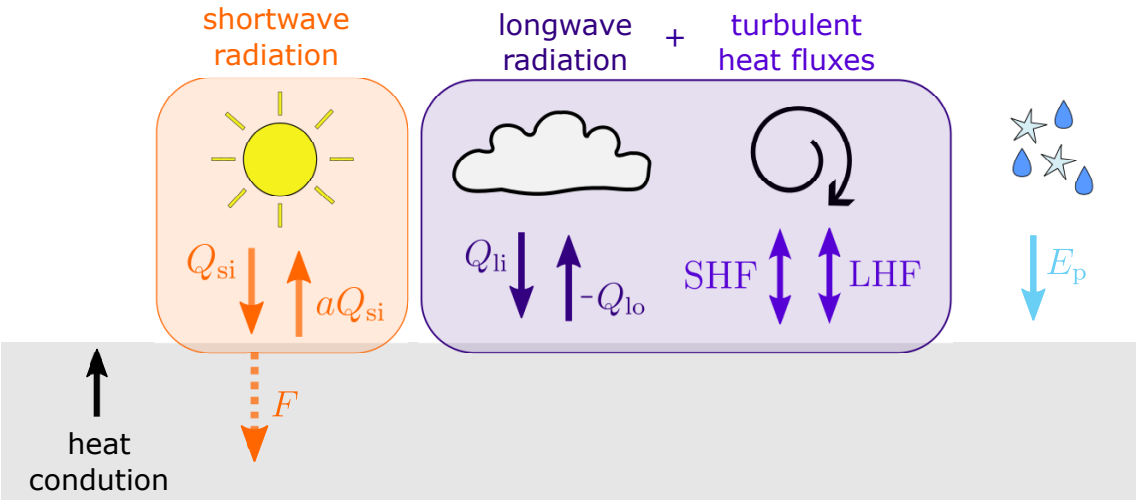


Figure 1.8: Schematic of the surface energy balance (1.7), and the internal shortwave radiation F that penetrates below the surface. The sum of the surface energy components shown gives the energy $\rho_w \mathcal{L} m_{surf}$ available to melt the surface, following equation (1.7). It is the balance between the shortwave radiation Q_{si} (orange box) and the combined shortwave and longwave radiation (represented by Q_0 from Chapter 2 onwards, purple box) that determine the state of the weathering crust. Clear, sunny conditions (high shortwave radiation) favour weathering crust growth, whereas warm, windy, cloudy conditions (high longwave radiation and turbulent heat fluxes) promote decay.

at the ice surface, where $-k\frac{\partial T}{\partial z}$ is the conductive heat flux from the ice below the surface (k is the thermal conductivity of the ice), $\chi(1-a)Q_{si}$ is the shortwave radiation absorbed 'at' the surface, Q_{li} is the incoming (incident) longwave radiation, Q_{lo} is the outgoing (emitted) longwave radiation, SHF is the sensible turbulent heat flux, LHF is the latent turbulent heat flux, E_p is the heat flux from precipitation (rainfall and snowfall), and $\rho_w \mathcal{L} m_{surf}$ is the energy available to melt (ρ_w is the density of water, $\mathcal{L}$ is the latent heat of fusion of water). All the components of the surface energy balance are energy fluxes with units W m^{-2} and are defined as positive when directed towards the surface. Hence, $Q_{lo} \leq 0$ since it represents emitted radiation, and $Q_{si}, Q_{li} \geq 0$ since they represent incident radiation. SHF and LHF can take either sign. Some components are explained in more detail below.

A comment on the vertical coordinate may be helpful at this stage. Throughout this thesis, z is used as a vertical coordinate pointing *upwards*, whereas Z is used as the vertical coordinate measured *downwards* from the ice surface.

1.6.4.1 Shortwave radiation

The shortwave (solar) radiation incident on the ice surface is Q_{si}. The total amount of shortwave radiation absorbed by the ice is determined by the albedo a as $(1-a)Q_{si}$.

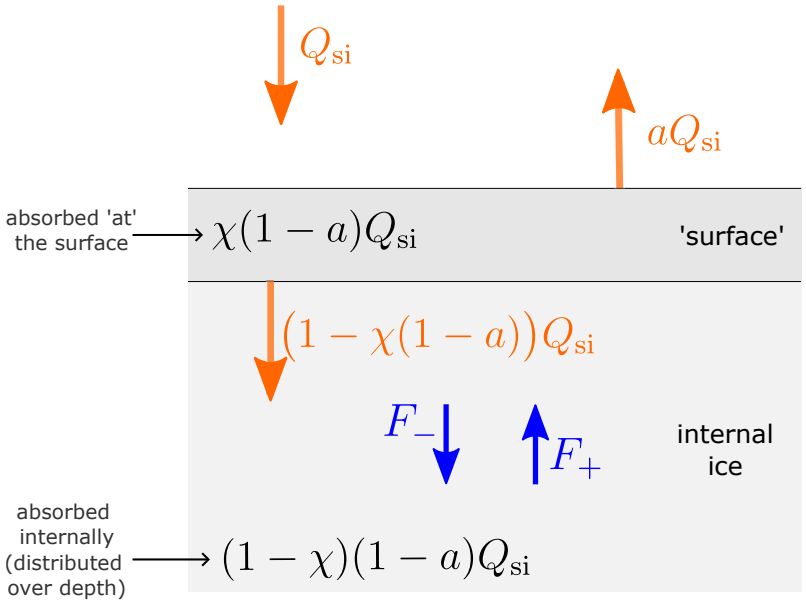


Figure 1.9: Partitioning of shortwave radiation Q_{si} between the surface and subsurface. An amount $\chi(1-a)Q_{\mathrm{si}}$ is absorbed immediately in a thin surface layer that is treated as being absorbed 'at' the surface. The remaining radiation penetrates through the surface into the internal ice, where it becomes internal radiation $F = F_- - F_+$ (net downwelling), which is modelled using a two-stream approximation (1.5), (1.6). An amount $(1-\chi)(1-a)Q_{\mathrm{si}}$ of the internal radiation is absorbed, distributed over depth. The rest, aQ_{si} is reflected back out through the surface. The albedo a determines the proportion of incident shortwave radiation that is reflected (not absorbed) by the ice. The partitioning parameter χ determines the proportion of the absorbed radiation which is absorbed 'at' the surface.

Using the above approach, an amount $\chi(1-a)Q_{\mathrm{si}}$ is absorbed 'at' the surface. The remainder penetrates and becomes subsurface 'internal' radiation, which we model using the two-stream approximation (Section 1.6.3). This partitioning of shortwave radiation is demonstrated in Figure 1.9.

1.6.4.2 Longwave radiation

The ice–sheet surface emits longwave (thermal) radiation Q_{lo} according to the Stefan-Boltzmann law (1.2), with a surface emissivity $\epsilon < 1$ to account for the fact that the ice is not a perfect black body, giving

$$Q_{\mathrm{lo}} = -\epsilon\sigma T^4, \tag{1.8}$$

where T is the temperature of the ice surface. (Note that the minus sign is due to Q_{lo} representing emitted radiation but being defined as positive when directed *towards* the surface.)

Some of the emitted longwave radiation is reflected back down to the ice surface off of clouds, or re-emitted from greenhouse gases, giving the incoming longwave radiation Q_{li}.

1.6.4.3 Turbulent heat fluxes

Turbulent heat fluxes take into account the fact that if the air is warmer than the ice surface then winds can cause turbulent eddies which transfer heat from the air to the surface. This gives the sensible turbulent heat flux SHF. Similarly, if the air above the surface is dry, turbulent mixing transfers moisture away from the surface, which is replaced by evaporation or sublimation, consuming latent heat. This gives the latent turbulent heat flux LHF [Cuffey and Paterson, 2010].

1.6.5 Linking to weather conditions

The behaviour of the weathering crust in different weather conditions can be described in terms of the surface energy balance components. The clear, sunny conditions that favour weathering crust growth correspond to high levels of shortwave radiation and low levels of longwave radiation and turbulent heat fluxes. The warm, windy, cloudy conditions which promote decay of the weathering crust correspond to large turbulent heat fluxes and longwave radiation, and low levels of shortwave radiation. It is the balance between shortwave radiation (some of which penetrates below the surface) and longwave radiation and turbulent heat fluxes (which only affect the surface energy balance) that is important for determining the state of the weathering crust [e.g. Schuster, 2001, Tedstone et al., 2020].

Chapter 2

Model development and steadily melting solutions

This chapter is adapted from work published in The Cryosphere in the manuscript 'A model of the weathering crust and microbial activity on an ice–sheet surface' [Woods and Hewitt, 2023]. Section 2.5.3 is adapted from work published in the IMA Journal of Applied Mathematics in the manuscript 'Modelling the evolution of an ice sheet's weathering crust' [Woods and Hewitt, 2024].

In this chapter, we will present the continuum mathematical model for the weathering crust that will be used throughout this thesis. We will also seek steady solutions to a reduction of the model that neglects meltwater flow. Before providing a more detailed outline of this chapter in Section 2.2, I will now discuss relevant existing models to motivate our work.

2.1 Existing models

Modelling is a powerful tool that has been used extensively to study various aspects of ice sheets, including the surface hydrological system. Examples include the routing of surface meltwater and its connections to the formation, refreezing and drainage of surface melt lakes [e.g. Buzzard et al., 2018, Law et al., 2020, Leeson et al., 2012, Banwell et al., 2012, Gantayat et al., 2023], the percolation of meltwater through firn [e.g. Meyer and Hewitt, 2017, Gray, 1996, Ligtenberg et al., 2011, Moure et al., 2023, Colbeck, 1972], and the lateral transport and storage of meltwater in firn aquifers [Miller et al., 2020, 2023].

However, existing studies of the weathering crust have primarily focussed on observations from the field rather than modelling [e.g. Müller and Keeler, 1969, Cooper et al., 2018, Cook et al., 2016, Chandler et al., 2015, Irvine-Fynn et al., 2021]. Until now, there have been limited attempts to model the weathering crust [Schuster, 2001, Hoffman et al., 2008, 2014], and these have focussed on specific aspects of the vertical structure. Schuster [2001], Hoffman et al. [2008, 2014] all present one-dimensional (vertical) models forced by shortwave and longwave radiation and turbulent heat fluxes (introduced in Chapter 1) from observed weather data. Schuster [2001] presented a physically-based 6-layer model for the density of the weathering crust, with density changes driven by internal melting resulting from internal shortwave radiation. At each 5 minute timestep, the melt volume in each layer is calculated directly from the internal shortwave radiation (and surface energy balance in the top layer), and this is used to adjust the density in each layer. They do not model the temperature of the ice. Their results compare well to ice core measurements, but they note that there is uncertainty in these measurements. Hoffman et al. [2008, 2014] modelled the temperature within the ice using the heat equation with a heat source provided by internal shortwave radiation, obtaining predictions of surface lowering and internal melt extent over time. The internal shortwave radiation was modelled using a two-stream approximation with spectrally dependent extinction coefficient. They do not evolve the density/porosity during model runs, but consider its effect when calculating surface lowering. Their results compare well to observed surface lowering when the refreezing and drainage of meltwater are accounted for. Both Schuster [2001] and Hoffman et al. [2014] consider the effect of allowing water to refreeze in the weathering crust when there is a negative energy available to melt, leading to a change in ice density. One way to improve on these existing models is to model both the evolution of the temperature and density/porosity at once. We do this in the model presented in this thesis.

Moreover, none of the existing weathering crust models have modelled the flow of meltwater through the weathering crust. Hoffman et al. [2014] considered the effect of lateral internal drainage by removing any meltwater exceeding a 10% melt fraction at each timestep, but they did not model any vertical flow within the crust. However, there have been several previous one-dimensional models for the vertical percolation of meltwater through snow which can be adapted to the weathering crust (see the model intercomparison by Vandecrux et al. [2020] for examples). Many models are inherently numerical, with water being transferred from one discrete layer to the next using a 'tipping bucket' scheme [e.g. Ligtenberg et al., 2011, Munneke et al., 2014, 2015]. In addition to this, some theoretical physics-based models for meltwater

percolation through snow have also been developed [e.g. Colbeck, 1972, 1974, 1976, Gray, 1996], using Darcy's law (described later in this chapter) to describe flow driven by gravity and capillary pressure. Many of these percolation models are isothermal [e.g. Colbeck, 1972, 1974, Sellers, 2000], but others have also considered phase change (melting and refreezing); coupling meltwater flow to thermodynamics [e.g. Colbeck, 1976, Meyer and Hewitt, 2017].

The snow models discussed above primarily focus on the percolation and refreezing of surface meltwater, and do not account for internal melting within the snow as a result of penetrating shortwave radiation. The snowpacks studied are typically tens of metres thick and shortwave radiation only penetrates to about 1 m depth (compared to several metres depth in ice) [e.g. Liston et al., 1999], so it is appropriate to treat all radiation absorption as occurring 'at' the surface. This is in contrast to the $\sim$ 1 m thick weathering crust, in which penetrating shortwave radiation is crucial for its formation [e.g. Müller and Keeler, 1969]. Models for internal shortwave radiation have already been discussed in Section 1.6 in Chapter 1, and are included in existing weathering crust models [Schuster, 2001, Hoffman et al., 2008, 2014].

In this thesis, we fill a gap in weathering crust modelling by developing a single continuum model that accounts for thermodynamics, internal shortwave radiation and meltwater flow.

2.2 Outline

In this chapter, we begin by developing a continuum model for the evolution of the weathering crust, incorporating thermodynamics and meltwater flow (Section 2.3). The model accounts for conservation of mass and energy, meltwater flow governed by Darcy's law, and internal and surface-absorbed radiation, allowing for melting internally and at the surface, and for internal refreezing. Our model gives predictions for the porosity and temperature, as well as the weathering crust thickness, water content, water fluxes, internal and surface melt rates, and surface lowering.

The model presented in Section 2.3 will be used throughout this thesis, and will be coupled to a model for microbes and nutrients within the weathering crust in Chapter 4. Later in this chapter (Sections 2.4, 2.5), we reduce the model to one dimension and focus on what we call *steadily melting solutions*, in which constant radiative and atmospheric conditions cause the surface to lower at a constant rate. Along with other simplifications (introduced in Section 2.3), this also means that

there is no water flow (something that will be reintroduced in Chapter 5 by including a parametrisation of lateral drainage).

We present the steadily melting reduction of the model in Section 2.4. In Section 2.5, we present the steadily melting solutions, use these solutions to investigate how the structure of the weathering crust is affected by the forcing conditions, and make some qualitative comparisons to the observed response of weathering crusts to different weather conditions. In Section 2.6, we summarise and identify links to the subsequent chapters in this thesis.

2.3 Weathering crust model

Firstly, we present a model for the evolution of the structure of the weathering crust, shown schematically in Figure 2.1. We model the weathering crust as porous ice with upper surface $z = h(t)$. The pores can contain both water and air. The ice takes up a volume fraction $1 - \phi$, where ϕ is the porosity. The saturation S describes the proportion of the pore space taken up by water, so ϕS is the volume fraction of water and $\phi(1 - S)$ is the volume fraction of air. Note that the saturation S is not well-defined when there is no pore space (i.e. when $\phi = 0$), but the volume fractions

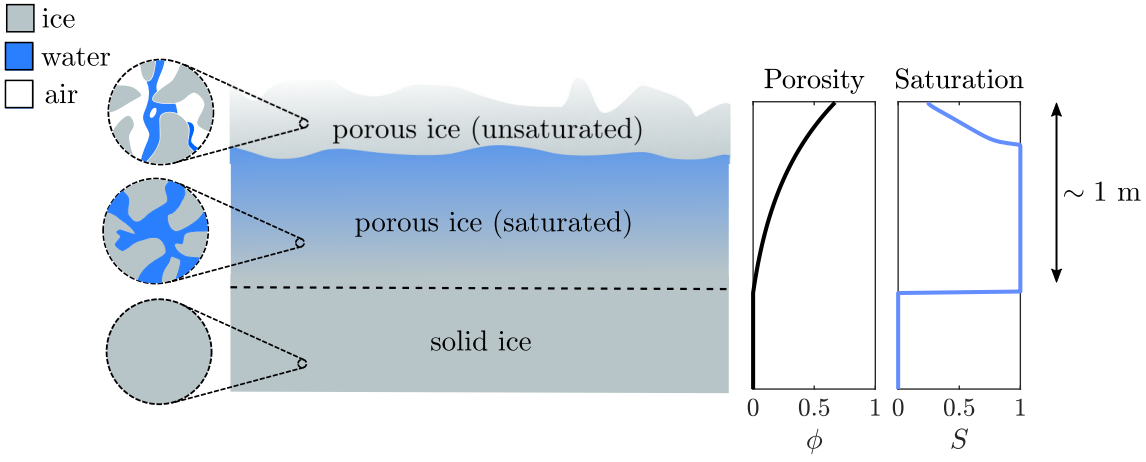


Figure 2.1: Schematic of a weathering crust - a near-surface layer of porous ice (above the dashed line), below which the ice is impermeable (though the "solid" ice shown here may contain small, closed-off air bubbles). The porosity of the weathering crust decreases with depth. Much of it is saturated with meltwater, with a thin unsaturated layer at the surface. The saturated layer is known as the "weathering crust aquifer". Typical porosity ϕ and water saturation S profiles are shown. Here, and in the rest of this thesis, we set $S = 0$ in solid ice ($\phi = 0$) to make the bottom of the weathering crust clearly visible in the S profile. Schematic based on Cooper et al. [2018], Moure et al. [2023].

ϕS and $\phi(1-S)$ are meaningful everywhere (and equal to zero when $\phi = 0$). When plotting solutions, we choose to set $S = 0$ where $\phi = 0$ to clearly mark the transition from saturated, porous ice ($S = 1$) to solid ice (with S set to 0) at the bottom of the weathering crust. The porosity and saturation can evolve by the ice melting internally at a rate m_{int} (with negative m_{int} corresponding to water freezing in the pores) and by the water flowing through the porous ice. The internal melting is driven by shortwave (solar) radiation penetrating below the ice surface. We now present the governing equations.

2.3.1 Mass conservation

Mass conservation equations for the ice, water and air, respectively, are

$$\frac{\partial}{\partial t}\Big((1-\phi)\rho_{\text{i}}\Big) + \nabla\cdot\Big((1-\phi)\rho_{\text{i}}\mathbf{u}_{\text{i}}\Big) = -m_{\text{int}}, \tag{2.1}$$

$$\frac{\partial}{\partial t}\Big(\phi S\rho_{\text{w}}\Big) + \nabla\cdot\Big(\phi S\rho_{\text{w}}\mathbf{u}_{\text{w}}\Big) = m_{\text{int}}, \tag{2.2}$$

$$\frac{\partial}{\partial t}\Big(\phi(1-S)\rho_{\text{a}}\Big) + \nabla\cdot\Big(\phi(1-S)\rho_{\text{a}}\mathbf{u}_{\text{a}}\Big) = 0, \tag{2.3}$$

where ρ_{i}, ρ_{w}, ρ_{a} are the densities of ice, water and air, respectively; and $\mathbf{u}_{\text{i}}$, $\mathbf{u}_{\text{w}}$, $\mathbf{u}_{\text{a}}$ are their velocities. Since air is much less dense than ice and water ($\rho_{\text{a}} \ll \rho_{\text{i}}, \rho_{\text{w}}$), we can neglect the air equation (2.3). The ice velocity $\mathbf{u}_{\text{i}}$ could be prescribed (or taken from a larger-scale ice–sheet model) to account for the upward advection of ice in the ablation zone. However, for our purposes in this study, we will later set $\mathbf{u}_{\text{i}}$ to zero for the specific one-dimensional solutions we consider.

2.3.2 Darcy's law

Darcy's law describes the flow of a fluid through a porous medium, driven by gravity and pressure gradients [e.g. Bear, 2018]. The volume flux $\mathbf{q}$ of water per unit area relative to the ice is given by Darcy's law as

$$\mathbf{q} = \phi S(\mathbf{u}_{\text{w}} - \mathbf{u}_{\text{i}}) = -\frac{k(\phi)k_{\text{rw}}(S)}{\mu}\left(\nabla p_{\text{w}} + \rho_{\text{w}} g\hat{\mathbf{k}}\right), \tag{2.4}$$

where p_{w} is the water pressure, $k(\phi)$ is the permeability, $k_{\text{rw}}(S)$ is the relative permeability, μ is the viscosity of water, g is the acceleration due to gravity, and $\hat{\mathbf{k}}$ is the upward pointing unit vector. In an unsaturated porous medium ($0 < S < 1$),

the water pressure p_w is determined by the capillary pressure as a function of S (see Section 2.3.2.3).

2.3.2.1 Permeability

The (absolute) permeability $k(\phi)$ is a material property of a porous material and is an indication of how easy it is for a fluid to flow through the material. The permeability depends on the porosity as well as microscopic properties of the material, such as the grain size and shape. In a continuum model, we do not have this microscopic detail, so we must express the permeability purely in terms of macroscopic properties such as the porosity. A commonly used parametrisation is the Carmen–Kozeny relationship [Kozeny, 1927, Carman, 1937]

$$k(\phi) = k_0 \frac{\phi^3}{(1-\phi)^2}. \tag{2.5}$$

However, in this thesis, we use a simplified form [e.g. Meyer and Hewitt, 2017]

$$k(\phi) = k_0 \phi^3, \tag{2.6}$$

which is a good approximation when the porosity is small. A rough scaling argument can be used to express k_0 in terms of a representative grain size d_p, as $k_0 = \frac{d_p^2}{180}$ [e.g. Fowler, 2011].

2.3.2.2 Relative permeability

The relative permeability $k_\mathrm{rw}(S)$ is used to modify the permeability when the pore space is unsaturated (i.e. there is air, as well as water, present in the pore space), with $k_\mathrm{rw} \in [0, 1]$ [e.g. Bear, 2018]. In general, the relative permeability must be measured experimentally for each different material and fluid [e.g. Bear, 2018, Pinder and Gray, 2008]. This results in a 'relative permeability curve' relating the saturation and relative permeability. In modelling applications, it is desirable to approximate the relative permeability curve by a one-to-one analytical relationship $k_\mathrm{rw}(S)$. This is a commonly used approach [e.g. Bear, 2018], but we should note that it does not provide a complete description. For example, the relative permeability can generally exhibit hysteresis, with the relationship between k_rw and S being different depending on whether the pores are filling or draining [Bear, 2018]. Although, in fact, hysteresis in k_rw is less significant than hysteresis in the capillary pressure p_c (see below) and

is usually ignored [Pinder and Gray, 2008, Bear, 2018]. Moreover, k_{rw} can generally depend on additional factors such as fluid properties and the pore-size distribution of the porous material Pinder and Gray [2008], which are not captured by the analytical representation $k_{\mathrm{rw}}(S)$.

Many analytical relationships between the relative permeability and saturation have been suggested [e.g. Bear, 2018]. These are typically informed by simplified models of porous media (such as a bundle of capillary tubes) and by fitting to experimental data [Bear, 2018]. Experiments show that relative permeability is an increasing function of saturation S [e.g. Pinder and Gray, 2008], so this should also be true of the analytical function $k_{\mathrm{rw}}(S)$. In addition, in materials such as fine-grained soils, there is a small residual amount of water, which cannot be removed when the material is drained [e.g. Fowler, 2011]. This is due to capillary pressure effects (discussed below). We can capture this behaviour in $k_{\mathrm{rw}}(S)$ by ensuring that $k_{\mathrm{rw}}(S) = 0$ when $S \leq S_{\mathrm{res}}$, where S_{res} is the residual saturation. Finally, $k_{\mathrm{rw}}(S)$ should satisfy $k_{\mathrm{rw}}(1) = 1$ (by definition). One such representation of the relative permeability is [e.g. Fowler, 2011]

$$k_{\mathrm{rw}}(S) = \left(\frac{S - S_{\mathrm{res}}}{1 - S_{\mathrm{res}}} \right)_+^3, \tag{2.7}$$

where $(*)_+ = \max(*, 0)$. In this thesis, we use the parametrisation

$$k_{\mathrm{rw}}(S) = S^3, \tag{2.8}$$

making the simplification to neglect the small residual saturation.

2.3.2.3 Capillary pressure

In the pore space of an unsaturated porous medium, the microscopic interfaces between the air and water are curved, causing a suction effect due to surface tension [e.g. Fowler, 2011, Bear, 2018]. In equilibrium, the curvature is constant throughout the pore space, with the value of the curvature depending on the saturation. The less water there is, the greater the curvature. In turn, a higher curvature results in a greater suction due to surface tension across the air/water interface. The difference between the air and water pressures can therefore be expressed in terms of the mean curvature and hence S. This is represented by the *capillary pressure* $p_{\mathrm{c}}(S)$ which relates the air and water pressures, p_{a} and p_{w}, as,

$$p_{\mathrm{a}} - p_{\mathrm{w}} = p_{\mathrm{c}}(S). \tag{2.9}$$

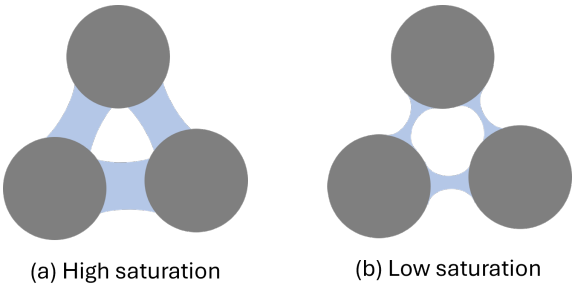


Figure 2.2: Schematic of water (blue) and air (white) in the pore space of an unsaturated porous medium for both (a) high and (b) low water saturations S. As the saturation S increases, the curvature of the water-air interface decreases, since the contact angle between the solid (e.g. ice) grains (grey circles) and water remains constant in equilibrium. This idea is used to develop the parametrisation (2.10) for the capillary pressure.

In practice, the capillary pressure $p_\mathrm{c}(S)$ displays hysteresis, behaving differently depending on whether the saturation is increasing or decreasing. However, for our model, we require p_c to be a one-to-one function of the saturation. We choose to use the parametrisation used by Meyer and Hewitt [2017] for snow,

$$p_\mathrm{c}(S) = \frac{\gamma}{d_p} S^{-2}, \tag{2.10}$$

where γ is the surface tension and d_p is the mean grain size. Having assumed negligible air density, p_a is constant, so we set it to zero without loss of generality. This means that $p_\mathrm{w} = -p_\mathrm{c}$. Following Gray [1996], Meyer and Hewitt [2017], the exponents in the parametrisation for k_rw and p_c have been chosen to prevent singularities in the Darcy flux (2.4) as $S \to 0$.

If the pore space is saturated, the water pressure is instead found by solving the elliptical equation that results from combining equations (2.1), (2.2), (2.4). The boundary conditions are atmospheric pressure at the surface, continuity of pressure at the interface between saturated and unsaturated regions, and no flux at solid interfaces. More details are given in Chapter 5.

2.3.3 Energy equation

We also need to model the evolution of the temperature T, which we assume to be homogeneous across the ice–water–air mixture (by assuming local thermal equilibrium). We assume that if water is present in a particular region ($\phi > 0, S > 0$) then this region is at the melting temperature T_m. If there is no water present ($S = 0$), then the ice can be below the melting temperature, $T \leq T_\mathrm{m}$.

Conservation of energy leads to the equation

$$\begin{aligned}\frac{\partial}{\partial t}\Big[((1-\phi)\rho_{\mathrm{i}}c_{\mathrm{i}}+\phi S\rho_{\mathrm{w}}c_{\mathrm{w}})T\Big]+\nabla\cdot\Big[((1-\phi)\rho_{\mathrm{i}}c_{\mathrm{i}}\mathbf{u}_{\mathrm{i}}+\phi S\rho_{\mathrm{w}}c_{\mathrm{w}}\mathbf{u}_{\mathrm{w}})T\Big]\\ =\nabla\cdot\Big[(k_{\mathrm{i}}(1-\phi)+k_{\mathrm{w}}\phi S)\nabla T\Big]-\nabla\cdot\mathbf{F}-\mathcal{L}m_{\mathrm{int}}.\end{aligned} \tag{2.11}$$

The terms on the left-hand side represent the rate of change and advection of heat energy. The terms on the right hand side correspond to heat conduction according to Fourier's law, the heat source provided by internal shortwave radiation $\mathbf{F}$ (discussed further below), and the energy available for melting the ice. Here, c_{i}, c_{w} are the specific heat capacities and k_{i}, k_{w} are the thermal conductivities for ice and water respectively; and $\mathcal{L}$ is the latent heat of fusion of water. Consistent with assuming negligible density of air, we ignore both the heat content and the conductive heat flux in the air. We have assumed a simple volume averaging for the effective thermal conductivity of the combined ice–water mixture.

The energy equation captures two distinct situations. Firstly, when the system is below the melting temperature ($T < T_{\mathrm{m}}$), there cannot be any internal melting ($m_{\mathrm{int}} = 0$) and there is no water present ($S = 0$). The energy equation (2.11) then determines the temperature. Alternatively, when the system is at the melting temperature ($T = T_{\mathrm{m}}$), melting is possible ($m_{\mathrm{int}} \geq 0$) and water can be present ($S \geq 0$). Since we know that $T = T_{\mathrm{m}}$ in this case, the energy equation (2.11) instead determines the internal melt rate m_{int}.

2.3.4 Radiation model

The internal melting of the ice is caused by some of the shortwave radiation from the sun penetrating the ice and being absorbed below the surface, acting as an internal heat source. We model the internal shortwave radiation flux $\mathbf{F}$ following the two-stream approximation introduced in Section 1.6.3. That is, we assume that the net radiation flux can be decomposed into downward F_- and upward F_+ travelling components. The net radiation flux is then $\mathbf{F} = (F_+ - F_-)\hat{\mathbf{k}}$, where $\hat{\mathbf{k}}$ is the upward-pointing unit vector, with $F_\mp$ satisfying

$$\frac{\partial F_-}{\partial z} = (\alpha + r)F_- - rF_+, \tag{2.12}$$

$$\frac{\partial F_+}{\partial z} = -(\alpha + r)F_+ + rF_-, \tag{2.13}$$

where α and r are absorption and scattering coefficients, respectively, with $\alpha, r > 0$. We assume that α and r represent bulk properties of the ice–water mixture and, for now, we also assume that α and r are constant.

2.3.5 Kinematic conditions

The kinematic conditions for the ice and the water at the surface $z = h(t)$ are, respectively,

$$\rho_{\mathrm{i}}(1-\phi)\left(\mathbf{u}_{\mathrm{i}}\cdot\hat{\mathbf{k}}-\dot{h}\right)=\rho_{\mathrm{w}}m_{\mathrm{surf}} \quad \text{at} \quad z=h(t), \tag{2.14}$$

$$\rho_{\mathrm{w}}\phi S\left(\mathbf{u}_{\mathrm{w}}\cdot\hat{\mathbf{k}}-\dot{h}\right)=\rho_{\mathrm{w}}(r_{\mathrm{off}}-m_{\mathrm{surf}}) \quad \text{at} \quad z=h(t), \tag{2.15}$$

where $\mathbf{u}_{\mathrm{i}}\cdot\hat{\mathbf{k}}$ and $\mathbf{u}_{\mathrm{w}}\cdot\hat{\mathbf{k}}$ are the upward ice and water velocities (which, in the case of water, we expect to be negative), $\dot{h} = \mathrm{d}h/\mathrm{d}t$ is the velocity of the surface, m_{surf} is the rate of surface melting, and r_{off} is the rate of runoff.

We assume that any water at the surface drains down into the ice below, provided that the ice is unsaturated. If the surface becomes saturated, we assume that any excess water immediately runs off. (In reality, this corresponds to horizontal flow to other parts of the ice surface, and ultimately into the ocean.) The runoff term r_{off} is therefore only non-zero when the surface is saturated.

2.3.6 Surface energy balance

The energy balance at the surface $z = h(t)$ is based on the surface energy balance (1.7) presented in Chapter 1. For simplicity, we neglect latent heat transfer, LHF, due to evaporation/ablation since Van den Broeke et al. [2008, 2011] showed this contribution to be small compared to the other terms, at least in the ablation zone of the west Greenland ice sheet. The sensible turbulent heat flux SHF can be parametrised as [Cuffey and Paterson, 2010]

$$\mathrm{SHF} = \tilde{C}p_{\mathrm{a}}u(T_{\mathrm{a}}-T), \tag{2.16}$$

where $\tilde{C}$ is a heat transfer coefficient, p_{a} is the air pressure, u is the wind speed, T_{a} is the air temperature, and T is the surface temperature of the ice. The values of p_{a}, u and T_{a} are typically taken at a reference height of ~ 2 m above the surface.

We also assume that there is no rainfall or snowfall, so $E_\mathrm{p} = 0$. This results in

$$-\Big((1-\phi)k_\mathrm{i} + \phi S k_\mathrm{w}\Big)\frac{\partial T}{\partial z} + \chi(1-a)Q_\mathrm{si} \\ -\epsilon\sigma T^4 + Q_\mathrm{li} + \tilde{C}p_\mathrm{a}u(T_\mathrm{a} - T) = \rho_\mathrm{w}\mathcal{L}m_\mathrm{surf} \quad \text{at} \quad z = h(t), \tag{2.17}$$

where the terms in order from left to right represent conduction of heat from the porous ice; the shortwave radiation absorbed at the surface; emitted longwave radiation given by the Stefan–Boltzmann law for a black body (1.8); incoming longwave radiation (for example from reflection off clouds); sensible turbulent heat transfer; and latent heat flux available for surface melting at rate m_surf.

As discussed in Section 1.6, we use the parameter $\chi < 1$ — the proportion of the total amount of shortwave radiation absorbed by the ice that is absorbed at the surface — to allow some of the shortwave radiation to penetrate into the subsurface ice, where we model it explicitly as the internal shortwave radiation flux $\mathbf{F}$ in equations (2.12) and (2.13). In particular, this means that the downward internal radiation flux F_-, at the surface $z = h(t)$, is $(1 - \chi(1-a))Q_\mathrm{si}$ (see Figure 1.9). The upward flux F_+ is aQ_si. Note that in this model the albedo a is not an independent parameter. It is a result of the internal radiation calculation, dependent on the scattering and absorption coefficients α and r (see Sect. 2.5).

By linearising about the melting temperature, the surface energy balance can be re-written as

$$-\Big((1-\phi)k_\mathrm{i} + \phi k_\mathrm{w}\Big)\frac{\partial T}{\partial z} + \chi(1-a)Q_\mathrm{si} \\ +Q_0 - \upsilon(T - T_\mathrm{m}) = \rho_\mathrm{w}\mathcal{L}m_\mathrm{surf} \quad \text{at} \quad z = h(t), \tag{2.18}$$

where $Q_0 = Q_\mathrm{li} - \epsilon\sigma T_\mathrm{m}^4 + \tilde{C}p_\mathrm{a}u(T_\mathrm{a} - T_\mathrm{m})$ is a combination of longwave radiation and turbulent heat flux, which we will prescribe as a function of time; and $\upsilon = \tilde{C}p_\mathrm{a}u + 4\epsilon\sigma T_\mathrm{m}^3$ is an effective heat transfer coefficient, combining turbulence and radiation. A discussion of how weather observations, or a model, could be used to determine $Q_0(t)$ is given in Chapter 6.

2.3.7 Model summary

The full weathering crust model is given by the mass conservation equations (2.1) and (2.2) for ice and water, Darcy's law (2.4), the energy equation (2.11), and the two-stream equations (2.12) and (2.13) for the internal shortwave radiation, along

with a prescription of the ice velocity $\mathbf{u}_\mathrm{i}$, and suitable boundary conditions. As well as the kinematic conditions (2.14) and (2.15), the surface energy balance (2.18), and the condition for downward-travelling radiation F_- at the surface, we also require a condition on the upward-travelling radiation F_+ and the temperature T in the far-field (discussed below). The incoming shortwave radiation Q_si and the combined longwave radiation and turbulent heat fluxes Q_0 are prescribed functions of time, representing the climate forcing. As well as the temperature T, porosity ϕ, saturation S and water flux $\mathbf{q}$, additional outputs from the model are the surface and internal melt rates m_surf and m_int, and surface runoff r_off. Default parameter values used in the model are shown in Table 2.2.

2.3.8 Simplifications

We now make some simplifications to our model. Firstly, we make the approximation that the ice and water have the same material and thermal properties, introducing a shared density $\rho = \rho_\mathrm{i} = \rho_\mathrm{w}$, thermal conductivity $k = k_\mathrm{i} = k_\mathrm{w}$ and specific heat capacity $c = c_\mathrm{i} = c_\mathrm{w}$. Further, we reduce our model to one dimension, considering a vertical column of ice. We also assume suitable forcing conditions that result in a weathering crust with an impermeable base. These assumptions will hold throughout this thesis.

An effect of the impermeable base in the one-dimensional domain is that, once the weathering crust becomes saturated with meltwater, it will remain saturated and there will be no water flow. There is no mechanism for water to flow out of the domain (other than excess meltwater being removed from the surface as runoff). Therefore, we also assume in this chapter that the porous ice is saturated ($S = 1$) and that there is no flow of ice or water ($\mathbf{u}_\mathrm{i} = \mathbf{u}_\mathrm{w} = \mathbf{0}$). In reality, water flows laterally through the weathering crust [e.g. Cooper et al., 2018, Irvine-Fynn et al., 2021], and it is of interest what impact this has on the overall transport of meltwater across the ice–sheet surface. However, observed lateral flow speeds are slow (less than about 0.13 m d^{-1}) [Irvine-Fynn et al., 2021], which justifies neglecting horizontal water velocities for now and using a one-dimensional model. In particular, it allows us to focus of the evolution of the vertical structure of the weathering crust, to get a grasp on the conditions that promote growth and decay (i.e. a change in crust thickness) in a simplified setting. The assumption of no meltwater flow will be relaxed in Chapter 5, where we introduce a parametrisation for lateral drainage within the weathering crust.

Quantity	Symbol	Default value	Units
Density of ice	ρ	910	kg m^{-3}
Specific heat capacity of ice at 0°C	c	2097	J kg^{-1} K^{-1}
Thermal conductivity	k	2.1	kg m^{-3} K^{-1}
Melting temperature	T_m	273.15	K
Latent heat of melting	$\mathcal{L}$	334000	m^2 s^{-2}
Heat transfer coefficient[a]	$\tilde{C}$	2.58×10^{-5}	
Air pressure[a]	p_a	8×10^4	Pa
Wind speed[a]	u	5	m s^{-1}
Surface emissivity[b]	ϵ	0.97	
Stefan-Boltzmann constant	σ	5.67×10^{-8}	W m^{-2} K^{-1}
Albedo	a	0.6	
Proportion of absorbed shortwave radiation that is absorbed at the surface[c]	χ	0.36	
Extinction coefficient of internal shortwave radiation[d]	κ	1.5	m^{-1}
Unnamed optical property[e]	s	0.7009	
Absorption coefficient[e]	α	0.2637	m^{-1}
Scattering coefficient[e]	r	4.1338	m^{-1}
Mean grain size[b]	d_p	10^{-4}	m
Surface tension[b]	γ	0.07	N m^{-1}
Permeability constant[f]	k_0	5.56×10^{-11}	m^2
Viscosity of water	μ	10^{-3}	Pa s
Incoming shortwave radiation flux	Q_{si}	200	W m^{-2}
Turbulent heat and longwave radiation flux[g]	Q_0	-20	W m^{-2}
Effective heat transfer coefficient[h]	υ	14.8	W m^{-2} K^{-1}
Temperature at depth	T_∞	-10	°C

Table 2.2: Default values of the parameters in the weathering crust model. [a]Cuffey and Paterson [2010]. [b]Meyer and Hewitt [2017]. [c]Motivated by Hoffman et al. [2014]. [d]Taylor and Feltham [2005]. [e]Calculated from κ, a and χ using (2.32) and definitions of κ and s. [f]Calculated as $k_0 = d_p^2/180$ [Fowler, 2011]. [g]Inferred from Van den Broeke et al. [2011]. [h]Calculated as $\upsilon = \tilde{C} p_a u + 4\epsilon\sigma T_m^3$. Many of the ice properties are taken from Cuffey and Paterson [2010].

2.4 Steadily melting states

We now seek what we will refer to as 'steadily melting' solutions. These are solutions in which the surface is lowering at a constant rate $(-\dot{h})$, with the subsurface ice melting at exactly rate m_{int} to maintain a steady porosity profile below the surface. Therefore, relative to the surface, the solution looks the same at each snapshot in time, as if the column of porous ice is simply being translated downwards, as shown in Figure 2.3 (a). However, this effect is produced by internal and surface melting,

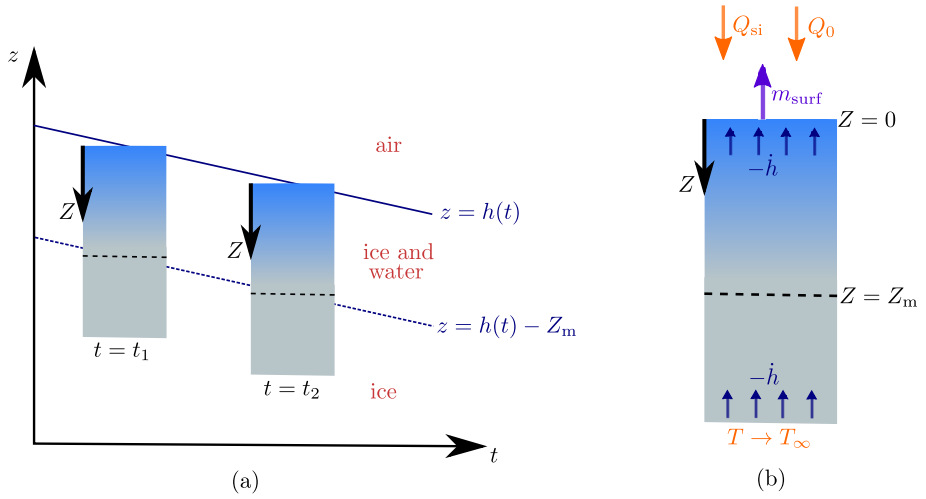


Figure 2.3: Schematic of the steadily melting setup. (a) shows how the surface of the ice $z = h(t)$ lowers over time in the steadily melting state, with the ice melting in such a way that it looks like the ice column is simply being translated downwards. (b) shows this column of ice in the $Z = h(t) - z$ frame. The forcings Q_{si}, Q_0, T_∞, and the surface melt rate m_{surf} are also shown.

not by the ice moving (recall that the ice velocity is zero, by assumption; in reality the downward melting of the ice surface may be counteracted by the upward advection of ice from the interior of the ice sheet). The steadily melting states correspond to an equilibrium between internal melting and surface lowering, which Schuster [2001] observed can occur on cloudy days when the crust is transitioning between growth and decay. It is not expected that this equilibrium lasts long; the weathering crust is very changeable, growing and decaying over a few hours as weather conditions change [Schuster, 2001]. We will seek time-dependent solutions to our model in Chapters 3, 5 and 6 to capture this variation. However, for simplicity and to gain some initial insight, we first use steady forcings.

The steadily melting setup suggests a natural change of coordinates to

$$Z = h(t) - z, \tag{2.19}$$

where Z is the depth below the surface $z = h(t)$ (see Figure 2.3). Note that Z points downwards. In the Z-frame, the melting surface of the ice is fixed at $Z = 0$, and the ice below gets advected upwards towards the surface at rate $-\dot{h}$, as shown in Figure 2.3(b). Making this transformation, and using the simplifications previously discussed, we can turn our general weathering crust equations into equations for the steadily melting solution. The two-stream equations (2.12) and (2.13) for the

internal radiation $F = F_- - F_+$ become

$$\frac{\mathrm{d}F_-}{\mathrm{d}Z} = -(\alpha + r)F_- + rF_+. \tag{2.20}$$

$$\frac{\mathrm{d}F_+}{\mathrm{d}Z} = (\alpha + r)F_+ - rF_-, \tag{2.21}$$

Both the ice and water mass conservation equations (2.1) and (2.2) reduce to

$$\rho\dot{h}\frac{\mathrm{d}\phi}{\mathrm{d}Z} = m_{\mathrm{int}}, \tag{2.22}$$

and the energy equation (2.11) becomes

$$\rho c\dot{h}\frac{\mathrm{d}T}{\mathrm{d}Z} = k\frac{\mathrm{d}^2T}{\mathrm{d}Z^2} - \frac{\mathrm{d}F}{\mathrm{d}Z} - \mathcal{L}m_{\mathrm{int}}. \tag{2.23}$$

The advective terms $\dot{h}\mathrm{d}/\mathrm{d}Z$ come from the time derivatives under the transformation $z \to Z$. As for boundary conditions, the kinematic conditions (2.14) and (2.15) tell us that

$$-\dot{h}(1-\phi) = m_{\mathrm{surf}} \quad \text{at} \quad Z = 0, \tag{2.24}$$

and that the runoff rate is

$$r_{\mathrm{off}} = -\dot{h}. \tag{2.25}$$

The linearised surface energy balance (2.18) becomes

$$k\frac{\mathrm{d}T}{\mathrm{d}Z} + \chi(1-a)Q_{\mathrm{si}} + Q_0 = \rho\mathcal{L}m_{\mathrm{surf}} \quad \text{at} \quad Z = 0, \tag{2.26}$$

where we have used the fact that $T = T_{\mathrm{m}}$ at the surface in order for surface melting to be possible. In addition to these conditions, we also prescribe a cold temperature $T_\infty < T_{\mathrm{m}}$ at depth, so

$$T \to T_\infty \quad \text{as} \quad Z \to \infty. \tag{2.27}$$

Finally, the boundary conditions for the two-stream equations (2.20) and (2.21) become

$$F_- = (1 - \chi(1-a))Q_{\mathrm{si}} \quad \text{at} \quad Z = 0, \tag{2.28}$$

and

$$F_+ \to 0 \quad \text{as} \quad Z \to \infty, \tag{2.29}$$

since we assume there is no source of shortwave radiation at depth. We also have

$$F_+ = aQ_{\mathrm{si}} \quad \text{at} \quad Z = 0, \tag{2.30}$$

which serves to determine the albedo a. Note that in some cases it may be more natural to prescribe the albedo a as a known (ie. measured) quantity, as we do when using Greenland weather data to force our model in Chapter 6. In this model, the albedo is related to χ, α and r, so independently prescribing a would mean that one of these other parameters must be prescribed consistently (see condition (2.32) below).

There are three forcings in our model, which we prescribe. These are the incoming shortwave radiation Q_{si}, the combined longwave radiation and turbulent heat fluxes Q_0, and the temperature of the ice at depth, T_∞. The outputs of the model are the internal shortwave radiation F, porosity ϕ and temperature T, as well as the internal melt rate m_{int}, surface melt rate m_{surf}, runoff r_{off} and rate of change of surface height $-\dot{h}$. We choose values of the forcings such that the surface is melting ($m_{\mathrm{surf}} > 0$) and the deep ice is cold. Therefore, as shown in Figure 2.3, we expect there to be a temperate region $0 < Z < Z_{\mathrm{m}}$ near the surface where the ice is porous ($\phi > 0$) and at the melting temperature ($T = T_{\mathrm{m}}$). This region is the weathering crust. In the region $Z > Z_{\mathrm{m}}$, the ice is solid ($\phi = 0$) and cold ($T < T_{\mathrm{m}}$). Z_{m} marks the bottom of the weathering crust, which must also be determined by the model. Unless there is a solid ice layer at the surface (as happens in Chapter 3), Z_{m} also represents the weathering crust thickness, which is how we refer to Z_{m} in this chapter.

2.5 Results

2.5.1 Steadily melting solutions

In the case where we have uniform (independent of Z) absorption coefficient α and scattering coefficient r, we can find the steadily melting solution analytically. Firstly, the two-stream equations (2.20) and (2.21) can be solved with boundary conditions (2.28) and (2.29) to find that the the internal radiation $F = F_- - F_+$ decreases exponentially with depth,

$$F_- = (1 - \chi(1 - a))Q_{\mathrm{si}}e^{-\kappa Z}, \quad F_+ = sF_-, \tag{2.31}$$

where the extinction coefficient κ is related to the absorption and scattering coefficients α and r by $\kappa = \sqrt{\alpha^2 + 2\alpha r}$, and $s = (\kappa - \alpha)/(\kappa + \alpha)$ [e.g. Taylor and Feltham,

2004, 2005]. The extra boundary condition (2.30) for F_+ tells us that

$$a = s(1 - \chi(1 - a)). \tag{2.32}$$

This is the relationship that tells us that we can only prescribe three of α, r, a and χ (or equivalently, three of κ, s, a and χ). Using the condition (2.32), we can eliminate s from F_+ to obtain

$$F = F_- - F_+ = (1 - a)(1 - \chi)Q_{\mathrm{si}}e^{-\kappa Z}. \tag{2.33}$$

This is the familiar Beer's law, previously used to model radiation attenuation in sea ice [e.g. Maykut and Untersteiner, 1971] and glaciers [e.g. Kelliher et al., 1996]. We chose to use the two-stream approximation to model the internal radiation rather than assuming Beer's law straight away so that our model can later be extended to non-uniform, non-constant absorption and scattering coefficients α and r. We also note that Cooper et al. [2021] recently made observations of the spectral attenuation of light through bare ice on the Greenland Ice Sheet, observing that attenuation is greater than through pure ice due to the presence of impurities. However, since our model considers a single band of wavelengths of radiation, we choose to follow Taylor and Feltham [2005] in using $\kappa = 1.5$ m^{-1}. This is towards the lower end of the range of values observed by Cooper et al. [2021] ($\sim$0.9–8 m^{-1} for 350–750 nm), but is at least in the right ballpark.

We can now analytically solve for the steadily melting temperature T, porosity ϕ and internal melt rate m_{int}. As mentioned previously, we seek solutions with a temperate region $0 < Z < Z_{\mathrm{m}}$ above a cold region $Z > Z_{\mathrm{m}}$. The boundary conditions between the two regions are

$$\phi = 0, \quad T = T_{\mathrm{m}}, \quad \frac{\mathrm{d}T}{\mathrm{d}Z} = 0 \quad \text{at} \quad Z = Z_{\mathrm{m}}, \tag{2.34}$$

where the final condition comes from continuity of conductive heat flux. Also, since $T = T_{\mathrm{m}}$ everywhere in $0 < Z < Z_{\mathrm{m}}$, there is no conductive heat flux at the surface, so the surface energy balance (2.26) directly tells us the surface melt rate,

$$m_{\mathrm{surf}} = \frac{\chi(1 - a)Q_{\mathrm{si}} + Q_0}{\rho\mathcal{L}}. \tag{2.35}$$

In the cold region, we integrate the temperature equation (2.11) and apply the far-field condition (2.27), along with the fact that a uniform far-field temperature means

that the heat flux tends to zero, to obtain

$$\rho c\dot{h}T - k\frac{\mathrm{d}T}{\mathrm{d}Z} + F = \rho c\dot{h}T_\infty, \tag{2.36}$$

for $Z > Z_\mathrm{m}$. Evaluating this at $Z = Z_\mathrm{m}$ and using the boundary conditions (2.34) gives us an expression which can be rearranged to tell us Z_m in terms of $\dot{h}$,

$$Z_\mathrm{m} = -\frac{1}{\kappa}\log\left(\frac{-\rho c\dot{h}(T_\mathrm{m} - T_\infty)}{(1-\chi)(1-a)Q_\mathrm{si}}\right). \tag{2.37}$$

The expression (2.36) can be integrated once more, using the boundary condition (2.34) for T, to find that the temperature is

$$T = \begin{cases} T_\mathrm{m}, & 0 < Z < Z_\mathrm{m}, \\ T_\mathrm{m} - \dfrac{(1-\chi)(1-a)Q_\mathrm{si}}{k\kappa + \rho c\dot{h}}\left(e^{-\kappa Z} - e^{-\kappa Z_\mathrm{m}}e^{\frac{\rho c\dot{h}}{k}(Z-Z_\mathrm{m})}\right) & \\ \qquad\qquad + T_\infty\left(1 - e^{\frac{\rho c\dot{h}}{k}(Z-Z_\mathrm{m})}\right), & Z > Z_\mathrm{m}. \end{cases} \tag{2.38}$$

In the temperate region, the energy equation (2.23) determines the internal melt rate m_int from the internal radiation F as

$$m_\mathrm{int} = \begin{cases} \dfrac{\kappa(1-\chi)(1-a)Q_\mathrm{si}}{c\mathcal{L}}e^{-\kappa Z}, & 0 < Z < Z_\mathrm{m}, \\ 0, & Z > Z_\mathrm{m}. \end{cases} \tag{2.39}$$

In turn, ϕ can be calculated from m_int using the mass conservation equation (2.22), giving

$$\phi = \begin{cases} -\dfrac{(1-\chi)(1-a)Q_\mathrm{si}}{\rho c\dot{h}\mathcal{L}}\left(e^{-\kappa Z} - e^{-\kappa Z_\mathrm{m}}\right), & 0 < Z < Z_\mathrm{m}, \\ 0, & Z > Z_\mathrm{m}. \end{cases} \tag{2.40}$$

Finally, the kinematic condition (2.24) determines the rate of change of surface height $\dot{h}$ as

$$\dot{h} = -\frac{(1-a)Q_\mathrm{si} + Q_0}{\rho\mathcal{L} + \rho c(T_\mathrm{m} - T_\infty)}, \tag{2.41}$$

which can be substituted into the expression (2.37) for the melting depth to give

$$Z_\mathrm{m} = \frac{1}{\kappa}\log\left(\left(\frac{(1-a)(1-\chi)Q_\mathrm{si}}{\rho c(T_\mathrm{m} - T_\infty)}\right)\Big/\left(\frac{(1-a)Q_\mathrm{si} + Q_0}{\rho\mathcal{L} + \rho c(T_\mathrm{m} - T_\infty)}\right)\right). \tag{2.42}$$

As automatic from (2.25), the surface runoff in this situation is equal to the rate of surface lowering, $r_\mathrm{off} = -\dot{h}$. Example solutions for temperature, porosity, internal

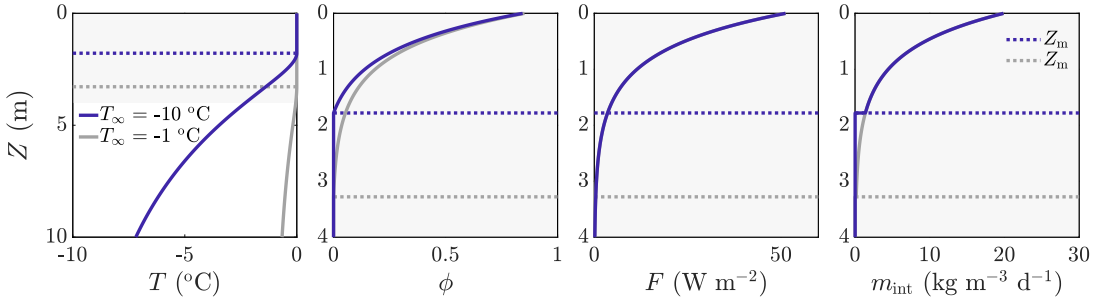


Figure 2.4: Example solution for $T_\infty = -10^\circ$C (dark purple) and $T_\infty = -1^\circ$C (grey). The dotted lines show the melting depth $Z_{\rm m}$, with $Z_{\rm m} \approx 1.8$ m when $T_\infty = -10^\circ$C and $Z_{\rm m} \approx 3.3$ m when $T_\infty = -1^\circ$C. The rate of change of surface height is $\dot{h} \approx -1.6$ cm d^{-1} when $T_\infty = -10^\circ$C and $\dot{h} \approx -1.7$ cm d^{-1} when $T_\infty = -1^\circ$C. The surface melt rate is $m_{\rm surf} \approx 0.25$ cm d^{-1} in both cases. The other parameter values are those shown in Table 2.2. The shaded region on the left panel corresponds to the smaller region shown in the other panels.

radiation and internal melt rate are shown in Figure 2.4 for two different values of the deep-ice temperature T_∞. Unsurprisingly, a colder deep-ice temperature (blue lines) leads to a smaller porous region, with the dotted lines indicating $Z = Z_{\rm m}$.

For our assumption that the surface is melting to be valid, we need the surface melt rate $m_{\rm surf}$ to be positive. Using the expression (2.35) for $m_{\rm surf}$, this gives a restriction on the possible values of the prescribed radiations $Q_{\rm si}$ and Q_0,

$$\chi(1-a)Q_{\rm si} + Q_0 > 0. \tag{2.43}$$

Furthermore, the solution found here, with a non-trivial porous ice region occupying $0 < Z < Z_{\rm m}$, is only valid if the calculated $Z_{\rm m}$ is positive, and hence the argument of the logarithm in (2.42) must be greater than one. Physically, this can be interpreted as requiring that the raising of the internal temperature dominates the surface lowering, as we will now explain.

Firstly, as more of the internal ice is raised to the melting temperature, the size of the porous region (and hence $Z_{\rm m}$) increases. This is represented by the term

$$\frac{(1-a)(1-\chi)Q_{\rm si}}{\rho c(T_{\rm m} - T_\infty)} \tag{2.44}$$

in the expression (2.42) for $Z_{\rm m}$. The numerator is the amount of radiation absorbed internally — that is the energy available to heat and melt the internal ice. The denominator represents the energy needed to raise the ice temperature from T_∞ at depth to the melting temperature — that is the energy required to raise the internal

ice to the melting temperature. Therefore, the fraction (2.44) can be thought of as a measure of raising the internal ice to the melting temperature.

On the other hand, as the surface lowers, the size of the porous region (and hence Z_{m}) decreases, since the porous ice at the surface gets removed as meltwater. Surface lowering is represented by the term

$$\frac{(1-a)Q_{\mathrm{si}} + Q_0}{\rho\mathcal{L} + \rho c(T_{\mathrm{m}} - T_\infty)} \tag{2.45}$$

in the expression (2.42) for Z_{m}. The numerator is the total amount of radiation absorbed by the ice, accounting for both internal and surface absorption. This is the total energy available for melting the ice, both at the surface and internally. The denominator represents the energy required to melt cold ice; the temperature must first be raised from T_∞ to T_{m}, then latent heat is needed to effect the phase change. Indeed, it is this fraction that also gives the surface lowering rate $-\dot{h}$ in (2.41). (It is different from the surface *melt* rate m_{surf}, since melting occurs in two stages: first the ice can melt internally, lowering the porosity; then the remaining ice melts at the surface.)

As previously mentioned, we expect $Z_{\mathrm{m}} > 0$ when raising the internal temperature dominates surface lowering. Using the above interpretations of the fractions (2.44) and (2.45), this happens when

$$\frac{(1-a)(1-\chi)Q_{\mathrm{si}}}{\rho c(T_{\mathrm{m}} - T_\infty)} > \frac{(1-a)Q_{\mathrm{si}} + Q_0}{\rho\mathcal{L} + \rho c(T_{\mathrm{m}} - T_\infty)}, \tag{2.46}$$

and (2.42) then gives $Z_{\mathrm{m}} > 0$.

The conditions (2.43) and (2.46) tell us the range of parameter values for which we can have steadily melting solutions with a non-trivial porous region, i.e. for which a weathering crust exists. Figure 2.5(a),(b) illustrates this graphically, showing the range of values of shortwave radiation Q_{si} and combined longwave radiation and turbulent heat fluxes Q_0 for which the steadily melting states with a non-trivial weathering crust are possible (blue to yellow region). For a fixed amount of shortwave radiation Q_{si}, increasing the combined longwave radiation and turbulent heat fluxes Q_0 increases the amount of surface lowering but not the internal heating. This is because Q_0 is completely absorbed at the surface. If Q_0 is too large (positive), surface lowering is so large that ice gets advected to the surface so quickly that it does not have the chance to get heated up to the melting temperature internally first. Hence there is no internal melting. This results in a steadily melting state

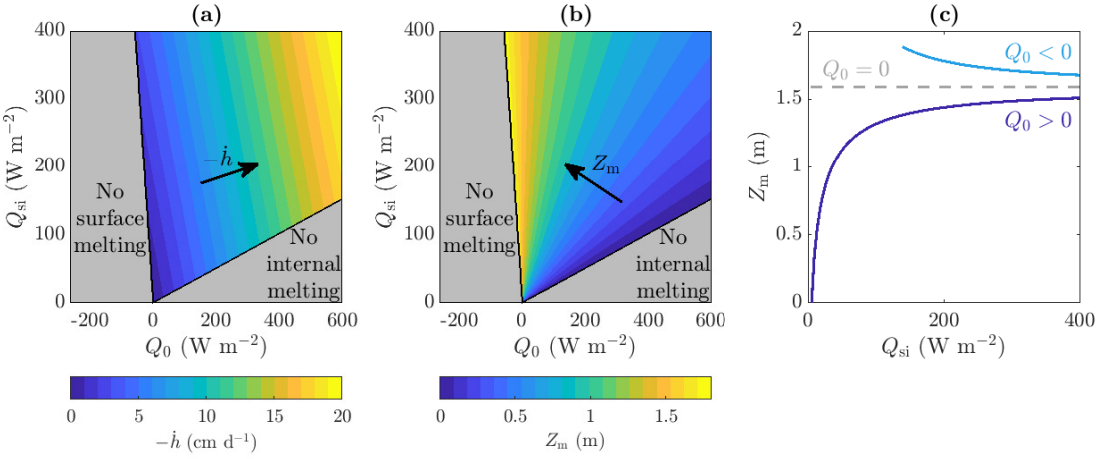


Figure 2.5: (a), (b): The range of Q_{si} and Q_0 values for which steadily melting states with both internal and surface melting are possible, as well as the regions for which there is no surface melting and no internal melting (grey) — see Figure 2.6. Contours of (a) rate of surface lowering $-\dot{h}$ and (b) weathering crust thickness Z_m are shown, ranging from $-\dot{h} = 0$ cm d^{-1} to $-\dot{h} = 20$ cm d^{-1} and from $Z_m = 0$ m to $Z_m = 1.9$ m with 1 cm d^{-1} and 0.1 m spacing between contours, respectively. (c): The dependence of Z_m on the shortwave radiation Q_{si} when $Q_0 = 20$ W m^{-2}, $Q_0 = -20$ W m^{-2} and $Q_0 = 0$ W m^{-2}. The other parameter values are those shown in Table 2.2.

with no weathering crust (bottom right region). If Q_0 is too large and negative, there is not enough energy to melt the surface (left-hand region).

2.5.2 Comparison to observations

The weathering crust thicknesses Z_m found from our model broadly agree with the ice core measurements taken by Cooper et al. [2018] in the south-western Greenland ice sheet ablation zone. They found the weathering crust in that region to be at least 1 m and up to about 2 m thick, in line with our results in Figure 2.5. Moreover, Figure 2.5(b) and (c) show how the weathering crust thickness Z_m depends on the incoming shortwave radiation Q_{si} and the combined longwave radiation and turbulent heat fluxes Q_0. There is a qualitative difference between the behaviour of Z_m with Q_{si} depending on the sign of Q_0. We see that Z_m increases with Q_{si} when $Q_0 > 0$ but decreases with Q_{si} when $Q_0 < 0$. The reason for this relates back to our interpretation of Z_m being determined by a balance between internal heating and surface lowering. If $Q_0 < 0$, doubling Q_{si} doubles the internal heating term (2.44) and more than doubles the surface lowering term (2.45). Therefore, as Q_{si} increases, surface lowering becomes more significant compared to internal heating, so the porous region (and hence Z_m) decreases. On the other hand, if $Q_0 > 0$, surface lowering becomes less significant as Q_{si} increases, so the porous

region (and hence Z_{m}) increases. In both cases, a weathering crust can only exist if the shortwave radiation Q_{si} is large enough. Physically, positive Q_0 corresponds to conditions of warm air temperature, strong wind, and cloud cover, when the ice surface would melt even in the absence of solar radiation. Such conditions favour removal of the weathering crust [Müller and Keeler, 1969, Schuster, 2001], as we observe in Figure 2.5 when Q_0 becomes too large. Negative Q_0 corresponds to conditions when the surface would freeze in the absence of solar radiation. In the ablation zone of the west Greenland ice sheet, we would typically expect the net longwave radiation to be negative and the turbulent heat fluxes to be positive, with the combination giving Q_0 as slightly negative [Van den Broeke et al., 2008, 2011]. An exception is in regions near the margin where ice-free tundra causes positive turbulent heat fluxes to dominate [Van den Broeke et al., 2008, 2011]. However, the weather conditions on the Greenland ice sheet are very changeable [e.g. Fausto et al., 2021], rapidly changing between clear, sunny conditions that favour weathering crust formation and cloudy, windy, warm weather that favours removal of the crust [Müller and Keeler, 1969, Schuster, 2001]. Therefore, we choose to investigate both positive and negative Q_0 to explore the different behaviours exhibited during these changeable conditions. The sensitivity of the weathering crust thickness Z_{m} to the values of Q_{si} and Q_0, demonstrated by our model, might partly explain why the weathering crust tends to form and be removed by changing weather conditions. These ideas will be explored further in Chapter 3.

2.5.3 Steady solution (non-melting)

Figure 2.6 shows an extended version of the regime diagram in Figure 2.5(b), with the addition of steady solutions for which there is no melting. If Q_0 is too small (regions A and B of Figure 2.6), there is not enough energy to melt the surface. Hence a steadily melting state (as occurs in regions C and D) is not possible. Instead, it is possible to have steady states with no surface lowering ($\dot{h} = 0$). Depending on the values of Q_{si} and Q_0, these steady states consist of either: pure ice (region A), or a layer of surface ice below which there is pure water (region B). The latter is not physically realistic, but is included here for completeness.

The temperature profile in the non-melting steady states is found by solving the energy equation (2.11) in the steady state. This gives

$$T = T_{\mathrm{m}} + \frac{1}{\upsilon}((1-a)Q_{\mathrm{si}} + Q_0) + \frac{1}{\kappa k}(1-\chi)(1-a)Q_{\mathrm{si}}(1-e^{-\kappa Z}). \tag{2.47}$$

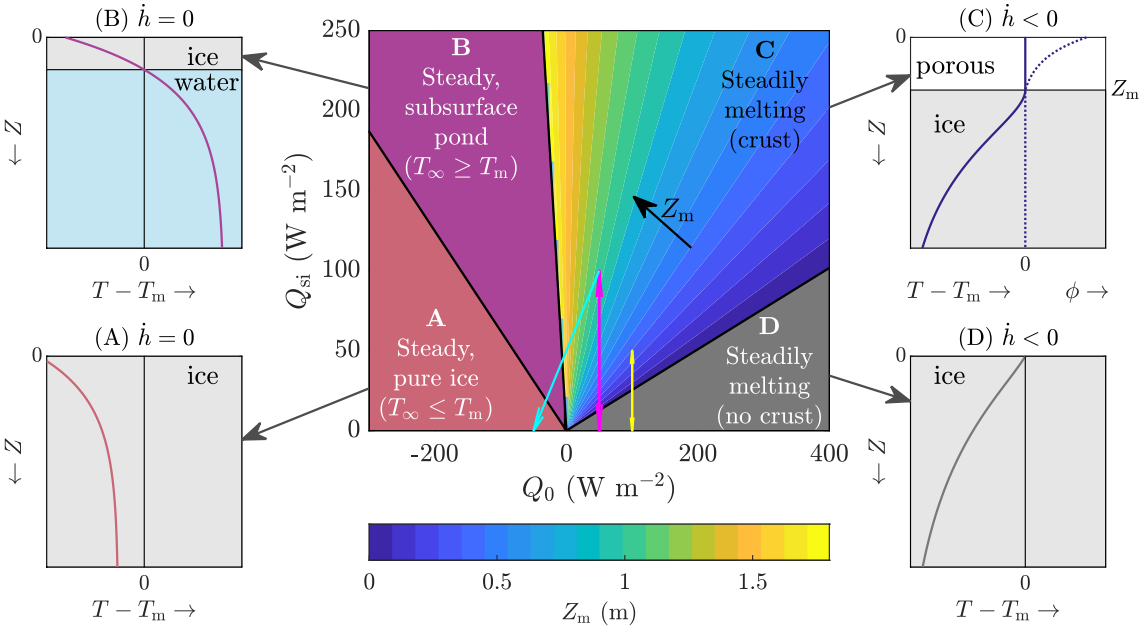


Figure 2.6: The types of steady ($\dot{h} = 0$) and steadily melting ($\dot{h} < 0$) solutions that are possible for different values of Q_{si} and Q_0. The plot shows the regions of the Q_{si}–Q_0 plane for which there are: (A) steady (no melt) solutions with pure ice, (B) steady (no melt) solutions with a subsurface pond, (C) steadily melting solutions with a porous weathering crust, and (D) steadily melting solutions with no crust. Contours of weathering crust thickness Z_m are shown in region C. Typical temperature profiles in each region are shown, with the porosity in the weathering crust also shown in region C. In regions A and B, the far-field temperature T_∞ is determined as part of the solution. In regions C and D, $T_\infty = -10^oC$ is prescribed. All other parameter values are as listed in Table 2.2. The coloured arrows in the main plot show the change in forcing used in Figures 3.4, 3.5, 3.10 (magenta), Figure 3.6 (cyan) and Figure 3.9 (yellow) in Chapter 3.

In the steadily melting solutions, ice is being advected towards the surface in the Z-frame as a result of the physical surface $z = h(t)$ lowering at rate $-\dot{h} > 0$. This allows us to prescribe the temperature T_∞ at depth. In contrast, there is no advection in the non-melting steady states, so it is not possible to prescribe the temperature at depth, but only to prescribe that $\frac{\partial T}{\partial Z}$ tends to zero as $Z \to \infty$. The far-field temperature T_∞ is instead determined as part of the solution. The sign of $T_\infty - T_m$ determines whether we have a pure-ice solution ($T_\infty \leq T_m$, region A) or subsurface pond solutions ($T_\infty \geq T_m$, region B), with the boundary between the two regions given by the line

$$Q_0 + \left(\frac{\upsilon}{k\kappa}(1-\chi) + 1\right)(1-a)Q_{si} = 0. \tag{2.48}$$

2.6 Discussion and summary

In this chapter, we have presented a continuum, mathematical model for the weathering crust, including thermodynamics, phase change (melting and freezing), internal radiation and meltwater flow. Throughout this thesis, we use a one-dimensional reduction of the model, focussing on the vertical structure of the weathering crust.

The focus of this chapter has been steadily melting solutions of a saturated weathering crust with no flow, where the internal and surface melt rates balance to produce a weathering crust of a steady size. These solutions have given insight into the porosity distributions in the weathering crust. Our model shows that the porosity decreases non-linearly with depth, in agreement with previous observations [Schuster, 2001, Cooper et al., 2018] and modelling [Schuster, 2001]. This is due to the radiation, and hence internal melting, decreasing with depth. However, the surface values of porosity in our model are larger than observed by Schuster [2001] and Cooper et al. [2018] (~ 0.85 compared to ~ 0.65). This could be due to our assumption that the entire crust is saturated, neglecting the observed unsaturated surface layer. The presence of near-surface water in our model leads to increased absorption and melting compared to if the near-surface was unsaturated. Moreover, we would expect the crust to disintegrate once the porosity gets above a certain limit, but this is not included in our model.

Furthermore, the steadily melting solutions to our model have provided initial insight into the effect of weather and climate conditions on the weathering crust. We have observed that it is the balance between internally absorbed radiation and surface forcings that controls the thickness of the weathering crust. This is in line with observations that it is the balance between shortwave radiation (some of which is absorbed internally), and longwave radiation and turbulent heat fluxes (absorbed completely at the surface) that determines the state of the weathering crust [e.g. Schuster, 2001, Tedstone et al., 2020]. Increasing longwave radiation and turbulent heat fluxes Q_0 relative to shortwave radiation Q_{si} enhances surface melting and runoff, which results in removal and thinning of the weathering crust.

Later in this thesis, we further explore temporal dynamics of the weathering crust in response to changing weather conditions by seeking time-dependent solutions to our weathering crust model. In Chapter 3, we consider idealised scenarios, and in Chapter 6, we use weather data from south-western Greenland and compare our model results to observations. The insight we have gained from our steadily melting solutions into which values of Q_{si} and Q_0 favour weathering crust growth and which

favour removal (shown in the regions of Figure 2.6) informs how we should force the time-dependent model to reproduce the growth and decay behaviour we are interested in.

Moreover, the model presented in this chapter does not account for microbes and nutrients in the weathering crust. An extension to include a model for microbes and nutrients is presented in Chapter 4, allowing us to explore the interactions between the weathering crust and microbes. Until then, we continue to neglect microbes.

In the current chapter and much of the rest of this thesis, it is assumed that the weathering crust is saturated ($S = 1$) and there is no flow through the crust – a natural result of the weathering crust's impermeable base in a one-dimensional setting. In reality, the lateral flow of meltwater through the weathering crust is important for the transport of meltwater, nutrients and microbes across the ice sheet [e.g. Irvine-Fynn et al., 2021, Stibal et al., 2012]. In Chapter 5, we extend the model presented here to include a parametrisation for lateral meltwater flow, making meltwater flow in our one-dimensional model possible.

Chapter 3

Weathering crust evolution without flow

This chapter is adapted from work published in the IMA Journal of Applied Mathematics in the manuscript 'Modelling the evolution of an ice sheet's weathering crust' [Woods and Hewitt, 2024].

We now turn to seeking solutions of the time-dependent extension to the one-dimensional steadily-melting weathering crust model in Chapter 2, to gain insight into the processes involved in the dynamic growth and decay of the weathering crust. We retain our previous assumptions that the crust is saturated with water and there is no water flow.

As previously discussed, the weathering crust is very variable. It can only form in the summer months when there is enough shortwave radiation to cause internal (subsurface) melting [e.g. Cook et al., 2016]. It also responds on shorter timescales to changing weather conditions, and can be formed or completely removed from one day to the next [e.g. Schuster, 2001, Tedstone et al., 2020, Chandler et al., 2015]. This results in temporal variations in the surface structure, meltwater transport and albedo [Tedstone et al., 2020, Chandler et al., 2015], and hence the amount of melting and runoff, which we would like to understand and quantify.

The steadily melting solutions from Chapter 2 (in which internal and surface melting balance to maintain a constant weathering crust thickness) provide some insight into the conditions which favour growth and decay of the weathering crust. Firstly, they support observations [e.g. Schuster, 2001, Tedstone et al., 2020] in demonstrating that it is the balance between shortwave radiation Q_{si} and longwave radiation and

turbulent heat fluxes Q_0 that determines the state of the weathering crust. Recall that clear, sunny conditions (in which shortwave radiation Q_{si} dominates) favour weathering crust growth, whereas warm, windy cloudy conditions (in which longwave radiation and turbulent heat fluxes dominate) favour decay [Müller and Keeler, 1969, Schuster, 2001, Tedstone et al., 2020]. Secondly, the steadily melting model provides additional quantitative insights. We are able to say, for any given *constant* values of Q_{si} and Q_0, whether or not a steadily melting weathering crust exists and, if so, its thickness, as shown in Figure 2.6 in Chapter 2. The steadily melting solutions do not give us any information about the *transient* behaviour of the weathering crust during growth and decay. Studying the full time-dependent problem is crucial for extending our understanding of the physical processes governing weathering crust evolution, and exploring the response of the weathering crust, melting and runoff to changing weather and climate conditions. This is the focus of the current chapter.

We use the time-dependent extension to the steadily melting model in Chapter 2 to explore the dynamic growth and decay of the weathering crust when conditions transition between those favouring growth and those favouring decay. We begin in Section 3.1 by presenting the one-dimensional, time-dependent weathering crust model with no water flow. We then describe the numerical enthalpy method we use for solving the time-dependent equations in Section 3.2. In Section 3.3 we consider idealised 'switching' experiments (motivated by the steadily melting solutions) to gain insight into the physical processes controlling the growth and decay of the weathering crust. In Section 3.4 we use sinusoidal forcings to explore behaviour closer to reality. Finally, we discuss our findings and connections to the rest of this thesis in Section 3.6.

3.1 Time-dependent model

In Chapter 2, we presented a fully three-dimensional continuum model for the evolution of the weathering crust, accounting for mass conservation, energy conservation and internal shortwave radiation. Here, we present a simplified version of that model under the following assumptions (the same as those made for the steadily melting solutions in Chapter 2). We restrict ourselves to one (vertical) dimension, and assume that the weathering crust is completely saturated with meltwater. Given that there is always a layer of impermeable ice beneath the weathering crust, this results in no flow of meltwater. Furthermore, we assume that the ice and water have

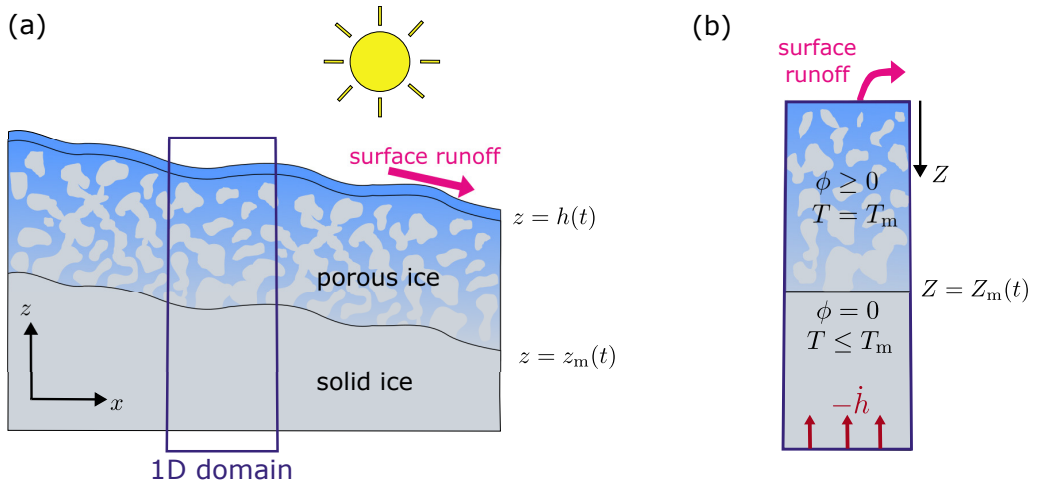


Figure 3.1: The setup for the saturated weathering crust model without flow in (a) the general two-dimensional case and (b) the one-dimensional case. In the simplest case, the domain consists of two regions: a porous region saturated with water (the weathering crust) above a cold, solid ice region. Blue represents water and grey represents ice. Variables are defined within the main text. In the one-dimensional domain, we transform coordinates to $Z = h(t) - z$, meaning that the ice surface is fixed and the cold ice below gets advected towards the surface at rate $-\dot{h}$. Any surface meltwater is removed instantaneously.

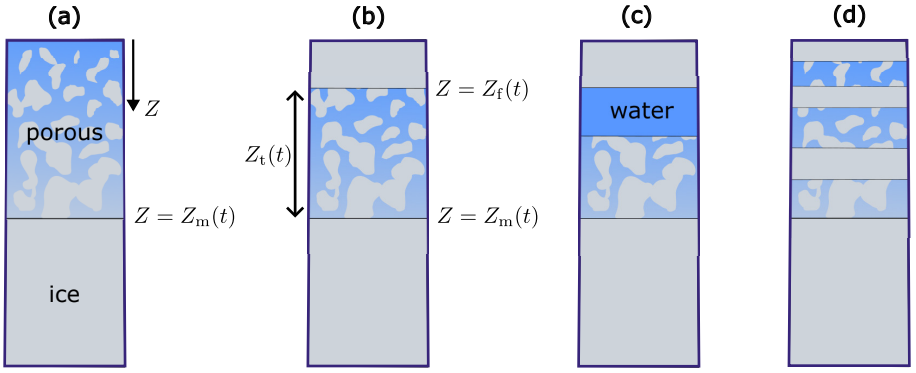


Figure 3.2: Possible transient configurations of the saturated weathering crust model without flow. It is possible to have layers of pure ice, pure water, and porous ice that is saturated with water. Blue represents water and grey represents ice. Configurations (a) and (b) are encountered in this study. Configurations (c) and (d) are other, more general, possibilities.

shared material and thermal properties, such as density ρ, thermal conductivity k and specific heat capacity c.

As in the steadily melting model in Chapter 2, we transform coordinates to $Z = h(t) - z$, the depth below the ice surface $z = h(t)$. The equations are presented in terms of the Z coordinate, where the ice surface is now at $Z = 0$. The model setup is shown in Figure 3.1. Schematics of possible transient configurations are shown in Figure 3.2.

In the time-dependent solutions we are seeking, we no longer enforce the assumption made in the steadily melting solutions that the surface of the ice is melting. It is possible to have a solid layer of ice above the top of the weathering crust (see Figure 3.2(b)). In this case, we call the location of the top of the weathering crust (the porous region) $z = z_{\mathrm{f}} = h - Z_{\mathrm{f}}$, where Z_{f} is the depth of the top of the weathering crust below the surface. As before, the bottom of the weathering crust is located at $z = z_{\mathrm{m}} = h - Z_{\mathrm{m}}$, where Z_{m} is the depth of the bottom of the weathering crust below the surface. The weathering crust thickness is defined as $Z_{\mathrm{t}} = Z_{\mathrm{m}} - Z_{\mathrm{f}}$.

A comment on notation may be useful at this stage. Typical timescales used in this thesis are days and years, which we represent using the notation 'd' and 'y', respectively.

We now present the reduced version of the full weathering crust model (from Section 2.3), under the above assumptions.

3.1.1 Mass conservation

The mass conservation equations (2.1), (2.2) for the ice and water reduce to

$$\rho\left(\frac{\partial\phi}{\partial t} + \dot{h}\frac{\partial\phi}{\partial Z}\right) = m_{\mathrm{int}}, \tag{3.1}$$

where m_{int} is the internal melt rate, and $\dot{h}$ (≤ 0) is the rate of change of surface height. The second term on the left-hand side accounts for advection of ice towards the surface. In the physical z-frame, the ice is stationary and melting causes the surface $z = h(t)$ to lower at rate $-\dot{h}$. In the Z-frame, in which the ice surface is fixed at $Z = 0$, this manifests itself as the ice advecting upwards towards $Z = 0$.

3.1.2 Energy equation

The energy equation (2.11) reduces to

$$\rho c\left(\frac{\partial T}{\partial t}+\dot{h}\frac{\partial T}{\partial Z}\right)=k\frac{\partial^2 T}{\partial Z^2}-\frac{\partial F}{\partial Z}-\mathcal{L}m_{\text{int}}, \tag{3.2}$$

where F is the net downwelling internal shortwave radiation, and $\mathcal{L}$ is the latent heat of fusion for water. The second term on the left-hand side again accounts for advection of ice towards the top of the domain $Z = 0$. The terms on the right-hand side represent the conduction of heat following Fourier's law, the internal heat source provided by the internal shortwave radiation F, and the energy sink associated with melting the ice. (This can also be a source, when $m_{\text{int}} < 0$, which corresponds to refreezing).

3.1.3 Internal shortwave radiation

The penetration of some shortwave radiation beneath the ice surface is a key ingredient for forming a weathering crust (see Section 1.6). In Chapter 2, we modelled the upward and downward travelling components of the internal (penetrating) shortwave radiation using a two-stream approximation (2.20), (2.21). Here, as in the steadily melting model in Chapter 2, we assume that the absorption and scattering coefficients are uniform, resulting in an analytical solution for the net downwards internal shortwave radiation F,

$$F=(1-\chi)(1-a)Q_{\text{si}}e^{-\kappa Z}, \tag{3.3}$$

where $\kappa=\sqrt{\alpha^2+2\alpha r}$ is the extinction coefficient, related to the absorption coefficient α and the scattering coefficient r. In this chapter, we also assume α and r, and consequently κ, to be constant in time. The internal shortwave radiation, and the internal heat source it provides, decay exponentially with depth. The explicit modelling of the upwelling radiation coming back out of the ice surface also determines a relationship between the absorption and scattering coefficients and the albedo (2.32), which can be rearranged as

$$a=\frac{(1-\chi)(\kappa-\alpha)}{(1-\chi)\kappa+(1+\chi)\alpha}. \tag{3.4}$$

3.1.4 Kinematic condition

The kinematic condition (2.14) for the ice at the ice surface $Z = 0$ is

$$-\rho(1-\phi)\dot{h} = \rho m_{\text{surf}} \quad \text{at} \quad Z = 0, \tag{3.5}$$

where m_{surf} is the surface melt rate. We assume that any excess water at the ice surface runs off instantaneously (rather than allowing it to pool on the surface). Combining the rate of surface melting m_{surf} with the rate $-\phi\dot{h}$ at which already-liquid water is released from the lowering surface, this means that the runoff occurs at rate $r_{\text{off}} = -\dot{h}$.

3.1.5 Surface energy balance

The surface energy balance (2.18) is written as

$$k\frac{\partial T}{\partial Z} + \chi(1-a)Q_{\text{si}} + Q_0 - \upsilon(T - T_{\text{m}}) = \rho\mathcal{L}m_{\text{surf}} \quad \text{at} \quad Z = 0, \tag{3.6}$$

where Q_{si} is the incoming shortwave radiation, and $Q_0 - \upsilon(T - T_{\text{m}})$ is a linear approximation to the net incoming longwave radiation and turbulent heat flux. It is possible to calculate Q_{si}, Q_0 and υ from observed weather data (see Chapter 6). In this chapter, however, we prescribe Q_{si} and Q_0 as idealised, time-dependent forcings, and take υ to be constant.

The way that the surface energy balance is interpreted depends on whether or not the surface is melting. When the surface is melting, the surface energy balance determines the surface melt rate $m_{\text{surf}} > 0$, and the boundary condition for the temperature is $T = T_{\text{m}}$ at $Z = 0$. When the surface is not melting, $m_{\text{surf}} = 0$ and the surface energy balance provides the boundary condition for the temperature $T \leq T_{\text{m}}$ at $Z = 0$.

3.1.6 Far-field boundary conditions

We also prescribe that the ice is cold at depth,

$$T \to T_\infty \quad \text{as} \quad Z \to \infty, \tag{3.7}$$

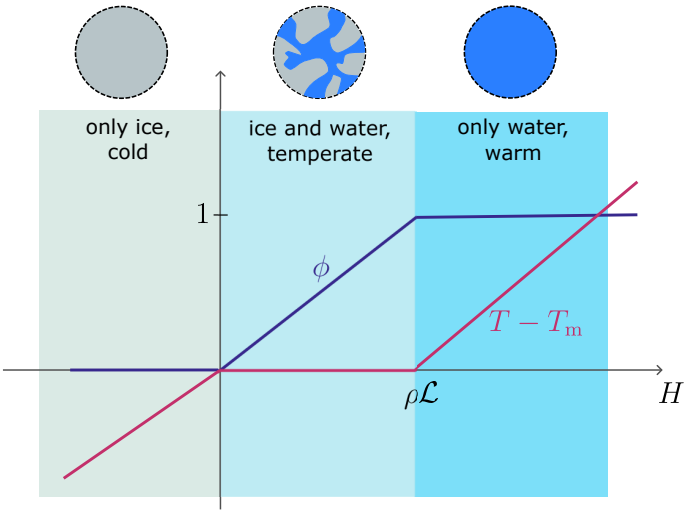


Figure 3.3: How the porosity ϕ (blue line) and scaled temperature $T - T_m$ (red line) are both recovered from the single variable H – the enthalpy – when the pore space is saturated, as represented in equations (3.8), (3.9). The relationship depends on whether a given region consists of only ice (cold), only water (warm), or both ice and water (temperate). Here, cold, warm and temperate refer to the temperature being below, above and at the melting temperature T_m, respectively. In regions of only ice, we know that $\phi = 0$, and then $H \leq 0$ determines $T \leq T_m$. Similarly, in regions of only water, we know that $\phi = 1$, and then $H \geq \rho\mathcal{L}$ determines $T \geq T_m$. In regions containing both ice and water, we know that $T = T_m$, and instead the enthalpy $0 < H < \rho\mathcal{L}$ determines the porosity $0 < \phi < 1$.

where $T_\infty < T_m$ is the deep temperature of the ice. Consistent with previous assumptions, this also means that it is solid ice, $\phi = 0$.

3.2 Enthalpy method

We are interested in solutions of the time-dependent model presented in Section 3.1. To find these, we reframe the problem in terms of enthalpy, and solve it numerically.

There are three different types of regions we could have in the model domain: (1) cold regions of only ice ($T < T_m$, $\phi = 0$), (2) temperate regions with a mixture of ice and water ($T = T_m$, $0 < \phi < 1$), and (3) warm regions of only water ($T \geq T_m$, $\phi = 1$) (see Figure 3.3). We know the porosity in the only-water and only-ice regions, and we know the temperature in the ice–and–water regions. Hence, in each of the three regions, we only need to solve for one of ϕ and T: we solve the mass conservation equation (3.1) for ϕ in ice–and–water regions, and solve the energy equation (3.2) for T in the only-ice and only-water regions. To implement this

directly would require tracking the free-boundaries between neighbouring regions and solving different equations in different parts of the domain.

The enthalpy method [e.g. Crank, [1984] 1987, Alexiades and Solomon, 1993, Voller and Cross, 1981, Aschwanden et al., 2012, Meyer and Hewitt, 2017, Hewitt and Schoof, 2017] is an alternative approach which we choose to use here. It removes the need to track the free boundaries between the three different types of regions, and allows us to solve a single equation for the enthalpy H in the whole domain. This also has the advantage of accommodating situations in which there are multiple free boundaries, and in which these boundaries come and go, automatically.

The enthalpy is defined as

$$H = \rho c(T - T_\mathrm{m}) + \rho \mathcal{L} \phi, \tag{3.8}$$

i.e. the sum of the sensible and latent heat. The porosity ϕ and temperature T can be recovered from the enthalpy H as follows:

$$\begin{aligned} \phi &= \begin{cases} 0, & H \leq 0, \\ \frac{H}{\rho \mathcal{L}}, & 0 < H < \rho \mathcal{L}, \\ 1, & H \geq \rho \mathcal{L}, \end{cases} \\ T &= \begin{cases} T_\mathrm{m} + \frac{H}{\rho c}, & H \leq 0, \\ T_\mathrm{m}, & 0 < H < \rho \mathcal{L}, \\ T_\mathrm{m} + \frac{H}{\rho c} - \frac{\mathcal{L}}{c}, & H \geq \rho \mathcal{L}, \end{cases} \end{aligned} \tag{3.9}$$

as shown in Figure 3.3. These three different cases correspond to there being only ice ($H \leq 0$), both ice and water ($0 < H < \rho \mathcal{L}$), and only water ($H \geq \rho \mathcal{L}$). The first case holds in the cold, solid ice beneath the weathering crust, and the second holds in the weathering crust. In the simplest weathering crust setup (as shown in Figure 3.1), we have only these two regions. In general, we could have a combination of only–ice, only–water and ice–and–water layers (such as the examples shown in Figure 3.2. The enthalpy method means that a more complicated situation like this should be no more difficult to solve than the simple two layer case.

By combining the mass conservation equation (3.1) and the energy equation (3.2) to eliminate the internal melt rate m_int, we get a single equation for the enthalpy,

$$\frac{\partial H}{\partial t} + \dot{h} \frac{\partial H}{\partial Z} = k \frac{\partial^2 T}{\partial Z^2} - \frac{\partial F}{\partial Z}, \tag{3.10}$$

which is solved everywhere in the domain. Note that the temperature T has not been completely eliminated, and that the remaining temperature term in the enthalpy equation (3.10) requires careful treatment when solving for H (see Appendix B). Once we have solved the enthalpy equation (3.10) for H, we can recover T and ϕ using (3.9). The boundaries between ice–only and ice–and–water regions are identified as where $H = 0$, and boundaries between water–only and ice–and–water regions are identified by $H = \rho\mathcal{L}$.

Details of the numerical implementation of the enthalpy method are found in Appendix B. This includes a description of how we decide which of the two different cases (melt or no-melt) of the surface energy balance (3.6) to use in an implicit timestepping setting, and how to deal with the diffusion term in the enthalpy equation (3.10).

3.3 'Switching' forcing - growth and decay of the weathering crust

3.3.1 Setup

To gain some initial understanding of the growth and decay of the weathering crust, we consider 'switching' experiments, in which we start with a steadily melting state (with constant forcings $Q_{\text{si}}^{\text{old}}$, Q_0^{old}), then instantaneously switch to a new set of constant forcings ($Q_{\text{si}}^{\text{new}}$, Q_0^{new}), and investigate how the weathering crust responds. Such changes in forcing are demonstrated in Figures 3.4, 3.5, 3.6.

We consider the following three scenarios, informed by the steadily melting results (particularly Figure 2.6): (1) growth of a weathering crust, (2) removal of a weathering crust by melting from the surface, and (3) removal of a weathering crust by freezing from the surface. The values of $Q_{\text{si}}^{\text{old}}$, Q_0^{old}, $Q_{\text{si}}^{\text{new}}$, Q_0^{new} used to achieve this are informed by the steadily melting solutions, moving between the different regions in Figure 2.6.

The specific forcings used in the switching experiments below are shown by the magenta and cyan arrows in Figure 2.6 in Chapter 2.

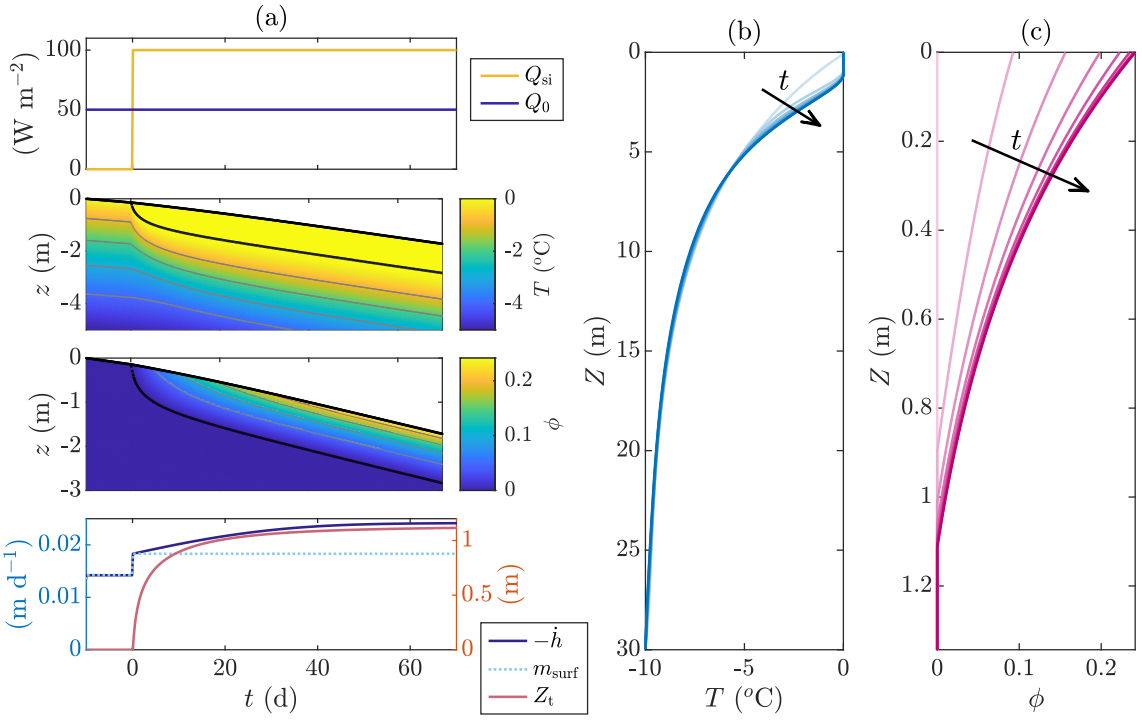


Figure 3.4: Growth of a weathering crust from a steadily melting, no-crust solution. The second and third plots in panel (a) show the evolution of the temperature T and porosity ϕ profiles over times. The bottom, $z = z_m$, and top, $z = h$, of the weathering crust are shown as black lines. Contours of T (1°C spacing) and ϕ (0.05 spacing) are shown in grey. The corresponding forcings Q_{si}, Q_0, and the resulting surface lowering $-\dot{h}$, surface melt rate m_{surf} and the weathering crust thickness Z_{int} are shown in the first and fourth plots. Snapshots are shown of (b) temperature and (c) porosity at 10 day intervals, from day 0 to day 70. Note the different z scales in (b) and (c). The forcings were switched at time $t = 0$. The other parameter values used are those shown in Table 2.2.

3.3.2 Growth of a weathering crust

We first consider the growth of a weathering crust from a no-crust steadily melting state, as shown in Figure 3.4. We start with no shortwave radiation Q_{si}, then turn it on to $Q_{si} = 100$ W m^{-2} whilst keeping $Q_0 = 50$ W m^{-2} fixed (magenta arrow in Figure 2.6, moving from region D to C). The snapshots of the temperature and porosity profiles in panels (b) and (c) show that the weathering crust develops to close to its final thickness quite quickly (over a few days), but with very low porosity initially. The porosity in the crust then continues to increase, as does the temperature in the top ~ 6 m of the ice, with the crust thickness changing very little. The resulting porosity and temperature profiles are always roughly exponential, due to the exponential decay of the internal shortwave radiation F (3.3), which acts as the internal heat source.

Note that, although the weathering crust appears by eye to have reached a constant thickness, a steadily melting state is not reached in the timescales shown in Figure 3.4. The porosity profile is close to the steadily melting solution, but the temperature profile is still far from it due to the slow nature of heat conduction. The timescale for heat to conduct through the ice is

$$t_{\text{cond}} = \frac{\rho c [Z]^2}{k}, \tag{3.11}$$

where $[Z]$ is the lengthscale. This tells us it takes about 10 days to conduct ~ 1 m into the ice, and about 1000 days to conduct ~ 10 m into the ice. This ties into the response of ice sheets to approximately sinusoidal forcings of different timescales. For surface variations with frequency ω, the amplitude of the effect of those variations at a depth Z below the surface is $\exp(-Z\sqrt{\pi\omega\rho c/k})$ [Cuffey and Paterson, 2010]. That is, the effect of lower frequency variations is felt deeper in the ice than higher frequency variations. In particular, diurnal variations are concentrated near the surface, whereas annual variations penetrate deeper [Cuffey and Paterson, 2010].

3.3.3 Removal via surface melting

We now consider removing the weathering crust by melting from the surface. Figure 3.5 shows the reverse experiment to that shown in Figure 3.4. This time, we are removing a steadily melting crust by turning off the shortwave radiation Q_{si} (and maintaining positive longwave radiation and turbulent heat fluxes Q_0, magenta arrow in Figure 2.6, moving from region C to D) — an exact reversal of the forcings just considered. We see that removal happens through a combination of melting from the surface and freezing from below. Also note, from the porosity contour plot, that the porosity at each point in space remains unchanged until that point is either frozen or melted, signified by the lines of constant ϕ lying horizontally in the physical z-frame. The only way the porosity can change in the bulk of the domain is through melting due to the internal heat source provided by the internal radiation F. Therefore, when Q_{si} (and hence F) is turned off, the internal melting ceases. Freezing also changes the porosity, but this can only happen at interfaces between porous and solid ice (e.g. at $Z = Z_{\text{m}}$), and results in a jump in porosity (see Figure 3.5(c)). The jump in porosity satisfies the Stefan condition (in the z-frame)

$$-k\frac{\partial T}{\partial z} = -\rho\mathcal{L}\phi\dot{z}_{\text{m}} \quad \text{at} \quad z = z_{\text{m}}, \tag{3.12}$$

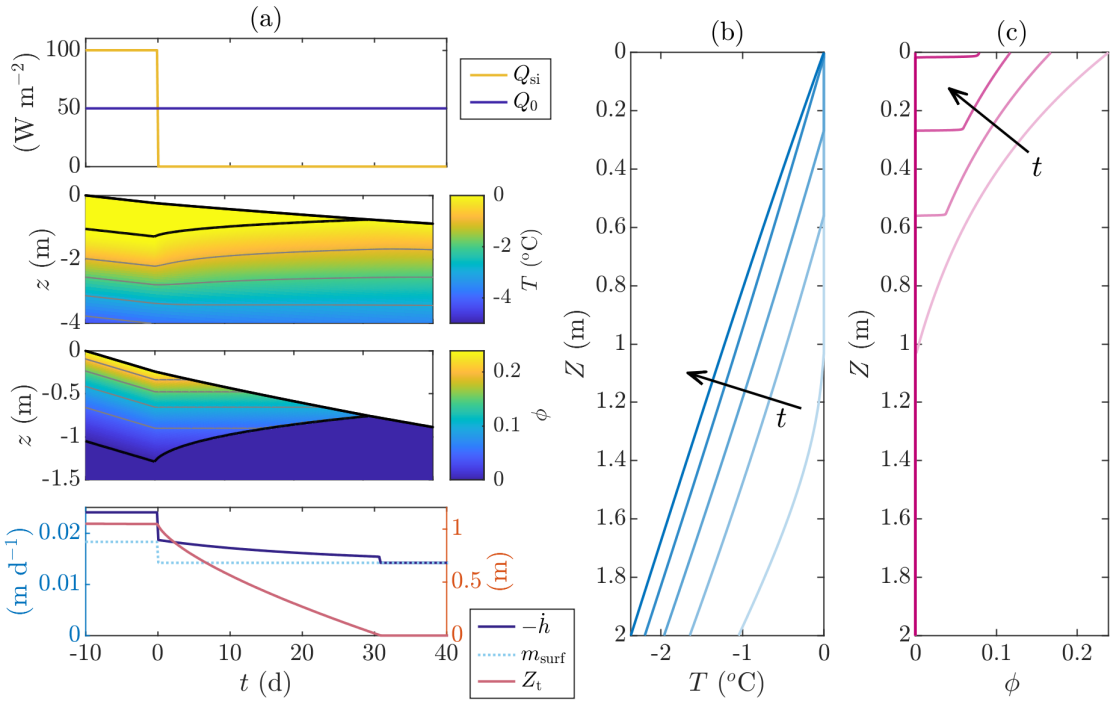


Figure 3.5: Removal of a steadily melting weathering crust by melting from the surface. The second and third plots in panel (a) show the evolution of the temperature T and porosity ϕ profiles over times. The bottom, $z = z_m$, and top, $z = h$, of the weathering crust are shown as black lines. Contours of T (1°C spacing) and ϕ (0.05 spacing) are shown in grey. The corresponding forcings Q_{si}, Q_0, and the resulting surface lowering $-\dot{h}$, surface melt rate m_{surf} and the weathering crust thickness Z_t are shown in the first and fourth plots. Snapshots are shown of temperature (b) and porosity (c) at 10 day intervals, from day 0 to day 40. The forcings were switched at time $t = 0$. The other parameter values used are those shown in Table 2.2.

where $z_m = h - Z_m$ is the bottom of the weathering crust, ϕ is the porosity value on the crust side of the interface (with $\phi = 0$ on the other side), and the temperature derivative is that on the no-crust side (being equal to zero on the crust side). The Stefan condition (3.12) is satisfied automatically by the solution of the enthalpy equation when discretised in a conservative manner.

The slight jump in the surface lowering rate $-\dot{h}$ that can be observed at the instant the crust is removed (around $t = 30$ d) can be explained by a combination of (1) the freezing from below causing a discontinuity of ϕ at the freezing front at the bottom of the crust, and (2) the surface lowering rate $-\dot{h}$ depending on the surface porosity ϕ (with m_{surf} being constant). When the final thickness of crust is removed, the surface porosity jumps from non-zero to zero, but m_{surf} remains the same, resulting in a jump in $\dot{h}$. Physically, this is because the same amount of energy is now being used to melt solid ice rather than porous ice, so a smaller decrease in surface height is achieved for the same amount of energy (see discussion below).

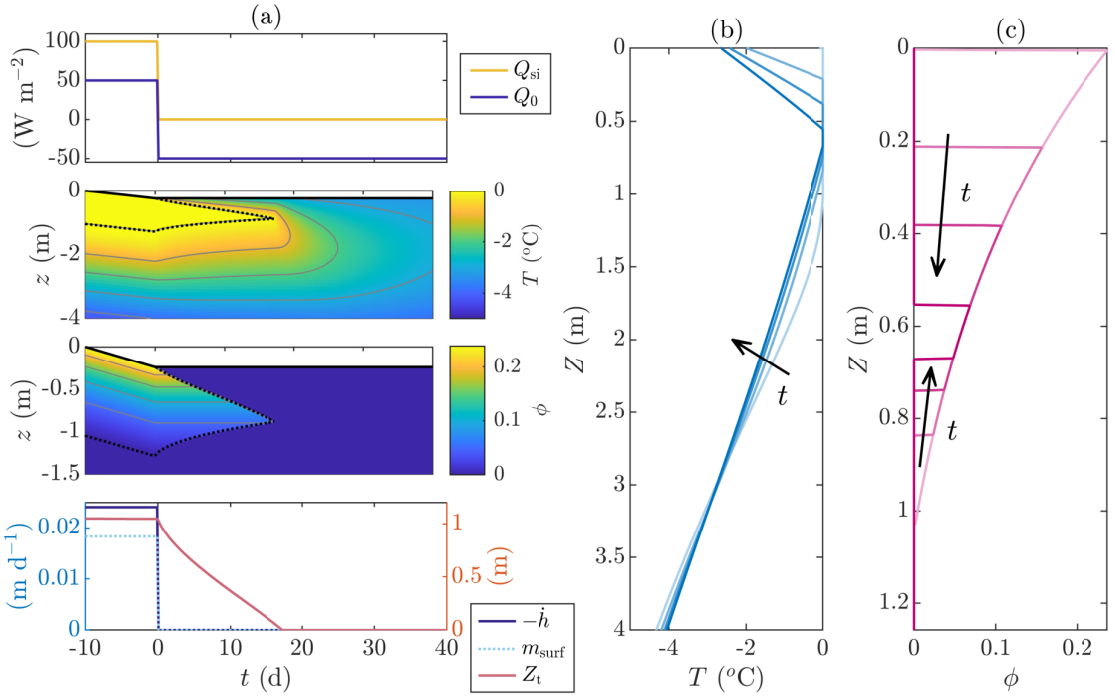


Figure 3.6: Removal of a steadily freezing weathering crust by melting from the surface. The second and third plots in panel (a) show the evolution of the temperature T and porosity ϕ profiles over times. The bottom, $z = z_m$, and top, $z = z_f$, of the weathering crust are shown as dotted black lines. Contours of T (1°C spacing) and ϕ (0.05 spacing) are shown in grey. The corresponding forcings Q_{si}, Q_0, and the resulting surface lowering $-\dot{h}$, surface melt rate m_{surf} and the weathering crust thickness Z_t are shown in the first and fourth plots. Snapshots are shown of temperature (b) and porosity (c) at 5 day intervals, from day 0 to day 15. Note the different z scales in (b) and (c). The forcings were switched at time $t = 0$. The other parameter values used are those shown in Table 2.2.

3.3.4 Removal via surface freezing

The final case we consider is the switching experiment in which we remove a steadily melting weathering crust by freezing from the surface, as well as from below. We start with the same steadily melting state as used in the removal-by-melting test, and again switch to $Q_{si} = 0$ W m^{-2}, but this time the new value of Q_0 takes negative, instead of positive, values (cyan arrow in Figure 2.6) — we are moving into region A of Figure 2.6 in which there is no surface melting. The solution is shown in Figure 3.6. In this case, the upper boundary of the weathering crust does not coincide with the ice surface $z = h(t)$. Instead, there is a layer of solid ice above the weathering crust, and a freezing front at $z = z_f(t)$. As in Figure 3.6, when $Q_{si} = 0$ W m^{-2}, there is no internal melting, so the porosity at each point in the crust remains unchanged until it jumps to zero when it is passed by one of the

freezing fronts (the top $z = z_{\mathrm{f}}$, or the bottom $z = z_{\mathrm{m}}$). As a result, the porosity profile simply gets 'truncated' over time, as shown particularly in Figure 3.6(c).

Despite the internal heat source being removed (by turning off the shortwave radiation Q_{si}), the temperature deeper in the ice increases over time (see Figure 3.6(b)). This is because the more dominant effect is that the surface lowering has stopped, meaning that there is no longer any advection of cold ice at depth upwards towards the surface. The freezing of the water in the weathering crust releases heat, which conducts downwards and initially warms the ice lower down. Meanwhile the cooling of the surface due to negative Q_0 causes the temperature near the surface to decrease.

3.3.5 Dependence on the value of Q_0^{new}

We also explore how the *rate* of the removal of a weathering crust depends on the change in the values of Q_{si} and Q_0. Firstly, we investigate the impact of Q_0^{new}. We explore what happens when we turn off the shortwave radiation (set $Q_{\mathrm{si}}^{\mathrm{new}} = 0$ W m^{-2}) and vary the new value of Q_0^{new} (Figure 3.7). We consider both melting ($Q_0^{\mathrm{new}} > 0$) and freezing ($Q_0^{\mathrm{new}} < 0$) from the surface. (Figures 3.5 and 3.6 have already shown examples of such solutions for the specific cases $Q_0^{\mathrm{new}} = 50$ W m^{-2} and $Q_0^{\mathrm{new}} = -50$ W m^{-2}.)

Broadly, we see that the time taken to remove the weathering crust by melting is shorter when Q_0^{new} is more positive ('+' markers in Figure 3.7(e),(g)), and the time taken to remove the weathering crust by freezing is shorter when Q_0^{new} is more negative ('o' markers in Figure 3.7(e),(g)).

Comparing the melting and freezing cases, we see that the freezing from the surface removes the weathering crust much more quickly than melting from the surface when the porosities are small (e.g. ≤ 0.05 in left-hand side of Figure 3.7). Smaller porosities mean that much more energy is required to melt the ice fraction (0.95) than freeze the water fraction (0.05). On the contrary, when the porosities are larger (0.61 at the surface initially, right-hand side of Figure 3.7), the removal times are more similar. This time, melting removes the crust more quickly than freezing, since there is less ice to melt than water to freeze.

The fact that it takes less time to remove the weathering crust by freezing from the surface when Q_0^{new} is more negative can be explained by the surface energy balance (3.6) (with $m_{\mathrm{surf}} = 0$ in this case). To maintain the surface energy balance, a

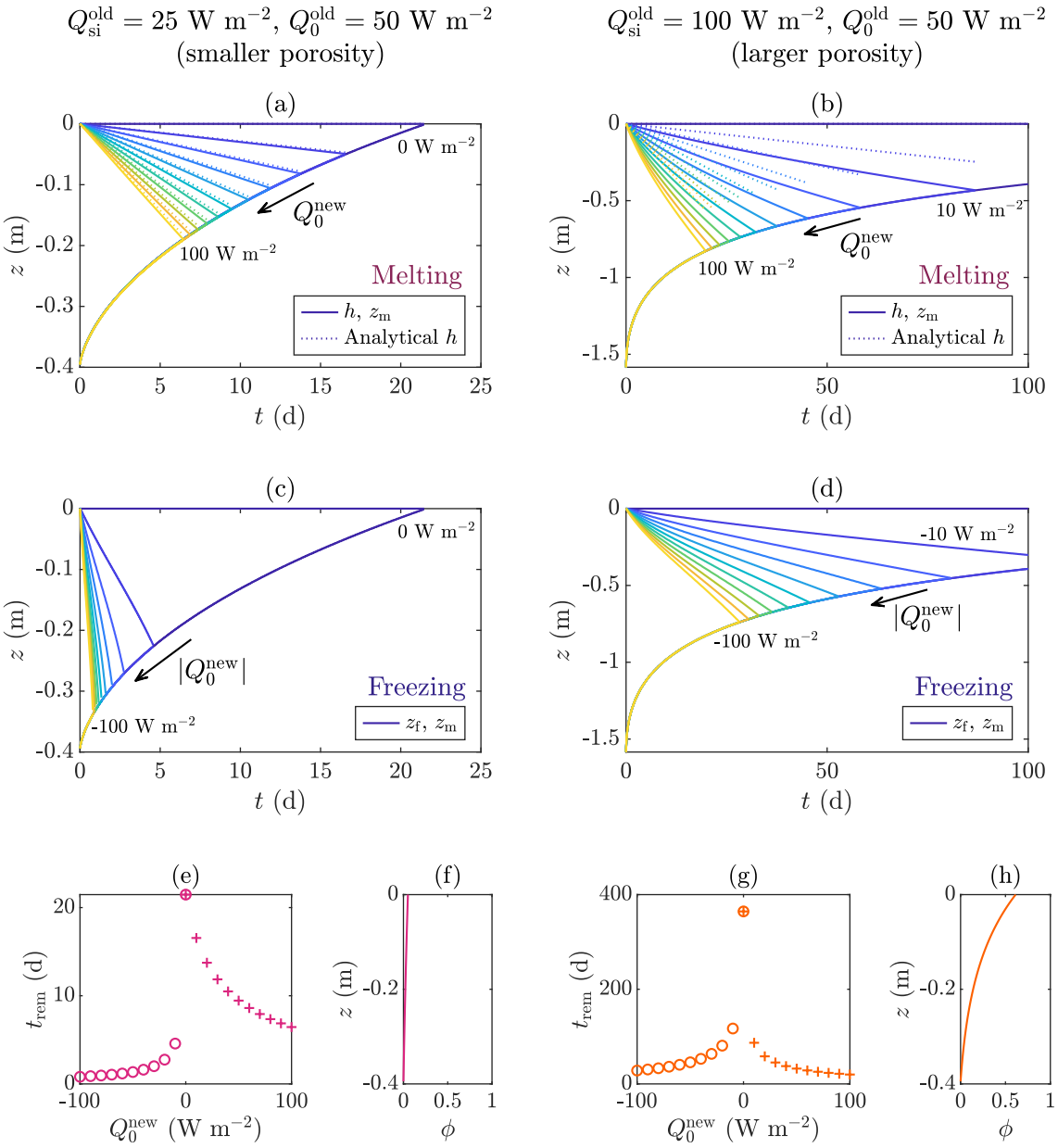


Figure 3.7: Removal of the weathering crust by (a,b) melting from the surface and (c,d) freezing from the surface, for different values of Q_0. Initially, there was a steadily melting crust with $Q_{si} = 25$ W m^{-2} and $Q_0 = 50$ W m^{-2} (a,c,e,f), and $Q_{si} = 100$ W m^{-2} and $Q_0 = 50$ W m^{-2} (b,d,g,h). In both cases, at $t = 0$, the forcings were switched to $Q_{si}^{new} = 0$ W m^{-2} and values of $|Q_0^{new}|$ from 0 to 100 W m^{-2}, in steps of 10 W m^{-2} (positive for melting, negative for freezing). Solid lines show the top ($z = h(t)$ when melting, $z = z_f$ when freezing) and bottom ($z = z_m$) of the weathering crust for different values of Q_0. The analytical approximation (3.14) for $z = h(t)$ for small ϕ is also shown (dotted). Panels (e) and (g) show how the time t_{rem} taken to remove the crust depends on Q_0^{new}. Panels (f) and (h) shown the porosity profiles of the initial steadily melting solutions, taking values of 0.05 and 0.61 at the surface, respectively. The other parameter values used are those shown in Table 2.2.

decrease in Q_0 must be compensated for by either decreasing the surface temperature T or by increasing the heat flux $k\frac{\partial T}{\partial Z}$ towards the surface from the ice below, acting to cool the internal ice. Both processes promote freezing.

The reason that the time taken to remove the crust by melting is shorter when Q_0^{new} is more positive is that increasing Q_0 increases the amount of surface melting. The surface melt rate given by the surface energy balance (3.6) (when $Q_{\text{si}} = 0$, as here) is

$$m_{\text{surf}} = \frac{Q_0}{\rho\mathcal{L}}. \tag{3.13}$$

This in turn leads to an increase in the rate of surface lowering $-\dot{h}$, according to the kinematic condition (3.5). For small surface porosity, the surface lowering rate can be approximated analytically from (3.5) as

$$-\dot{h} = \frac{m_{\text{surf}}}{1-\phi} \approx m_{\text{surf}}, \tag{3.14}$$

giving an approximately constant rate of surface lowering. This is observed in Figure 3.7(a), where there is good agreement between the analytical (dotted) and numerical (solid) solutions for $z = h$. In this case, the small ϕ assumption is valid, with $\phi \approx 0.05$ at the surface in the initial steadily melting state. However, the agreement is less good in Figure 3.7(b) where $\phi \approx 0.61$ at the surface, making the small ϕ assumption less valid.

We also observe in Figure 3.7 that the evolution of the bottom of the weathering crust $z = z_{\text{m}}$ is independent of the value of Q_0. We can see this mathematically by writing down the problem for the temperature in the solid ice below the weathering crust in the absence of shortwave radiation. This is

$$\rho c\frac{\partial T}{\partial t} = k\frac{\partial^2 T}{\partial z^2} \tag{3.15}$$

in $z < z_{\text{m}}(t)$, with three boundary conditions: the far-field condition (3.7) as $z \to -\infty$, and the Stefan condition (3.12), together with continuity of temperature $T = T_{\text{m}}$, at $z = z_{\text{m}}$. We have one more boundary condition than required to solve the heat equation, enabling us to also solve for the moving boundary $z = z_{\text{m}}(t)$. We note that this problem is independent of the boundary conditions at $z = h$, hence $z = z_{\text{m}}$ can be solved for independent of Q_0 (although, with the given initial temperature and porosity profiles, it is unfortunately not straightforward to solve analytically).

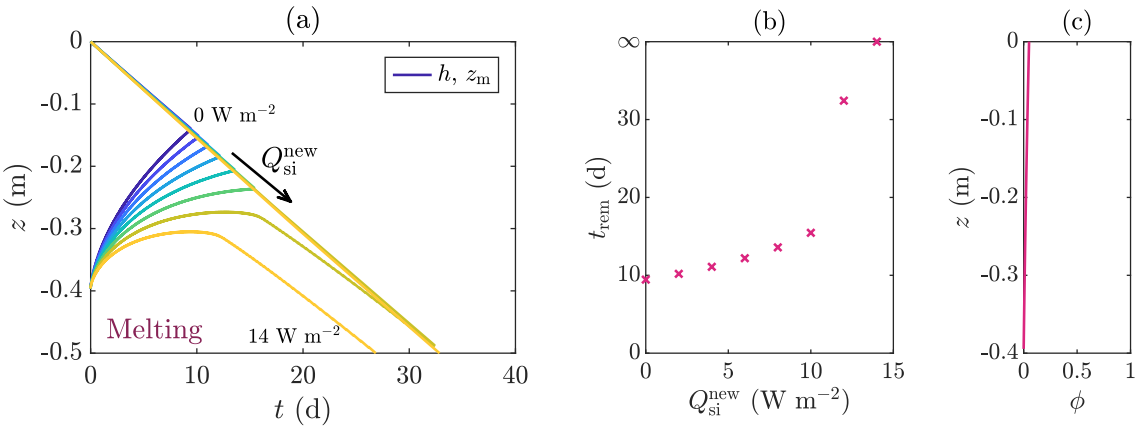


Figure 3.8: Removal of the weathering crust by melting from the surface for different values of Q_{si}. Initially, there was a steadily melting crust with $Q_{si} = 25$ W m^{-2} and $Q_0 = 50$ W m^{-2}. The forcings were switched at $t = 0$ to $Q_0 = 50$ W m^{-2} (unchanged) and various values of Q_{si}, from 0 to 14 W m^{-2} (dark blue to yellow in panel (a)), in steps of 2 W m^{-2}. Panel (a) shows the evolution of the top ($z = h$, lines beginning at $z = 0$ m at day 0) and bottom ($z = z_m$, lines beginning at $z = -0.4$ m at day 0) of the weathering crust for different values of Q_{si}^{new}. Note that $z = h$ is almost independent of Q_{si}^{new} in this example, with only the $Q_{si}^{new} = 14$ W m^{-2} (yellow) line being clearly visible. Panel (b) shows how the time t_{rem} taken to remove the crust depends on the new value of Q_{si}. Panel (c) shows the porosity profile of the initial steadily melting solutions, taking a value of 0.05 at the surface. The other parameter values used are those shown in Table 2.2.

3.3.6 Dependence on the value of Q_{si}^{new}

We now explore how the removal of the weathering crust is affected by the new value of the shortwave radiation Q_{si}, which affects both the internal melting (via the internal radiation F (3.3)) and surface melting (via the surface energy balance (3.6)). We do this by starting with the steadily melting state with $Q_{si}^{old} = 25$ W m^{-2} and $Q_0^{old} = 50$ W m^{-2}, then switching Q_{si} to a new, lower value, whilst keeping Q_0 fixed. Figure 3.8(a) shows that the effect of this is to change the rate of freezing at $z = z_m$, whereas the rate of surface lowering changes very little. The surface lowering is approximately constant in this example because all the values of Q_{si}^{new} are small (ranging from 0 to 14 W m^{-2}), so the surface melt rate (3.13) is dominated by the Q_0 term. This is amplified by Q_{si} being multiplied by $\chi(1-a) \approx 0.2 < 1$, representing the fact that not all the shortwave radiation is absorbed at the surface: some is reflected (aQ_{si}) and some is absorbed internally ($(1-\chi)(1-a)Q_{si}$). If Q_0^{new} was closer to 0 and Q_{si}^{new} was larger, the change in surface lowering with Q_{si}^{new} would be more noticeable.

The main effect of varying Q_{si}^{new} is to change the internal heat source, generated by the internal shortwave radiation F (3.3). The smaller Q_{si}^{new} is, the greater the

reduction in the internal heat source (as Q_{si} switches from $Q_{\mathrm{si}}^{\mathrm{old}}$ to $Q_{\mathrm{si}}^{\mathrm{new}}$ in equation (3.3)), and hence the crust gets frozen from below more quickly. There is a maximum value of $Q_{\mathrm{si}}^{\mathrm{new}}$ for which the crust gets removed (12.7 W m^{-2} here), given by the boundary between regions C and D in the contour plot in Figure 2.6 (with the equation for this line given in Chapter 2). Any value larger than this results in a new steadily melting crust of a different thickness being formed, determined by Figure 2.6. As $Q_{\mathrm{si}}^{\mathrm{new}}$ tends towards its maximum value for removal, the removal time tends to infinity (Figure 3.8(b)).

3.4 Periodic forcing

Although the switching experiments in Section 3.3 provide insight into the basic behaviours of weathering crust growth and removal, such sudden forcing transitions are not very realistic. In reality, we do not expect the forcings to remain constant for sustained periods of time. As previously discussed, the weathering crust and the weather conditions that force it are highly variable, changing on the order of hours and days [e.g. Fausto et al., 2021], with the weathering crust growing and decaying over short timescales as a result [Schuster, 2001]. Therefore, a more relevant test is sinusoidal variations of forcings, representing, for example, diurnal or annual variations.

In all of the experiments considered in this section, a sinusoidal forcing is run until a roughly periodic state is reached. Note that the forcings here are not necessarily realistic diurnal or annual variations (since these are not sinusoidal in amplitude), but serve to demonstrate the kind of periodic behaviour that is possible from our model. As noted by Schuster [2001], the initial conditions of the weathering crust (e.g. how porous it is) will likely have a strong effect on the amount and type (surface or internal) of melt resulting from given forcing conditions. Periodic solutions provide a way to examine the behaviour of the weathering crust whilst eliminating the impact of the initial conditions.

3.4.1 Periodic growth and complete removal

Figure 3.9 shows an example where the weathering crust is periodically completely removed (by melting from the surface and freezing from below), then regrown, as a result of daily variations in Q_{si}, with Q_0 remaining constant. In this example, the

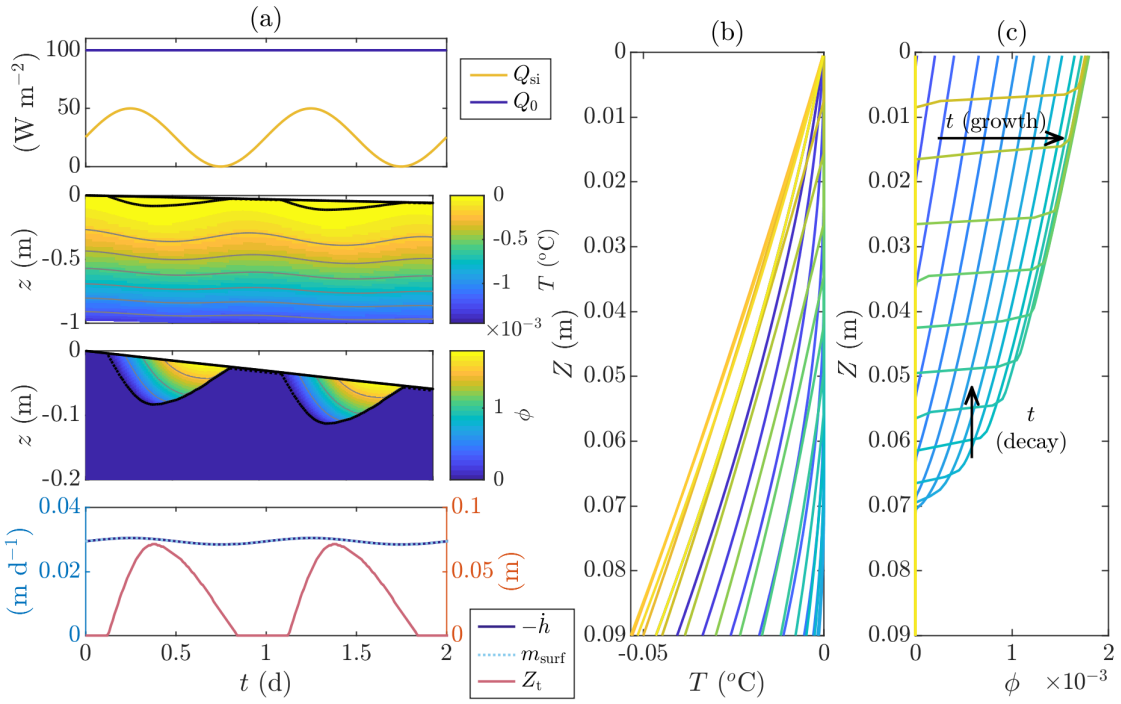


Figure 3.9: Periodic weathering crust generated by sinusoidal forcing, with complete removal each period by surface melting. The second and third plots of panel (a) show the evolution of the temperature T and porosity ϕ profiles over times. The bottom, $z = z_m$, and top, $z = h$, of the weathering crust are shown by black lines. Contours of T (0.2°C spacing) and ϕ (0.5×10^{-3} spacing) are shown in grey. The corresponding forcings Q_{si}, Q_0, and the resulting surface lowering $-\dot{h}$, surface melt rate m_{surf} and weathering crust thickness Z_t are shown in the first and fourth plots. Snapshots are shown of temperature (b) and porosity (c) at 1 hour intervals over the course of 1 day. The other parameter values used are those shown in Table 2.2.

porosity in the weathering crust is very small ($\sim 10^{-3}$), due to the limited time for the crust to grow. A key point to note is the asymmetric behaviour in the growth and removal of the crust, with the crust growing at a faster rate than it decays. We see that when the crust is growing (blue to green snapshots in panel (c)), the porosity smoothly increases from zero at the bottom of the crust, with the depth of the crust and the porosity at each depth increasing smoothly (as in Figure 3.4). In contrast, when the crust is removed, the freezing from below results in a jump in the porosity at the bottom of crust, according to the Stefan condition (3.12) (as in Figures 3.5 and 3.6). Compared to the switching examples in Figures 3.5 and 3.6 in which the $Q_{si} = 0$, here $Q_{si} > 0$, so there continues to be internal melting whilst freezing from the bottom of the crust is occurring. We see this in the fact that the lines of constant porosity slope downwards in the t-z plane here, compared to being horizontal in Figures 3.5 and 3.6. Also note the lag in the crust thickness. The crust thickness continues to increase for a short while after Q_{si} has begun to decrease,

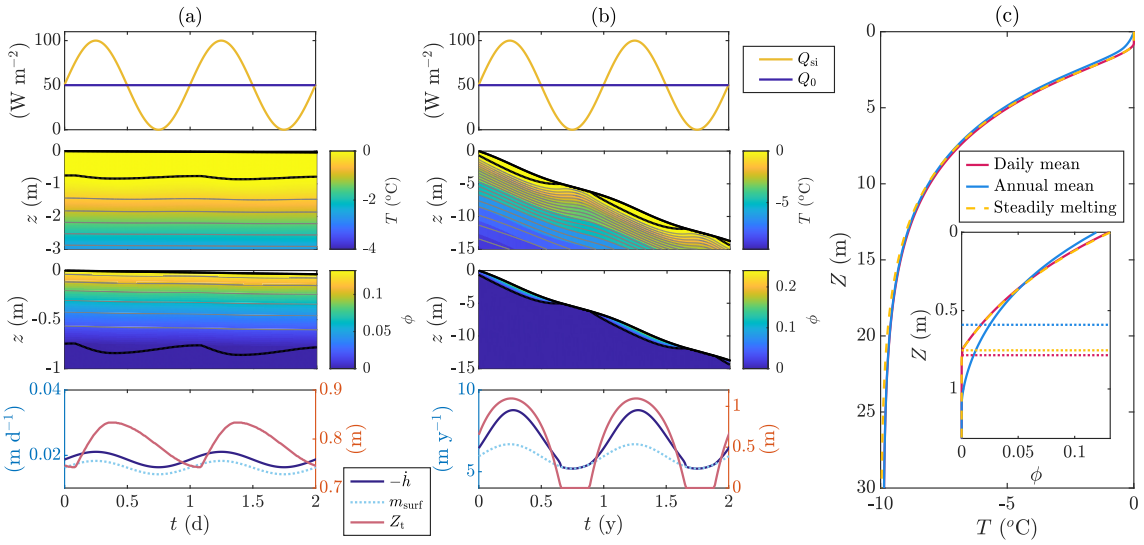


Figure 3.10: Periodic weathering crust generated by periodic forcing, for the same forcings but over different timescales (a) diurnal and (b) annual. The simulations have been run to reach a roughly periodic state: 100 days for the daily forcings, 10 years for the yearly. The second and third plots in panels (a) and (b) show the evolution of the temperature T and porosity ϕ profiles over times. The bottom, $z = z_m$, and top, $z = h$, of the weathering crust are shown by black lines. Contours of T (0.5°C spacing) and ϕ (0.02 spacing) are shown in grey. The corresponding forcings Q_{si}, Q_0, and the resulting surface lowering $-\dot{h}$, surface melt rate m_{surf} and weathering crust thickness Z_t are shown in the first and fourth plots. Panel (c) compares the time mean solutions to the steadily melting solution for the mean forcings. The other parameter values used are those shown in Table 2.2.

and Q_{si} almost reaches its maximum before the crust begins to re-form. This is explained by the fact that the weathering crust does not respond instantaneously to the changes in Q_{si} and Q_0, as demonstrated in the switching experiments in Section 3.3. It takes time for heat to conduct through the domain.

3.4.2 Diurnal vs. annual forcing

We now explore the impact of the period of the forcing. Figure 3.10 shows two periodic solutions driven by the same periodic forcings (Q_{si} varying between 0 and 100 W m^{-2}, Q_0 constant at 50 W m^{-2}), but with different periods: 1 day and 1 year. We see that with the 1 day period, the crust thickness undergoes small variations ($\sim$ 0.1 m), with the crust remaining present and of approximately constant thickness throughout. With the 1 year period, the crust gets completely removed (and regrown) periodically. This is in line with the switching experiment in Figure 3.5, in which it took $\sim$ 1 month to remove the steadily melting weathering crust

corresponding to $Q_{\mathrm{si}} = 100$ W m^{-2}, $Q_0 = 50$ W m^{-2} by turning off the shortwave radiation (i.e. the switching version of the periodic forcing in Figure 3.10).

We can also compare the periodic solutions to steadily melting solutions for the same mean forcing (Figure 3.10(c)). We see that the mean ϕ, T and Z_{m} of the periodic solution are close to, but not equal to, the steadily melting solution of the mean forcing ($Q_{\mathrm{si}} = 50$ W m^{-2}, $Q_0 = 50$ W m^{-2}). Firstly, the mean porosity is non-zero as far down as the greatest depth to which the porosity is non-zero at any time during the period. This is deeper than the mean crust depth in the steadily melting porosity profile. The depth to which non-zero porosity is reached is largest for the annual forcing since there is more time for heat to conduct deeper into the ice. However, the annual mean crust thickness is lower than both the steadily melting crust thickness and the mean thickness for the diurnal period because the crust is completely removed for periods of time. The crust would continue to thin further during some of this time if there was more ice available to melt (i.e. if the crust was thicker in the first place). Since this is not possible, it leads to a proportionately thinner mean crust thickness. On the other hand, the mean crust thickness for the diurnal period is quite close to the steadily melting crust thickness. This is due to the diurnal variations being faster than the timescale over which the crust significantly evolves, so the oscillations in forcing are effectively averaged out. The mean crust thickness for the diurnal variations is slightly larger that the steadily melting crust thickness, and we attribute this to the asymmetric growth and decay of the weathering crust. As seen in Figure 3.9(a),(c), growth occurs more quickly than removal, favouring a crust that is thicker on average than if the constant mean of the forcing was applied.

3.4.3 Superimposed diurnal and annual forcing

As well as considering diurnal and annual variations in isolation, it is informative to consider diurnal variations superimposed onto annual variations. This is representative of the increased solar radiation during the day compared to at night, and during the summer compared to winter. When modelling the evolution of a system that responds to the solar cycle, such as the weathering crust, we would like to know how important the short-term diurnal variations in forcing are. When considering longer timescales (many years, e.g. to investigate the response to changing climate conditions), it would be preferable to be able to ignore the diurnal variations, enabling us to take longer timesteps in numerical computations. Here, we explore the impact

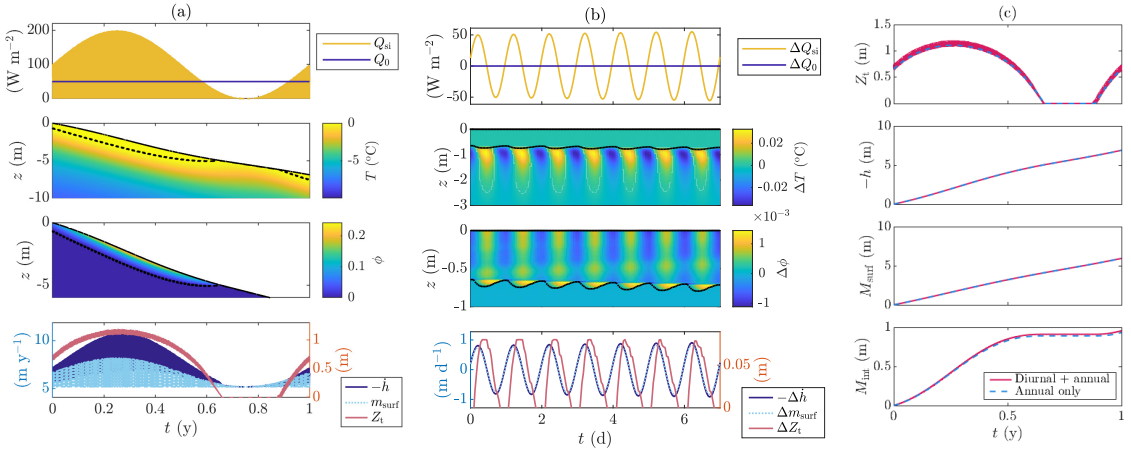


Figure 3.11: Periodic weathering crust generated by diurnal sinusoidal variations superimposed onto annual sinusoidal variations (panel (a)). The diurnal variations are such that Q_{si} goes to zero each night. The simulations have been run for 22 years to reach a periodic state. Panel (b) shows the *difference* between the solution with superimposed diurnal variations in panel (a) and the solution with only annual variations shown in Figure 3.10 ('Δ = diurnal-and-annual – annual-only'). The second and third plots in panels (a) and (b) show the evolution of the temperature T and porosity ϕ profiles over time. The black dashed line shows the bottom of the weathering crust, $z = z_m$. The corresponding forcings Q_{si}, Q_0, and the resulting surface lowering $-\dot{h}$, surface melt rate m_{surf} and weathering crust thickness Z_t are shown in the first and fourth plots. Panel (c) shows weathering crust thickness Z_t, the surface lowering $-h$, cumulative surface melt M_{surf}, and cumulative internal melt M_{int} for the diurnal-and-annual forcings (panel (a)) and the purely annual forcings (Figure 3.10(b)). The other parameter values used are those shown in Table 2.2.

of these superimposed diurnal variations on the growth and decay of the weathering crust.

To do this, we take the shortwave radiation to be

$$Q_{si}(t) = Q_{si}^{year}(t)(1 + \sin(2\pi t/t_{day})), \tag{3.16}$$

where $Q_{si}^{year}(t)$ is the annually-varying diurnal-mean,

$$Q_{si}^{year}(t) = \bar{Q}_{si} + A\sin(2\pi t/t_{year}), \tag{3.17}$$

with mean $\bar{Q}_{si}$ and amplitude A. Here, t_{day} is the period of 1 day, t_{year} is the period of 1 year. This form of Q_{si} takes a minimum of 0 in each daily cycle (at night). We take $Q_{si}^{year}(t)$ to be the same as the shortwave radiation forcing used for the annual variations in Figure 3.10, with $A = \bar{Q}_{si} = 50$ W m^{-2}.

The overall behaviour of the solution (shown in Figure 3.11(a)) is similar to that with the annual variations only (Figure 3.10(b)). The difference between the two

solutions is shown in Figure 3.11(b). The main effect of superimposing diurnal variations onto the annual variations is to create diurnal oscillations in the porosity, temperature, weathering crust thickness, internal and surface melt rates, and surface lowering rate.

The oscillations in temperature are of order 0.01°C, and the oscillations in porosity are of order 0.001 (Figure 3.11(b)). The oscillations in weathering crust thickness (Figure 3.11(b)) are once again of order 0.1 m, consistent with the diurnal variations in Figure 3.10(a).

We see that the cumulative surface lowering $-h$ ($= \int -\dot{h}\ \mathrm{d}t$), cumulative surface melt M_{surf} ($= \int m_{\mathrm{surf}}\ \mathrm{d}t$) and cumulative internal melt M_{int} ($= \frac{1}{\rho} \int \int \max(m_{\mathrm{int}}, 0)\ \mathrm{d}z\ \mathrm{d}t$) over 1 year are largely unaffected by the diurnal variations (Figure 3.11(c)). The surface lowering has contributions from surface melting and internal melting. Internal melting lowers the porosity, and the resulting non-zero surface porosity means that more surface lowering occurs than would be accounted for by surface melting alone. Any already-liquid water at the surface (produced by internal melt) adds to the surface melt and runs off as the surface lowers. In general, not all the internal meltwater runs off at the surface; some of it can instead refreeze (or run off internally in the extension considered in Chapter 5). In this example, however, the amount that refreezes is small, so almost all the internal meltwater is removed at the surface. Hence, the surface lowering is approximately equal to the sum of the internal and surface melting.

Nevertheless, slightly more internal melting does occur in the diurnal-and-annual solution than the annual-only solution, due to the diurnal refreezing and then remelting at the bottom of the weathering crust. This is demonstrated by the difference in porosity between the solutions with and without diurnal variations (Figure 3.11(b)). The amount of additional internal melting produced as a result of this diurnal freeze-melt cycle is small, since the porosity at the bottom of the weathering crust is close to zero. For larger variations in Q_0 as well as Q_{si}, it can be larger.

3.5 Discussion

3.5.1 Growth and decay behaviour and timescales

In line with observations [Schuster, 2001, Müller and Keeler, 1969], we have observed in the current chapter as well as Chapter 2 that it is the balance between shortwave

radiation (Q_{si}) and longwave radiation and turbulent heat fluxes (Q_0) that controls the growth and decay of the weathering crust, with clear, sunny conditions (high Q_{si}, low Q_0) favouring growth, and warm, windy, cloudy conditions favouring decay (low Q_{si}, high Q_0). In addition to this, the time-dependent solutions found in the current chapter have allowed us to observe different mechanisms of growth and decay. The weathering crust grows via internal melting (Figure 3.4), resulting from some shortwave radiation penetrating beneath the surface. Decay/removal of the crust can occur by (1) melting from the surface (Figure 3.5), or (2) freezing from the surface (Figure 3.6), combined with (3) freezing from below (Figures 3.5 and 3.6).

Moreover, there is an asymmetry in the growth and decay behaviour, made clear by our study of sinusoidal forcings. Growth maintains a smooth porosity profile ($\phi \to 0$ smoothly at the bottom of the weathering crust), whereas decay by freezing (from above or below) results in a jump in porosity as phase change occurs. In a periodic setting, growth occurs more quickly than decay. This is true across a number of different cases: (1) when the weathering crust is periodically completely removed by surface melting (Figure 3.9), (2) when it oscillates in thickness but is never removed (Figure 3.10(a)), or (3) when it is periodically completely removed by surface freezing (not shown here). The asymmetry in timescales means that a weathering crust produced by a sinusoidal forcing about a certain mean value has a thicker weathering crust on average than if the forcing was held constant at the mean value, unless the crust is completely removed during the cycle (Figure 3.10).

The timescale for removal in the specific examples studied here is typically on the order of several days. The removal time decreases with increasing magnitude of Q_0 (with $Q_0 > 0$ corresponding to removal by surface melting, and $Q_0 < 0$ corresponding to removal by surface freezing). The porosity, particularly at the surface, also affects the rate of removal of the weathering crust: a more porous crust is easier to remove by melting, and harder to remove by freezing.

3.5.2 Actual vs. potential surface lowering

In Section 3.3.3, we observed that the surface porosity ϕ_{surf} affects the rate of surface lowering, with a jump in ϕ at the surface resulting in a jump in the rate $-\dot{h}$ of surface lowering. In Section 3.4.3, we saw that the surface lowering is less than the surface melting due to the non-zero surface porosity (see kinematic condition (3.5)). This ties into ideas discussed by Schuster [2001]. They studied the different stages of weathering crust growth and decay in terms of the ratio R between the actual

(observed) surface lowering and the potential surface lowering (based on the total energy available to melt). In our case,

$$R = \frac{\text{actual surface lowering}}{\text{potential surface lowering}} = \frac{-\dot{h}}{((1-a)Q_{\text{si}} + Q_0)/\rho\mathcal{L}}, \tag{3.18}$$

where the potential surface lowering comes from the total melt energy: the sum of the energy absorbed at the surface, $\chi(1-a)Q_{\text{si}}+Q_0$, and the energy absorbed internally, $(1-\chi)(1-a)Q_{\text{si}}$. It is expected that $R < 1$ during crust growth because some of the melt energy is used for internal melting, which is not visible at the surface. During crust decay (removal via melting), it is expected that $R > 1$ because the porous ice requires less energy to remove than solid ice [Schuster, 2001]. Phrasing this differently, the observed surface lowering would suggest more (less) melting is occuring during decay (growth) than is truly the case [Müller and Keeler, 1969]. This can lead to errors in surface ablation (mass loss) predictions based on observed surface lowering, although these errors resulting from short-term crust variations are expected to cancel out over longer timescales [Müller and Keeler, 1969].

Using the kinematic condition (3.5) and the expression (3.13) for the surface melt rate m_{surf}, we can rewrite R as

$$R = \left(\frac{\chi(1-a)Q_{\text{si}} + Q_0}{(1-a)Q_{\text{si}} + Q_0}\right)\left(\frac{1}{1-\phi_{\text{surf}}}\right), \tag{3.19}$$

where the first fraction is the proportion of the total energy available for melt that is used to melt the surface. This shows that the key factors causing a discrepancy between the observed and expected surface lowering are (1) the fact that some of the shortwave radiation penetrates and is absorbed below the surface, determined by the parameter χ, and (2) the high surface porosity of the weathering crust.

3.6 Summary

In this chapter, we have explored time-dependent solutions of the one-dimensional reduction of the continuum model for the weathering crust we presented in Chapter 2, under the assumptions that the weathering crust is saturated with water and there is no water flow. We have used an enthalpy method to numerically solve the model equations, removing the need to track the boundaries between the porous, pure-ice and pure-water regions of the domain. Our choice of idealised 'switching'

and sinusoidal forcings has enabled us to gain insight into the physical processes controlling the growth and decay of the weathering crust in response to changing weather conditions (represented in our model by the shortwave radiation Q_{si} and the longwave radiation and turbulent heat fluxes Q_0). We find that our model produces broadly realistic behaviours when compared qualitatively to observations, suggesting that it could be used as a tool to make predictions about the response of the weathering crust to future weather and climate conditions. There are, however, improvements and extensions that could be made to the model. Those made later in this thesis are mentioned below. Further extensions are discussed in Chapter 7.

One key process missing from the current model is lateral flow of meltwater *within* the weathering crust, and the possibility for the crust to become partially saturated (have air as well as water in the pore space), as occurs in reality [Cooper et al., 2018, Irvine-Fynn et al., 2021]. So far in this thesis, we have assumed that the weathering crust is saturated ($S = 1$) and there is no flow through the crust – a natural result of the weathering crust's impermeable base in a one-dimensional setting. Correspondingly, we have assumed that all surface meltwater instantaneously runs off at the surface, but any internal meltwater can only stay in place and potentially refreeze later on. In Chapter 5, we extend the model presented here to include a parametrisation for lateral meltwater flow, making meltwater flow in our one-dimensional model possible.

Moreover, the forcings used in this study were idealised 'switching' and sinusoidal forcings. Although informed by the conditions under which we expect growth and removal of the weathering crust (see Figure 2.6), these forcings do not exactly replicate reality. In Chapter 6, we extend the work in the current chapter by forcing the model with observed weather data from the Greenland Ice Sheet, and comparing to more observations of surface lowering, porosity and temperature.

Chapter 4

Microbes and feedbacks

Most of this chapter is adapted from work published in The Cryosphere in the manuscript 'A model of the weathering crust and microbial activity on an ice–sheet surface' [Woods and Hewitt, 2023]. Section 4.4 is new content.

4.1 Introduction

We now turn to considering the evolution of microbes in the weathering crust, and the interactions between microbes, ice structure and melting. Recall that the weathering crust is home to many microorganisms and that these microbes lower the albedo and can enhance melting, both directly and via their interactions with the ice structure [e.g. Irvine-Fynn and Edwards, 2014, Benning et al., 2014, Tedstone et al., 2020, McCutcheon et al., 2021]. In this chapter, we explore the effect of microbes using a model for microbes and nutrients in the weathering crust. We begin in Section 4.2 by presenting a model for microbes and nutrients, which we couple to our weathering crust model. In Section 4.3, we seek steadily melting solutions (first introduced in Chapter 2) to explore the effect of microbe and nutrient parameters on the microbe and nutrient distributions. In Section 4.4, we seek time-dependent solutions in a saturated weathering crust with no flow (as studied in Chapter 3) to investigate the growth of microbes within an evolving weathering crust. In Section 4.5, we study the feedbacks between microbial growth, albedo and melting. Finally, in Section 4.6, we summarise and conclude.

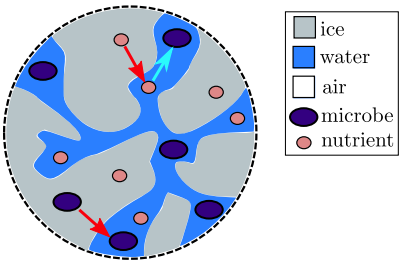


Figure 4.1: Schematic illustration of how microbes (big purple dots) and nutrients (small pink dots) are included in the model. Both are transferred from ice (grey) to water (blue) as the ice melts (red arrows), and the microbes in the water then consume nutrients in the water (bright blue arrow).

4.2 Microbes and nutrients model

We now extend our weathering crust model (presented in Chapter 2) to include microbes and nutrients. Our model focusses on the microbes within the weathering crust aquifer and does not account for the glacier ice algae found right on the ice–sheet surface (see Sections 4.6 and 7.2.2 for further discussion). In order to keep things simple, we model a single 'representative' nutrient, the concentration of which influences the microbial growth. In reality, there may be multiple sources of such nutrients located within the modelled space. The microbial growth will also depend on the shortwave radiation flux F. We also model a single representative type of phototrophic microbe (a microbe that obtains energy from solar radiation), rather than considering separately different primary and secondary producers (see discussion in Section 4.6).

We assume that both the microbes and the nutrient can exist in both the ice and the water, and when the ice melts, they are transferred from the ice to the water. Microbes in the water can consume nutrients from the water, but not from the ice, and microbes in the ice cannot consume any nutrients (see Figure 4.1). Therefore, only microbes in the water are able to proliferate. We model the microbial abundance of microbes in the water A_w and ice A_i (cells mL^{-1}) separately, and similarly for the nutrient concentrations C_w and C_i (μmol L^{-1}).

To model the water microbial abundance A_w, we adapt a simple logistic growth model [Murray, 1993],

$$\begin{aligned}\frac{\partial}{\partial t}\Big(\phi S A_\mathrm{w}\Big) + \nabla\cdot\Big(\phi S A_\mathrm{w}\mathbf{u}_\mathrm{w}\Big) = g(F,\phi S C_\mathrm{w})\phi S A_\mathrm{w}\left(1-\frac{A_\mathrm{w}}{A_\mathrm{max}}\right) - d_\mathrm{w}\phi S A_\mathrm{w} \\ + \frac{A_\mathrm{i}}{\rho_\mathrm{i}}\max(m_\mathrm{int},0) + \frac{A_\mathrm{w}}{\rho_\mathrm{w}}\min(m_\mathrm{int},0),\end{aligned} \tag{4.1}$$

On the left-hand side, we have the time derivative and an advection term, with the microbes being advected at the water velocity $\mathbf{u}_\mathrm{w}$. On the right-hand side we have a growth term, a death term (with death rate d_w), and source/sink terms due to melting/freezing. The growth term, of the form $g\phi S A_\mathrm{w}(1 - A_\mathrm{w}/A_\mathrm{max})$, is the standard form for logistic growth, with A_max being the maximum microbial abundance. We base the form of the logistic growth rate g on that used by Jorgensen and Bendoricchio [2001] for algal growth, in which g depends on the intensity of photosynthetically active radiation, the volume-averaged nutrient concentration $\phi S C_\mathrm{w}$ and the temperature, since these are limiting factors for growth of photosynthetic microbes. (We can ignore the temperature dependence, since we assume that the water is always at the melting temperature.) We follow Jorgensen and Bendoricchio [2001] in using a Michaelis-Menten form of the growth term,

$$g(F, \phi S C_\mathrm{w}) = \beta_A \left(\frac{\alpha_\mathrm{PAR} F}{k_\mathrm{PAR} + \alpha_\mathrm{PAR} F} \right) \left(\frac{\phi S C_\mathrm{w}}{k_C + \phi S C_\mathrm{w}} \right), \tag{4.2}$$

where $\alpha_\mathrm{PAR} = 0.56$ is the proportion of the total incident solar radiation that is photosynthetically active (i.e. that can be used for photosynthesis). Photosynthesis, like weathering crust formation, is driven by shortwave radiation. Here, the broadband radiation F represents all wavelengths of shortwave radiation. The factor α_PAR accounts for the fact that the two processes in fact use slightly different (overlapping) parts of the spectrum. k_PAR and k_C are constants that control the sensitivity of the growth rate to the radiation and nutrient concentration. β_A represents the growth rate if there is abundant radiation and nutrients (in which case the two bracketed factors are essentially 1). We refer to β_A as the growth rate constant. The final two terms in equation 4.1 represent the transfer of microbes between the ice and water during melting and freezing. We are assuming that when ice melts ($m_\mathrm{int} > 0$), all the microbes in that ice are released into the produced meltwater, so the ice microbes (A_i) become water microbes (A_w). Similarly, when water freezes ($m_\mathrm{int} < 0$), all the microbes in that water are frozen into the ice, becoming ice microbes.

The ice microbial abundance equation is simpler. We assume that the population of microbes in the ice cannot grow, but can die (with death rate d_i), and are fixed within the ice (so they are advected at the ice velocity $\mathbf{u}_\mathrm{i}$). Hence A_i satisfies

$$\begin{aligned} \frac{\partial}{\partial t}\Big((1-\phi)A_\mathrm{i}\Big) + \nabla \cdot \Big((1-\phi)A_\mathrm{i}\mathbf{u}_\mathrm{i}\Big) = -d_\mathrm{i}(1-\phi)A_\mathrm{i} - \frac{A_\mathrm{i}}{\rho_\mathrm{i}} \max(m_\mathrm{int}, 0) \\ - \frac{A_\mathrm{w}}{\rho_\mathrm{w}} \min(m_\mathrm{int}, 0). \end{aligned} \tag{4.3}$$

We expect that $d_\mathrm{i} \geq d_\mathrm{w}$, meaning that the death rate of microbes in the ice is greater than the death rate in the water.

Nutrients are transported through the weathering crust aquifer, often from nutrient-rich cryoconite holes [Cook et al., 2016]. To model the nutrient transport in the water, we use similar ideas to those used to model bioreactors [e.g. Shakeel et al., 2013]. The nutrients in the water can be advected and consumed by microbes. The melting of ice provides a source of nutrients into the water (and a sink from the ice), and water freezing provides a corresponding sink. The nutrients in the ice are advected with the ice, but cannot be consumed because microbes cannot access the nutrients in the ice. The equations describing this are

$$\frac{\partial}{\partial t}\Big(\phi S C_\mathrm{w}\Big) + \nabla \cdot \Big(\phi S C_\mathrm{w} \mathbf{u}_\mathrm{w}\Big) = -\beta_C \phi S A_\mathrm{w} \left(\frac{\alpha_\mathrm{PAR} F}{k_\mathrm{PAR} + \alpha_\mathrm{PAR} F}\right)\left(\frac{\phi S C_\mathrm{w}}{k_C + \phi S C_\mathrm{w}}\right) + \frac{C_\mathrm{i}}{\rho_\mathrm{i}} \max(m_\mathrm{int}, 0) + \frac{C_\mathrm{w}}{\rho_\mathrm{w}} \min(m_\mathrm{int}, 0), \tag{4.4}$$

for the nutrients in the water, and

$$\frac{\partial}{\partial t}\Big((1-\phi) C_\mathrm{i}\Big) + \nabla \cdot \Big((1-\phi) C_\mathrm{i} \mathbf{u}_\mathrm{i}\Big) = -\frac{C_\mathrm{i}}{\rho_\mathrm{i}} \max(m_\mathrm{int}, 0) - \frac{C_\mathrm{w}}{\rho_\mathrm{w}} \min(m_\mathrm{int}, 0), \tag{4.5}$$

for the nutrients in the ice. The uptake term has a similar form to the growth rate in (4.1), since we expect the consumption of nutrients to be related to the growth rate of the microbes. The constant β_C represents a maximum nutrient uptake rate, and controls the degree to which microbes influence the nutrient concentration.

A further assumption we make is that microbes and nutrients get instantaneously removed in surface runoff. This would need to be modified if we extended our model to include surface ice algae, which are able to persist on the ice surface, even in the presence of surface runoff (see Section 7.2.2).

Equations (4.1), (4.3), (4.4) and (4.5) for the microbial abundances A_w and A_i and nutrient concentrations C_w and C_i are coupled to equations (2.1), (2.2), (2.11), (2.12) and (2.13) for the weathering crust evolution, since they depend on porosity ϕ, saturation S and radiation F.

Throughout the rest of this chapter, we maintain the assumptions made in Chapters 2 and 3 that the weathering crust is fully saturated with water ($S = 1$), there is no water (or ice) flow ($\mathbf{u}_\mathrm{w} = \mathbf{u}_\mathrm{i} = \mathbf{0}$), and that the ice and water have shared material

Quantity	Symbol	Default value	Units
Proportion of solar radiation that is PAR[a]	α_{PAR}	0.56	
Maximum microbial growth rate	β_A	20	d^{-1}
Maximum nutrient uptake rate	β_C	10^{-6}	μmol cell^{-1} d^{-1}
Measure of nutrient limitation	k_C	1	μmol L^{-1}
Measure of radiation limitation	k_F	100	W m^{-2}
Maximum microbial abundance[b]	$A_{\max}$	10^4	cells mL^{-1}
Death rate of microbes in water	d_{w}	0	d^{-1}
Death rate of microbes in ice	d_{i}	0	d^{-1}
Microbial abundance at in deep ice[c]	A_∞	10^2	cells mL^{-1}
Nutrient concentration in deep ice[d]	C_∞	1	μmol L^{-1}

Table 4.2: Default values of the parameters in the microbe and nutrient model. [a]Jorgensen and Bendoricchio [2001]. [b]Motivated by Christner et al. [2018]. [c]Inferred from Van den Broeke et al. [2011]. [d]Motivated by Holland et al. [2019]. The default ice parameters are as shown in Table 2.2. The notation 'd' represents the time unit 'day'.

and thermal properties (ρ, c, k). We will often work with the volume-averaged microbial abundance $\phi S A_{\mathrm{w}}$ and nutrient concentration $\phi S C_{\mathrm{w}}$ in the water, instead of A_{w} and C_{w} directly. Since we are assuming $S = 1$, we express the volume-averaged quantities as ϕA_{w} and ϕC_{w}, respectively, for simplicity.

4.3 Steadily melting solutions

We now return to the steadily melting states considered in Chapter 2. Recall that the steadily melting states are solutions with constant forcings Q_{si} and Q_0 such that the surface lowers at a constant rate $\dot{h} < 0$, the weathering crust occupies a region between the surface and a constant depth Z_{m}, and the temperature and porosity profiles in the Z-frame (where Z is the depth below the surface) are constant in time. Under these same assumptions, and making the same change of coordinates to $Z = h - z$, equations (4.1) and (4.4) for the microbial abundance and nutrient concentration in the water become

$$\dot{h}\frac{\mathrm{d}}{\mathrm{d}Z}\Big(\phi A_{\mathrm{w}}\Big) = \beta_A \phi A_{\mathrm{w}} \left(\frac{\alpha_{\mathrm{PAR}} F}{k_{\mathrm{PAR}} + \alpha_{\mathrm{PAR}} F}\right)\left(\frac{\phi C_{\mathrm{w}}}{k_C + \phi C_{\mathrm{w}}}\right)\left(1 - \frac{A_{\mathrm{w}}}{A_{\max}}\right) - d_{\mathrm{w}}\phi A_{\mathrm{w}} + \frac{A_{\mathrm{i}} m_{\mathrm{int}}}{\rho}, \tag{4.6}$$

$$\dot{h}\frac{\mathrm{d}}{\mathrm{d}Z}\Big(\phi C_{\mathrm{w}}\Big) = -\beta_C \phi A_{\mathrm{w}} \left(\frac{\alpha_{\mathrm{PAR}} F}{k_{\mathrm{PAR}} + \alpha_{\mathrm{PAR}} F}\right)\left(\frac{\phi C_{\mathrm{w}}}{k_C + \phi C_{\mathrm{w}}}\right) + \frac{C_{\mathrm{i}} m_{\mathrm{int}}}{\rho}. \tag{4.7}$$

As an additional simplification, we make the assumption that the microbes in the water and in the ice do not die, so $d_\mathrm{w} = d_\mathrm{i} = 0$. In this particular situation, equations (4.3) and (4.5) for A_i and C_i simply tell us that the microbial abundance and nutrient concentration in the ice are constant. Since we prescribe the microbial abundance and nutrient concentration in the deep ice to be A_∞ and C_∞, respectively, this leads to $A_\mathrm{i} = A_\infty$ and $C_\mathrm{i} = C_\infty$ everywhere.

Referring back to Figure 2.3, water is only present in the porous region $0 < Z < Z_\mathrm{m}$, so it is in this region that we solve equations (4.6) and (4.7) for A_w and C_w. For continuity at the interface $Z = Z_\mathrm{m}$ between the porous ice and the solid ice, we prescribe

$$A_\mathrm{w} = A_\mathrm{i} \quad \text{at} \quad Z = Z_\mathrm{m}, \tag{4.8}$$

$$C_\mathrm{w} = C_\mathrm{i} \quad \text{at} \quad Z = Z_\mathrm{m}. \tag{4.9}$$

These two boundary conditions are motivated by the fact that if solid ice melts (as happens at the bottom of the weathering crust in the steadily melting solutions), then the water produced will have the same microbial abundance as the ice that melted.

For simplicity, we assume for now that absorption of shortwave radiation is independent of microbial abundance (with this assumption being relaxed in Section 4.5). As a result, the microbe and nutrient problem decouples from the weathering crust problem. The analytical solution to the weathering crust problem found in Section 2.5 can first be used to calculate ϕ, m_int, $\dot{h}$ and Z_m. These steadily melting solutions are repeated here for convenience:

$$\phi = \begin{cases} -\dfrac{(1-\chi)(1-a)Q_\mathrm{si}}{\rho c \dot{h} \mathcal{L}} \left(e^{-\kappa Z} - e^{-\kappa Z_\mathrm{m}} \right), & 0 < Z < Z_\mathrm{m}, \\ 0, & Z > Z_\mathrm{m}, \end{cases} \tag{4.10}$$

$$m_\mathrm{int} = \begin{cases} \dfrac{\kappa(1-\chi)(1-a)Q_\mathrm{si}}{c\mathcal{L}} e^{-\kappa Z}, & 0 < Z < Z_\mathrm{m}, \\ 0, & Z > Z_\mathrm{m}, \end{cases} \tag{4.11}$$

$$\dot{h} = -\frac{(1-a)Q_\mathrm{si} + Q_0}{\rho\mathcal{L} + \rho c(T_\mathrm{m} - T_\infty)}, \tag{4.12}$$

$$Z_\mathrm{m} = \frac{1}{\kappa} \log \left(\left(\frac{(1-a)(1-\chi)Q_\mathrm{si}}{\rho c(T_\mathrm{m} - T_\infty)} \right) \Big/ \left(\frac{(1-a)Q_\mathrm{si} + Q_0}{\rho\mathcal{L} + \rho c(T_\mathrm{m} - T_\infty)} \right) \right). \tag{4.13}$$

Then, using these results, equations (4.6) and (4.7) can be solved (numerically) with the boundary conditions (4.8) and (4.9) for A_w and C_w. We do this using the

boundary value problem solver `bcp4c` in MATLAB.

Before looking at some solutions, we discuss what we expect to be typical values of the microbial abundance and nutrient concentrations. Motivated by Christner et al. [2018], we choose $A_{\max} = 10^4$ cells mL^{-1} and $A_\infty = 10^2$ cells mL^{-1} as sensible values for the maximum microbial abundance and the microbial abundance deep in the ice. The nutrient concentration deep in the ice C_∞ gives the maximum value of C_w in the steadily melting model. To estimate a value for C_∞, we note that Holland et al. [2019] measured concentrations of dissolved organic and inorganic nitrogen, phosphorous and carbon near the surface of the Greenland ice sheet dark zone varying in orders of magnitude from about 0.1 μmol L^{-1} to over 100 μmol L^{-1}. The nutrient concentration of interest will be that of the most limiting nutrient, which could potentially be any of these. Therefore, as a ballpark figure, we take $C_\infty = 1$ μmol L^{-1}. In fact, the actual numerical values of nutrient concentration are not particularly important to the model and we will show the nutrient concentration solutions normalised by C_∞.

4.3.1 Effect of microbe growth rate

Figure 4.2 shows an example solution of how the volume-averaged microbial abundance ϕA_w and nutrient concentration ϕC_w vary with depth in the weathering crust shown in Figure 2.4. The solutions are shown for two different values of microbial growth rate constant: $\beta_A = 20$ d^{-1} (dark purple line) and $\beta_A = 5$ d^{-1} (grey line). (The latter value is loosely based on observed doubling times of algal blooms on the Greenland ice sheet [Stibal et al., 2017, Williamson et al., 2018] — see Appendix

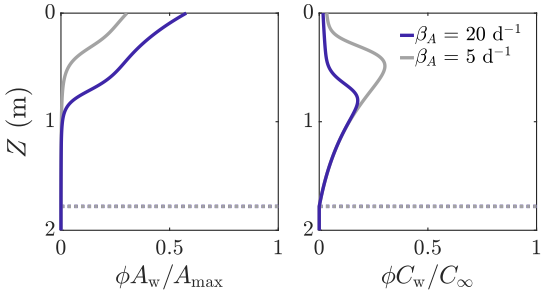


Figure 4.2: The effect of microbe growth rate β_A on volume-averaged microbial abundance ϕA_w and nutrient concentration ϕC_w. Solutions correspond to the weathering crust solutions (dark purple lines) in Figure 2.4. The solutions are shown for $\beta_A = 20$ d^{-1} (dark purple line) and $\beta_A = 5$ d^{-1} (grey line). The dotted line shows $Z = Z_\mathrm{m}$. The other parameter values are those shown in Tables 2.2 and 4.2.

C. We note that these observations are of lateral spreading of algal blooms on the ice–sheet surface, not microbial growth within the weathering crust. Therefore, our approximate values of β_A are crude, but still serve to demonstrate the key behaviour it is possible to capture with our model.) Even in the porous region (above the dotted line showing where $Z = Z_\mathrm{m}$), there is an inner region where the microbial abundance A_w and nutrient concentration C_w are still approximately their deep ice values, and hence $\phi A_\mathrm{w}/A_\mathrm{max} \approx \phi A_\infty/A_\mathrm{max}$ $(= 0.01\phi)$ and $\phi C_\mathrm{w}/C_\infty \approx \phi$. Above this, A_w increases towards the surface and C_w decreases. This is because there is more shortwave radiation nearer the surface, enabling more microbial growth. In turn, more microbes mean that more nutrient gets consumed. We can see that, as we would expect, there are more microbes when the growth rate is higher (dark purple line). The turning point in the nutrient profiles is the point above which the nutrient concentration C_w changes significantly from the deep-ice value C_∞, causing the bulk nutrient concentration ϕC_w to move off the exponential porosity profile.

4.3.2 Effect of nutrient parameters

We now investigate how the distribution of microbes is affected by parameters related to the uptake of the nutrient. In particular, we look at the parameters β_C and k_C. Firstly, β_C is the maximum nutrient uptake rate, with a larger value of β_C meaning that the microbes consume more nutrients to achieve the same amount of growth. Figure 4.3(a) shows the distribution of microbial abundance A_w and

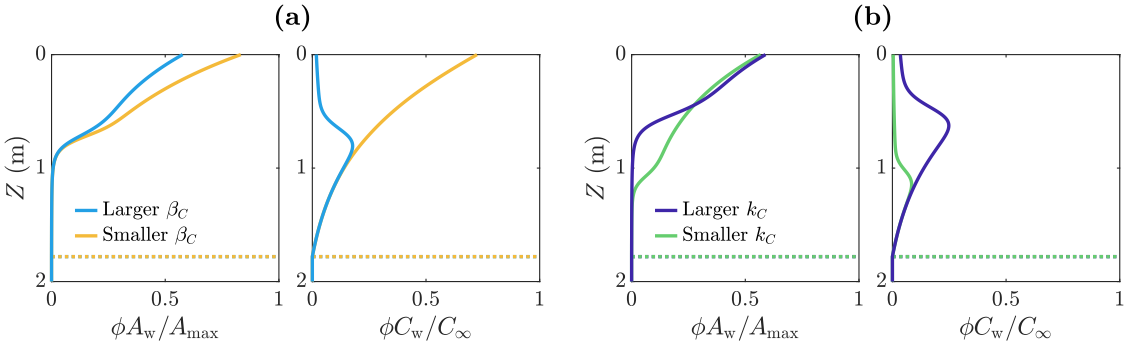


Figure 4.3: The effect of nutrient parameters β_C and k_C on volume-averaged microbial abundance ϕA_w and nutrient concentration ϕC_w. Panel (a) shows the solutions for $\beta_C/C_\infty = 10^{-3}$ mL cell^{-1} d^{-1} (light blue) and $\beta_C/C_\infty = 10^{-5}$ mL cell^{-1} d^{-1} (yellow). Panel (b) shows the solutions for $k_C = 2C_\infty$ (dark purple) and $k_C = 0.2C_\infty$ (green). These solutions correspond to the weathering crust solutions (dark purple lines) in Figure 2.4. The dotted lines show the melting depth $Z_\mathrm{m} \approx 1.78$ m. The other parameter values are those shown in Tables 2.2 and 4.2.

nutrient concentration C_{w} with depth for two values of β_C — one 100 times larger (light blue) than the other (yellow). Consistent with our interpretation of β_C, the nutrient concentration C_{w} is lower when β_C is larger. Correspondingly, the microbial abundance A_{w} is lower because the nutrient has been used up more quickly by the microbes, so less nutrient is available for further microbial growth.

The second nutrient parameter k_C is a measure of the point at which the nutrient stops being a limiting factor for the microbes. The larger k_C is, the higher the volume-averaged nutrient concentration ϕC_{w} must be before the microbial growth rate becomes independent of ϕC_{w}. Equivalently, the smaller k_C is, the lower the volume-averaged nutrient concentration must get before the nutrient becomes a limiting factor. Figure 4.3(b) shows the distribution of microbial abundance A_{w} and nutrient concentration C_{w} with depth for two values of k_C — one 10 times larger (dark purple) than the other (green). The effect of decreasing k_C is to increase the size of the region in which there is a significant number of microbes. This is because the porosity decreases with depth, which in turn means the volume-averaged nutrient concentration ϕC_{w} decreases with depth in the region near $Z = Z_{\mathrm{m}}$ where $C_{\mathrm{w}} \approx C_{\infty}$. Therefore, as k_C becomes smaller, the depth at which the nutrient is a limiting factor (controlled by the size of ϕC_{w} relative to k_C) increases, so the microbes grow deeper into the ice. By contrast, note that decreasing β_C does not affect the depth to significant microbial growth, because the size of β_C does not change the conditions required for microbial growth — it only affects the rate at which nutrients are consumed.

4.3.3 Total microbial abundance

As we did for the weathering crust in Chapter 2, we can examine how the steadily melting solution varies with radiative forcing, assuming fixed microbe and nutrient parameters. Firstly, we show solutions for different Q_0 and Q_{si} in Figure 4.4. Secondly, we look at the dependence of the total amount of microbes in the water $A_{\mathrm{tot,w}}$, defined as

$$A_{\mathrm{tot,w}} = \int_0^{Z_{\mathrm{m}}} \phi A_{\mathrm{w}} \mathrm{d}Z. \tag{4.14}$$

This has units cells m^{-2}. Recall that changing weather conditions (represented by the radiative forcings Q_{si} and Q_0 in our model) lead to the formation and removal of the weathering crust. Therefore, we choose to investigate the response of microbes to changes in both Q_{si} and Q_0, including positive and negative Q_0, to capture the

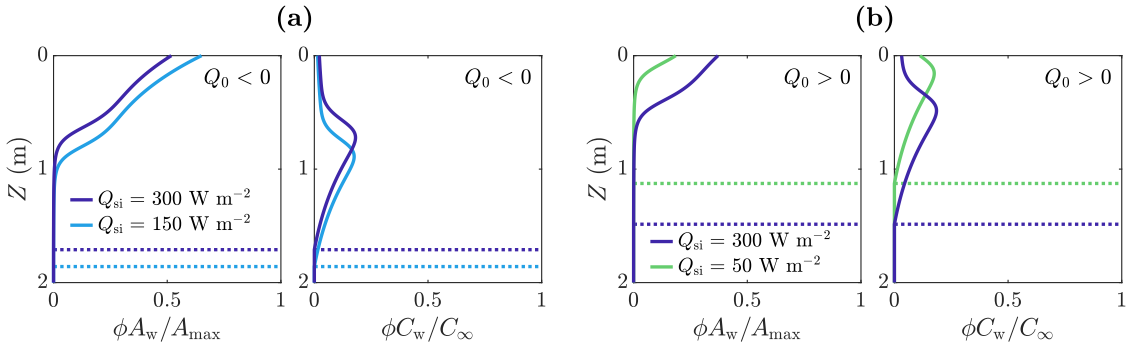


Figure 4.4: The effect of Q_{si} and Q_0 on volume-averaged microbial abundance ϕA_w and nutrient concentration ϕC_w. Panel (a) shows the solutions for $Q_0 = -20$ W m^{-2} (negative) in the case $Q_{si} = 150$ W m^{-2} (light blue) and $Q_{si} = 300$ W m^{-2} (dark purple). Panel (b) shows the solutions for $Q_0 = 20$ W m^{-2} (positive) in the case $Q_{si} = 50$ W m^{-2} (green) and $Q_{si} = 300$ W m^{-2} (dark purple). The dotted lines show the weathering crust thickness Z_m. The other parameter values are those shown in Tables 2.2 and 4.2.

range of conditions experienced by microbes in the weathering crust. For a weathering crust to form, the shortwave radiation Q_{si} must be large enough. Positive Q_0 corresponds to conditions of high turbulent heat flux (warm, cloudy, windy), which promote removal of the weathering crust. Negative Q_0 means that the surface would freeze in the absence of shortwave radiation. The observed behaviour is quite different in these two cases.

Figure 4.5(a) shows that when $Q_0 > 0$ and for small values of Q_{si} — below the critical value required to produce internal melting — there are no water microbes, because there is no water. Then, as Q_{si} increases, $A_{tot,w}$ increases due to the increase in internal radiation leading to an increase in microbial growth and an increase in the size of the weathering crust Z_m (i.e. the region in which microbes can grow). As shown in Figure 4.5(c), if Q_{si} is increased further (to less physical values), the total amount of microbes $A_{tot,w}$ starts to decrease again. This is because the internal radiation reaches the level above which it is no longer a limiting factor for the microbes. Increasing the shortwave radiation further does not increase the microbial growth but does continue to increase the surface lowering and runoff, meaning that the removal of microbes in runoff begins to dominate microbial growth, causing a reduction in $A_{tot,w}$.

However, when $Q_0 < 0$, the total number of microbes $A_{tot,w}$ decreases monotonically with increasing Q_{si} (compared to increasing when $Q_0 > 0$). The reason for this relates back to Figure 2.5. As previously discussed in Chapter 2, when $Q_0 < 0$, the melting depth Z_m decreases as Q_{si} increases because surface lowering increases at a faster rate than internal melting. Therefore, the region in which microbes

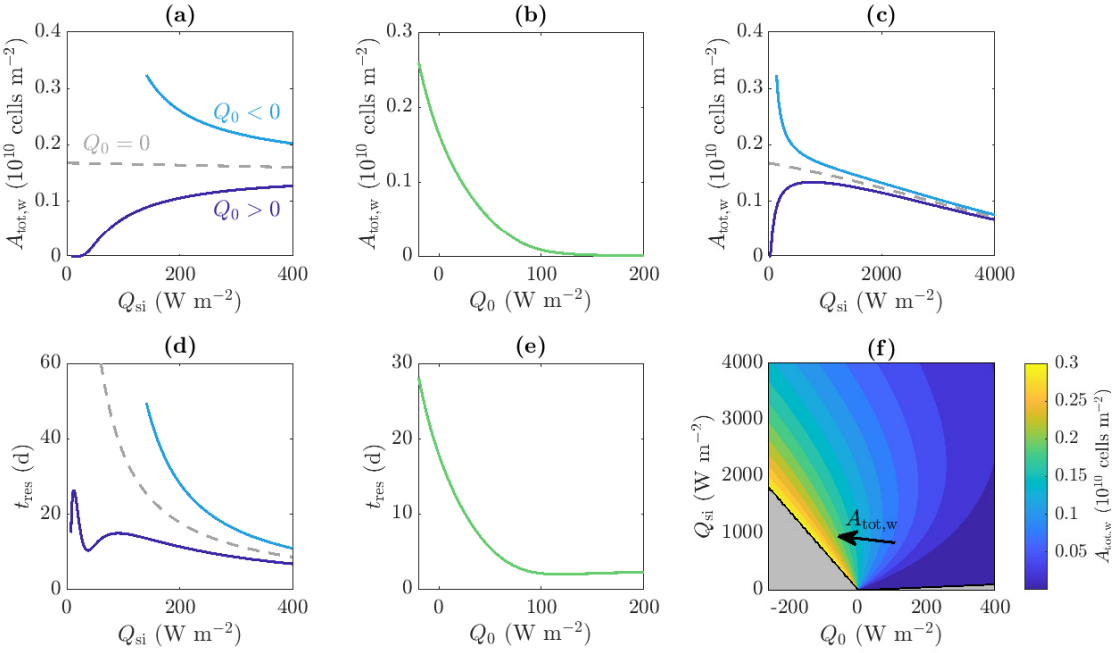


Figure 4.5: Dependence of (a,b,c,f) total microbes in the water $A_{\mathrm{tot,w}}$, and (d,e) approximate residence time of the microbes t_{res}, on the incoming shortwave radiation Q_{si} and other surface radiation Q_0. (a), (c) and (d) show the solutions for $Q_0 = 20$ W m^{-2} (dark purple line), $Q_0 = -20$ W m^{-2} (light blue line) and $Q_0 = 0$ W m^{-2} (grey dashed line). (b) and (e) show solutions with $Q_{\mathrm{si}} = 200$ W m^{-2}. (c) is an extension of (a) to larger Q_{si} values. (f) shows contours of $A_{\mathrm{tot,w}}$ in the region for which steadily melting states with both internal and surface melting are possible. The contour spacing is 0.02×10^{10} cells m^{-2}. The regions for which there is no surface melting and no internal melting are also shown (grey, see Figure 2.5). The other parameter values are those shown in Tables 2.2 and 4.2.

can grow gets smaller, with the microbe distribution shifting upwards, as shown in Figure 4.4(a).

Figure 4.5(b) also shows how $A_{\mathrm{tot,w}}$ depends on the other surface radiation Q_0, which is a combination of net longwave radiation and turbulent heat fluxes, for a fixed value of shortwave radiation Q_{si}. We see that $A_{\mathrm{tot,w}}$ is a decreasing function of Q_0. This is because increasing Q_0 increases the surface melting without affecting the internal melting or microbial growth. Hence the surface runoff increases without microbial growth increasing to compensate. When Q_0 gets large enough, there is no time for any microbial growth before the microbes get removed in runoff, so the microbial abundance remains close to the small background value A_∞.

The combined effect of Q_{si} and Q_0 on $A_{\mathrm{tot,w}}$ is shown in the contour plot in Figure 4.5(f). In addition to the behaviour captured by Figure 4.5(a)–(c), this shows how increasing Q_0 to larger positive values causes the maximum of the dark purple $A_{\mathrm{tot,w}}$ against Q_{si} curve in Figure 4.5(c) to decrease and move to a higher value of

Q_{si}. As discussed, the total number of microbes $A_{\mathrm{tot,w}}$ is determined by a balance between the microbial growth in the interior and removal of microbes at the surface in runoff, with the position of the maximum being controlled by the point past which increasing Q_{si} further no longer increases the microbial growth significantly. When Q_0 is more positive, this point is delayed to larger Q_{si} because the size of the region in which microbial growth is possible, Z_{m}, takes longer to tend to its maximum value (see Figure 2.5). Hence, for more positive Q_0, Q_{si} must get larger before $A_{\mathrm{tot,w}}$ starts decreasing with Q_{si}.

Importantly, the key result from Figure 4.5(f) is that the total number of microbes in the water is largest when Q_0 is negative and Q_{si} is just large enough to allow surface melting, which are the conditions under which weathering crust growth is most favoured.

4.3.4 Residence times

Another quantity of interest is the residence time of the microbes — that is, how long the microbes remain in the weathering crust before being removed in runoff. This is of interest because it affects the carbon fluxes from the ice sheet — in particular whether or not the ice sheet is a net source or sink of CO_2. Cook et al. [2012] showed the Greenland ice sheet to be in a stable state of autotrophy (net removal of CO_2 from the atmosphere) due to the presence of cryoconite and surface algae, with increased warming leading to increased biomass and carbon fixation. However, they warned that too much warming could lead to the removal of microbes in runoff, reducing the removal of CO_2 from the atmosphere.

In our steadily melting model, we approximate the average residence time by

$$t_{\mathrm{res}} = \frac{A_{\mathrm{tot,w}}}{q_{\mathrm{microbe}}}, \tag{4.15}$$

where

$$q_{\mathrm{microbe}} = -\dot{h}\phi A_{\mathrm{w}}|_{Z=0} \tag{4.16}$$

is the microbial runoff rate at the surface. The expression (4.15) for t_{res} is the ratio between the amount of microbes in the water of the weathering crust and the rate at which the microbes are removed from the weathering crust. Therefore, we can think of t_{res} as being the average amount of time it would take to remove all the microbes from the weathering crust water. We can also interpret this as the average amount of time each microbe spends in the weathering crust, i.e. the residence time.

Figure 4.5(d) shows the dependence of t_{res} on the incoming shortwave radiation Q_{si}. This is shown for positive (dark purple line) and negative (light blue line) values of Q_0. As with the total number of microbes $A_{\text{tot,w}}$, the observed behaviour is quite different depending on the sign of Q_0.

When $Q_0 > 0$, the global behaviour (ignoring the local minimum in Figure 4.5(d) which we will discuss shortly) is that as Q_{si} increases, t_{res} initially increases then decreases again, for the same reasons as those just discussed around $A_{\text{tot,w}}$: as Q_{si} initially increases, the microbial growth rate increases so there are more microbes in the water and these have to wait longer until they can be removed. Once Q_{si} is large enough to no longer be a limiting factor, the removal of microbes at the surface starts to dominate. This agrees with the previously discussed behaviour expected by Cook et al. [2012]: increased warming leads to increased biomass (and residence times), until the microbes get removed by runoff. The local minimum observed in Figure 4.5(d) occurs because the microbial abundance in the ice is small, $A_{\text{i}}/A_{\max} = A_\infty/A_{\max} = 0.01$. As Q_{si} increases, the microbial abundance A_{w} initially does not increase very much from A_∞ (seen from the flat section in Figure 4.5(a) for small Q_{si}). When significant microbial growth does begin, growth first occurs at the surface, with the surface microbial abundance becoming quite large before the region of significant growth spreads downwards. When near-surface growth dominates, the microbial runoff rate q_{microbe} (which depends on the surface value of the microbial abundance) grows much more rapidly with Q_{si} than the total number of microbes $A_{\text{tot,w}}$ because the microbial abundance is only growing significantly near the surface. Hence the residence time t_{res} decreases. Once significant microbial growth begins spreading into the interior, $A_{\text{tot,w}}$ grows more quickly than q_{microbe}, so t_{res} increases again.

However, when $Q_0 < 0$, t_{res} decreases monotonically with increasing Q_{si} (as does $A_{\text{tot,w}}$). The residence time decreases for the same reason that it decreases for large Q_{si} when $Q_0 > 0$ — increasing Q_{si} increases the surface lowering but does not increase the growth rate because radiation is high enough that it is no longer limiting. The non-monotonic behaviour for smaller Q_{si} is not present because Q_{si} cannot take such small values when $Q_0 < 0$, otherwise surface melting, and hence steadily melting states, would not be possible (see Figure 2.5 and surrounding discussion).

Figure 4.5(e) also shows that the approximate residence time t_{res} is a decreasing function of Q_0 for a fixed value of Q_{si}. This is for the same reasons (already discussed) that $A_{\text{tot,w}}$ is a decreasing function of Q_0 for a fixed value of Q_{si}.

4.3.5 Summary

Our steadily melting state model has shown that microbial abundance in the weathering crust generally decreases with depth, as expected by Cook et al. [2016] and observed by Christner et al. [2018]. This is because the radiation — which the microbes need to grow — decreases with depth. We have seen that significant microbial growth often only occurs in a top portion of the weathering crust, with the size of this region being controlled by microbial growth and nutrient parameters.

Furthermore, we have seen that the radiative forcings Q_{si} and Q_0 have a significant impact on the total number of microbes in the weathering crust and their residence time. This impact is via the balance between internal radiation (which favours growth of microbes and the weathering crust) and surface radiation (which increases surface melting and removal of microbes via runoff). In general, increasing internal radiation at a greater rate than surface radiation leads to an increase in the number of microbes and their residence time. In line with this, we observe different behaviour depending on the size of the shortwave radiation Q_{si} and the sign of the combined longwave radiation and turbulent heat fluxes Q_0, suggesting that the behaviour of the microbial population varies during the changeable conditions that lead to the formation and removal of the weathering crust.

4.4 Time-dependent solutions

We now seek time-dependent solutions to the microbe and nutrient problem, to gain an understanding of the dynamic behaviour. The steadily melting solutions have provided insight into the conditions that favour microbial growth, but we would also like to understand the mechanisms involved in growth, as well as how the microbes and weathering crust evolve together.

4.4.1 Time-dependent model

We continue to assume that the weathering crust is saturated ($S = 1$) and that there is no flow. Under these assumptions, the one-dimensional time-dependent equations

for the microbial abundances A_w, A_i and the nutrient concentrations C_w, C_i are

$$\begin{aligned}\frac{\partial}{\partial t}\Big(\phi A_\mathrm{w}\Big)+\dot{h}\frac{\partial}{\partial Z}\Big(\phi A_\mathrm{w}\Big)&\\ = \beta_A\left(\frac{\alpha_\mathrm{PAR}F}{k_\mathrm{PAR}+\alpha_\mathrm{PAR}F}\right)\left(\frac{\phi C_\mathrm{w}}{k_C+\phi C_\mathrm{w}}\right)\phi A_\mathrm{w}\left(1-\frac{A_\mathrm{w}}{A_\mathrm{max}}\right)&\\ - d_\mathrm{w}\phi A_\mathrm{w}+\frac{A_\mathrm{i}}{\rho}\max(m_\mathrm{int},0)+\frac{A_\mathrm{w}}{\rho}\min(m_\mathrm{int},0),&\end{aligned} \tag{4.17}$$

$$\begin{aligned}\frac{\partial}{\partial t}\Big((1-\phi)A_\mathrm{i}\Big)+\dot{h}\frac{\partial}{\partial Z}\Big((1-\phi)A_\mathrm{i}\Big) = -d_\mathrm{i}(1-\phi)A_\mathrm{i}-\frac{A_\mathrm{i}}{\rho}\max(m_\mathrm{int},0)&\\ -\frac{A_\mathrm{w}}{\rho}\min(m_\mathrm{int},0),&\end{aligned} \tag{4.18}$$

$$\begin{aligned}\frac{\partial}{\partial t}(\phi C_\mathrm{w})+\dot{h}\frac{\partial}{\partial Z}(\phi C_\mathrm{w}) = -\beta_C\phi A_\mathrm{w}\left(\frac{\alpha_\mathrm{PAR}F}{k_\mathrm{PAR}+\alpha_\mathrm{PAR}F}\right)\left(\frac{\phi C_\mathrm{w}}{k_C+\phi C_\mathrm{w}}\right)&\\ +\frac{C_\mathrm{i}}{\rho}\max(m_\mathrm{int},0)+\frac{C_\mathrm{w}}{\rho}\min(m_\mathrm{int},0),&\end{aligned} \tag{4.19}$$

$$\frac{\partial}{\partial t}\Big((1-\phi)C_\mathrm{i}\Big)+\dot{h}\frac{\partial}{\partial Z}\Big((1-\phi)C_\mathrm{i}\Big) = -\frac{C_\mathrm{i}}{\rho}\max(m_\mathrm{int},0)-\frac{C_\mathrm{w}}{\rho}\min(m_\mathrm{int},0). \tag{4.20}$$

The corresponding weathering crust evolution equations were presented in Chapter 3 and are repeated here for convenience:

$$\rho\left(\frac{\partial\phi}{\partial t}+\dot{h}\frac{\partial\phi}{\partial Z}\right) = m_\mathrm{int}, \tag{4.21}$$

$$\rho c\left(\frac{\partial T}{\partial t}+\dot{h}\frac{\partial T}{\partial Z}\right) = k\frac{\partial^2 T}{\partial Z^2}-\frac{\partial F}{\partial Z}-\mathcal{L}m_\mathrm{int}, \tag{4.22}$$

with the internal radiation $F = F_- - F_+$ given by the two-stream approximation (2.20), (2.21):

$$\frac{\mathrm{d}F_-}{\mathrm{d}Z} = -(\alpha+r)F_- + rF_+, \tag{4.23}$$

$$\frac{\mathrm{d}F_+}{\mathrm{d}Z} = (\alpha+r)F_+ - rF_-. \tag{4.24}$$

4.4.2 Microbial growth

Firstly, we are interested in the dynamics of microbial growth from a small background microbial abundance. This is of relevance for the initial growth of microbes, for example the initialisation of algal blooms, such as those that occur on south-western Greenland during the summer months [e.g. Ryan et al., 2018]. It has been suggested that these blooms are initialised by microbes that have been stored, dormant (i.e. unable to grow) in the winter ice [Bradley et al., 2023]. Microbes such as algae can be frozen into the ice at the end of one melt season and stored there, dormant, throughout the winter, with some of them surviving in this state until the start of the next melt season. At the start of the next melt season, once there is sufficient shortwave radiation and melting begins, the microbes (and stored nutrients) are melted out of the ice, become active again, and soon begin to proliferate [Bradley et al., 2023]. Therefore, in the examples studied in this section, we initialise the microbes and nutrients to be at the small background values A_∞, C_∞ everywhere, representing those that have survived the winter. We first study the growth of microbes in a fixed, steadily melting crust, to isolate microbial growth from weathering crust evolution (Section 4.4.2.1). We then look at the simultaneous growth of a weathering crust and microbes from a no-crust state, to replicate growth at the start of a melt season (Section 4.4.2.2).

4.4.2.1 Growth in a steadily melting weathering crust

We first consider the growth of microbes in a steadily melting weathering crust (in particular, the steadily melting crust with $T_\infty = -10$ °C shown in Figure 2.4 in Chapter 2, with $Q_{\mathrm{si}} = 200$ W m^{-2} and $Q_0 = -20$ W m^{-2}). We prescribe the microbial abundance and nutrient concentration in the water to initially be their background values, $A_{\mathrm{w}} = A_\infty$, $C_{\mathrm{w}} = C_\infty$, and allow the microbes and nutrients to evolve under the constant forcings until they reach a steadily melting solution. Figure 4.6 shows the resulting behaviour, in the form of snapshots of the scaled microbial abundance $\phi A_{\mathrm{w}}/A_{\max}$ and nutrient concentration $\phi C_{\mathrm{w}}/C_\infty$ profiles over time, with the steadily melting profiles shown as dashed lines. Microbial growth is most significant near the surface, where there is most water, radiation and nutrients available. As the microbes grow, they consume nutrients, resulting in a decrease in nutrient concentration ϕC_{w} near the surface and hence a decrease in the microbial growth rate (4.2). After some time, ($t = 5$ d) the nutrient concentration and microbial growth rate become low enough that microbial growth can no longer outpace

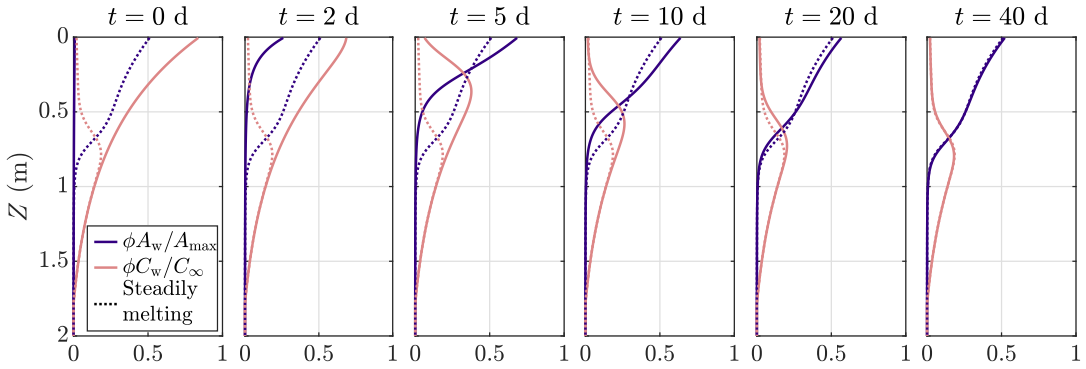


Figure 4.6: Growth of microbes in a steadily melting weathering crust, with $A_\mathrm{w} = A_\infty$, $C_\mathrm{w} = C_\infty$ initially. Snapshots of scaled microbial abundance $\phi A_\mathrm{w}/A_\mathrm{max}$ and nutrient concentration $\phi C_\mathrm{w}/C_\infty$ are shown, with the dashed lines representing the steadily melting solutions. The parameter values used are $\beta_A = 20$ d^{-1}, $A_\infty = 0.01 A_\mathrm{max}$, with all other values as shown in Tables 2.2 and 4.2.

the removal of microbes in surface runoff. (Note that the snapshots in Figure 4.6 are shown in the Z-frame where we treat the surface as fixed, but in fact the surface of the ice is melting and lowering over time.) Instead, microbes begin to be removed at a faster rate than growth, causing the microbial abundance near the surface to decrease over time until there is a balance between growth and removal, and a steadily melting solution is reached ($t = 10$ d to $t = 40$ d).

We now explore the effect of the microbial growth rate constant β_A and background microbial abundance A_∞ on the growth of microbes towards a steady state. Figure 4.7 shows the evolution of the total microbial abundance $A_\mathrm{tot,w}$ and the total amount of nutrients in the water $C_\mathrm{tot,w}$, defined as

$$C_\mathrm{tot,w} = \int_0^{Z_\mathrm{m}} \phi C_\mathrm{w} \, \mathrm{d}Z, \tag{4.25}$$

during microbial growth in a steadily melting weathering crust. $C_\mathrm{tot,w}$ has units μmol m^{-2}. Firstly, panel (a) shows that having a larger growth rate β_A results (unsurprisingly) in faster growth and the steadily melting state being reached faster. If t is rescaled with $1/\beta_A$ (not shown), the initial growth curves collapse onto each other and the final values are reached in approximately the same (scaled) time. The final value of $A_\mathrm{tot,w}$ is also larger with larger β_A because faster growth means that higher microbial abundances can be reached before the microbes are removed in surface runoff.

The final value of $A_\mathrm{tot,w}$ is also increased by having a greater background nutrient abundance A_∞, as shown in panel (b). This time, the removal of microbes in surface

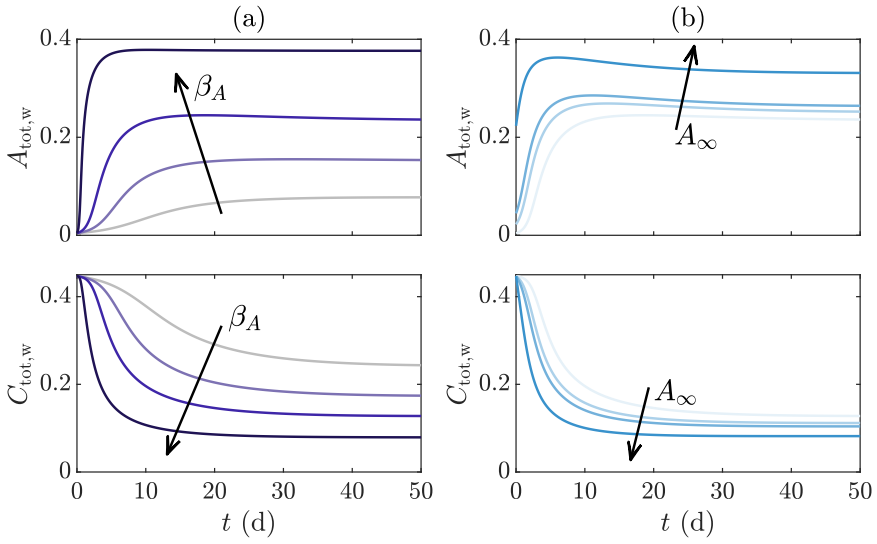


Figure 4.7: Evolution of total microbial abundance $A_{\mathrm{tot,w}}$ and total amount of nutrient $C_{\mathrm{tot,w}}$ during growth of microbes in a steadily melting weathering crust, with $A_{\mathrm{w}} = A_\infty$, $C_{\mathrm{w}} = C_\infty$ initially. The effect of different values of (a) microbial growth rate β_A $(5, 10, 20, 100\ \mathrm{d}^{-1})$ and (b) microbial abundance A_∞ at depth $(A_\infty/A_{\max} = 0.01, 0.05, 0.1, 0.5)$ are shown. The variables on the vertical axis are scaled variables. The scalings of $A_{\mathrm{tot,w}}$ and $C_{\mathrm{tot,w}}$ are 10^{10} cells m^{-2} and 10^3 μmol m^{-2}, respectively. The other parameter values are those shown in Tables 2.2 and 4.2.

runoff is increasingly compensated for by an increased supply of microbes into the meltwater when ice (with microbial abundance $A_{\mathrm{i}} = A_\infty$ in the steadily melting state) melts. The increased supply of microbes by melting also results in growth beyond the steadily melting solution extending deeper into the weathering crust, increasing the overshoot in $A_{\mathrm{tot,w}}$ before it settles on its steadily melting value. The growth rate is unchanged by the value of A_∞.

4.4.2.2 Combined microbial and crust growth

It is also interesting to explore how a weathering crust and microbes grow together, and how their growth timescales compare. To do this, we return to the growth 'switching' experiment considered in Chapter 3 (Figure 3.4). Such an experiment is useful for exploring how the microbial growth initialises, for example at the start of the melt season. We begin with a steadily melting no-crust solution ($Q_{\mathrm{si}} = 0$ W m^{-2}, $Q_0 = 50$ W m^{-2}). At $t = 0$, we switch to new constant forcings ($Q_{\mathrm{si}} = 100$ W m^{-2}, $Q_0 = 50$ W m^{-2}) which causes a weathering crust to grow. The evolution of the weathering crust is shown in Figure 3.4. (Note that, since we are not including any feedback of the microbes on the weathering crust (see Section 4.5), the weathering crust solution is independent of the microbe and nutrient problem so our previous

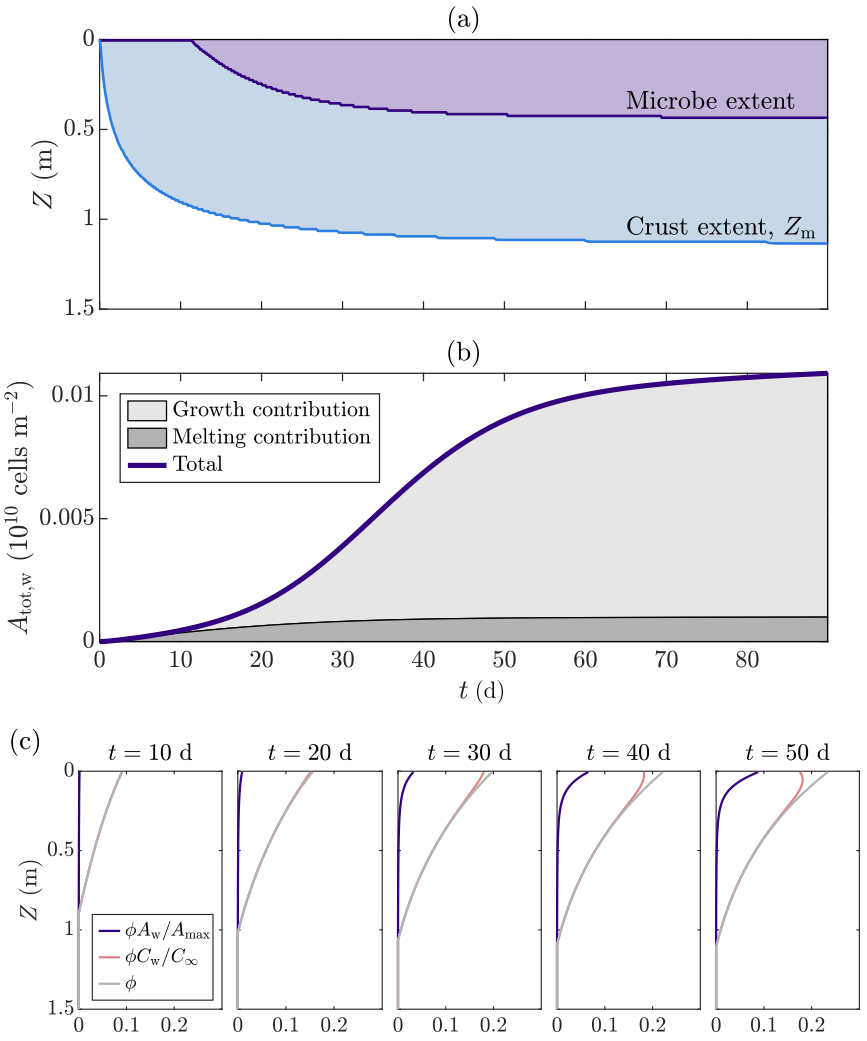


Figure 4.8: Growth of a weathering crust and microbes under constant forcings from an initial no-crust state. Panel (a) shows evolution of the size of the weathering crust and the size of the microbe-dense region (defined as the region where $\phi A_w/A_{max} > 2 \times 10^{-3}$). Panel (b) shows the evolution of the total microbial abundance $A_{tot,w}$ and its decomposition into components from growth and the release of microbes by melting ice. Panel (c) shows snapshots of the microbe, nutrient and porosity profiles. The initial condition was a steadily melting state with no crust ($Q_{si} = 0$ W m^{-2}, $Q_0 = 50$ W m^{-2}). At $t = 0$. the forcings were switched to $Q_{si} = 100$ W m^{-2}, $Q_0 = 50$ W m^{-2} and held constant. The other parameter values are those shown in Tables 2.2 and 4.2.

solution still holds.) Here, we examine the microbial growth, in Figure 4.8. Firstly, we see that there is a lag between crust growth and microbial growth. Panel (a) shows how the extent of the weathering crust and the region which contains significant amounts of microbes (defined here as where $\phi A_{\mathrm{w}}/A_{\max} > 2 \times 10^{-3}$) evolve over time. The weathering crust thickens quickly at first, then continues to thicken gradually. The rapid growth phase is almost over by the time significant microbial growth occurs. The microbe layer then also grows significantly at first, followed by a continued gradual growth phase. The snapshots of $\phi A_{\mathrm{w}}/A_{\max}$ and ϕ in panel (c) show that the porosity and microbial abundance both continue to increase once the gradual thickening phases have been reached, resulting in a continued increase in the total amount $A_{\mathrm{tot,w}}$ of microbes in the crust (panel (b)). In contrast to the behaviour for ϕ, the increase in ϕA_{w} is focused very near the surface (see $t = 40$ d to 50 d).

The evolution of the total amount $A_{\mathrm{tot,w}}$ of microbes in panel (b) also shows that, at early time, the increase is purely due to microbes being melted out of the ice. At later times, once enough nutrients and water have also been melted out of the ice, microbial growth picks up and becomes the dominant contribution.

4.4.3 Freezing of microbes

So far in this chapter, we have only considered examples where there is no freezing. As previously mentioned, this means that the microbial abundance A_{i} in the ice is constant; A_{i} is only changed when microbes get frozen into the ice or die, and here we are assuming the death rate to be zero.

Here, we briefly demonstrate the 'freezing-in' of microbes that can occur in our model. We do this by adding microbes and nutrients to the switching experiment considered in Section 3.3.4, in which a steadily melting weathering crust is removed by freezing from the surface (and from below). The weathering crust solution is unchanged by the presence of microbes and nutrients, since we are ignoring any feedbacks of microbes and nutrients on the weathering crust. We also initialise the microbes and nutrients in a steadily melting state. Figure 4.9 shows the evolution of the microbes in the water and ice as freezing occurs. At the freezing fronts, all microbes in the water get transferred to the ice as the water freezes. The microbial abundance ϕA_{w} in the water drops to zero, and there is a corresponding jump increase in the microbial abundance $(1-\phi)A_{\mathrm{i}}$ in the ice, such that the total microbial abundance $\phi A_{\mathrm{w}} + (1-\phi)A_{\mathrm{i}}$ is conserved.

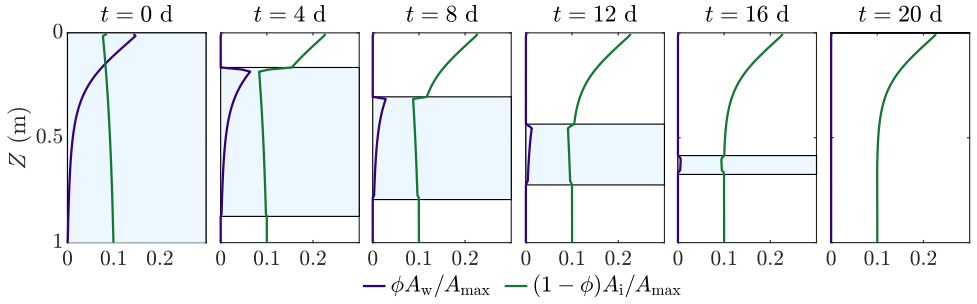


Figure 4.9: Freezing-in of microbes when a weathering crust is removed by freezing. This is the same 'switching' experiment as in Figure 3.6 (where a steadily melting weathering crust is removed by freezing), but with the addition of microbes and nutrients (also in a steadily melting state at $t = 0$ d). The microbial abundance $\phi A_\mathrm{w}/A_\mathrm{max}$ and $(1-\phi)A_\mathrm{i}/A_\mathrm{max}$ in the water and ice, respectively, are shown. The blue shaded regions show the extent of the weathering crust. The microbe and nutrient parameters used are $\beta_A = 20\ \mathrm{d}^{-1}$, $A_\infty = 0.1A_\mathrm{max}$, with the rest as in Table 4.2.

It is this mechanism by which microbes that have grown during one period of melt can be stored, dormant (i.e. not growing), in the ice until the next period of melt. Our model currently neglects the death of microbes, but in reality we expect that some of the microbes stored in the ice die ($d_\mathrm{i} > 0$), so that the microbial abundance at the start of the next period of melt is lower than when freezing occurred. The values of the growth and death rates compared to the period of growth and removal cycles of the weathering crust will go part of the way to determining how the longer-term growth of microbes is affected by the changing weathering crust in response to changing weather conditions. The effect of removing microbes in surface runoff will also be important.

4.5 Feedbacks between microbe growth, albedo, and melting

The weathering crust and the microbes within it give rise to some potential albedo feedbacks that can lead to amplified reductions in albedo and increases in melting. Here we will discuss the melt-albedo feedback [e.g. Box et al., 2012] and the microbe-albedo feedback [e.g. Tedstone et al., 2020, McCutcheon et al., 2021] and explore the ability of our model to capture and quantify these feedbacks. We first briefly outline the potential feedbacks.

As the surface of an ice sheet melts, the surface transitions from snow-covered to bare ice to having meltwater on the surface. The change in surface type from snow-covered to water-covered leads to a reduction in the albedo. This in turn means that more radiation is absorbed so more melting occurs, reducing the albedo further. The result is a positive feedback: the melt–albedo feedback [e.g. Box et al., 2012].

The surface of ice sheets can also be made darker by biological factors, especially glacier ice algae and cryoconite [Hotaling et al., 2021], with glacier ice algae thought to be a key contributor to the darkening of the Greenland ice sheet [Benning et al., 2014]. There is thought to be a potential positive feedback between ice algae and meltwater, whereby the presence of algae on the ice–sheet surface lowers the albedo, increasing melting, which releases nutrients that had been frozen in the ice, enabling more algal growth [e.g. Tedstone et al., 2020, McCutcheon et al., 2021]. The darkening effect is particularly strong for surface ice algae because the algae have a special dark pigment to protect them from high levels of UV and photosynthetically active radiation [Williamson et al., 2019, 2020]. However, a similar, but weaker, feedback can be expected for microbes in the weathering crust. Furthermore, the framework we provide here for studying the microbe–albedo feedback in the weathering crust can be easily adapted to ice algae.

4.5.1 Model

To introduce the melt–albedo and microbe–albedo feedbacks into our steadily-melting model, we make the absorption coefficient α a linearly increasing function of either the porosity ϕ or the bulk microbial abundance $A_{\text{bulk}} = \phi A_{\text{w}} + (1-\phi)A_{\text{i}}$. This captures the fact that more shortwave radiation is absorbed when there is more water (compared to ice), or when there are more microbes. The albedo a is then calculated as an output of the model from the additional boundary condition (2.30), as discussed in Chapter 2. The absorption coefficient functions we chose are

$$\alpha = \alpha_0\Big(1 + 3\phi\Big) \tag{4.26}$$

to capture the melt–albedo feedback, and

$$\alpha = \alpha_0\Big(1 + 3(A_{\text{bulk}} - A_\infty)\Big) = \alpha_0\Big(1 + 3\phi(A_{\text{w}} - A_\infty)\Big) \tag{4.27}$$

to capture the microbe–albedo feedback, where we have used that $A_{\text{i}} = A_\infty$ in our steadily-melting setup. Here, α_0 is the absorption coefficient of pure ice containing

the small background abundance of microbes A_∞. The specific linear forms of (4.26) and (4.27) have been chosen as a simple way to include the feedbacks in our model. The value 3 we have chosen in (4.26) and (4.27) is arbitrary, and using other positive values leads to qualitatively the same results. We are not aware of any literature detailing the dependence of the absorption coefficient on porosity and microbial abundance.

4.5.2 Results

By making the absorption coefficient a function of the porosity ϕ and/or the microbial abundance A_w, the steadily melting weathering crust problem can no longer be solved analytically. Furthermore, a dependence on A_w fully couples the microbe and nutrient problem to the weathering crust problem — we can no longer solve the weathering crust problem on its own first. Therefore, we must solve the full problem numerically. It is still possible to find the solution in $Z > Z_\mathrm{m}$ analytically, whereas the solution in $Z < Z_\mathrm{m}$ is found numerically using the boundary value problem solver `bvp4c` in MATLAB.

As expected, making the absorption of shortwave radiation increase with water content or microbial abundance causes a reduction in albedo in our model (Figure 4.11(c)). We find that including the meltwater coupling (4.26) reduces the albedo to 0.47 compared to 0.6 in the uncoupled case with $\alpha = \alpha_0$. Similarly, the microbe coupling (4.27) reduces the albedo of the steadily melting solution to 0.51 from 0.6.

Figure 4.10 shows a comparison between the porosity, internal radiation and microbial abundance distributions in the coupled and uncoupled cases. The effects of including meltwater coupling and microbe coupling are similar. In both cases, more radiation is absorbed by the ice than in the uncoupled case (seen in the reduction in albedo). However, the internal radiation does not increase everywhere — it is higher than the uncoupled case near the surface but lower at depth. This is because there is more water and more microbial biomass near the surface, so absorption of radiation is greatest near the surface, which in turn means that there is less radiation left to penetrate deeper into the ice.

The overall effect of including the coupling is to decrease the size of the weathering crust (decrease Z_m), lower the porosity and reduce the total amount of microbes (Figure 4.10). This might seem counterintuiutive; the feedbacks previously discussed

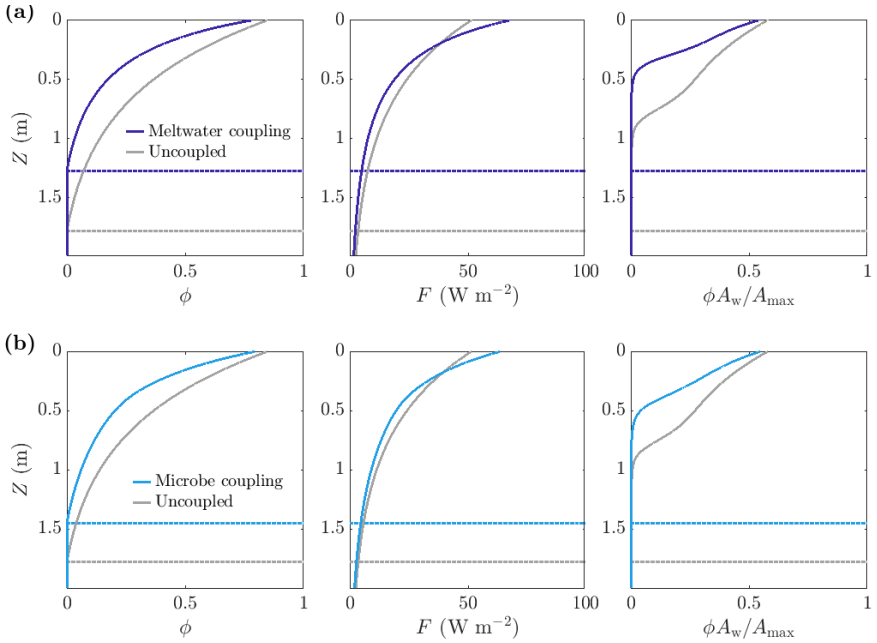


Figure 4.10: Comparison of steadily melting solutions with albedo feedbacks (dark and light blue) and without (grey). (a) Meltwater coupling, where $\alpha = \alpha_0(1+3\phi)$, so that the absorption increases with water content. The albedo in the coupled case is 0.47, compared to 0.6 in the uncoupled case. (b) Microbe coupling, where $\alpha = \alpha_0(1 + 3\phi(A_w - A_\infty))$, so that the absorption increases with the bulk microbial abundance. The albedo in the coupled case is 0.51. The dotted lines show the melting depth Z_m. The parameter values are those shown in Tables 2.2 and 4.2.

would suggest that making the absorption depend on water content or microbial abundance would lead to an increase in water content and microbial abundance, since more water and microbes leads to greater absorption resulting in even more melting and microbial growth. However, we are observing the previously discussed removal of microbes in runoff, proposed by Cook et al. [2012]. The increase in absorption has led to an increase in surface melting, lowering and runoff, with enhanced removal of microbes in runoff dominating any increase in microbial growth. Therefore, including the coupling leads to an upward translation of the microbial abundance distribution, as we saw in Section 4.3.2.

Figure 4.11 reproduces the plots of total number of microbes in the water $A_{tot,w}$ and residence time t_{res} as a function for Q_{si} from Figure 4.5, this time showing the results for meltwater coupling and microbe coupling as well as the uncoupled case from Figure 4.5 (grey). The variation with Q_{si} for $Q_0 < 0$ (top row) and $Q_0 > 0$ (middle row) is shown, as well as the variation with Q_0 (bottom row). These show that including the meltwater or microbe coupling reduces the total number of microbes and reduces their residence time, with the main effect when $Q_0 > 0$ being to reduce the second local maximum. This is because the region of significant

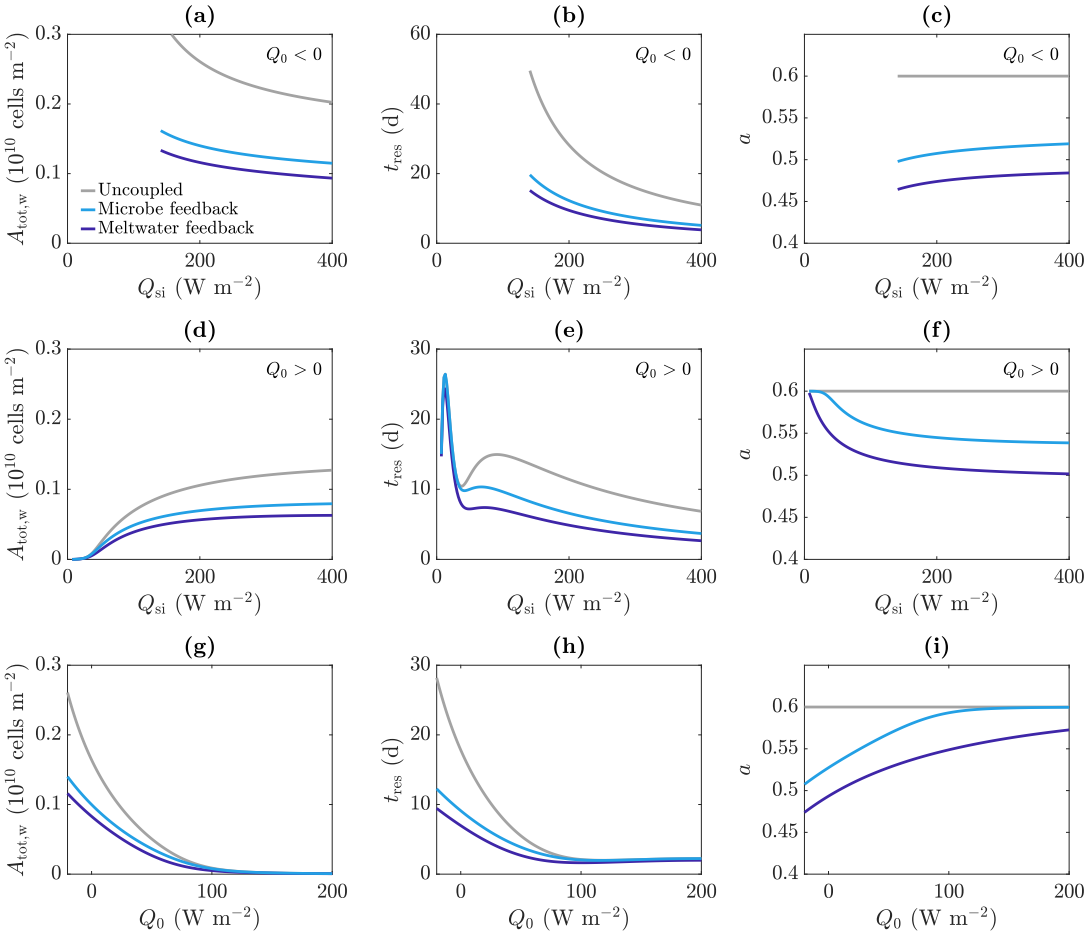


Figure 4.11: Dependence of (a,d,g) total microbes in the water $A_{\mathrm{tot,w}}$, (b,e,h) approximate residence time of the microbes t_{res}, and (c), (f), (i) albedo a, on the incoming shortwave radiation Q_{si} ((a)-(f)) and other surface radiation Q_0 ((e)-(g)). The uncoupled (grey), meltwater coupling (dark purple) and microbe coupling (light blue) cases are shown. The value of Q_0 is -20 W m $^{-2}$ (negative) in (a)-(c), and 20 W m $^{-2}$ (positive) in (d)-(f). The value of Q_{si} is 200 W m^{-2} in (g)-(i). The other parameter values are those shown in Tables 2.2 and 4.2.

microbial growth is smaller with coupling (Figure 4.10), so the increase in t_{res} from the local minimum to the second local maximum, which corresponds to the spread of the significant microbial growth region deeper into the ice (discussed around Figure 4.5), is reduced.

Note that Figure 4.11 shows that the total number of microbes, residence time and albedo are all lower with meltwater coupling than microbe coupling, but too much should not be read into this. The forms of the absorption coefficient functions (4.26) and (4.27) are illustrative only and could easily be modified such that the the microbe coupling has a larger effect (e.g. by replacing 3 in (4.27) with a larger value). The main point to take away from this investigation is that including coupling between meltwater, microbes and radiation absorption can lead to a reduction in albedo, but

also a reduction in the size of the weathering crust and the total microbial abundance within the weathering crust aquifer.

4.6 Discussion and conclusion

In this chapter, we have presented a mathematical model for microbes within the weathering crust and a nutrient for the microbes, which is coupled to the weathering crust model presented in Chapter 2. We focussed firstly on steadily melting solutions, where the internal and surface melt rates balance to produce a weathering crust of a steady size, and have also explored idealised time-dependent solutions.

We have made a number of simplifications in order to produce a reduced problem from which we can gain informative insights. One simplification of reality is our treatment of the microbes and their nutrients. We have assumed that there is a single type of phototrophic microbe and a single representative nutrient for the microbe. In reality, the weathering crust contains a range of different microbes: primary producers (e.g. algae and filamentous cyanobacteria) which use solar radiation as their energy source, and heterotrophs which use autochthonous organic carbon produced by the primary producers as their energy source [Stibal et al., 2012]. Our model could be thought of as describing a single representative type of primary producer, which requires both solar radiation and nutrients for growth. Alternatively, it could be interpreted as modelling (crudely) the combined influence of all microbes. Clearly there are more complex interactions that could be added, at the expense of introducing further parameters and potentially losing interpretability.

Similarly, the reality is that microbes require multiple nutrients to survive and grow, namely carbon (C), nitrogen (N), phosphorous (P) and a variety of micronutrients. Our model can be interpreted as whichever of the three macronutrients (C, N or P) is limiting. In the case of glacier ice algae and cryoconite microbial communities, P is usually the limiting nutrient [McCutcheon et al., 2021, Stibal and Tranter, 2007, Bagshaw et al., 2013].

We have also used a simplified treatment of 'active' (able to grow) and 'dormant' (unable to grow) microbes. Glacial microbes use dormancy as a mechanism to survive unfavourable environmental conditions, switching between being active and dormant in response to a range of factors, such as temperature, nutrient availability, and UV radiation [Bradley et al., 2023]. In our model, we simply treat the microbes in the water as active and the microbes in the ice as dormant. This is a reasonable

simplification, since it has been shown that glacial microbes transition rapidly from active to dormant during freezing (and vice versa on thawing) [Bradley et al., 2023].

Our model has given insight into the microbe distributions in the weathering crust. We have found that the microbial abundance in the weathering crust generally decreases with depth. This agrees with the expectation of Cook et al. [2016] and the observations of Christner et al. [2018]. Since radiation decreases with depth, it is expected that there will be more primary producers (with protective pigments) near the surface and more heterotrophs (which are less light-adapted) deeper down [Cook et al., 2016]. The decrease in radiation with depth also leads to a decrease in porosity and melting with depth.

Furthermore, we have observed that the climate forcing (represented by the shortwave radiation Q_{si} and combined longwave radiation and turbulent heat fluxes Q_0 in our model) has a clear impact on the residence time and abundance of microbes in the weathering crust. In general, increasing the surface forcings relative to internal radiation (for example, increasing the turbulent heat fluxes and longwave radiation Q_0) causes the size of the weathering crust, the residence time and the total number of microbes in the crust to all decrease. This is due to enhanced surface melting and runoff causing removal of the weathering crust and the microbes within it. This is in line with the suggestion that excessive warming could lead to a removal of microbes in runoff, threatening the Greenland ice sheet's state of autotrophy (net removal of CO_2) [Cook et al., 2012].

Time-dependent solutions to our model have demonstrated that there is a lag between the growth of the weathering crust and the growth of microbes at the start of a melt season. Enough microbes and nutrients must be melted out of the ice before microbial growth becomes significant. These results suggest that if the weathering crust is grown and removed over sufficiently short timescales in response to changing weather conditions, the microbes in the weathering crust might be unable to grow significantly before being frozen or washed away when the weathering crust is removed, reducing their potential impact on the albedo. This demonstrates the importance of considering the weathering crust and microbial community together as one system.

Our model also allows for the investigation of positive feedbacks. We have explored melt–albedo and microbe–albedo feedbacks by making the absorption of shortwave radiation a function of the water and microbe content of the weathering crust, respectively. These feedbacks lead to enhanced melting of the ice–sheet surface. Our

model suggests that both feedbacks act to reduce the weathering crust size and number of microbes in the weathering crust aquifer, as well as their residence times. This is due to enhanced melting leading to an increased runoff rate, so more microbes get removed from the surface. Hence these feedbacks are self limiting; the reduction in albedo cannot keep going un-limited because the increased melting leads to the removal of the microbes and meltwater that cause the albedo reduction.

However, we caution that we have focussed on microbes that live within the weathering crust aquifer (transported by meltwater), and have ignored the glacier ice algae that live on the surface of the weathering crust (affixed to the ice). Extending the model to account for glacial ice algae is a potential area for future work. This and other possible extensions to the model are discussed in Chapter 7.

Chapter 5

Weathering crust evolution with flow

5.1 Introduction

In this chapter, we neglect microbes and nutrients, and turn to extending our weathering crust model to include vertical and lateral flow of meltwater. The motivation for this extension is that (1) flow of water through the weathering crust is a key part of the observed behaviour, and (2) previous modelling work has suggested that the inclusion of meltwater drainage is necessary to reproduce observed weathering crust properties.

Firstly, the lateral flow of meltwater through the weathering crust plays an important role in transporting meltwater, microbes and nutrients into nearby surface streams

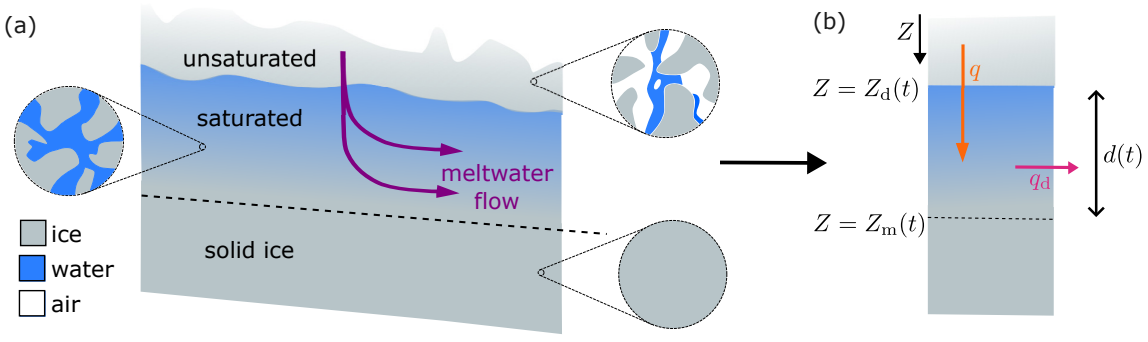


Figure 5.1: A schematic of the flow of meltwater through the weathering crust (panel (a)) and how we represent this in the one-dimensional model (panel (b)), using the downward water flux q and a parametrisation q_{d} for the lateral drainage. The thickness of the saturated region is $d = Z_{\mathrm{m}} - Z_{\mathrm{d}}$, where $Z = Z_{\mathrm{d}}$ is the position of the water table and $Z = Z_{\mathrm{m}}$ is the bottom of the weathering crust.

[Cooper et al., 2018, Irvine-Fynn et al., 2021, Chandler et al., 2015, Cook et al., 2016]. The drainage of meltwater through the crust also impacts the albedo of the surface. If a weathering crust forms on a wet, bare ice surface, the surface water is able to drain away through the weathering crust, drastically changing the appearance of the ice surface (increasing the albedo) [Tedstone et al., 2020].

In addition to this, Hoffman et al. [2014] demonstrated the importance of including lateral drainage in their one-dimensional weathering crust model for correctly capturing the observed surface lowering, porosity and temperature in an Antarctic setting. They found that, without lateral drainage, porosity is underestimated, and the time taken for the weathering crust to cool and freeze-up at the end of the summer is overestimated. The drainage of meltwater internally removes latent heat resulting in more rapid cooling of the ice, and enables the weathering crust to become unsaturated and hence refreeze with non-zero porosity.

The impermeable base of the weathering crust plays a key role in inducing lateral flow. Once meltwater reaches the base, it cannot percolate downwards anymore, so instead flows laterally over the impermeable base, in the downslope direction. This lateral drainage of meltwater frees up space for more meltwater to flow vertically downwards into the space left behind. The result is to have both lateral and vertical flow, and some regions of the crust that are unsaturated with meltwater (i.e. there is also air present in the pore space), as shown in Figure 5.1.

With a purely one-dimensional model, we can only capture transient unsaturated flow; the impermeable base and one-dimensional nature of the model means that once the weathering crust fills up with meltwater, there is nowhere for it to go (other than running off at the surface). This justifies the assumption made so far in this thesis that the weathering crust is saturated with water ($S = 1$) and there is no meltwater flow. To allow for longer-term unsaturated (vertical) flow, in this chapter we include a parametrisation of lateral flow in our one-dimensional model. This acts to represent the observed lateral drainage of meltwater, but in a one-dimensional setting.

In this chapter, we begin in Section 5.2 by presenting a one-dimensional reduction of the general three-dimensional model presented in Chapter 2, with the new addition of a parametrisation for lateral drainage to enable meltwater flow in a one-dimensional setting. We describe the numerical method used to solve the model equations in Section 5.3. In Sections 5.4 and 5.5, we apply the model to two test cases for which we can find semi-analytical solutions: (1) isothermal water transport (the infiltration of water into temperate ice with no melting), and (2) the extension of

the steadily melting solutions in Chapter 2 to include lateral drainage. We then consider idealised periodic and switching experiments analogous to those applied to the saturated model in Sections 3.4 and 3.3, respectively. In Section 5.6, we seek solutions with a periodic forcing, and in Section 5.7, we use a switching experiment to investigate the effect of lateral drainage during alternating spells of melting and freezing.

5.2 Model

The model used in this chapter is a one-dimensional reduction of the general three-dimensional weathering crust model presented in Chapter 2, retaining the simplifying assumptions made in Chapter 2 that the ice and water have shared material and thermal properties (density ρ, thermal conductivity k, specific heat capacity c).

5.2.1 Darcy's law

Recall that flow through a porous medium is driven by gravity and capillary forces, described by Darcy's law (2.4). This was introduced in Chapter 2 and is repeated here for convenience. The volume flux $\mathbf{q}$ of water per unit area relative to the ice is given by Darcy's law as

$$\mathbf{q} = \phi S(\mathbf{u}_\mathrm{w} - \mathbf{u}_\mathrm{i}) = -\frac{k(\phi)k_\mathrm{rw}(S)}{\mu}\left(\nabla p_\mathrm{w} + \rho_\mathrm{w} g\hat{\mathbf{k}}\right), \tag{5.1}$$

where p_w is the water pressure, $k(\phi)$ is the (absolute) permeability, $k_\mathrm{rw}(S)$ is the relative permeability, μ is the viscosity of water, g is the acceleration due to gravity, and $\hat{\mathbf{k}}$ is the upward pointing unit vector. We retain our assumption from Chapter 2 that there is no flow of ice ($\mathbf{u}_\mathrm{i} = \mathbf{0}$). As discussed in Chapter 2, we parametrise the permeability (2.6) and relative permeability (2.8) in terms of the porosity ϕ and saturation S, respectively, as

$$k(\phi) = k_0\phi^3, \quad k_\mathrm{rw}(S) = S^3. \tag{5.2}$$

5.2.2 Lateral flow

To incorporate the lateral flow of water into our one-dimensional model, we use a parametrisation for lateral drainage based on Darcy's law, giving the lateral drainage

flux q_d as

$$q_d = \frac{\rho g}{\mu} k_\mathrm{h}(\phi) k_\mathrm{rw}(S) \sin(\theta). \tag{5.3}$$

This represents downslope, gravity-driven flow through a weathering crust with surface slope $\sin(\theta)$, where θ is the (small) angle between the horizontal and the ice surface, and

$$k_\mathrm{h}(\phi) = \beta_\mathrm{h} k(\phi) \tag{5.4}$$

is the horizontal permeability. The permeability of the weathering crust is anisotropic, with structural features such as horizontal, impermeable ice layers making it easier for water to flow horizontally than vertically. We account for this in our model using the anisotropy factor $\beta_\mathrm{h} > 1$ to enhance the permeability in the lateral drainage parametrisation. Since the surface slope is typically small [e.g. $\sin(\theta) = 0.022$ Irvine-Fynn et al., 2021], the horizontal and downslope directions are approximately equal, and it is appropriate to use the *downslope* component of gravity with the *horizontal* permeability in the lateral flow parametrisation (5.3).

The lateral drainage q_d is assumed to occur over a lengthscale L_d, which could represent the distance between supraglacial streams into which the weathering crust water drains. This results in a 'sink' term $-q_\mathrm{d}/L_\mathrm{d}$ in the one-dimensional model below.

5.2.3 One-dimensional model equations

Here we present the one-dimensional time-dependent model equations with lateral drainage and unsaturated flow. As in previous chapters, we make a change of coordinates to $Z = h(t) - z$, the depth below the ice surface $z = h(t)$.

The mass conservation equations (2.1) and (2.2) for ice and water become

$$\rho\left(\frac{\partial}{\partial t}(1-\phi) + \dot{h}\frac{\partial}{\partial Z}(1-\phi)\right) = -m_\mathrm{int}, \tag{5.5}$$

$$\rho\left(\frac{\partial}{\partial t}(\phi S) + \dot{h}\frac{\partial}{\partial Z}(\phi S) + \frac{\partial q}{\partial Z}\right) = m_\mathrm{int} - \rho\frac{q_\mathrm{d}}{L_\mathrm{d}}, \tag{5.6}$$

where q_d is the lateral drainage (5.3) over lengthscale L_d, and q is the downward water flux, given by Darcy's law (5.1) as

$$q = \frac{k(\phi)k_\mathrm{rw}(S)}{\mu}\left(\rho g - \frac{\partial p_\mathrm{w}}{\partial Z}\right). \tag{5.7}$$

In unsaturated regions ($0 < S < 1$), the water pressure is parametrised in terms of the saturation S as

$$p_{\mathrm{w}}(S) = -\frac{\gamma}{d_p} S^{-2}, \tag{5.8}$$

using the capillary pressure parametrisation 2.10 from Chapter 2. In saturated regions ($S = 1$), p_{w} must be solved for. Details are given in Section 5.3.

The energy equation (2.11) becomes

$$\begin{aligned} \rho c\left(\frac{\partial}{\partial t}((1-\phi+\phi S)T) + \dot{h}\frac{\partial}{\partial Z}((1-\phi+\phi S)T) + \frac{\partial}{\partial Z}(qT)\right) \\ = k\frac{\partial}{\partial Z}\left((1-\phi+\phi S)\frac{\partial T}{\partial Z}\right) - \frac{\partial F}{\partial Z} - \mathcal{L}m_{\mathrm{int}} - \rho c\frac{q_{\mathrm{d}}T}{L_{\mathrm{d}}}, \end{aligned} \tag{5.9}$$

where the additional final term represents the heat removed from the system by the internal lateral drainage of water. The net downward internal shortwave radiation F is modelled using the two stream approximation (2.20), (2.21) and boundary conditions (2.28), (2.29) presented in Chapter 2 (not repeated here). The boundary conditions for the mass and energy conservation equations are the surface energy balance (2.18), kinematic conditions (2.14), (2.15), and far-field condition (2.27), which reduce to

$$\begin{aligned} k(1-\phi+\phi S)\frac{\partial T}{\partial Z} + \chi(1-a)Q_{\mathrm{si}} + Q_0 \\ - (\upsilon + \rho c(R_{\mathrm{r}} + R_{\mathrm{s}}))(T - T_{\mathrm{m}}) = \rho\mathcal{L}m_{\mathrm{surf}} \quad \text{at} \quad Z = 0, \end{aligned} \tag{5.10}$$

$$-\rho(1-\phi)\dot{h} = \rho(m_{\mathrm{surf}} - R_{\mathrm{s}}) \quad \text{at} \quad Z = 0, \tag{5.11}$$

$$-\rho(q + S\phi\dot{h}) = \rho(r_{\mathrm{off}} - m_{\mathrm{surf}} - R_{\mathrm{r}}) \quad \text{at} \quad Z = 0, \tag{5.12}$$

and

$$T \to T_\infty \quad \text{as} \quad Z \to \infty, \tag{5.13}$$

respectively, in the one-dimensional case.

5.2.4 Enthalpy formulation

To solve the saturated ($S = 1$), time-dependent problem in Chapter 3, we formulated the model in terms of the enthalpy H. This enabled us to solve one equation for the single variable H everywhere in the domain. Here, we extend the enthalpy formulation to the unsaturated case ($0 < S < 1$). This is achieved by updating the definition of the enthalpy H and introducing the total water content W. The total

water content W, defined as the sum of both the ice and liquid water contributions, is

$$W = 1 - \phi + S\phi, \tag{5.14}$$

and the enthalpy H, defined as the sum of the sensible and latent heat, is

$$H = \rho c W (T - T_{\mathrm{m}}) + \rho \mathcal{L} \phi S. \tag{5.15}$$

By considering the three separate cases of only–ice, ice–and–water, and only–water (as we did in Chapter 3), we can recover the porosity ϕ, saturation S and temperature T from the total water content W (5.14) and the enthalpy H (5.15) as:

$$\begin{aligned}
\phi &= \begin{cases} 1 - W, & H \leq 0, \\ 1 - W + \frac{H}{\rho \mathcal{L}}, & 0 < H < \rho \mathcal{L} W, \\ 1, & H \geq \rho \mathcal{L} W, \end{cases} \\
S &= \begin{cases} 0, & H \leq 0, \\ \frac{H}{\rho \mathcal{L} \phi}, & 0 < H < \rho \mathcal{L} W, \\ W, & H \geq \rho \mathcal{L} W, \end{cases} \\
T &= \begin{cases} T_m + \frac{H}{\rho c W}, & H \leq 0, \\ T_m, & 0 < H < \rho \mathcal{L} W, \\ T_m + \frac{H}{\rho c W} - \frac{\mathcal{L}}{c}, & H \geq \rho \mathcal{L} W. \end{cases}
\end{aligned} \tag{5.16}$$

Here, the three cases $H < 0$, $0 < H < \rho \mathcal{L} W$ and $H > \rho \mathcal{L} W$ correspond to there being no water, both ice and water, and no ice, respectively.

We are able to manipulate the model equations to express the problem in terms of W and H instead of T, ϕ and S. Summing the two mass conservation equations (5.5) and (5.6), we eliminate the melt rate m_{int} to get an equation for the total water content W,

$$\frac{\partial W}{\partial t} + \frac{\partial}{\partial Z}\left(\dot{h} W + q\right) = -\frac{q_{\mathrm{d}}}{L_{\mathrm{d}}}. \tag{5.17}$$

To obtain an equation for the enthalpy H, we use the water mass conservation equation (5.6) to eliminate m_{int} from the energy equation (5.9), then subtract off $\rho c T_{\mathrm{m}}$ times the W equation (5.17), to obtain

$$\begin{aligned}
\frac{\partial H}{\partial t} + \frac{\partial}{\partial Z}\left(\dot{h} H - k W \frac{\partial T}{\partial z} + F + \left(\rho \mathcal{L} + \rho c (T - T_{\mathrm{m}})\right) q\right) = &- \rho \mathcal{L} \frac{q_{\mathrm{d}}}{L_{\mathrm{d}}} \\
&- \rho c (T - T_{\mathrm{m}}) \frac{q_{\mathrm{d}}}{L_{\mathrm{d}}}.
\end{aligned} \tag{5.18}$$

Furthermore, summing the two kinematic conditions (5.11) and (5.12) eliminates the surface melt rate m_{surf} to give a surface boundary condition in terms of W,

$$q + \dot{h}W = R_{\text{s}} + R_{\text{r}} - r_{\text{off}} \quad \text{at} \quad Z = 0, \tag{5.19}$$

where R_{s} is the snowfall (solid accumulation) rate, R_{r} is the rainfall rate, and r_{off} is the surface runoff rate. When the surface is unsaturated ($S < 1$ at $Z = 0$), we assume that surface water can percolate down into the pore space. Hence the runoff r_{off} is zero, and (5.19) provides a boundary condition relating q and S at $Z = 0$. When the surface is saturated ($S = 1$ at $Z = 0$), we assume that excess surface water is removed instantaneously as surface runoff, with r_{off} given by (5.19). In this case, we prescribe that $p_{\text{w}} = p_{\text{a}}$ at $Z = 0$ as the surface boundary condition, where p_{a} is atmospheric pressure (set to zero without loss of generality), which allows us to solve for the water pressure p_{w} and hence water flux q in the saturated region (see Section 5.3 for more details).

The surface energy balance (5.10) can be written in terms of W as

$$kW\frac{\partial T}{\partial Z} + \chi(1-a)Q_{\text{si}} + Q_0 - (\upsilon + \rho c(R_{\text{s}} + R_{\text{r}}))(T - T_{\text{m}}) = \rho\mathcal{L}m_{\text{surf}} \quad \text{at} \quad Z = 0. \tag{5.20}$$

5.2.5 Non-dimensionalisation

For much of this chapter, we choose to work with dimensionless variables. This allows to justify neglecting certain small terms in our equations, making analytical solutions possible (see Section 5.4).

We non-dimensionalise our model by scaling $T = T_{\text{m}} + [T]\hat{T}$ and scaling all other variables about zero with

$$\begin{gathered}[T] = \frac{[t][F]}{\rho c[Z]}, \quad [m_{\text{int}}] = \frac{\rho}{[t]}, \quad [m_{\text{surf}}] = [R_{\text{s}}] = [R_{\text{r}}] = [r_{\text{off}}] = \frac{[Z]}{[t]}, \\ [H] = \rho c[T], \quad [q] = \frac{[Z]}{[t]}, \quad [p_{\text{w}}] = \rho g[Z], \quad [h] = [Z],\end{gathered} \tag{5.21}$$

with $[Z]$, $[t]$ and $[F]$ prescribed. Typically, we use $[Z] = 1$ m, $[F] = 200$ W m^{-2}, and $[t] = 1$ day or 1 year. Typical values of the other scalings, calculated from the parameter values in Table 2.2, are shown in Table 5.1.

Scaling	Typical value
$[t]$	1 day
$[Z]$	1 m
$[F]$	200 W m^{-2}
$[T]$	9.05 K
$[m_{\mathrm{surf}}]$, $[R_{\mathrm{s}}]$, $[R_{\mathrm{r}}]$, $[r_{\mathrm{off}}]$, $[q]$	1 m d^{-1}
$[H]$	1.7 $\times 10^7$ kg m^{-1} s^{-2}
$[p_{\mathrm{w}}]$	8.9 kPa
$[m_{\mathrm{int}}]$	910 kg m^{-3} d^{-1}
$[h]$	1 m

Table 5.1: Scalings used to non-dimensionalise the weathering crust model. The typical values are calculated from the values shown in Table 2.2. Note that W, ϕ and S are already dimensionless, so are not listed here.

Symbol	Typical value	Dimensionless parameter
$\mathcal{S}$	17.6	Stefan number
$\hat{k}$	0.095	Dimensionless thermal conductivity
a	0.6	Albedo
χ	0.36	Proportion of absorbed shortwave radiation absorbed at the surface
$\hat{\alpha}$	0.26	Dimensionless absorption coefficient
$\hat{r}$	4.1	Dimensionless scattering coefficient
$\hat{\kappa}$	1.5	Dimensionless extinction coefficient
$\mathcal{K}$	42.9	Hydraulic conductivity scale
$\mathcal{B}$	12.8*	Bond number
$\mathcal{K}_{\mathrm{d}}$	0.01 – 100	Lateral drainage strength/efficiency
$\mathcal{Q}_{\mathrm{si}}$	0 – 5	Dimensionless shortwave radiation
$\mathcal{Q}_0$	-3 – 2	Dimensionless longwave radiation and turbulent heat fluxes
$\hat{\upsilon}$	0.67	Dimensionless effective heat transfer coefficient
$\mathcal{T}_\infty$	-1.1	Dimensionless far-field temperature

Table 5.3: Dimensionless parameters in the weathering crust model. Typical values used in this chapter are shown, calculated using the parameters values and scalings shown in Table 2.2 and Table 5.1. Parameters below the line are the dimensionless model forcings. *The Bond number is assumed to be infinite in Sections 5.4 and 5.5.

The following dimensionless parameters are thus introduced:

$$\begin{aligned} \hat{k} = \frac{k[t]}{\rho c[Z]^2}, \quad \mathcal{S} = \frac{\mathcal{L}}{c[T]}, \quad \hat{\alpha} = \alpha[Z], \quad \hat{r} = r[Z], \quad \hat{\kappa} = \kappa[Z], \\ \mathcal{K} = \frac{k_0 \rho g[t]}{\mu[Z]}, \quad \mathcal{B} = \frac{\rho g[Z] d_p}{\gamma}, \quad \mathcal{K}_{\mathrm{d}} = \frac{\sin(\theta)\beta_{\mathrm{h}}[Z]}{L_{\mathrm{d}}}, \end{aligned} \tag{5.22}$$

where $\hat{k}$ is the dimensionless thermal conductivity, $\mathcal{S}$ is the Stefan number (the

ratio of latent heat to sensible heat, with a larger latent heat meaning more energy is required to achieve the same amount of melting), $\hat{\alpha}$ and $\hat{r}$ are dimensionless absorption and scattering coefficients, $\hat{\kappa}$ is the dimensionless extinction coefficient, $\mathcal{K}$ is the dimensionless hydraulic conductivity (a measure of how easily water can flow through the porous ice), $\mathcal{B}$ is the Bond number (a measure of the effect of gravity compared to capillary pressure), and $\mathcal{K}_\mathrm{d}$ is the dimensionless lateral drainage strength/efficiency. $\mathcal{K}_\mathrm{d}$ accounts for the effect of surface slope and the anisotropy of the permeability. The dimensionless forcings are

$$\mathcal{Q}_\mathrm{si} = \frac{Q_\mathrm{si}}{[F]}, \quad \mathcal{Q}_0 = \frac{Q_0}{[F]}, \quad \hat{v} = \frac{v[T]}{[F]}, \quad \mathcal{T}_\infty = \frac{T_\infty - T_\mathrm{m}}{[T]}. \tag{5.23}$$

Typical values of the dimensionless parameters and forcings are shown in Table 5.3. We now summarise the dimensionless model.

The dimensionless enthalpy H and total water content W are expressed in terms of the temperature T, porosity ϕ and saturation S as

$$H = WT + \mathcal{S}\phi S, \tag{5.24}$$

$$W = 1 - \phi + \phi S. \tag{5.25}$$

The porosity, saturation and temperature are recovered as

$$\phi = \begin{cases} 1 - W, & H \leq 0, \\ 1 - W + \frac{H}{\mathcal{S}}, & 0 < H < \mathcal{S}W, \\ 1, & H \geq \mathcal{S}W, \end{cases} \tag{5.26}$$

$$S = \begin{cases} 0, & H \leq 0, \\ \frac{H}{\mathcal{S}\phi}, & 0 < H < \mathcal{S}W, \\ W, & H \geq \mathcal{S}W, \end{cases} \tag{5.27}$$

$$T = \begin{cases} \frac{H}{W}, & H \leq 0, \\ 0, & 0 < H < \mathcal{S}W, \\ \frac{H}{W} - \mathcal{S}, & H \geq \mathcal{S}W. \end{cases} \tag{5.28}$$

The dimensionless mass and energy conservation equations are

$$\frac{\partial}{\partial t}(1 - \phi) + \dot{h}\frac{\partial}{\partial Z}(1 - \phi) = -m_\mathrm{int}, \tag{5.29}$$

$$\frac{\partial}{\partial t}(\phi S) + \dot{h}\frac{\partial}{\partial Z}(\phi S) + \frac{\partial q}{\partial Z} = m_{\rm int} - q_{\rm d}, \tag{5.30}$$

$$\frac{\partial}{\partial t}(WT) + \dot{h}\frac{\partial}{\partial Z}(WT) + \frac{\partial}{\partial Z}(qT) = \hat{k}\frac{\partial}{\partial Z}\left(W\frac{\partial T}{\partial Z}\right) - \frac{\partial F}{\partial Z} - \mathcal{S}m_{\rm int} - q_{\rm d}T. \tag{5.31}$$

The net downward radiation is $F = F_+ - F_-$, where the two-stream approximation is

$$\frac{\partial F_-}{\partial Z} = -(\hat{\alpha} + \hat{r})F_- + \hat{r}F_+, \tag{5.32}$$

$$\frac{\partial F_+}{\partial Z} = (\hat{\alpha} + \hat{r})F_+ - \hat{r}F_-. \tag{5.33}$$

The dimensionless equations used in the enthalpy method (equivalent to equations (5.29), (5.30) and (5.31)) are

$$\frac{\partial W}{\partial t} + \frac{\partial}{\partial Z}\left(\dot{h}W + q\right) = -q_{\rm d}, \tag{5.34}$$

$$\frac{\partial H}{\partial t} + \frac{\partial}{\partial Z}\left(\dot{h}H - \hat{k}W\frac{\partial T}{\partial Z} + F + (\mathcal{S}+T)q\right) = -(\mathcal{S}+T)q_{\rm d}, \tag{5.35}$$

where the lateral drainage flux (5.3) is

$$q_d = \mathcal{K}_{\rm d}\mathcal{K}k(\phi)k_{\rm rw}(S), \tag{5.36}$$

and the downward water flux (5.7) is

$$q = \mathcal{K}k(\phi)k_{\rm rw}(S)\left(1 - \frac{\partial p_{\rm w}}{\partial Z}\right) \tag{5.37}$$

with

$$k(\phi) = \phi^3, \quad k_{rw}(S) = S^3. \tag{5.38}$$

Either $S = 1$ and $p_{\rm w}$ must be solved for, or $0 < S < 1$ and $p_{\rm w}$ is parametrised in terms of S as

$$p_{\rm w}(S) = -\frac{1}{\mathcal{B}}S^{-2}, \tag{5.39}$$

with details given in Section 5.3. The internal melt rate $m_{\rm int}$ is given by

$$m_{\rm int} = \frac{\partial \phi}{\partial t} + \dot{h}\frac{\partial \phi}{\partial Z}. \tag{5.40}$$

The boundary conditions are

$$\hat{k}W\frac{\partial T}{\partial Z} + (\chi(1-a)\mathcal{Q}_{\rm si} + \mathcal{Q}_0) - (\hat{v} + R_{\rm s} + R_{\rm r})T = \mathcal{S}m_{\rm surf} \quad \text{at} \quad Z = 0, \tag{5.41}$$

$$q + \dot{h}W = R_{\mathrm{s}} + R_{\mathrm{r}} - r_{\mathrm{off}} \quad \text{at} \quad Z = 0, \tag{5.42}$$

$$m_{\mathrm{surf}} = R_{\mathrm{s}} - (1-\phi)\dot{h}, \quad \text{at} \quad Z = 0, \tag{5.43}$$

$$F_{-} = (1 - \chi(1-a))\mathcal{Q}_{\mathrm{si}} \quad \text{at} \quad Z = 0, \tag{5.44}$$

$$T \to \mathcal{T}_{\infty} \quad \text{as} \quad Z \to \infty, \tag{5.45}$$

$$W \to 1 \quad \text{as} \quad Z \to \infty, \tag{5.46}$$

$$F_{+} \to 0 \quad \text{as} \quad Z \to \infty, \tag{5.47}$$

with

$$F_{+} = a\mathcal{Q}_{\mathrm{si}} \quad \text{at} \quad Z = 0 \tag{5.48}$$

being used to define the albedo.

In Sections 5.3, 5.4 and 5.5, we work with dimensionless variables. In Sections 5.6 and 5.7, we return to working with dimensional variables.

5.3 Numerical method

We solve the enthalpy equation (5.35) and total water content equation (5.34) using a finite volume scheme with semi-implicit timestepping. Full details of the numerical method are given in Appendix B.2. Here, I present an overview of how we solve for the water pressure p_{w} and water flux q, as alluded to above.

5.3.1 Calculating water pressure and flux

The water pressure p_{w} and water flux q are calculated differently in saturated ($S = 1$) and unsaturated ($0 < S < 1$) regions.

In unsaturated regions, p_{w} is parametrised in terms of saturation (given by (5.39)) and so the expression (5.37) for q becomes

$$q = \mathcal{K}k(\phi)\left(S^3 - \frac{2}{B}\frac{\partial S}{\partial Z}\right) \quad \text{when} \quad 0 < S < 1. \tag{5.49}$$

In saturated regions, the flux becomes

$$q = \mathcal{K}k(\phi)\left(1 - \frac{\partial p_{\mathrm{w}}}{\partial Z}\right) \quad \text{when} \quad S = 1, \tag{5.50}$$

and satisfies (from (5.35) with $W = 1$)

$$\frac{\partial q}{\partial Z} = -q_{\mathrm{d}}, \tag{5.51}$$

where $q_{\mathrm{d}} = \mathcal{K}_{\mathrm{d}}\mathcal{K}k(\phi)$ when $S = 1$. Hence the water pressure p_{w} satisfies the elliptical equation

$$\frac{\partial}{\partial Z}\left(\mathcal{K}k(\phi)\left(1 - \frac{\partial p_{\mathrm{w}}}{\partial Z}\right)\right) = -\mathcal{K}_{\mathrm{d}}\mathcal{K}k(\phi). \tag{5.52}$$

In most saturated regions, we solve equation (5.52) for p_{w}. The boundary conditions are continuity with atmospheric pressure $p_{\mathrm{w}} = p_{\mathrm{a}}$ at the surface and at interfaces between saturated and unsaturated regions (noting that we have already set $p_{\mathrm{a}} = 0$, without loss of generality), and no flux at impermeable, solid boundaries. The flux q is then calculated using equation (5.50). (We apply $p_{\mathrm{w}} = p_{\mathrm{a}}$ at saturated–unsaturated interfaces, instead of continuity with the unsaturated pressure $p_{\mathrm{w}} = p_{\mathrm{a}} - \frac{1}{\mathcal{B}}S^{-2}$, to avoid numerical issues when there are large unresolved gradients in S at these interfaces, and note that the two conditions are equivalent when $\mathcal{B} \to \infty$.)

In saturated regions with a solid base (e.g. the bottom of the weathering crust), the no-flux condition at the impermeable base allows us to integrate the q equation (5.51) directly to find q, without ever needing to solve for p_{w}. In our numerical method, we do this for saturated regions bounded on both sides by solid ice, since the p_{w} equation is ill-posed in these regions. (The pressure is only determined up to a constant.)

5.4 Isothermal water transport

To start, we consider some idealised test cases for which we can find analytical solutions. We compare these to our numerical solutions as a test of the numerical method. In this section and Section 5.5, we work with dimensionless variables.

One test case is to consider the infiltration of (rain)water into temperate (i.e. at the melting temperature) porous ice, with constant temperature and porosity. This removes the thermal aspect of the problem, allowing us to isolate and test the water flow. We assume that the porous ice is at the melting temperature everywhere for all time, so that both water and ice can be present. We also assume that there is no melting (internal or surface) or freezing, meaning that the porosity ϕ is constant, so

$\phi = \phi(Z)$. These conditions are achieved by setting $T = 0$ initially and having no prescribed radiation. We force the model with prescribed constant rainfall $R_\mathrm{r} = q_0$ at the surface, and assume that there is no water present initially ($S = 0$).

The porosity in the weathering crust is observed to decrease roughly exponentially with depth, before becoming zero at the bottom of the weathering crust. We therefore prescribe the porosity to be

$$\phi(Z) = \phi_0 \exp\left(-\frac{Z}{Z_0}\right), \tag{5.53}$$

for some constants ϕ_0 and Z_0. To make finding an analytical solution more tractable, this assumed porosity profile does not go to zero at finite depth. We could truncate the profile at some depth to introduce an impermeable base, but the flow behaviour before the impermeable base is reached will be identical to what we find here.

5.4.1 Qualitative solution

Solutions for different values of lateral drainage are shown in Figures 5.2 and 5.3 (and, later, Figure 5.4). The influx of water at the surface into the initially dry porous ice results in a wetting front $Z_\mathrm{w}(t)$ propagating downwards, behind which there is unsaturated flow (Figure 5.2 until $t = 0.3$; Figure 5.3 top until $t = 0.8$ and bottom for all time). Provided that the lateral drainage q_d is small enough, the exponentially decreasing porosity with depth means that the saturation (given later by (5.67)) increases with depth and, after some time, saturation occurs (i.e. $S = 1$) at the wetting front (Figure 5.2, $t = 0.4$; Figure 5.3 $t = 0.8$). This results in a growing saturated region that grows both upwards and downwards (Figure 5.2, $t = 0.4$ onwards; Figure 5.3, $t = 0.8$ onwards). We call the boundaries of the saturated region the top and bottom saturation fronts $Z_\mathrm{t}(t)$ and $Z_\mathrm{b}(t)$. The lower saturation front is the continuation of the wetting front. If the lateral drainage is large enough, the saturation decreases with depth and saturation never occurs (Figure 5.3, $\mathcal{K}_\mathrm{d} = 10$).

5.4.2 Approximate solution neglecting capillary pressure

In order to find a semi-analytical solution for the wetting and saturation fronts, we assume that the Bond number is large, meaning that gravity dominates capillary pressure. The method is adapted from that in Meyer and Hewitt [2017], which

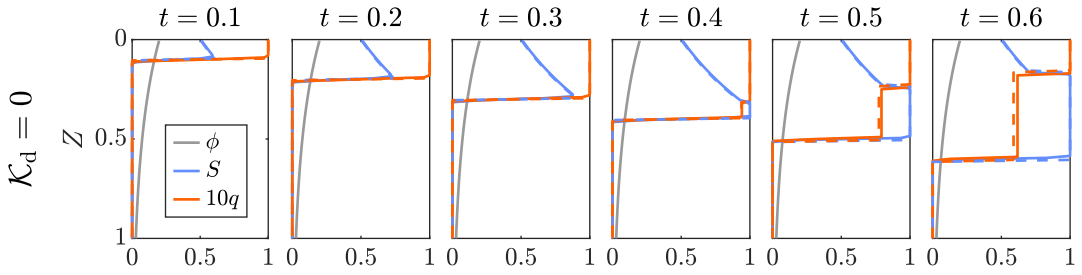


Figure 5.2: Isothermal water transport with **no** lateral drainage ($\mathcal{K}_\mathrm{d} = 0$). Analytical (dashed lines) and numerical (solid lines) solutions for saturation S (blue) and 10 times the water flux q (orange), with the fixed porosity profile shown in grey. Note that q is multiplied by 10 to make it more visible in the plots. Other parameters are $\mathcal{K} = 100$, $\phi_0 = 0.2$, $Z_0 = 0.5$, $q_0 = 0.1$, with $\mathcal{B} = 10^{10}$ in the numerical simulations. Solutions shown are dimensionless.

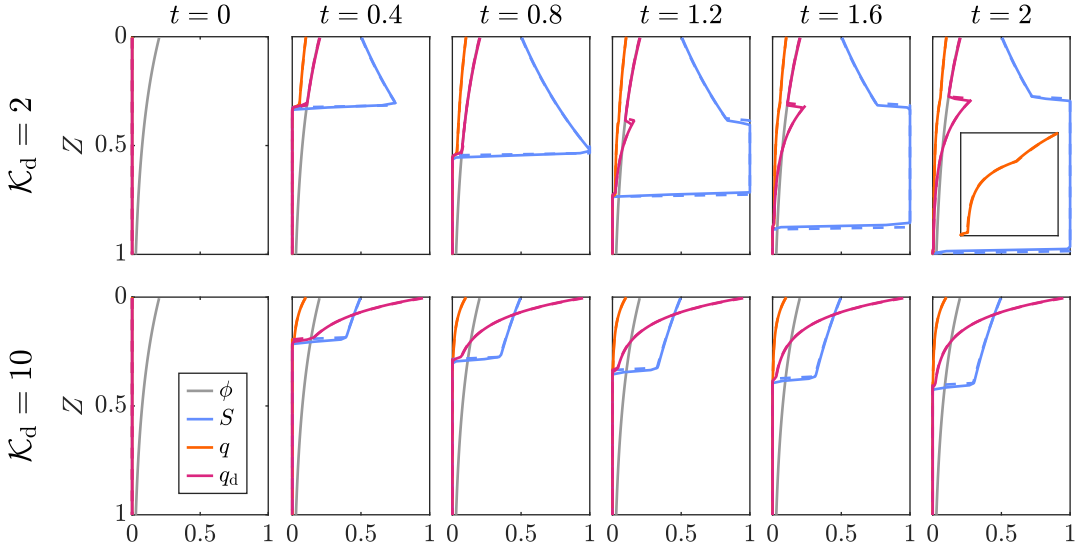


Figure 5.3: Isothermal water transport with **with** lateral drainage for $\mathcal{K}_\mathrm{d} = 2$ (top) and $\mathcal{K}_\mathrm{d} = 10$ (bottom). Analytical (dashed lines) and numerical (solid lines) solutions for saturation S (blue), downward water flux q (orange) and lateral drainage q_d (pink), with the fixed porosity profile shown in grey. The inset demonstrates the discontinuities in the gradient of q across the saturation fronts. Other parameters are $\mathcal{K} = 100$, $\phi_0 = 0.2$, $Z_0 = 0.5$, $q_0 = 0.1$, with $\mathcal{B} = 10^{10}$ in the numerical simulations. Solutions shown are dimensionless.

addresses the case of no lateral drainage. Since the $1/\mathcal{B}$ term in the flux (5.49) gives rise to a diffusion term in the saturation equation, neglecting it means that the semi-analytical solution has discontinuities in S, which are smoothed out in the numerical solution.

With $\mathcal{B} \gg 1$, the water pressure in the unsaturated regions is approximately zero (i.e. equal to atmospheric pressure). This means that the downward water flux q (5.37) is gravity-driven, and the lateral drainage q_d is therefore proportional to q, as

$$q_\mathrm{d} = \mathcal{K}_\mathrm{d} q \tag{5.54}$$

in unsaturated regions. The total water content equation (5.34) in unsaturated regions, $0 < S < 1$, can therefore be expressed as

$$\frac{\partial}{\partial t}(\phi S) + \frac{\partial q}{\partial Z} = -\mathcal{K}_\mathrm{d} q \quad \text{with} \quad q = \mathcal{K}\phi^3 S^3. \tag{5.55}$$

In saturated regions, where $S = 1$, we have $q_\mathrm{d} = \mathcal{K}_\mathrm{d}\mathcal{K}\phi^3$, and therefore

$$\frac{\partial q}{\partial Z} = -\mathcal{K}_\mathrm{d}\mathcal{K}\phi^3 \quad \text{with} \quad q = \mathcal{K}\phi^3\left(1 - \frac{\partial p_\mathrm{w}}{\partial Z}\right), \tag{5.56}$$

with p_w to be determined. In (5.56), we have used that ϕS is time independent (since $S = 1$ and $\phi = \phi(Z)$). The initial and boundary conditions are

$$S = 0 \quad \text{at} \quad t = 0, \tag{5.57}$$

$$q = q_0 \quad \text{at} \quad Z = 0. \tag{5.58}$$

5.4.2.1 Wetting fronts — before saturation occurs

In the initial phase before saturation occurs, we only need to solve the unsaturated form of equation (5.55), which it is helpful express in terms of a new variable $\tilde{W} = \phi S$, as

$$\frac{\partial \tilde{W}}{\partial t} + 3\mathcal{K}\tilde{W}^2\frac{\partial \tilde{W}}{\partial Z} = -\mathcal{K}_\mathrm{d}\mathcal{K}\tilde{W}^3. \tag{5.59}$$

This can be solved using the method of characteristics. The characteristic equations are

$$\dot{t} = 1, \quad \dot{Z} = 3\mathcal{K}\tilde{W}^2, \quad \dot{\tilde{W}} = -\mathcal{K}_\mathrm{d}\mathcal{K}\tilde{W}^3, \tag{5.60}$$

where $\dot{\square}$ denotes the derivative along the characteristics. Along the characteristics,

$$\frac{\mathrm{d}\tilde{W}}{\mathrm{d}Z} = \frac{\dot{\tilde{W}}}{\dot{Z}} = -\frac{\mathcal{K}_\mathrm{d}}{3}\tilde{W}, \tag{5.61}$$

and so

$$\tilde{W} = Ae^{-\mathcal{K}_\mathrm{d}Z/3}, \tag{5.62}$$

where A is constant along each characteristic.

There are two sets of characteristics: one set from $t = 0$ (to which we apply the initial condition (5.57)) and one set from $Z = 0$ (to which we apply the boundary condition (5.58)). Our initial condition (5.57) is expressed in terms of $\tilde{W}$ as

$$\tilde{W} = 0 \quad \text{at} \quad t = 0. \tag{5.63}$$

Hence, on the characteristics starting from $t = 0$, we have $A = 0$. The boundary condition (5.58) for constant flux (rainfall) at the surface can be expressed in terms of $\tilde{W}$ as

$$\tilde{W} = \left(\frac{q_0}{\mathcal{K}}\right)^{1/3} \quad \text{at} \quad Z = 0. \tag{5.64}$$

Hence, the characteristics starting from $Z = 0$ have $A = (q_0/\mathcal{K})^{1/3}$.

The two sets of characteristics intersect (creating a 'shock') at a wetting front $Z = Z_\mathrm{w}(t)$, the depth to which water from the surface has infiltrated, with the region below this being dry. The position of $Z_\mathrm{w}(t)$ is found using the Rankine-Hugoniot condition [Ockendon et al., 2016], giving

$$\dot{Z}_\mathrm{w} = \frac{[\mathcal{K}\tilde{W}^3]^+_-}{[\tilde{W}]^+_-} = \mathcal{K}\tilde{W}^2_-, \tag{5.65}$$

where the square brackets represent the jump in the solution across Z_w, with '$-$' being the solution from the $Z = 0$ characteristics, and '$+$' being the solution from the $t = 0$ characteristics.

Combining the above expressions, we find the solution

$$\tilde{W} = \begin{cases} (\frac{q_0}{\mathcal{K}})^{1/3}e^{-\mathcal{K}_\mathrm{d}Z/3}, & Z < Z_\mathrm{w}(t), \\ 0, & Z > Z_\mathrm{w}(t), \end{cases} \tag{5.66}$$

from which we recover

$$S = \begin{cases} \frac{1}{\phi_0}(\frac{q_0}{\mathcal{K}})^{1/3} e^{(1/Z_0 - \mathcal{K}_\mathrm{d}/3)Z}, & Z < Z_\mathrm{w}(t), \\ 0, & Z > Z_\mathrm{w}(t), \end{cases} \tag{5.67}$$

and

$$q = \begin{cases} q_0 e^{-\mathcal{K}_\mathrm{d} Z}, & Z < Z_\mathrm{w}(t), \\ 0, & Z > Z_\mathrm{w}(t), \end{cases} \tag{5.68}$$

where the wetting front is given, from solving (5.65), by

$$Z_\mathrm{w}(t) = \frac{3}{2\mathcal{K}_\mathrm{d}} \log\left(1 + \frac{2}{3}\mathcal{K}_\mathrm{d}\mathcal{K}^{1/3} q_0^{2/3} t\right). \tag{5.69}$$

The solution presented here holds until saturation ($S = 1$) first occurs.

For sufficiently small lateral drainage ($\mathcal{K}_\mathrm{d} < 3/Z_0$), the saturation increases with depth, with $S = 1$ first being reached at the wetting front after a time t_s (e.g. $\mathcal{K}_\mathrm{d} = 2$ in Figures 5.4 and 5.3). The position Z_s at which this occurs is found by setting $S(Z_\mathrm{s}) = 1$, giving

$$Z_\mathrm{s} = \frac{Z_0}{3 - Z_0\mathcal{K}_\mathrm{d}} \log\left(\frac{\mathcal{K}\phi_0^3}{q_0}\right). \tag{5.70}$$

The time t_s at which saturation first occurs is then found by equating Z_s to the wetting from position Z_w (5.69), resulting in

$$t_\mathrm{s} = \frac{3}{2\mathcal{K}_\mathrm{d}\mathcal{K}^{1/3} q_0^{2/3}} \left(\left(\frac{\mathcal{K}\phi_0^3}{q_0}\right)^{\frac{2Z_0\mathcal{K}_\mathrm{d}}{9 - 3Z_0\mathcal{K}_\mathrm{d}}} - 1\right). \tag{5.71}$$

For this solution to hold, we must have $\mathcal{K}_\mathrm{d} < 3/Z_0$. That is, the lateral drainage must not be too large. If $\mathcal{K}_\mathrm{d} > 3/Z_0$, the saturation decreases with depth and never reaches 1.

5.4.2.2 Saturation fronts — after saturation first occurs

Once saturation first occurs at $Z = Z_\mathrm{s}$ at time $t = t_\mathrm{s}$, we have a growing saturated region $Z_\mathrm{t}(t) < Z < Z_\mathrm{b}(t)$ in which $S = 1$. The top boundary $Z_\mathrm{t}(t)$ moves upwards (decreases in value, given the orientation of Z) and the bottom boundary $Z_\mathrm{b}(t)$ moves downwards (increases in value). We can find these saturation fronts by solving the equations (5.56) for the water flux q and and water pressure p_w in the saturated

region. This tells us that the flux q in the saturated region is

$$q = q_{s0} + \frac{Z_0}{3}\mathcal{K}_d\mathcal{K}\phi^3 \quad \text{for} \quad Z_t(t) < Z < Z_b(t), \quad t > t_s, \tag{5.72}$$

for some $q_{s0}(t)$ independent of Z. The value of q_{s0} is found by integrating the expression in equation (5.56) for the flux in the saturated region from $Z = Z_t$ to $Z = Z_b$. This tells us that

$$p_w(Z_b) - p_w(Z_t) = Z_b - Z_t - \frac{q_{s0}}{\mathcal{K}}\int_{Z_t}^{Z_b} \frac{e^{-\mathcal{K}_d Z}}{\phi(Z)^3}\mathrm{d}Z. \tag{5.73}$$

We require the water pressure p_w to be continuous between saturated and unsaturated regions. In the unsaturated region, $p_w = 0$ (since we are neglecting capillary pressure), so we have that $p_w(Z_b) = p_w(Z_t) = 0$. Evaluating the integral tells us that

$$q_{s0} = \frac{(3 - Z_0\mathcal{K}_d)\mathcal{K}\phi_0^3(Z_b - Z_t)}{Z_0(e^{3Z_b/Z_0} - e^{3Z_t/Z_0})}. \tag{5.74}$$

To determine equations for the saturation fronts, we use jump conditions that must be satisfied at the fronts in order to conserve mass. These are found by integrating the mass conservation equation (5.55) across each front. This gives

$$0 = [q - \phi S\dot{Z}_t]_-^+, \quad 0 = [q - \phi S\dot{Z}_b]_-^+, \tag{5.75}$$

where, as previously, '+' indicates above the front and '−' indicates below. At $Z = Z_b$, we have $q_- = 0$, $S_- = 0$ (no water below the front) and $q_+ = q_s$, $S_+ = 1$ (saturated above the front). At $Z = Z_t$, we have $q_- = q_s$, $S_- = 1$ (saturated below) and q_+, S_+ are given by the unsaturated solutions (5.68), (5.67). Substituting all of this in gives the two coupled ordinary differential equations

$$\dot{Z}_t = -\frac{q_0 e^{-\mathcal{K}_d Z_t} - (q_{s0} + \frac{Z_0}{3}\mathcal{K}_d\mathcal{K}\phi_t^3)}{\phi_t - (q_0/\mathcal{K})^{1/3}e^{-\mathcal{K}_d Z_t/3}}, \quad \dot{Z}_b = \frac{q_{s0} + \frac{Z_0}{3}\mathcal{K}_d\mathcal{K}\phi_b^3}{\phi_b}, \tag{5.76}$$

for $Z_t(t)$ and $Z_b(t)$, where $\phi_t = \phi(Z_t)$, $\phi_b = \phi(Z_b)$. We solve the differential equations (5.76) for the saturation fronts numerically in MATLAB using `ode15s`, with initial conditions $Z_t = Z_b = Z_s$ at $t = t_s$.

5.4.2.3 Semi-analytical solution without lateral drainage

Without lateral drainage ($\mathcal{K}_d = 0$), the above solutions (5.66), (5.67), (5.68) for $\tilde{W}$, S and q before saturation still hold with $\mathcal{K}_d = 0$. However, the flux $q = q_s$ in the

saturated region is now uniform, given by

$$q_{\mathrm{s}} = \frac{3\mathcal{K}\phi_0^3(Z_{\mathrm{b}} - Z_{\mathrm{t}})}{Z_0(e^{3Z_{\mathrm{b}}/Z_0} - e^{3Z_{\mathrm{t}}/Z_0})}. \tag{5.77}$$

The behaviour of the wetting and saturation fronts is recovered from the the drainage solutions (5.69), (5.70), (5.71), (5.76) by taking the limit $\mathcal{K}_{\mathrm{d}} \to 0$. The wetting front position is

$$Z_{\mathrm{w}}(t) = q_0^{2/3}\mathcal{K}^{1/3}t. \tag{5.78}$$

Saturation first occurs at position

$$Z_{\mathrm{s}} = -\frac{1}{3}Z_0 \log\left(\frac{q_0}{\mathcal{K}\phi_0^3}\right), \tag{5.79}$$

and time

$$t_{\mathrm{s}} = -\frac{Z_0}{3q_0^{2/3}\mathcal{K}^{1/3}} \log\left(\frac{q_0}{\mathcal{K}\phi_0^3}\right). \tag{5.80}$$

Once saturation occurs, the saturation fronts $Z_{\mathrm{t}}(t)$, $Z_{\mathrm{b}}(t)$ satisfy the ordinary differential equations

$$\dot{Z}_{\mathrm{t}} = \frac{q_{\mathrm{s}} - q_0}{\phi_{\mathrm{t}} - (q_0/\mathcal{K})^{1/3}}, \quad \dot{Z}_{\mathrm{b}} = \frac{q_{\mathrm{s}}}{\phi_{\mathrm{b}}}, \tag{5.81}$$

with $Z_{\mathrm{t}} = Z_{\mathrm{b}} = Z_s$ at $t = t_s$, where $\phi_{\mathrm{t}} = \phi(Z_{\mathrm{t}})$, $\phi_{\mathrm{b}} = \phi(Z_{\mathrm{b}})$ and q_{s} is given by equation (5.77). Once again, we solve the differential equations (5.81) for the saturation fronts numerically in MATLAB using `ode15s`.

5.4.3 Comparison of drainage and no drainage

Figure 5.4 demonstrates the different behaviour observed for different values of lateral drainage $\mathcal{K}_{\mathrm{d}}$. Firstly, we see that the wetting front progresses more slowly with drainage than without, as evident by the logarithmic compared to linear behaviour with time seen in the analytical expressions for Z_{w}. With lateral drainage, there is less water left available to percolate downwards. This also means that saturation occurs at a greater depth, and the resulting saturated region grows more slowly.

Moreover, we clearly see the contrasting behaviour depending on whether the lateral drainage strength satisfies $\mathcal{K}_{\mathrm{d}} < 3/Z_0$ or $\mathcal{K}_{\mathrm{d}} > 3/Z_0$. For small lateral drainage, saturation occurs. For large enough lateral drainage, the saturation decreases with depth and saturation never occurs.

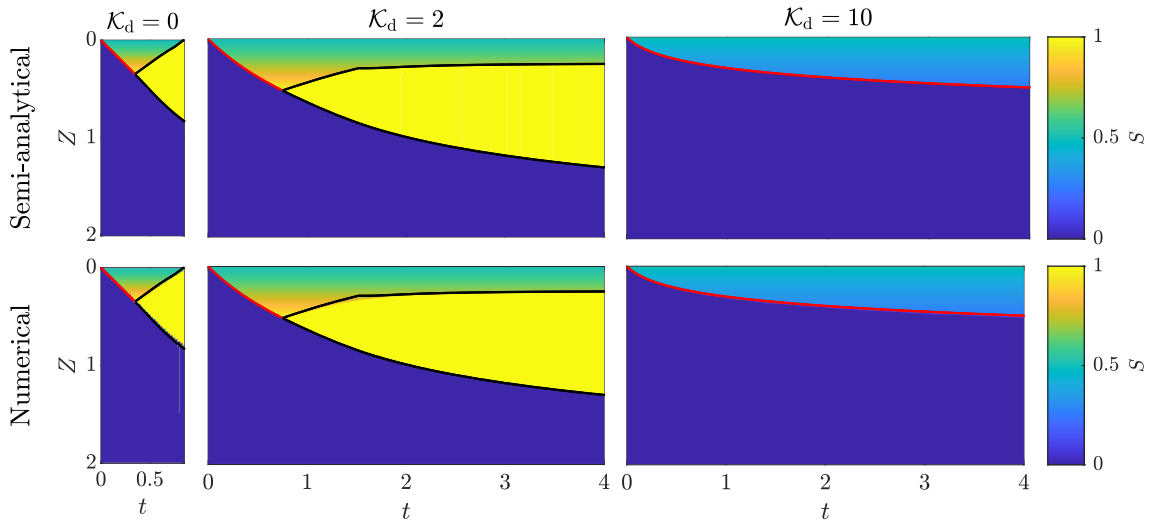


Figure 5.4: Dimensionless semi-analytical (top row) and numerical (bottom row) solution for the saturation S in the isothermal water transport problem for 3 different values of lateral drainage strength $\mathcal{K}_d$. The semi-analytical wetting front $Z_w(t)$ (red) and semi-analytical saturation fronts $Z_t(t)$, $Z_b(t)$ (black) are shown. Parameter values: $\mathcal{K} = 100$, $\phi_0 = 0.2$, $Z_0 = 0.5$, $q_0 = 0.1$, with $\mathcal{B} = 10^{10}$ in the numerical simulations. Solutions shown are dimensionless.

In the case when saturation occurs, the top saturation front Z_t tends to a constant value Z_t^* (as seen most clearly in the $\mathcal{K}_d = 2$ case in Figure 5.4). This follows from arguments of mass conservation. In order for the saturated region to grow, there must be more water flowing into the saturated region than there is draining out laterally. As the top saturation front gets higher, the lateral drainage q_d out of the saturated region grows at a faster rate than the downward flux q into the saturated region, as seen in Figure 5.3. When these quantities become approximately equal, i.e. when

$$q|_{Z=Z_t} \approx \int_{Z_t}^{Z_b} q_d \, dZ, \tag{5.82}$$

the saturated region does not grow upwards anymore. From this, we calculate that the limit Z_t^* for the top saturation front Z_t is given by

$$Z_t^* = \frac{1}{3/Z_0 - \mathcal{K}_d} \log\left(\frac{Z_0 \mathcal{K}_d \mathcal{K} \phi_0^3}{3 q_0}\right). \tag{5.83}$$

In deriving this expression, we have made use of the fact that the fluxes q and q_d at $Z = Z_b$ are negligible (see Figure 5.3, $\mathcal{K}_d = 2$, $t = 1.6, 2$), since ϕ and hence q and q_d decay exponentially with depth. The analytical expression for Z_t^* agrees with the values obtained from the semi-analytical and numerical solutions, and demonstrates the expected behaviour. The saturated region extends closer to the surface (Z_t decreases) when there is a greater influx q_0 or a smaller porosity ϕ_0, both of which

make it easier to fill the pore space, increasing the extent of the saturated region. Increasing the lateral drainage $\mathcal{K}_\mathrm{d}$ has the opposite effect, reducing the extent of the saturated region as more water gets drained away. In particular, we see that the saturated region ends up occupying the whole pore space if $\mathcal{K}_\mathrm{d} < 3q_0/(Z_0\mathcal{K}\phi_0^3)$.

Note that, despite the arguments above, Z_b still continues to increase over time. We treated the downward flux q at $Z = Z_\mathrm{b}$ as negligible when compared to the fluxes nearer the surface, but ϕ at $Z = Z_\mathrm{b}$ is also very small, enabling the saturated region to continue to slowly grow downwards, despite the very small water flux. From equation (5.76) for $\dot{Z}_\mathrm{b}$, it can be shown that the large time behaviour of Z_b is given by

$$Z_\mathrm{b} \sim \frac{Z_0}{2}\log(t). \tag{5.84}$$

5.5 Steady melting with lateral drainage

We now return to the steadily melting solutions studied in Chapter 2 to consider the effect of including lateral drainage. In this section we continue to work with dimensionless variables. Recall that steadily melting solutions are solutions to the model in Chapter 2 with constant forcings $\mathcal{Q}_\mathrm{si}$ and $\mathcal{Q}_0$ such that the surface lowers at a constant rate $\dot{h} < 0$; the weathering crust occupies a region between the surface and a constant depth Z_m, and the temperature and porosity profiles in the Z-frame are constant in time. By applying the steadily melting assumptions to the equations in the current chapter, the resultant ice mass conservation equation, energy conservation equations and their boundary conditions are the same as those found in Chapter 2 (equations (2.22)–(2.27)). Hence the saturated steadily melting solutions (2.38), (2.40), (2.41), (2.42) for T, ϕ, $\dot{h}$, Z_m hold in the unsaturated case too. The dimensionless forms of these solutions (as used in this chapter) are

$$T = \begin{cases} 0, & 0 < Z < Z_\mathrm{m}, \\ -\dfrac{(1-\chi)(1-a)\mathcal{Q}_\mathrm{si}}{\hat{k}\hat{\kappa}+\dot{h}}\left(e^{-\hat{\kappa}Z} - e^{-\hat{\kappa}Z_\mathrm{m}}e^{\frac{\dot{h}}{\hat{k}}(Z-Z_\mathrm{m})}\right) & \\ \qquad\qquad +\mathcal{T}_\infty\left(1-e^{\frac{\dot{h}}{\hat{k}}(Z-Z_\mathrm{m})}\right), & Z > Z_\mathrm{m}, \end{cases} \tag{5.85}$$

$$\phi = \begin{cases} -\dfrac{(1-\chi)(1-a)\mathcal{Q}_\mathrm{si}}{\dot{h}\mathcal{S}}\left(e^{-\hat{\kappa}Z} - e^{-\hat{\kappa}Z_\mathrm{m}}\right), & 0 < Z < Z_\mathrm{m}, \\ 0, & Z > Z_\mathrm{m}, \end{cases} \tag{5.86}$$

$$\dot{h} = -\frac{(1-a)\mathcal{Q}_{\mathrm{si}} + \mathcal{Q}_0}{\mathcal{S} - \mathcal{T}_\infty}, \tag{5.87}$$

$$Z_{\mathrm{m}} = \frac{1}{\hat{\kappa}} \log\left(\left(\frac{(1-a)(1-\chi)\mathcal{Q}_{\mathrm{si}}}{-\mathcal{T}_\infty} \right) \Big/ \left(\frac{(1-a)\mathcal{Q}_{\mathrm{si}} + \mathcal{Q}_0}{\mathcal{S} - \mathcal{T}_\infty} \right) \right). \tag{5.88}$$

The only difference is that now some of the porous region is unsaturated. We expect that the solution will have two layers: a saturated layer immediately above the impermeable base, with the rest of the weathering crust above this being unsaturated, as shown in Figure 5.1. The thickness d of the saturated layer will depend on the drainage strength, encoded by the parameter $\mathcal{K}_{\mathrm{d}}$. We refer to the boundary between the saturated and unsaturated regions as the water table, $Z = Z_{\mathrm{d}}$ $(= Z_{\mathrm{m}} - d)$.

5.5.1 Semi-analytical solution

As for the isothermal water transport example, we neglect capillary pressure (assuming $\mathcal{B} \gg 1$) to enable us to find a semi-analytical solution.

To find the saturation S, we combine the ice and water mass conservation equations (5.34), giving us a (dimensionless) equation for the total water content W (and hence saturation S),

$$\dot{h}\frac{\mathrm{d}W}{\mathrm{d}Z} + \frac{\mathrm{d}q}{\mathrm{d}Z} = -q_{\mathrm{d}}, \tag{5.89}$$

with boundary conditions

$$q + \dot{h}W = 0 \quad \text{at} \quad Z = 0, \tag{5.90}$$

$$q = 0 \quad \text{at} \quad Z = Z_{\mathrm{m}}. \tag{5.91}$$

We are assuming that the surface is unsaturated ($S < 1$) in (5.90), i.e. that the surface runoff r_{off} in (5.42) is zero.

We need to determine the saturation S in the unsaturated region and the position of the water table Z_{d}. To do this, we solve for the water flux q in the saturated region using the boundary condition (5.91) at $Z = Z_{\mathrm{m}}$, and we solve (5.89) for the saturation S in the unsaturated region using the boundary condition (5.90) at $Z = 0$. We then determine Z_{d} as the point at which $q + \dot{h}W$ for these two solutions are equal. (Integrating the W equation (5.89) across the water table gives that $q + \dot{h}W$ must be continuous there.)

In the saturated region, $W = 1$, and so equation (5.89) is

$$\frac{\mathrm{d}q}{\mathrm{d}Z} = -q_\mathrm{d} \quad \text{with} \quad q_\mathrm{d} = \mathcal{K}_\mathrm{d}\mathcal{K}\phi^3, \tag{5.92}$$

which is solved with boundary condition (5.90) and the steadily melting form of the porosity (5.86) to give

$$\begin{aligned} q = -\mathcal{K}_\mathrm{d}\mathcal{K}\phi_\mathrm{sm0}^3\Bigg(&-\frac{1}{3\hat{\kappa}}(e^{-3\hat{\kappa}Z} - e^{-3\hat{\kappa}Z_\mathrm{m}}) + \frac{3}{2\hat{\kappa}}(e^{-2\hat{\kappa}Z}e^{-\hat{\kappa}Z_\mathrm{m}} - e^{-3\hat{\kappa}Z_\mathrm{m}}) \\ &-\frac{3}{\hat{\kappa}}(e^{-\hat{\kappa}Z}e^{-2\hat{\kappa}Z_\mathrm{m}} - e^{-3\hat{\kappa}Z_\mathrm{m}}) - e^{-3\hat{\kappa}Z_\mathrm{m}}(Z - Z_\mathrm{m})\Bigg) \end{aligned} \tag{5.93}$$

in the saturated region, where

$$\phi_\mathrm{sm0} = -\frac{(1-\chi)(1-a)\mathcal{Q}_\mathrm{si}}{\dot{h}\mathcal{S}}. \tag{5.94}$$

Under the assumption that $\mathcal{B} \gg 1$, the downward water flux in the unsaturated region is $q = \mathcal{K}\phi^3 S^3$, so equation (5.89) becomes

$$\frac{\mathrm{d}}{\mathrm{d}Z}\Big(\mathcal{K}\phi^3 S^3 + \dot{h}(1 - \phi + \phi S)\Big) = -\mathcal{K}_\mathrm{d}\mathcal{K}\phi^3 S^3, \tag{5.95}$$

with the boundary condition (5.90) becoming

$$\mathcal{K}\phi^3 S^3 + \dot{h}(1 - \phi + \phi S) = 0 \quad \text{at} \quad Z = 0. \tag{5.96}$$

This uniquely determines the value of S (and hence $q = \mathcal{K}\phi^3 S^3$) at the surface, independent of $\mathcal{K}_\mathrm{d}$ (see Figure 5.5). We solve this unsaturated problem for S numerically in MATLAB using `fsolve` for the boundary condition (5.96) and `ode15s` for the differential equation (5.95). We then calculate $q = \mathcal{K}\phi^3 S^3$ and use continuity of $q + \dot{h}W$ at $Z = Z_\mathrm{d}$ to determine Z_d.

5.5.2 Numerical solution

We also find the steadily melting solution by running the full numerical model until a steady state is reached (until $||T^{k+1} - T^k||_2 + ||\phi^{k+1} - \phi^k||_2 + ||S^{k+1} - S^k||_2 < 10^{-4}$, where $||\cdot||_2$ is the Euclidean 2-norm and superscripts k, $k+1$ represent the numerical solutions at timesteps k, $k+1$). The numerical and semi-analytical solutions agree well (Figure 5.5), giving us confidence in our numerical method. The numerical

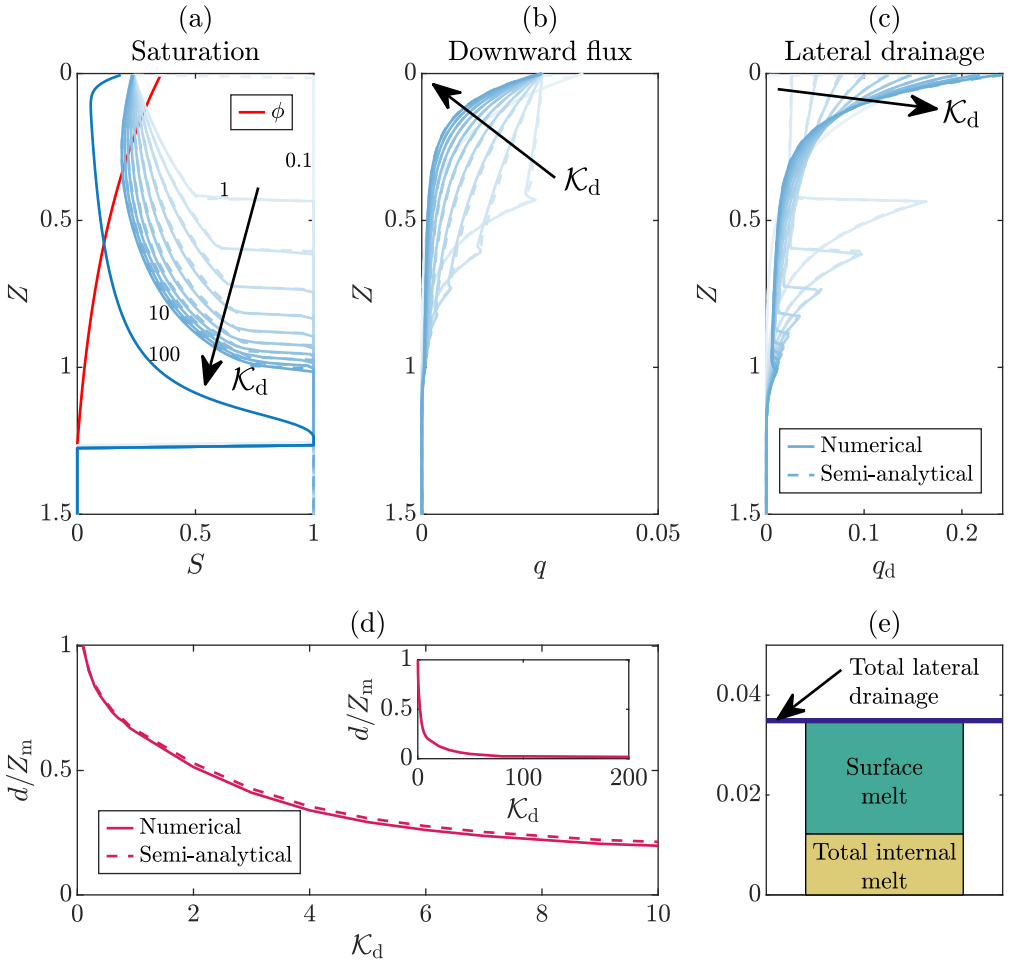


Figure 5.5: Comparison of how the steadily melting solution with lateral drainage varies with the drainage strength $\mathcal{K}_\mathrm{d}$. Both the numerical (solid) and semi-analytical (dashed) solutions are shown. Panels (a), (b) and (c) show the profiles of saturation S, downward water flux q and lateral drainage q_d, respectively, for different values of $\mathcal{K}_\mathrm{d}$. Panel (d) shows how the proportion d/Z_m of the weathering crust that is saturated with water varies with $\mathcal{K}_\mathrm{d}$. Panel (e) shows the contributions (independent of $\mathcal{K}_\mathrm{d}$) to the total lateral drainage $\int q_\mathrm{d}\,\mathrm{d}Z$ from surface melt m_surf and the total internal melt $\int m_\mathrm{int}\,\mathrm{d}Z$ when the surface is unsaturated. Note that semi-analytical solutions are not shown for $\mathcal{K}_\mathrm{d} = 100$ in panel (a), (b), (c) or in the inset of panel (d). Parameter values: $\mathcal{B} = 10^4$, $\mathcal{Q}_\mathrm{si} = 1$, $\mathcal{Q}_0 = 0.25$, with the other parameter values as shown in Table 5.3.

solutions presented here use $\mathcal{B} = 10^4$, so the large Bond number assumption made in the semi-analytical solution is reasonable.

5.5.3 Conservation of water

To conserve mass in the steadily melting solution, all meltwater produced must be drained away. This can be seen by integrating the steadily melting water mass conservation equation,

$$\dot{h}\frac{\partial}{\partial Z}(\phi S) + \frac{\partial q}{\partial Z} = m_{\text{int}} - q_{\text{d}}, \tag{5.97}$$

over the weathering crust ($Z = 0$ to $Z = Z_{\text{m}}$). We apply the no flux condition at $Z = Z_{\text{m}}$, and the kinematic condition (5.12) for water at the surface (neglecting rainfall here). This results in the total lateral drainage $\int q_{\text{d}}\ \text{d}Z$ being a sum of the total internal melt $\int m_{\text{int}}\ \text{d}Z$ and the surface melt m_{surf},

$$\int q_{\text{d}}\ \text{d}Z + r_{\text{off}} = \int m_{\text{int}}\ \text{d}Z + m_{\text{surf}}, \tag{5.98}$$

which says that the total lateral drainage and surface runoff rate must match the total melt rate. If $\mathcal{K}_{\text{d}}$ is sufficiently large that the surface is unsaturated then r_{off} is zero and the total lateral drainage $\int q_{\text{d}}\ \text{d}Z$ must (slightly counter-intuitively) be independent of the lateral drainage strength $\mathcal{K}_{\text{d}}$, as shown in Figure 5.5(e).

If the surface is saturated (i.e. if $\mathcal{K}_{\text{d}}$ is less than about 0.1), it is the sum of the total lateral drainage and the surface runoff that is independent of $\mathcal{K}_{\text{d}}$.

5.5.4 Inferring the value of $\mathcal{K}_{\text{d}}$

Figure 5.5(d) shows the relationship between the drainage strength $\mathcal{K}_{\text{d}}$ and the proportion d/Z_{m} of the weathering crust that is saturated. We see that the thickness of the saturated region decreases with increasing lateral drainage strength $\mathcal{K}_{\text{d}}$. This can help us inform a suitable value for $\mathcal{K}_{\text{d}}$ to use in our model, based on observations of the water table height. Typically, most of the weathering crust is saturated with meltwater. For example, in Greenland, the water table has been observed typically to lie ~ 0.1 m below the surface in weathering crusts that are ~ 1 m thick [Cooper et al., 2018, Irvine-Fynn et al., 2021]. Therefore, we expect d/Z_{m} closer to 1 than 0, suggesting the appropriate order of magnitude is $\mathcal{K}_{\text{d}} \sim 1$. However, the transient behaviour of the weathering crust and meltwater flow means that a different value of $\mathcal{K}_{\text{d}}$ might prove to be more appropriate in a transient setting.

An alternative method for inferring the value of $\mathcal{K}_\mathrm{d}$ is by using observations of the surface slope $\sin(\theta)$ and an appropriate lengthscale L_d over which lateral drainage occurs, such as the distance between supraglacial streams. For example, at a study site in south-western Greenland, Irvine-Fynn et al. [2021] measured the surface slope ($\sin(\theta)$) to be 0.022 m m^{-1} and the mean distance to a surface stream (L_d) to be 7.24 m, giving $\sin(\theta)/L_\mathrm{d} \approx 0.003$. However, this method would also require an estimation of the anisotropy factor β_h to calculate $\mathcal{K}_\mathrm{d}$.

5.6 Idealised periodic forcings

We now consider idealised periodic forcings, as we did in Chapter 3, but now allowing for lateral drainage and therefore unsaturated flow. In this section, we work with dimensional variables, to make it easier to relate this work to the reality. We force the model with sinusoidally varying shortwave radiation Q_si and combined longwave radiation and turbulent heat fluxes Q_0. We initialise the model with the (analytical) steadily melting solution for the mean forcing, but with $S = 0.5$ everywhere. We run the model until an approximately periodic state is reached.

We consider a periodic forcing that results in a weathering crust that varies in thickness but is never completely removed, using the same example as in Figure 3.10. Q_0 is constant but Q_si varies. The crust thickens when Q_si (and hence internal melting) is large, and thins when Q_si is small, causing freezing at the bottom of the weathering crust as the internal heat source is reduced. This is shown in Figure 5.6 for different values of $\mathcal{K}_\mathrm{d}$. The key result is that, as in the steadily melting case, the porosity and temperature profiles are the same with and without drainage, independent of the lateral drainage strength. The explanation for this is detailed below (similar to in the steadily melting case).

The amount of melting that occurs is the same with lateral drainage as in the saturated case. The internal melt rate m_int inside the weathering crust is given by

$$m_\mathrm{int} = -\frac{1}{\mathcal{L}}\frac{\partial F}{\partial Z}, \tag{5.99}$$

which comes from the energy equation (5.9). The internal radiation F used in the examples in Figure 5.6 is independent of the weathering crust properties; we take the absorption and scattering coefficients α and r to be constant and uniform. Therefore the amount of radiation absorbed internally, and hence the internal melt rate, is

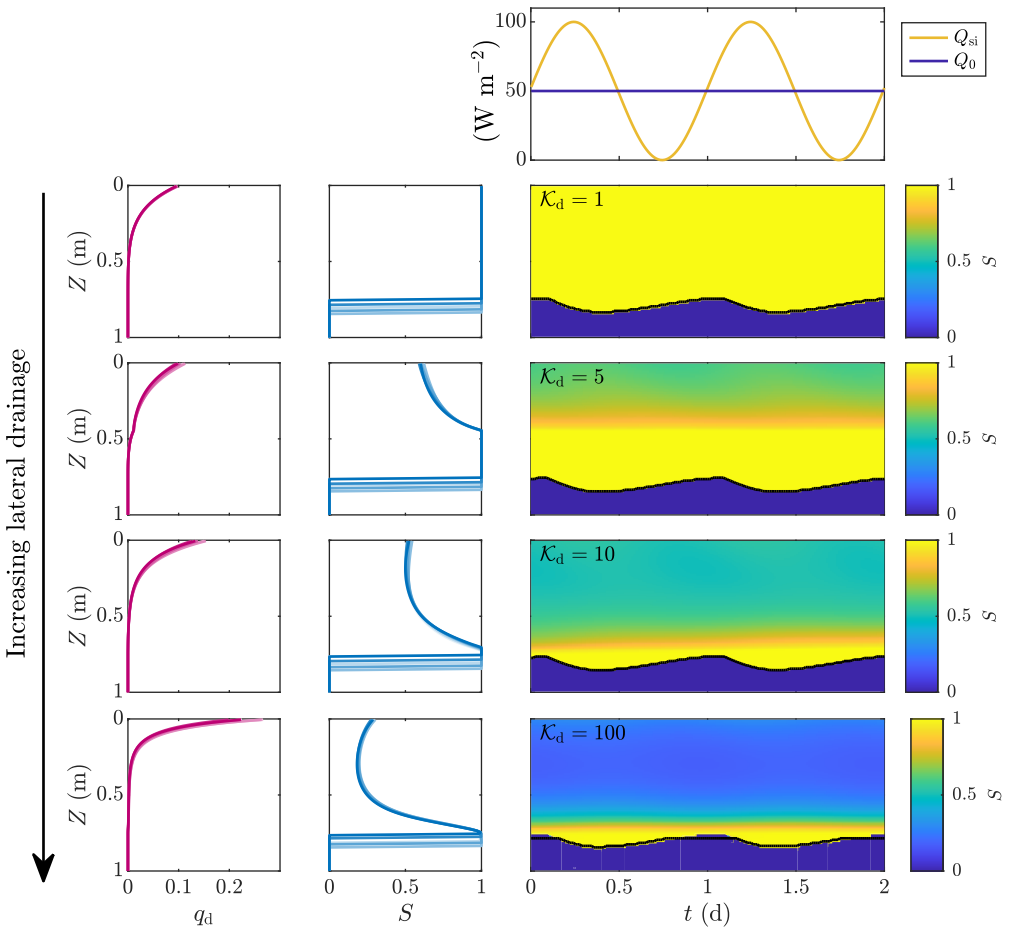


Figure 5.6: Periodic forcing of the weathering crust with different lateral drainage strengths $\mathcal{K}_d$ (increasing from top to bottom). The top panel shows the sinusoidal forcing for Q_{si} and (constant) Q_0 used. The left and middle panels show the scaled lateral drainage q_d and saturation S profiles with depth, with lines of different shades representing the solution at 0.2 day intervals in one period. Note that the only significant change throughout the period is the position of the bottom of the weathering crust (indicated by the horizontal lines in the S profiles). The right column shows the evolution of S over time, with the bottom of the weathering crust $Z = Z_m$ shown in black.

independent of the porosity and saturation. The porosity ϕ in the crust satisfies (5.5) and the temperature below the crust is given by the energy equation (5.9) as

$$\rho c\left(\frac{\partial T}{\partial t} + \dot{h}\frac{\partial T}{\partial Z}\right) = k\frac{\partial^2 T}{\partial Z^2} - \frac{\partial F}{\partial Z}. \tag{5.100}$$

Both of these equations do not feature S explicitly. The only way that S enters the model for T and ϕ explicitly is through the Stefan condition

$$k\frac{\partial T}{\partial Z} = -\rho\mathcal{L}\phi S\dot{z}_m \quad \text{at} \quad Z = Z_m, \tag{5.101}$$

where $z_m = h - Z_m$. However, we expect (and find) that $S = 1$ at $Z = Z_m$ because

the porosity, and hence the lateral drainage, there is very small, and the downward flow means that the weathering crust 'fills up' from the bottom. (In theory, if the saturated layer was thin enough to be completely refrozen within the periodic cycle, this could result in $S < 1$ at the bottom of the crust, but we do not observe this in our numerical examples.) Therefore, the temperature and porosity profiles are independent of S. The only effect that lateral drainage has is on the saturation, for example on the water table height, as shown in Figure 5.6. As we saw in the steadily melting case, stronger lateral drainage results in a thinner saturated region. Furthermore, Figure 5.6 demonstrates that there is very little variation in the lateral drainage (left column) and saturation (middle column) throughout a period.

The values of Q_{si} and Q_0 used here are such that the surface is always melting ($\chi(1-a)Q_{\mathrm{si}} + Q_0 > 0$), meaning that the surface energy balance (5.10) determines the surface melt rate m_{surf} and the kinematic condition (5.11) determines the surface lowering $-\dot{h}$. Both of these are therefore also independent of the lateral drainage. However, we would expect that including lateral drainage results in an increase in the amount of surface lowering if freezing occurs at the surface. If meltwater is removed, the crust can refreeze with non-zero porosity (being porous rather than solid), and that makes it easier to subsequently melt. We explore the behaviour exhibited by freezing an unsaturated region from the surface in Section 5.7.

5.7 Switching experiments

We now investigate the effect of lateral drainage on the weathering crust and surface lowering during alternating periods of melting and freezing. In this section, we again work with dimensional variables.

As just discussed, we expect that lateral drainage can increase the amount of surface lowering, because it enables regions of the crust to become frozen with non-zero porosity. The surface lowering rate $-\dot{h}$ is given by the kinematic condition (5.43) as

$$\dot{h} = -\frac{m_{\mathrm{surf}}}{1-\phi} \tag{5.102}$$

(in the absence of snowfall). Hence, if the surface is more porous, we get more surface lowering for the same surface melt rate m_{surf}, i.e. for the same Q_{si} and Q_0. With no lateral drainage, the surface is always solid after refreezing. With lateral drainage, the surface can be refrozen with $\phi > 0$ by having $S < 1$ at the point of freezing.

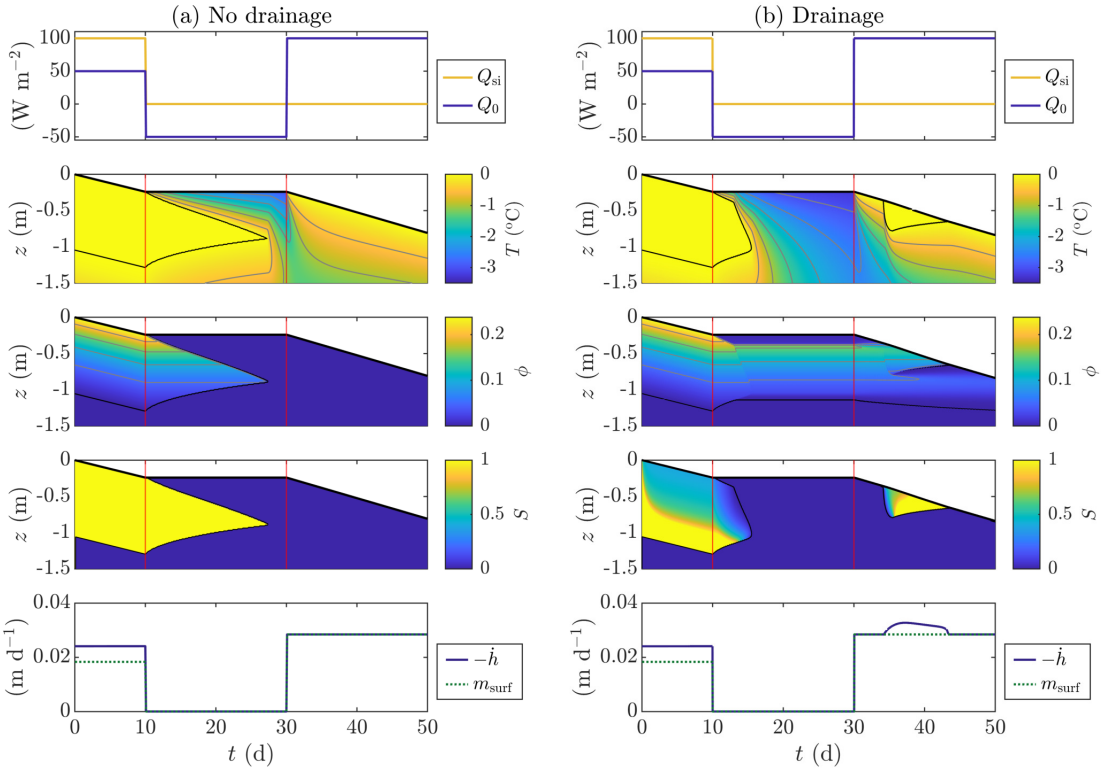


Figure 5.7: Evolution of the temperature T, porosity ϕ, saturation S, surface lowering rate $-\dot{h}$ and surface melt rate m_{surf} during the switching experiment (a) without ($\mathcal{K}_{\text{d}} = 0$) and (b) with ($\mathcal{K}_{\text{d}} = 3$) lateral drainage. The black lines in the T, ϕ and S plots show the zero contours of the respective variables. The grey lines in in the T and ϕ plots show contours of spacing 0.5^{o}C and 0.05 respectively. The red vertical lines show the transitions between stages 1, 2 and 3. The forcings used in the switching experiment are shown in the top panels.

To explore the effect of lateral drainage on surface lowering, we use a switching experiment similar to those considered in Chapter 3. This makes it easier to isolate the behaviour of interest than if a periodic forcing was used. In this case, our switching experiment has three stages:

1. run to a steadily melting state (both internal and surface melting) — this is reached within 10 days,
2. freeze from the surface for 20 days ($Q_0 < 0$, $Q_{\text{si}} = 0$),
3. melt from the surface for 20 days ($Q_0 > 0$, $Q_{\text{si}} = 0$).

The freezing stage is long enough such that all water is frozen.

Figure 5.7 shows the solutions both without (panel (a)) and with (panel (b)) lateral drainage, which are qualitatively different. In the no drainage case, the crust remains

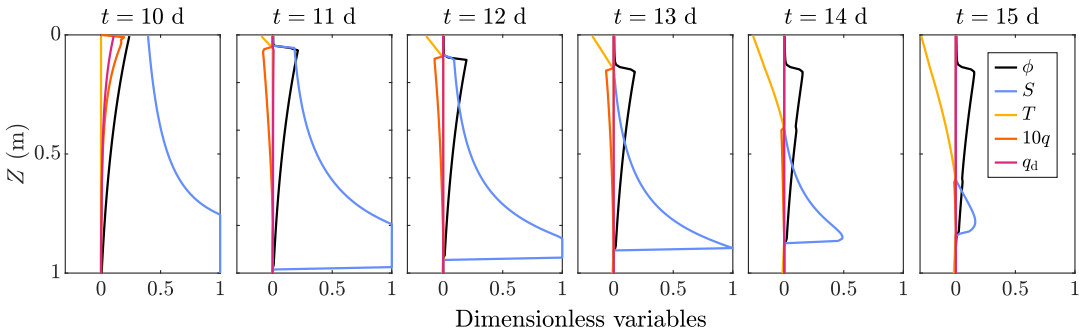


Figure 5.8: Snapshots of the freezing stage (stage 2) of the switching experiment with drainage ($\mathcal{K}_\mathrm{d} = 3$) shown in Figure 5.7. The porosity ϕ, saturation S, temperature T, downward water flux q, and the lateral drainage flux q_d are shown. Note that 10 times q is plotted to make it more visible. Dimensionless variables are plotted.

saturated with meltwater, and so refreezes with zero porosity. In stage 3, we then simply have melting of solid ice from the surface, with the surface lowering at rate $-\dot{h} = m_\mathrm{surf}$.

By contrast, the behaviour with drainage is much more interesting. The crust is largely unsaturated at the surface at the end of stage 1, meaning that freezing with non-zero porosity is possible. Moreover, it takes less time for the whole crust to freeze and be cooled to below the melting temperature during the freezing stage (stage 2), and the ice gets colder. Cooling is quicker because the lateral drainage of water removes latent heat. Freezing releases latent heat, so the fact that there is less meltwater to freeze when there is drainage means that the ice can get colder.

When stage 2 (surface freezing) first begins ($t = 10$ d) in the drainage case, the vertical water flux q becomes negative (upward flow) as a result of the capillary pressure term in the unsaturated form of the flux (5.49) driving the flow down the saturation gradient, towards the surface. This provides a supply of water to the surface, where the water then freezes, resulting in near-solid ice (e.g. at $t = 11$ d in Figure 5.8). This effect results in a freezing front propagating downwards, producing a surface layer of near-solid ice, until the saturation is reduced to 0 at the freezing front ($t = 13$ d in Figure 5.8). At this point, there is no longer a supply of water to fill the pore space and freeze. Instead, the freezing front continues to propagate through the region with near-zero saturation, resulting in refreezing with non-zero porosity ($t = 14$ d in Figure 5.8). This continues until all liquid water is frozen. The result ($t = 16$ d to $t = 30$ d in Figure 5.7(b), ϕ) is to have a near-solid surface layer above a dry, porous layer.

When melting occurs in stage 3, the solid surface layer is first melted away, exposing the porous layer. As the porous layer melts, the meltwater flows down into the cold, pore space below. The resulting phenomenon was explained by Meyer and Hewitt [2017], and is summarised here. When the meltwater enters cold ice ($T < T_{\mathrm{m}}$), some of the meltwater freezes at the wetting front. This reduces the porosity and warms the ice ahead (i.e. below). Once the wetting front reaches a depth with low enough porosity, the refreezing meltwater fills the pore space, creating an impermeable layer. This prevents the flow of any more water past this point. The porous region above the solid layer becomes saturated and excess meltwater runs off at the surface. Throughout this, melting of the porous surface ice continues, until the impermeable base is reached. Even once this impermeable ice layer has been melted through, there is no more infiltration of meltwater into the porous ice below. The ice is cold and the porosity is low enough that the wetting front from the surface instantly creates an impermeable ice layer at the surface. By contrast, in the no-drainage case, all the ice below the surface remains below the melting temperature, despite being warmer at the end of stage 2 than in the drainage case. An effect of including lateral drainage is that the temperature variations throughout the experiment are more extreme, due to the transfer of heat into and out of the crust by the advection of meltwater.

The bottom panels of Figure 5.7 compare the surface lowering rates for both the drainage and no drainage cases. Of particular interest is the surface lowering during stage 3. The rate $-\dot{h}$ of surface lowering in stage 3 is initially the same in the drainage case as in the saturated, no-drainage case whilst the solid surface layer is melted away. When the porous layer is reached, the surface lowering rate increases as a result of the non-zero porosity, following (5.102), before returning to the no-drainage value once the porous layer has been removed. The total effect over the 20 days of surface melting in stage 3 of the experiment is to have around 6 % more surface lowering with drainage compared to without.

Note that the arguments presented above suggest that it is not obvious that lateral drainage should enhance surface lowering. Although the resultant porous ice requires less energy to melt than solid ice, the frozen ice also gets colder, meaning more energy is required to heat the ice to the melting temperature. However, this is more than compensated for by the additional warming of the porous ice once melting commences, due to the refreezing of percolating meltwater. Hence the result is indeed that lateral drainage enhances surface lowering, in this particular example.

5.8 Summary

In this chapter, we have extended the one-dimensional weathering crust model presented in Chapter 2 to include a parametrisation for the lateral flow of meltwater, based on Darcy's law. This allows the weathering crust to become unsaturated and makes vertical meltwater flow possible. The result is a weathering crust that has a saturated layer at the base, above which it is unsaturated, as is observed in the field [e.g. Irvine-Fynn et al., 2021]. We have used an extension to the enthalpy method considered in Chapter 3 to solve the model equations numerically, and focussed on idealised solutions to the model. The model will be applied to the Greenland ice sheet in Chapter 6.

We have considered two test cases (isothermal meltwater infiltration and steadily melting solutions) for which we can find semi-analytical solutions by neglecting capillary pressure (assuming $\mathcal{B} \gg 1$), allowing us to validate our numerical solutions. We used the test cases and idealised periodic forcings to explore the effect of the lateral drainage strength $\mathcal{K}_\mathrm{d}$. We have observed that a greater lateral drainage strength $\mathcal{K}_\mathrm{d}$ results in a thinner saturated layer (a lower water table), with this relationship providing a method for inferring an appropriate value of $\mathcal{K}_\mathrm{d}$ from observations of water table height.

Furthermore, we have observed that including lateral drainage alters the porosity profile of the weathering crust and can enhance surface lowering, by allowing the weathering crust to refreeze with non-zero porosity, making it easier to melt than solid ice. This contrasts with the findings of Hoffman et al. [2014] that the inclusion of lateral drainage in their one-dimensional model led to a *decrease* in the amount of surface lowering. However, this is explained by the fact that Hoffman et al. [2014] used different values of the shortwave radiation partitioning parameter χ for their models with and without lateral drainage. This will be explored and discussed further in Chapter 6.

Another interesting result from the lateral drainage model is the formation of a transient, impermeable ice layer. It is observed that weathering crusts can contain alternating layers of porous and impermeable ice [e.g. Cooper et al., 2018]. As seen in Figure 5.7(b), the formation of impermeable layers can prevent the infiltration of meltwater into the porous ice below, potentially enhancing lateral meltwater flow and runoff, as also observed in snow and firn [e.g. Mikkelsen et al., 2016, Noël et al., 2017, Clerx et al., 2022]. It is therefore encouraging that our model shows promise for capturing such behaviour, which will be explored further in Chapter 6.

Chapter 6

Comparison with observations from Greenland

6.1 Introduction

So far in this thesis, we have studied idealised scenarios to explore the underlying physical processes governing the weathering crust. In this chapter, we force our weathering crust model with observed weather data from the Greenland ice sheet and compare the results of our model to observed porosity, temperature and surface lowering measurements. This comparison allows us to validate our model. Once again, we neglect microbes and nutrients in this chapter.

6.2 Data

6.2.1 PROMICE Automatic Weather Station (AWS) data

The observations we use to force our weathering crust model come from the Programme for Monitoring of the Greenland Ice Sheet (PROMICE) dataset [Fausto et al., 2021, How et al., 2022, https://promice.org/]. PROMICE has been measuring weather conditions and ice properties on the Greenland Ice Sheet since 2007, at around 25 automatic weather stations (AWSs) [Fausto et al., 2021] (Figure 6.1(a)). The weather stations are tripods (Figure 6.1(b)) that sit at various locations on the ice sheet, year-round, automatically recording and transmitting measurements of the climate conditions needed to calculate the surface energy balance, including radiative fluxes, air temperature, air pressure, relative humidity and wind speed

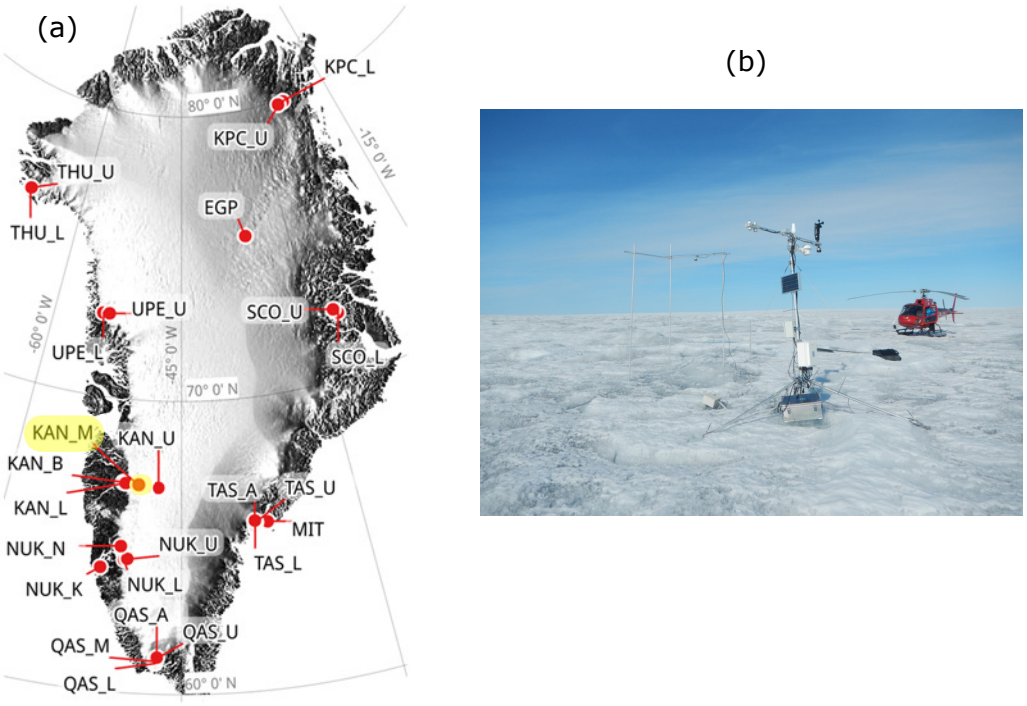


Figure 6.1: (a) Map of Greenland showing the PROMICE weather station locations. Figure modified from Fausto et al. [2021], used with permission from the authors. (b) Photo of the KAN_M PROMICE AWS in 2019. Credit: Nanna Karlsson.

(see Table 6.1). In addition to this, the surface ablation and ice temperature are measured. All these data are openly available in hourly, daily and monthly datasets at https://promice.org/ [How et al., 2022]. The version of the dataset used in this work was downloaded at 15:23 GMT on 22$^{\text{nd}}$ January 2024.

We use PROMICE data from the KAN_M weather station (67.0670°N, 48.8355°W), which lies in the middle of the ablation zone in south-western Greenland. This is the most relevant region of Greenland for weathering crusts and surface microbes.

6.2.2 Surface energy balance

A key use of PROMICE data is for calculating the surface energy balance, which determines the amount of surface melting. Recall, from Chapter 1, that the most general surface energy balance that accounts for penetrating shortwave radiation (via the parameter χ) is

$$-k\frac{\partial T}{\partial z} + \chi(Q_{\text{si}} + Q_{\text{so}}) + Q_{\text{li}} + Q_{\text{lo}} + \text{SHF} + \text{LHF} = \rho\mathcal{L}m_{\text{surf}} \quad \text{at} \quad z = h(t). \quad (6.1)$$

Symbol	Quantity	
Q_{li}	Incoming longwave radiation	Measured
Q_{lo}	Outgoing longwave radiation	Measured
Q_{si}	Incoming shortwave radiation	Measured
Q_{so}	Outgoing shortwave radiation	Measured
T_{a}	Air temperature	Measured
p_{a}	Air pressure	Measured
u	Wind speed	Measured
RH	Relative humidity	Measured
SHF	Sensible turbulent heat flux	Calculated
LHF	Latent turbulent heat flux	Calculated
a	Albedo	Calculated
	Below-ice temperatures at 1, 2, 3, 4, 5, 6, 7, 10 m	Measured

Table 6.1: Quantities from the PROMICE dataset [How et al., 2022] that are used to force our weathering crust model. Most quantities are measured directly, apart from the albedo and turbulent heat fluxes. The albedo is calculated as $a = Q_{\mathrm{so}}/Q_{\mathrm{si}}$ (for zenith angles less than 70°), and the latent heat fluxes are calculated using the parametrisations (6.2), (6.3) [Fausto et al., 2021]. The quantities T_{a}, p_{a}, u and RH are measured at a reference height (~ 2.5 m at KAN_M) above the surface.

The shortwave radiation Q_{si}, Q_{so} and longwave radiation Q_{li}, Q_{lo} are measured directly at the PROMICE weather stations. The turbulent heat fluxes are calculated from measured quantities using the parametrisations [Fausto et al., 2021]

$$\mathrm{SHF} = \rho_{\mathrm{a}} c_{\mathrm{a}} C_{\mathrm{S}}^{*} u (T_{\mathrm{a}} - T_{\mathrm{surf}}), \tag{6.2}$$

$$\mathrm{LHF} = \rho_{\mathrm{a}} \mathcal{L}_{v/s} C_{\mathrm{L}}^{*} u (\tilde{q}_{\mathrm{a}} - \tilde{q}_{\mathrm{surf}}), \tag{6.3}$$

where ρ_{a} is the air density, c_{a} is the specific heat capacity of air, $\tilde{q}_{\mathrm{a}}$ is the specific humidity of the air, $\mathcal{L}_{v/s}$ is the latent heat of evaporation/sublimation, and $C_{\mathrm{S/L}}^{*}$ are constants that depend on the surface roughness and the heights above the surface at which the measurements were taken. The specific humidity $\tilde{q}_{\mathrm{a}}$ (kg kg^{-1}) is a measure of moisture content, defined as the mass of water vapour in a unit mass of moist air. It is calculated from the measured relative humidity RH as

$$\tilde{q}_{\mathrm{a}} = \frac{RH}{100} \tilde{q}_{\mathrm{sat}}, \tag{6.4}$$

where $\tilde{q}_{\mathrm{sat}}$ is the specific humidity at saturation (i.e. the maximum mass of water vapour that can be held in a unit mass of air before condensation occurs). It is assumed that $\tilde{q}_{\mathrm{surf}} = \tilde{q}_{\mathrm{sat}}$, calculated as [Fausto et al., 2021]

$$\tilde{q}_{\mathrm{sat}} = \frac{\epsilon e_{\mathrm{sat}}}{p_{\mathrm{a}} - (1 - \epsilon e_{\mathrm{sat}})}, \tag{6.5}$$

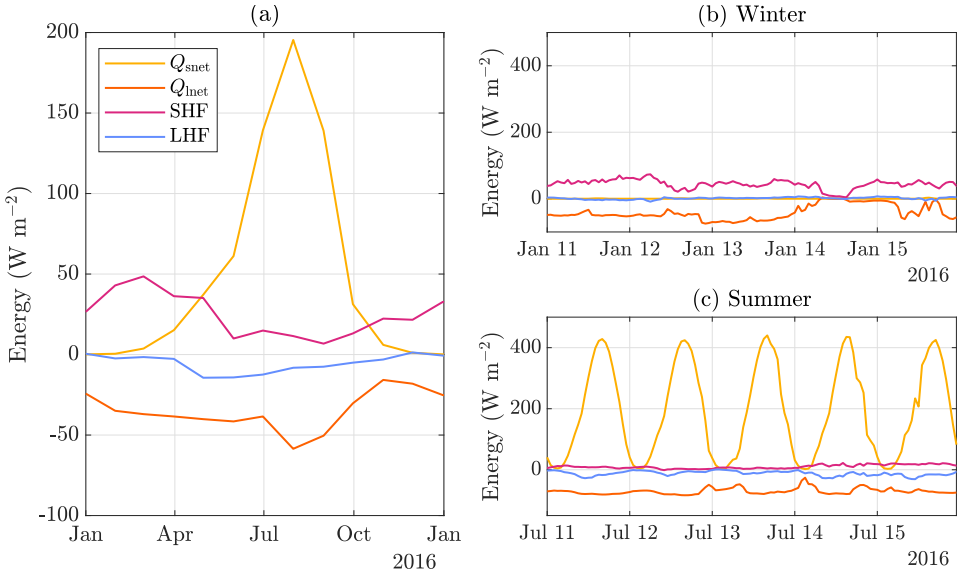


Figure 6.2: Observed surface energy balance components from the KAN_M PROMICE station in 2016 [How et al., 2022]: net shortwave radiation $Q_{\text{snet}} = Q_{\text{si}} + Q_{\text{so}}$, net longwave radiation $Q_{\text{lnet}} = Q_{\text{li}} + Q_{\text{lo}}$, sensible turbulent heat flux SHF, and latent turblent heat flux LHF. (a) shows the monthly averages. (b) and (c) show hourly averages for 5 days in winter and summer, respectively.

where $\epsilon = 0.622$ is the ratio between the specific gas constants for dry air and water vapour, and e_{sat} is the saturation vapour pressure, which depends on the temperature via the Clausius-Clapeyron equation [Fowler, 2011]. As discussed in Chapter 1, the sensible and latent turbulent heat fluxes are associated with the wind-driven transfer of heat between the air and the ice surface due to differences in temperature (SHF) and moisture content (LHF). This is captured by the parametrisations (6.2), (6.3).

Figure 6.2 shows the observed surface energy balance components at the KAN_M PROMICE weather station in 2016. The incoming and outgoing shortwave and longwave radiation have been combined as net shortwave $Q_{\text{snet}} = Q_{\text{si}} + Q_{\text{so}}$, and net longwave $Q_{\text{lnet}} = Q_{\text{li}} + Q_{\text{lo}}$. We see that the shortwave radiation dominates in the summer, and shows the greatest annual variation. The other three components (the net longwave radiation Q_{lnet} and the turbulent heat fluxes SHF and LHF) do not exhibit such strong annual variations. In the winter, the shortwave radiation and latent heat fluxes are both approximately zero, and the sensible heat fluxes and longwave radiation are of roughly equal magnitude but opposite sign. This represents the transfer of heat to the ice from the warmer air (SHF > 0), and the net emission of thermal radiation from the ice ($Q_{\text{lnet}} < 0$).

The shortwave radiation displays diurnal (as well as annual) variations, which are of much larger amplitude in the summer than in the winter. The KAN_M station is

within the Arctic circle, so experiences continuous night, and hence zero shortwave radiation, in the middle of winter. The longwave radiation and sensible and turbulent heat fluxes do not follow such clear diurnal cycles, but instead vary over hours and days. This is due to short-term changes in weather conditions, such as cloud cover and wind. Recall that high levels of longwave radiation and turbulent heat fluxes are associated with warm, windy, cloudy conditions that favour weathering crust decay, whereas high levels of shortwave radiation in clear, sunny conditions favour weathering crust growth [e.g. Müller and Keeler, 1969, Schuster, 2001]. Therefore, we expect the variable conditions shown in Figure 6.2 to result in short-term variations in the weathering crust.

6.2.3 Calculating model forcings from observations

To force our model with observed weather data, we need to calculate the following model forcings from the quantities in the PROMICE dataset (shown in Table 6.1): the incoming shortwave radiation Q_{si} (W m^{-2}), the combined longwave radiation and turbulent heat fluxes Q_0 (W m^{-2}), the effective heat transfer coefficient υ (W m^{-2} K^{-1}), the albedo a, and the temperature T_∞ deep in the ice ($^{\mathrm{o}}$C or K). Note that here we prescribe a rather than treating it as an output of the model (see Section 6.2.3.2). All of these quantities can be calculated or inferred from the data collected at the PROMICE automatic weather stations, as described below.

6.2.3.1 Surface energy balance components

The form of the surface energy balance we use in our model (equivalent to the general form (6.1)) is

$$-kW\frac{\partial T}{\partial z} + \chi(1-a)Q_{\mathrm{si}} + Q_0 - \upsilon(T - T_{\mathrm{m}}) = \rho\mathcal{L}m_{\mathrm{surf}} \quad \text{at} \quad z = h(t). \tag{6.6}$$

In this chapter, we calculate Q_0 and υ slightly differently to the expressions presented in Chapter 2. Here, we use

$$Q_0 = Q_{\mathrm{li}} + Q_{\mathrm{lo}} + \mathrm{LHF} + \upsilon(T_{\mathrm{a}} - T_{\mathrm{m}}), \tag{6.7}$$

$$\upsilon = \tilde{C}p_{\mathrm{a}}u, \tag{6.8}$$

where Q_{li}, Q_{lo}, LHF, T_{a}, p_{a} and u come from the PROMICE dataset. The differences from Chapter 2 are that the outgoing longwave radiation is simply measured rather

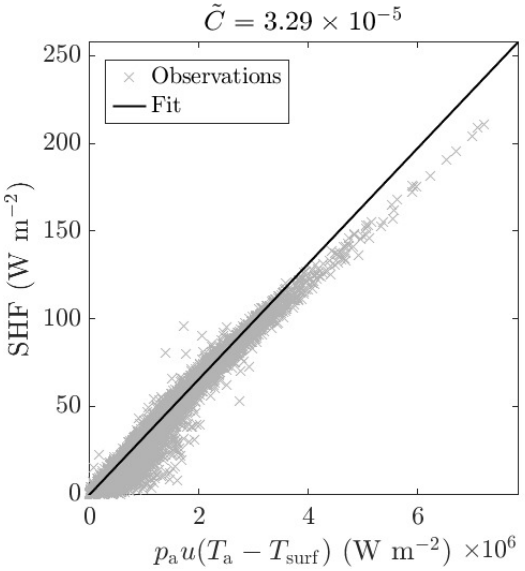


Figure 6.3: Fitting of parameter $\tilde{C}$ in sensible heat flux paramtrisation (6.9), using the first 10 years of hourly data points (crosses) at KAN_M, beginning at 14:00 on 2nd September 2008. SHF, p_a, u, T_a and T_{surf} all come from the PROMICE dataset [How et al., 2022]. A least-squares fit is shown (black line), the gradient of which determines $\tilde{C}$. Our value of $\tilde{C} = 3.29 \times 10^{-5}$ compares well to the value used by Cuffey and Paterson [2010]: $\tilde{C} = 2.58 \times 10^{-5}$.

than being expressed using the Stefan-Boltzmann law, and we no longer neglect latent turbulent heat fluxes (since these are of comparable magnitude to sensible turbulent heat fluxes in the KAN_M dataset). Instead of using the PROMICE SHF calculations directly, we parametrise SHF as

$$\text{SHF} = \tilde{C} p_a u (T_a - T_{surf}), \tag{6.9}$$

where p_a, T_a and u are the air pressure, air temperature and wind speed at a reference height (~ 2.5 m for KAN_M) above the ice surface, and T_{surf} is the temperature of the ice surface. All the quantities (apart from $\tilde{C}$) on the right-hand side of (6.9) are measured, and SHF is calculated, as part of the PROMICE dataset. We infer the constant $\tilde{C}$ from the PROMICE data by fitting a straight line (using least-squares) between SHF and $p_a u(T_a - T_{surf})$. Doing this using the first 10 years of data points in the hourly dataset for KAN_M (Figure 6.3) results in $\tilde{C} = 3.29 \times 10^{-5}$, which compares well to the value of $\tilde{C} = 2.58 \times 10^{-5}$ used by Cuffey and Paterson [2010].

6.2.3.2 Internal shortwave radiation

The albedo a is calculated from the observed shortwave radiation as $a = Q_{so}/Q_{si}$. We assume that the absorption and scattering of internal shortwave radiation are

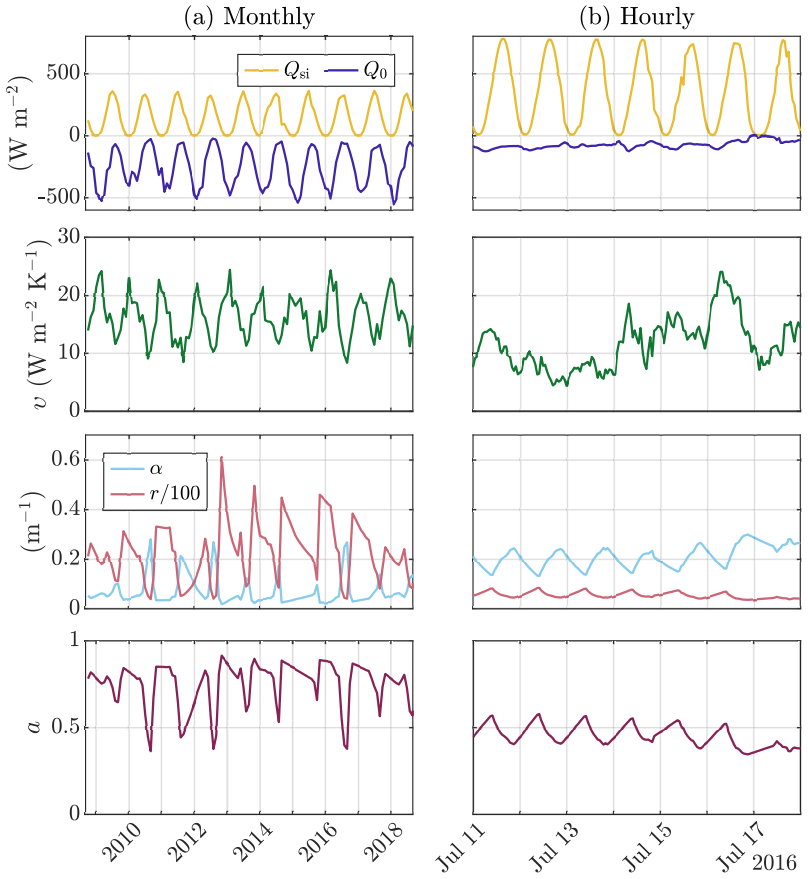


Figure 6.4: The forcings used in our weathering crust model, calculated from the PROMICE data from the KAN_M weather station on south-western Greenland [How et al., 2022], using (a) monthly averages over the first 10 years, and (b) hourly averages over one week in 2016. It is the hourly averages that are used to force the model. Note that we do not use α and r directly (see Section 6.2.3.2), but they are displayed for interest.

uniform with depth, meaning that internal radiation F is then given by (2.33),

$$F = (1-a)(1-\chi)Q_{\mathrm{si}}e^{-\kappa Z}. \tag{6.10}$$

We prescribe a constant, uniform extinction coefficient κ, the time-varying, observed albedo a, and a constant shortwave radiation partitioning parameter χ (see below). Recall from Chapter 2 that, when absorption and scattering are uniform, we are able to prescribe any three of α, r, κ, a and χ, with the other two being determined by the analytical relationship from Chapter 2:

$$\alpha = \frac{\kappa(1-s)}{1+s}, \quad r = \frac{\kappa^2-\alpha^2}{2\alpha}, \quad \text{where} \quad s = \frac{a}{1-\chi(1-a)}. \tag{6.11}$$

Although we do not use α and r in the model here, we show how the values of α and r calculated from κ, a and χ vary in time in Figure 6.4.

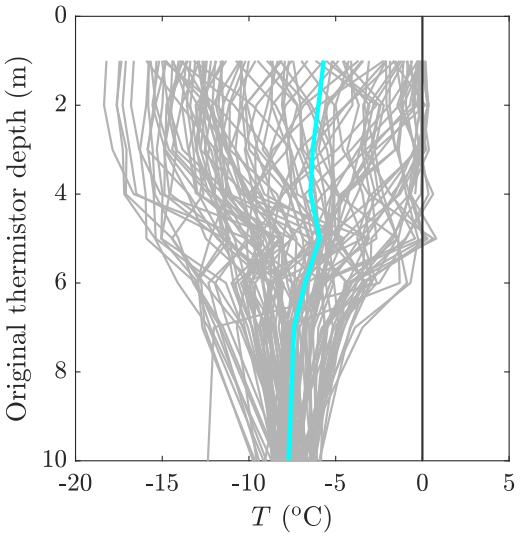


Figure 6.5: Monthly-averaged temperature profiles calculated from the thermistor string measurements at KAN_M (grey) (assuming that the thermistor depths are unchanged by ablation) [How et al., 2022]. The mean temperature profile (cyan) is also shown. At 10 m depth, the mean is -7.8°C. The black line shows $T = 0$°C.

6.2.3.3 Filling gaps in the PROMICE data

The KAN_M PROMICE data has some gaps in it. To use the data to force our model, we need to fill these gaps. This is done by replacing missing data with data from an 'average year'. That is, we take the Q_{si}, Q_0, υ, a calculated from the hourly KAN_M data from 4 years for which there is a complete dataset (2009, 2012, 2016 and 2017), and take an average over the 4 years. We use the corrected hourly-average data to force our weathering crust model, linearly interpolating to find the forcing value at each timestep. The resulting forcings are shown in Figure 6.4.

6.2.3.4 Temperature at depth

Another input of our model is the temperature T_∞ deep in the ice. This is difficult to measure, but can be estimated from temperature measurements taken in the top 10 m of the ice. Below-surface ice temperature measurements are taken at the PROMICE stations, using a thermistor string installed within the ice. Measurements taken at depths of 1, 2, 3, 4, 5, 6, 7, 10 m below the surface at the time of installation (but these depths change as the surface ablates). We use these temperature measurements (Figure 6.5) to infer T_∞, and choose a value of -9°C.

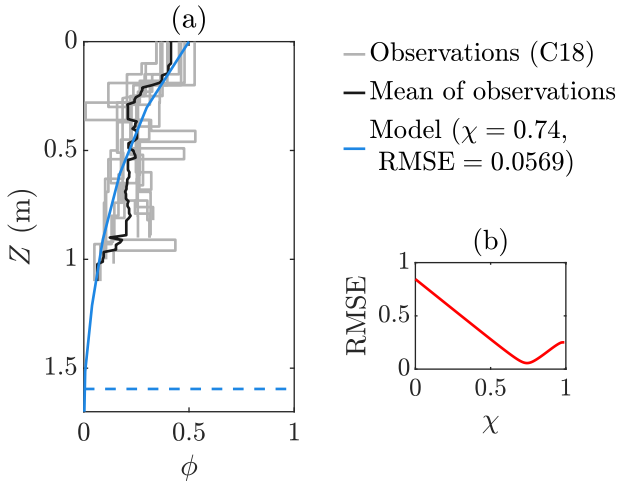


Figure 6.6: (a) Fitting χ using the ice-core porosity measurements from Cooper et al. [2018] (grey lines) and our steadily melting solutions. We found that $\chi = 0.74$ gives the steadily melting solution (blue line) that best agrees with the mean porosity profile from the ice-core measurements (black line). (b) The RMSE as a function of χ. We used $T_\infty = -9$°C. All other parameter values are as in Table 2.2.

6.2.3.5 Fitting χ

An important parameter in our model is χ, the proportion of absorbed shortwave radiation that is absorbed 'at' the surface. χ partitions the absorbed shortwave radiation between the surface and subsurface, and hence has a significant impact on the amount of surface melting relative to internal melting. In previous work, Hoffman et al. [2014], Law et al. [2020] found that their models for supraglacial lakes and the weathering crust, respectively, were highly sensitive to the value of χ (represented by $1 - I_0$ in Law et al. [2020]). We observe this sensitivity in our model as well (see Section 6.4.1 below). There is also uncertainty about what the value of χ should be. Previous studies have used a range of different χ values, with the studies considered by Hoffman et al. [2014] using values ranging from 0.36 to 0.8. The appropriate value of χ depends on various factors such as physical properties that vary with location (such as mean grain size), as well as the surface layer thickness and timestep in some models [e.g. Hoffman et al., 2008, 2014] (discussed in Section 6.4.1). Given this, we choose to find an appropriate value of χ by fitting to observational data. Hoffman et al. [2014] and Law et al. [2020] did this by fitting to observations of surface lowering and basal ablation, respectively. However, doing so is computationally costly because it requires many model runs over long time periods. Instead, we chose to fit to observed porosity measurements [Cooper et al., 2018] using our steadily melting model.

Cooper et al. [2018] present observations of the weathering crust porosity from a location in southwestern Greenland, about 8.3 km from the KAN_M PROMICE automatic weather station. The porosity observations come from ten 0.9–1.1 m ice cores taken on 11$^{\text{th}}$ and 12$^{\text{th}}$ July 2016 along an 800m transect. The porosity profiles from these ice cores are shown in grey in Figure 6.6. They also took two 1.8 m ice cores (but did not measure their densities), and found that one had crust throughout the entire depth (as for the ~ 1 m ice cores), whereas the other had solid ice for the bottom 20 cm, suggesting that the crust thickness could be around 1.6 m or more.

To fit χ, we calculate steadily melting solutions using the mean (hourly) KAN_M forcings over the 48 hour period of 11$^{\text{th}}$ and 12$^{\text{th}}$ July 2016 ($Q_{\text{si}} = 375$ W m^{-2}, $Q_0 = -97$ W m^{-2}, $a = 0.48$). We do this for different values of χ, and compare the solutions to the mean of the porosity profiles from the Cooper et al. [2018] ice-core measurements (black line in Figure 6.6). We select the 'best' value of χ as the one with the smallest root mean square error (RMSE) between the steadily melting solution and the mean observed porosity, giving $\chi = 0.74$. The corresponding steadily melting solution is shown in Figure 6.6 (blue line).

6.3 Time-dependent model solution

In this section, we run our weathering crust model using the Greenland weather data from KAN_M, as described in Section 6.2, and compare the model outputs to observations of temperature, porosity and surface lowering.

We run two versions of the model: (1) without lateral drainage ('no drainage') and (2) with lateral drainage ('drainage'). The 'no drainage' model is that used in Chapter 3, in which the weathering crust is always saturated ($S = 1$) and there is no flow of water. The 'drainage' model is the version used in Chapter 5, where we introduced a parametrisation of lateral drainage, making water flow possible and allowing the crust to become unsaturated ($0 < S < 1$). We compare the results of the different model versions to each other, as well as to observations.

Within the drainage model, we consider two values of lateral drainage strength: $\mathcal{K}_{\text{d}} = 1$ ('low drainage') and $\mathcal{K}_{\text{d}} = 50$ ('high drainage'). The former is the value found in Chapter 5 to produce broadly realistic water table heights in our steadily melting solutions (based on observations from Greenland [Irvine-Fynn et al., 2021]). The latter is chosen as an extreme case in which the weathering crust is almost completely dry.

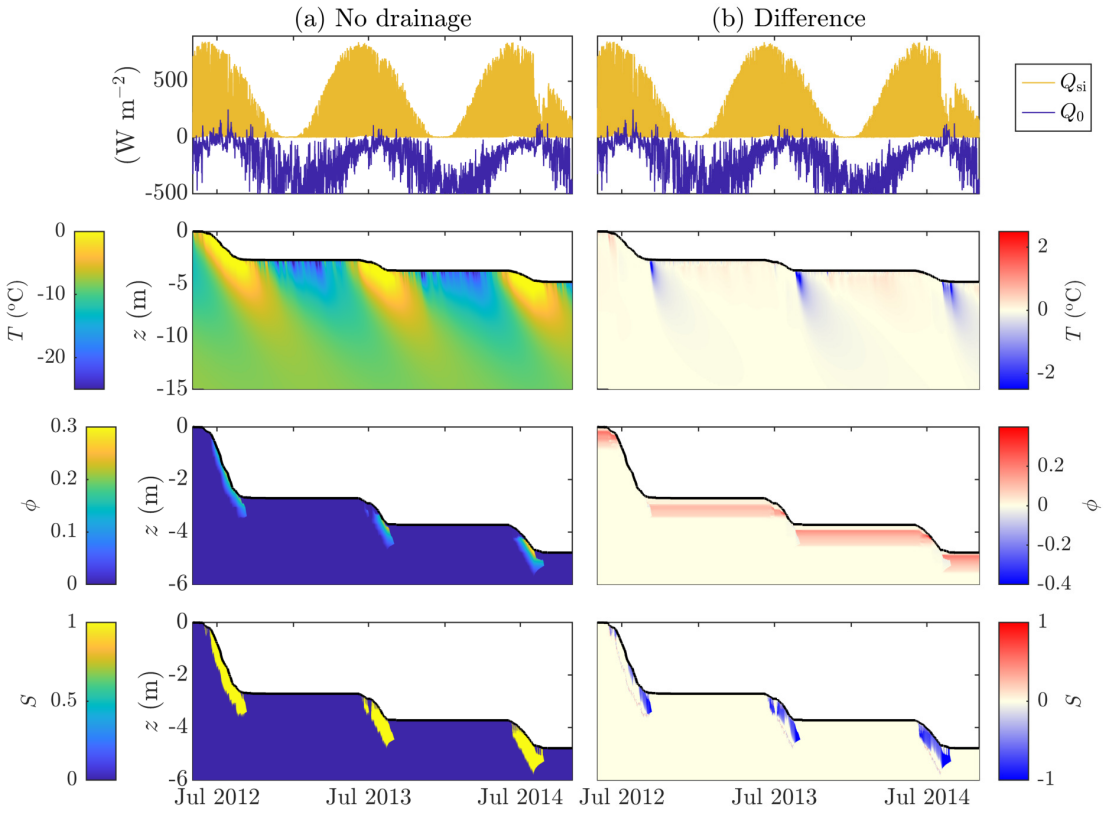


Figure 6.7: Model solution forced using weather data from the KAN_M PROMICE weather station on south-western Greenland [How et al., 2022]. The figure shows (a) the solution with no lateral drainage ($\mathcal{K}_\mathrm{d} = 0$), (b) the difference of the solution with lateral drainage ($\mathcal{K}_\mathrm{d} = 1$) from the solution without lateral drainage ($\mathcal{K}_\mathrm{d} = 0$). The first row shows the model forcings Q_si and Q_0. The second, third and fourth rows show the evolution of the temperature T, porosity ϕ and saturation S profiles, respectively, over time.

All model runs were initialised at the start of the KAN_M time series (14:00 on 2$^{\mathrm{nd}}$ September 2008) using the steadily melting solution corresponding to the mean forcing across the first 10 years of the KAN_M dataset, and simulated for 10 years.

6.3.1 Overall model behaviour

The overall behaviour of the model with and without lateral drainage is demonstrated in Figures 6.7 and 6.8. Figure 6.7 shows (a) the model solution without drainage over three melt seasons, (b) the difference between the solutions with ($\mathcal{K}_\mathrm{d} = 1$) and without lateral drainage over the same period. Figure 6.8 shows the 2016 melt season with (a) no drainage, (b) low drainage ($\mathcal{K}_\mathrm{d} = 1$), and (c) high drainage ($\mathcal{K}_\mathrm{d} = 50$).

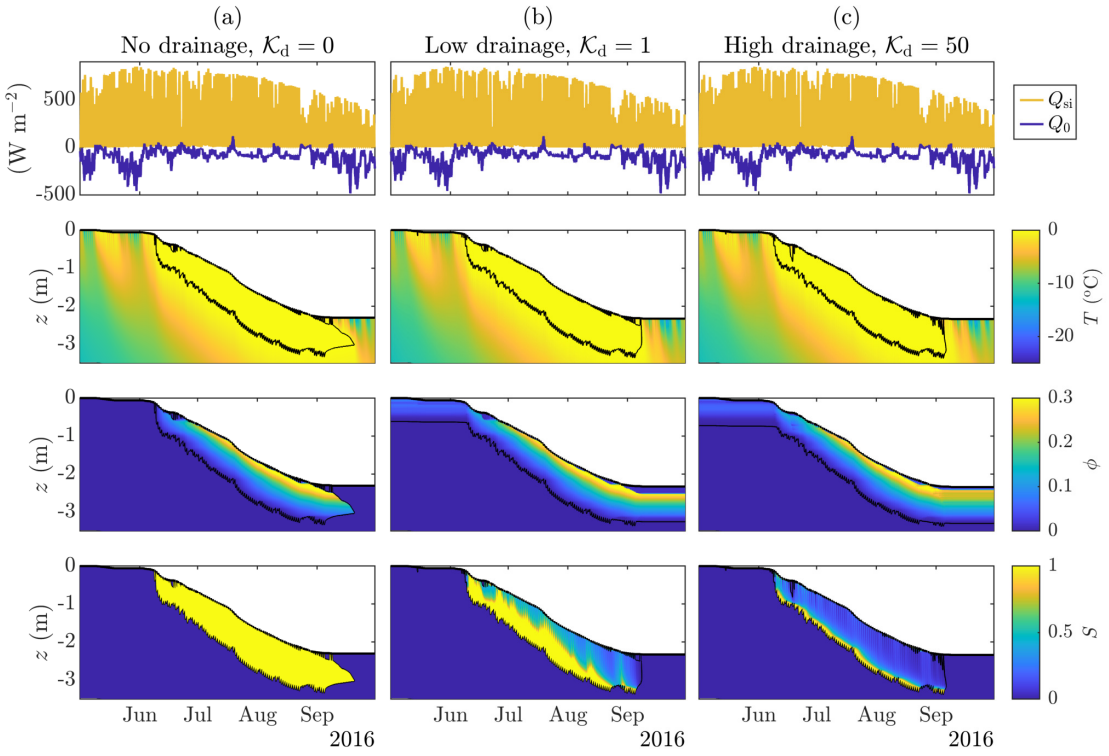


Figure 6.8: Modelled growth and removal of a weathering crust during 2016, forced using weather data from the KAN_M PROMICE weather station on south-western Greenland [How et al., 2022]. The solution is shown with (a) no lateral drainage, (b) low lateral drainage ($\mathcal{K}_d = 1$), and (c) high lateral drainage ($\mathcal{K}_d = 50$). The first row shows the model forcings Q_{si} and Q_0. The second, third and fourth rows show the evolution of the temperature T, porosity ϕ and saturation S profiles, respectively, over time. Zero contours of T, ϕ and S are shown in black.

The overall qualitative behaviour is the same with and without drainage. We see that the surface is frozen for most of the year, and a weathering crust forms for a few months during the summers (the yellow regions in the bottom panel of Figure 6.7(a)). During this time, there is melting internally and at the surface, resulting in the ice surface lowering by typically 1–3 m each year (see Section 6.3.4).

Throughout the melt season, the weathering crust gets thicker and thinner due to melting and freezing at the bottom of the crust (Figure 6.8). This is largely driven by the diurnal variations in shortwave radiation Q_{si} and hence internal radiation F, with the resultant internal heat source getting turned off during the night when $Q_{si} = 0$. At the end of the melt season, the (temperate) weathering crust is removed by freezing from the surface, as a result of the negative values of Q_0 (combined longwave radiation and turbulent heat fluxes) and reduced shortwave radiation Q_{si}.

The negative values of Q_0 throughout the melt season (indicating conditions that

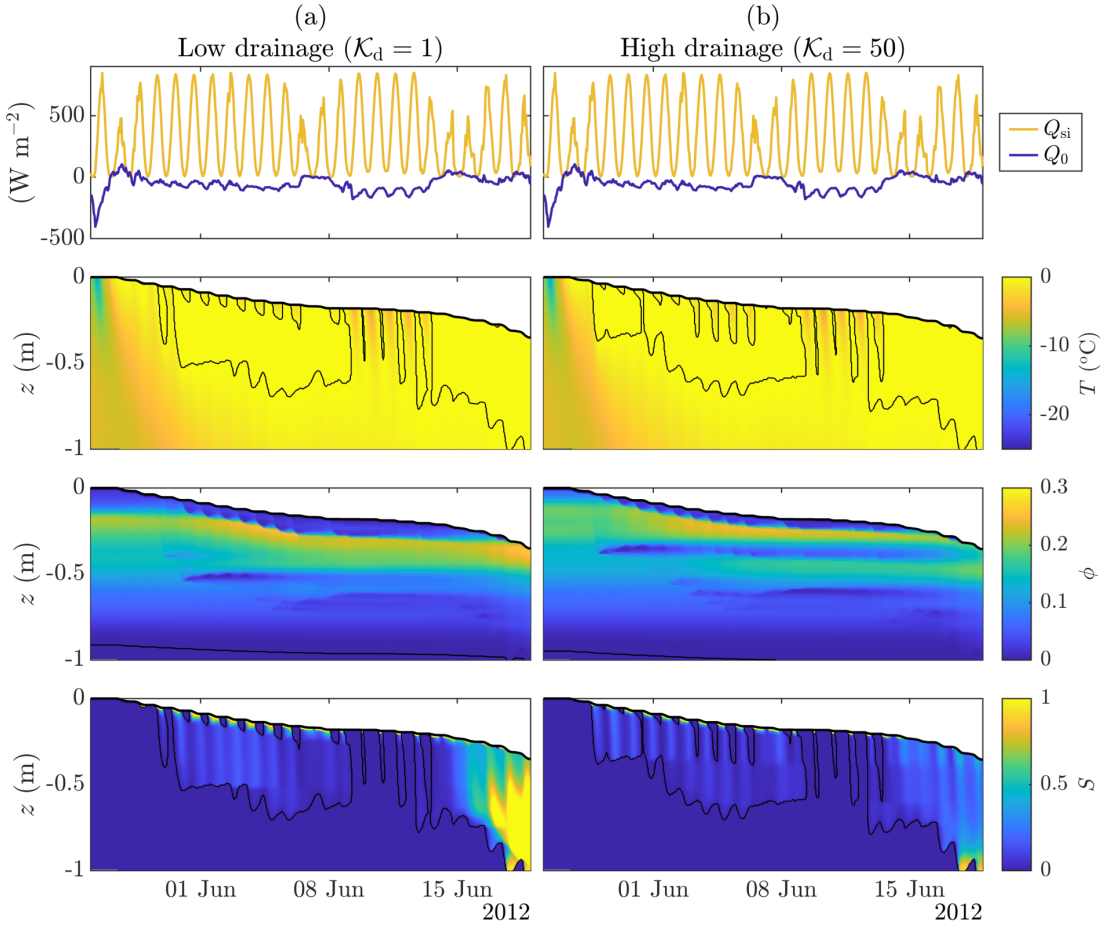


Figure 6.9: Diurnal melt-freeze cycles of the surface layer and formation of transient ice lenses at the start of the 2012 melt season at the KAN_M PROMICE weather station on south-western Greenland [How et al., 2022], using the drainage model with (a) $\mathcal{K}_d = 1$, and (b) $\mathcal{K}_d = 50$. The first row shows the model forcings Q_{si} and Q_0. The second, third and fourth rows show the evolution of the temperature T, porosity ϕ and saturation S profiles, respectively, over time. Zero contours of T, ϕ and S are shown in black.

favour surface freezing in the absence of shortwave radiation) mean that the weathering crust has a near-solid ice lid, a few centimetres thick, for much of the melt season, especially in 2016 (Figure 6.8). This near-solid layer is periodically frozen during the night (when Q_{si} drops to zero) and returned to the melting temperature during the day. This is demonstrated at the start of the 2012 melt season in Figure 6.9.

During the winter, Q_{si} is close to zero. Hence, there is not enough energy to melt the ice and the ice is correspondingly colder. However, there are still large fluctuations in the weather conditions (reflected in e.g. Q_0 and v) on sub-daily, daily and synoptic (a few days) timescales (as in Figure 6.4), resulting in large fluctuations in temperature (see Figure 6.7).

The main effect of including lateral drainage, as discussed in more detail in Chapter 5, is to allow the weathering crust to become unsaturated above a saturated layer at the base. Recall that, as seen in Figure 6.8, a greater value of $\mathcal{K}_\mathrm{d}$ leads to a thinner saturated region. The effect of this on the porosity, temperature and surface lowering are discussed in the following sections.

6.3.2 Porosity

The porosity during the winter is different for the drainage and no-drainage models. In the drainage case, the unsaturated region that forms in the weathering crust enables the crust to refreeze with non-zero porosity at the end of the melt season. Therefore, there is a surface layer of frozen, porous ice that persists through the winter until the next melt season. This is in contrast to the completely solid winter ice that results from freezing the saturated weathering crust in the no-drainage case.

Moreover, the model with drainage is able to produce interesting, transient structural features such as ice lenses (impermeable, horizontal ice layers), as discussed in Chapter 5, which do not form in the model without drainage. This is shown in Figure 6.9, which shows the start of the 2012 melt season. The exact nature of these features depends on the lateral drainage strength $\mathcal{K}_\mathrm{d}$, as seen in the figure.

However, during most of the melt season, the porosity (and temperature) is the same between the models with and without lateral drainage (e.g. as seen in Figure 6.10, introduced below). This is because, as discussed in Chapter 5, equations (5.5) for the porosity in the weathering crust and (5.9) for the temperature in the ice below are independent of the saturation, apart from at the freezing fronts. Therefore, in the time between the porous ice from the previous melt season melting away, and freeze-up at the end of the current melt season, the difference in saturation makes no difference to the porosity and temperature solutions. In reality, we expect that the saturation could change the absorption and scattering properties of the weathering crust, and hence F. This could be accounted for in future work by making the absorption and scattering coefficients α and r functions of S (see Section 6.5), similarly to how we made α and r functions of porosity and microbes in Section 4.5.

Figure 6.10(a) shows how the modelled porosity compares to the observations of porosity from Cooper et al. [2018] over the 48 hour period of 11^{th} and 12^{th} July 2016. The average of the model solutions over the 48 hour period has been plotted. The model (with and without drainage) slightly underestimates the observed porosity

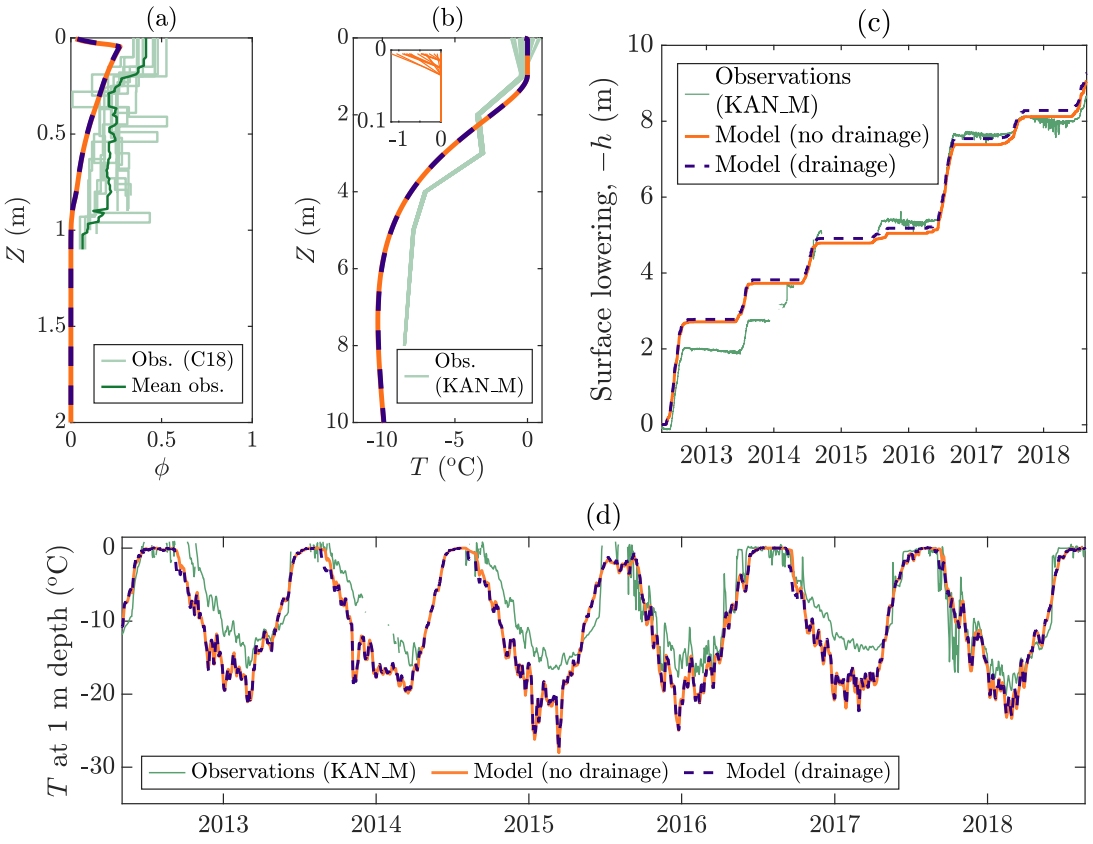


Figure 6.10: Comparison between the modelled and observed (a) porosity ϕ, (b,d) temperature T and (c) surface lowering at the KAN_M PROMICE weather station on south-western Greenland [How et al., 2022]. Model solutions both with ($\mathcal{K}_\mathrm{d} = 1$) and without ($\mathcal{K}_\mathrm{d} = 0$) lateral drainage are shown. The temperature and surface lowering observations are PROMICE measurements. The observed porosity is from ice cores taken by Cooper et al. [2018] during the 48 hour period of 11^{th} and 12^{th} July 2016. The temperature measurements in (b) are hourly PROMICE measurements over the same period, adjusted by 2 m to account for ablation. The model solutions in (a) and (b) are the mean of the (hourly) model solution over the 48 hour period. The inset in panel (b) shows the hourly temperature solutions near the surface. For clarity, for only the no-drainage model is shown; the drainage and no-drainage solutions would be indistinguishable. Panel (d) shows the temperature at 1 m depth below the surface, and uses daily mean observations from the upper thermistor.

from the ice cores. The porosity profile is broadly the correct shape, but the values are too small. The thickness of the weathering crust in our model (~ 1 m) is also thinner than that suggested by observations from Cooper et al. [2018] (perhaps up to 1.6 m), although their observations were based on just two ice cores. However, we should not read too much into the difference between our model and the ice core data because the ice cores [Cooper et al., 2018] were taken 8.3 km from the KAN_M weather station where weather observations were taken. Given the variability of the weathering crust, spatially as well as temporally [e.g. Tedstone et al., 2020], we would not necessarily expect the porosity to be the same at two points 8.3 km apart.

6.3.3 Temperature

The temperature is the same between the models with and without lateral drainage for most of the melt season, for the reasons given in Section 6.3.2.

Moreover, the temperature profiles in the model and observations broadly agree during this time. This is seen in Figure 6.10(b), which shows how the modelled temperature compares to the observed temperature from PROMICE (previously discussed) over the same 48 hour period as the porosity observations (11^{th} and 12^{th} July 2016). The temperature fluctuates around the melting temperature near the surface, then decreases with depth. The temperature fluctuations near the surface are of order -1 °C in the model and observations. The observed temperature goes above and below the melting point, but our model does not allow the melting temperature to be exceeded when ice is present. Note that there is some uncertainty in the depth of the thermistors at which the temperature observations are taken, because the position of these relative to the ice surface changes as the surface lowers. Based on the fact that there has been roughly 2 m of surface lowering since the start of the melt season, we have adjusted the thermistor depths by this amount.

The temperature is only significantly different between the models with and without drainage at the end of the melt season. Freeze-up and cooling at the end of the melt season happens more quickly with drainage than without (compare $T = 0$°C contours in Figure 6.8). This is because the internal drainage of meltwater removes latent heat (which would otherwise have been released, heating the ice, upon freezing) and means there is less water to freeze. This agrees with the modelling work of Hoffman et al. [2014], who found that their model without drainage took around 2 weeks longer to refreeze at the end of the melt season. In our model solution, the difference in 2016 is 9 days. At the start of the melt season, meltwater can percolate into the porous ice in the drainage case and refreeze, releasing heat. This can cause increased warming at the start of the melt season in some years (e.g. 2012, see Figure 6.7).

Figure 6.10(d) shows the longer-term evolution of the modelled temperature 1 m below the surface, and the observed temperature at the upper thermistor (initially 1 m below the surface). We see that there is very little difference between the model with and without drainage, and that the model broadly captures the observed temperature variations. However, the modelled temperature tends to be too cold in the winter, and cools down too quickly at the end of the summer in some years. The discrepancy could in part be explained by the position of the thermistors relative

to the surface changing as the ice ablates, meaning that the thermistors are closer to the surface by the end of the melt season (before being reset at the start of the next). However, using measurements from lower thermistors to correct for this (not shown) only makes a small difference. Another possible explanation, discussed in Section 6.5, is that we neglect accumulation (snowfall) in our model.

6.3.4 Surface lowering

The amount by which the ice surface lowers is measured as part of the PROMICE dataset at KAN_M, and provides a useful way to test our model predictions. Measurements are taken using a pressure transducer, which is attached to the end of a hose and buried at least 10 m deep in the ice. The other end of the hose is attached to a bladder that hangs from the weather station tripod. The hose is filled with antifreeze, and the bladder allows for inflow/outflow. As the ice surface melts, the tripod moves downwards with the surface, reducing the hydrostatic pressure of the column of liquid over the transducer. Hence, measuring the change in pressure at the bottom of the hose translates to knowing the change in surface height.

Both the models with and without lateral drainage compare well against the observed surface lowering (Figure 6.10(c)). Both models overestimated surface lowering during 2012 (well-known as a year of extreme melt on Greenland [Nghiem et al., 2012]), and underestimated it by an equal amount in 2014. All other years have very good agreement to observations.

There is about 2.2% more surface lowering when lateral drainage is included in the model ($\mathcal{K}_\mathrm{d} = 1$). This is due to the reasons discussed in Chapter 5, namely that the removal of meltwater internally allows for the crust to freeze with non-zero porosity, and the same (surface) melt energy results in greater surface lowering when the surface is porous compared to solid. However, this only makes a difference towards the start of the melt season when the ~ 1 m thick layer of porous ice from the previous melt season (present in the drainage case, but not the no-drainage case) is being melted away (i.e. the time taken for the red region to be removed in Figure 6.7(b)). Once this old porous layer has been melted through, the surface lowering and porosity is the same with and without drainage for the rest of the melt season. Increasing the lateral drainage further has very little impact on the surface lowering, with $\mathcal{K}_\mathrm{d} = 50$ only leading to 0.5% more surface lowering than $\mathcal{K}_\mathrm{d} = 1$. This difference would be almost indistinguishable in Figure 6.10(c), so $\mathcal{K}_\mathrm{d} = 50$ is not shown.

Our results here are in contrast to the findings by Hoffman et al. [2014], who found that including lateral drainage in their model resulted in a *decrease* in surface lowering. However, this is explained by the fact that they used different values of χ in their models with and without lateral drainage. They used a smaller value of χ in their drainage model. As will be discussed in Section 6.4.1, we have found χ to have a significant impact on surface lowering (and the model solution as a whole), more so than whether or not lateral drainage is included in our model (the value of $\mathcal{K}_\mathrm{d}$).

6.3.5 Meltwater production and removal

All meltwater that is produced during a melt season must be removed by the end of that melt season. This is to conserve mass, noting that the melt season begins and ends with no liquid water present. Meltwater is produced by (1) surface melting and (2) internal melting, and can be removed by (1) refreezing, (2) surface runoff or (3) internal runoff (lateral drainage). That is

$$\int m_\mathrm{surf}\ \mathrm{d}t + \int\int \max(m_\mathrm{int}, 0)\ \mathrm{d}Z\ \mathrm{d}t = -\int\int \min(m_\mathrm{int}, 0)\ \ \mathrm{d}Z\ \mathrm{d}t + r_\mathrm{tot}, \quad (6.12)$$

where

$$r_\mathrm{tot} = \int r_\mathrm{off}\ \mathrm{d}t + \int\int q_\mathrm{d}\ \mathrm{d}Z\ \mathrm{d}t \quad (6.13)$$

is the total amount of runoff (surface and internal combined). This is an extension of the mass conservation presented in Section 5.5.3. Note that the internal melt rate m_int corresponds to melting when positive and freezing when negative.

Figure 6.11 shows this mass conservation for the 2016 melt season for the model with no, low and high lateral drainage. In all three cases, the majority (73%) of melting happens at the surface. When there is no lateral drainage, most of the meltwater (73%) is removed by surface runoff, with the rest being refrozen internally. When lateral drainage is included, lateral drainage becomes the dominant meltwater removal mechanism, with both surface runoff and refreezing reducing to compensate. Increasing $\mathcal{K}_\mathrm{d}$ increases the proportion removed as internal drainage. Note that a small amount (6–7%) of mass is lost by the model during the melt season (the thin grey bars in Figure 6.11), which is believed to be due to the numerical discretisation.

Cycles of melting and meltwater removal also happen throughout the melt season. For example, when there is high drainage ($\mathcal{K}_\mathrm{d} = 50$), internal melting happens during the day when $Q_\mathrm{si} > 0$ and is almost completely drained (or refrozen) away during the night (see Figure 6.8(c), bottom panel). When $\mathcal{K}_\mathrm{d}$ is smaller, these oscillations

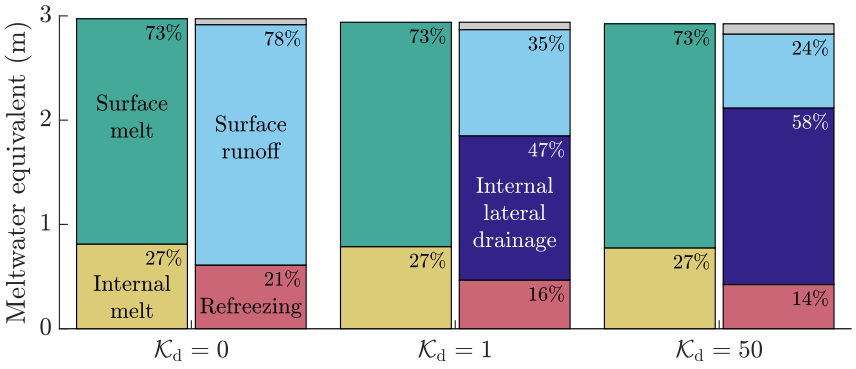


Figure 6.11: The partitioning of the production and removal of melt during the 2016 melt season. This is shown for the model without ($\mathcal{K}_\mathrm{d} = 0$) and with ($\mathcal{K}_\mathrm{d} = 1, 50$) lateral drainage. For each case, the left-hand bar shows how much of the total melt is surface melt vs. internal melt, and the right-hand bar shows how much of this meltwater is removed by surface runoff, refreezing, and internal lateral drainage. The percentages of the total melt are shown. The thin grey bars at the top represent the small (1–3%) mass loss due to the numerical discretisation.

still occur, but about a larger saturation value. The diurnal melt–freeze cycles, at the top (see Figure 6.9) and bottom (see Figure 6.8) of the crust, account for most of the total refreezing over the melt season. Only a small amount is due to the final freeze-up at the end of the melt season.

6.4 Discussion

6.4.1 Shortwave radiation partitioning χ

An important parameter in our model is χ, which partitions the absorbed shortwave radiation between the surface and subsurface. Here, we compare the use of χ in our model to previous models, and discuss the sensitivity of the model solution to χ.

The parameter χ has also been used in previous models, such as those considered by Hoffman et al. [2014]. In these models the appropriate value of χ depends on the discretisation used in the model (in addition to the ice properties).

Recall that the parameter χ was introduced to account for the fact that, within the shortwave radiation band, longer wavelengths are absorbed more quickly nearer the surface. χ is the proportion of absorbed shortwave radiation that is absorbed in some thin surface layer, thought of as being 'at' the surface. Unlike our model, most existing models [e.g. Greuell and Oerlemans, 1989, Bintanja and Van Den Broeke,

1995, Hoffman et al., 2014] include this thin surface layer explicitly. They treat the top grid cell of the model domain as the 'surface', and it is in this grid cell that the surface energy balance is applied and the 'surface-absorbed' shortwave radiation is absorbed. Many models are based on Greuell and Oerlemans [1989], who treated shortwave radiation with wavelengths longer than 0.8 μm as being absorbed in a 6 cm surface layer (i.e. a 6 cm top grid cell), giving a χ value of 0.36.

In these existing models, the thickness of the surface layer and the value of χ are often related; if a thicker layer is treated as the 'surface', then a greater proportion of shortwave radiation (up to a shorter wavelength cutoff) is absorbed in that layer and less is left available to penetrate into the ice below [Hoffman et al., 2014].

Similarly, the 'best' value of χ (and associated surface layer thickness) – found by fitting to observations (see Section 6.2.3.5) – has been shown to depend on the timestep of the model, with a larger timestep resulting in a larger value of χ and larger surface layer thickness [Hoffman et al., 2008]. This is because the surface layer thickness can be thought of as the thickness of ice that interacts with the atmosphere within one timestep [Hoffman et al., 2008].

In our model, we apply the surface energy balance at the surface (on the top edge of the top grid cell) rather than in the top cell, effectively shrinking our surface layer to zero. Moreover, the value of χ used in our model is fitted using steadily melting solutions rather than the time dependent solution used in previous studies [e.g. Hoffman et al., 2014, Law et al., 2020], so our 'best' value of χ is independent of our choice of timestep size Δt.

We have found our model solutions to be very sensitive to the value of χ, in agreement with the findings of Hoffman et al. [2014], Law et al. [2020]. This is demonstrated in Figure 6.12. Increasing χ significantly increases surface lowering, by increasing the proportion of shortwave radiation absorbed at the surface and decreasing the proportion absorbed internally. It is reassuring that our model reproduces surface lowering well (Figure 6.10), even though χ was fitted based on ice core porosities, rather than surface lowering (as has been done in previous models [e.g. Hoffman et al., 2014]).

Increasing χ also has the effect of decreasing the porosity, because less radiation penetrates below the surface. This also results in a decrease in the temperature below the weathering crust. The thickness of the zero-porosity surface layer in Figure 6.12 decreases because more energy is directed into melting the surface.

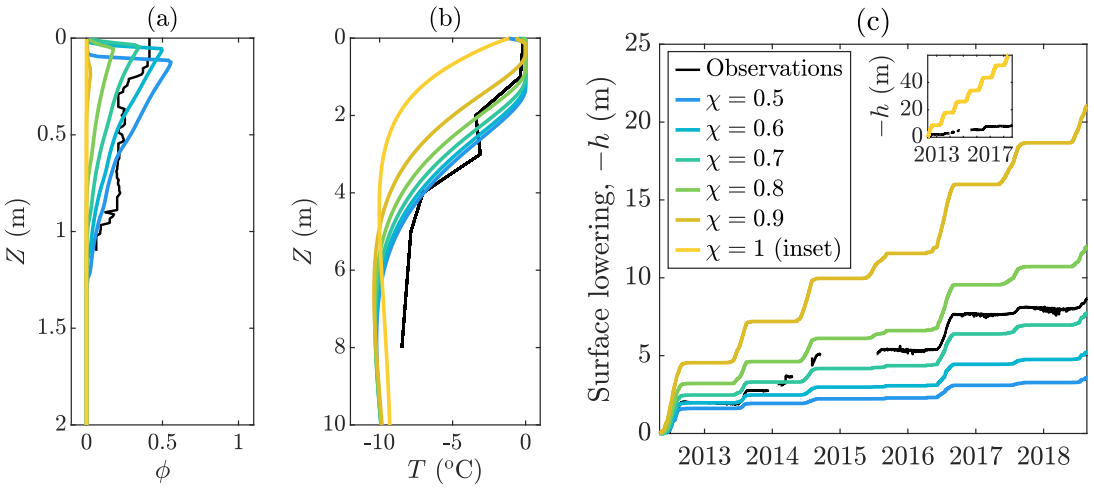


Figure 6.12: Effect of varying χ in the weathering crust model without lateral drainage. The model solutions for different values of χ are compared to (a) porosity observations from Cooper et al. [2018], and (b) temperature and (c) surface lowering observations from the PROMICE weather station at KAN_M [How et al., 2022]. In panels (a) and (b), the mean of each model solution and the mean of observations, both taken over the 48 hour period of 11$^{\text{th}}$ and 12$^{\text{th}}$ July 2016, are shown.

All of this demonstrates that χ is a very important parameter in the model. It also informs us that the partition between shortwave radiation between the surface and subsurface is a key physical process for governing the near-surface melting behaviour in these regions. It is therefore crucial to consider the weathering crust when modelling quantities such as surface lowering. Traditionally, models often assume that all the shortwave radiation is absorbed at the surface ($\chi = 1$), neglecting the near-surface layer. Our work demonstrates that such an approach results in significant overestimates of the surface lowering and mass loss, and underestimates of near-surface temperature (Figure 6.12).

6.4.2 Lateral drainage

Varying the lateral drainage strength $\mathcal{K}_\text{d}$ in our model changes the water table height (i.e. the thickness of the saturated region), with a larger $\mathcal{K}_\text{d}$ resulting in a thinner saturated region. In Chapter 5, we used this relationship to infer $\mathcal{K}_\text{d} = 1$ as a roughly appropriate value for reproducing observed water table heights from Greenland [Irvine-Fynn et al., 2021] using steadily melting solutions to our model.

However, the time-dependent results from our model with $\mathcal{K}_\text{d} = 1$ slightly underestimate the thickness of the saturated region compared to these observations. The water table height in the model solution is variable, but we find the water table

to typically lie ~ 0.5 m below the surface in a ~ 1 m thick crust, compared to the ~ 0.1 m below the surface found by Cooper et al. [2018], Irvine-Fynn et al. [2021] for weathering crusts of a comparable thickness. This suggests that a slightly smaller value of $\mathcal{K}_\mathrm{d}$ might be more appropriate. However, the results given with $\mathcal{K}_\mathrm{d} = 1$ are still useful for making qualitative comparisons between the model with and without lateral drainage.

In that regard, we have found the modelled porosity, temperature during the melt season, and longer-term surface lowering and total runoff to be very similar between the versions of the model with and without lateral drainage. Therefore, we suggest that, if we are interested solely in the overall behaviour, such as porosity, temperature during the melt season, and mass loss over multiple years, then using the model without drainage should suffice. To capture finer details — such as transient ice lenses at the beginning of the melt season and the distribution of runoff between the surface and subsurface — the model with lateral drainage is necessary.

Being able to use the model without drainage is beneficial, since the model requires much smaller timesteps to run when lateral drainage is included. This is because the vertical percolation of meltwater must then be modelled, and this occurs on a much faster timescale than the the evolution of the ice. For example, we use typical timestep values of 1 hour when there is no drainage and 5×10^{-3} hours (18 seconds) when there is drainage.

Moreover, the fact that the model solution is much more sensitive to the value of χ than the value of $\mathcal{K}_\mathrm{d}$ suggests that the partitioning of shortwave radiation between the surface and subsurface is a more important physical process for determining the amount of surface lowering and mass loss than the internal drainage and flow of meltwater through the weathering crust.

6.5 Summary

Overall, we see that our weathering crust model does well at reproducing observations from south-western Greenland. Qualitatively, our model captures the formation of a variable weathering crust during the summer. More quantitatively, the modelled surface lowering agrees very well with the observations from 2012 to 2018. This gives us confidence in our model, and also in our choice of the parameter χ. Our model appears to underestimate the observed porosity, but this might be due to observations being taken at a different site to where the weather data was recorded.

The model also broadly reproduces observed subsurface temperatures, but often underestimates the subsurface temperature during the winter.

One possible explanation of the discrepancies between our model and observations is the neglect of accumulation (snowfall) in our model. During the winter, snowfall accumulates on the frozen surface on which the weathering crust will form in the summer. The layer of snow can insulate the ice below during the winter, and could explain why our model underestimates winter temperatures. However, the snow layer can also prevent some of the shortwave radiation that would have been used to heat the ice below from penetrating through the snow, having the opposite effect [Hoffman, 2011]. In addition, some energy that would otherwise be used to melt the ice is required to melt the snow at the start of the summer, affecting the surface lowering. The PROMICE observations at KAN_M show there to be typically up to 1 m of snowfall each year, which is significant compared to the typical 1–3 m of surface lowering. Therefore, incorporating accumulation into our model to explore these effects is an area for future work.

We have further explored the effect of including lateral drainage in our model, by comparing model solutions with and without lateral drainage. We suggest that the model without drainage is sufficient for capturing overall behaviour such as weathering crust structure and longer term surface lowering. However, we expect that making the absorption and scattering coefficients functions of saturation and porosity (as we investigated in the saturated model in Section 4.5) could make the effect of lateral drainage in the model more significant. For example, we expect that a saturated crust will absorb more and scatter less radiation than an unsaturated crust.

The work in this chapter demonstrates that the partitioning of shortwave radiation absorption (and hence melt) between the surface and subsurface is a key physical process in determining the mass loss from south-western Greenland, more so than internal drainage of meltwater. Correctly capturing this weathering crust process in models is crucial for making accurate predictions, but is made challenging by the partitioning parameter χ being poorly constrained (with the most appropriate value depending on the specific study) and the fact that the model solutions are very sensitive to its value.

Chapter 7

Summary and conclusions

7.1 Summary

The weathering crust is a layer of porous ice that forms at the surface of ice sheets and glaciers, as a result of shortwave radiation penetration. It plays an important role in the surface albedo, how much near-surface melting occurs, and the transport of meltwater, microbes and nutrients. In this thesis, we have developed and used a continuum mathematical model for the weathering crust and the microbes that live within it to explore: (1) the effect of the weathering crust on the production and transport of meltwater; (2) how the weathering crust responds to changing weather conditions; and (3) how microbes and the weathering crust interact and affect albedo, melting and runoff.

Our weathering crust model accounts for thermodynamics, mass conservation, internal shortwave radiation and meltwater flow. We couple to this a logistic–growth-based model for microbes and nutrients that live within the crust. We have restricted our solutions to the model to one dimension (the vertical), although we note that the model itself applies more generally. Extending to higher dimensions is a key area for future work, discussed in Section 7.2. For much of the thesis (Chapters 2, 3, 4), we have neglected meltwater flow and considered a weathering crust that is fully saturated with water. We included meltwater flow in Chapters 5 and 6, by incorporating a parametrisation for subsurface lateral drainage. We first used our model in an idealised setting to investigate the physical processes governing the weathering crust, before applying our model to real data from the Greenland ice sheet in Chapter 6. We have solved the model numerically using an enthalpy method, and have also found analytical solutions in some idealised scenarios.

Detailed conclusions for each chapter are given at the end of each chapter, in Sections 2.6, 3.6, 4.6, 5.8, 6.5. Here, I frame the main conclusions from this thesis in terms of the three motivating questions raised in Chapter 1, and then outline key areas for future work.

7.1.1 How does the weathering crust affect the production and transport of meltwater on an ice-sheet surface?

We explored the effect of the weathering crust on melting and runoff in Chapters 5 and 6. In particular, we investigated the role of two key physical processes that occur in the crust: penetration of shortwave radiation, and subsurface drainage of meltwater.

We have demonstrated that correctly capturing the partitioning of shortwave radiation absorption, and hence melt, between the surface and subsurface (described by the parameter χ in our model) is crucial for correctly quantifying mass loss on south-western Greenland. Neglecting the weathering crust and subsurface radiation results in significant overestimates of mass loss. However, the model is very sensitive to χ and its value is poorly constrained, indicating an area of future work.

We suggest that subsurface drainage of meltwater plays a less important role than penetrating shortwave radiation in determining melting and runoff. Including subsurface lateral drainage in our model increases surface lowering, but we have shown the effect to not be very significant. Therefore, we propose that the model without subsurface drainage will suffice for quantifying mass loss over several years, but note that including subsurface drainage is necessary for capturing structural features such as ice lenses, and the partitioning of runoff between the surface and subsurface.

7.1.2 How does the weathering crust respond to changing weather conditions?

We have investigated the effect of different weather conditions on the weathering crust structure and evolution, primarily in Chapters 2 and 3.

We find that clear, sunny conditions (where shortwave radiation Q_{si} dominates) favour weathering crust growth, whereas warm, windy, cloudy conditions (where

turbulent heat fluxes and longwave radiation Q_0 dominate) favour decay, in agreement with qualitative observations [Müller and Keeler, 1969, Schuster, 2001].

In particular, the 'steadily melting' solutions found in Chapter 2 enabled us to identify for which values of Q_{si} and Q_0 it is possible to have a weathering crust, and of what thickness. We demonstrated that it is the balance between internal melting and surface melting that determines the thickness of the weathering crust.

In addition, we explored the dynamics of growth and decay in Chapter 3. Using idealised 'switching' experiments and periodic forcings, we found that the weathering crust can grow by internal melting, and be removed by melting or freezing from the surface, depending on the weather conditions.

Finally, we applied our model to real weather data from the south-western Greenland ice sheet in Chapter 6. The model generally performs well when compared to observations of porosity, temperature and surface lowering on south-western Greenland, suggesting that it could be used as a tool to make predictions about the response of the weathering crust to future weather and climate conditions.

7.1.3 How do the weathering crust and microbes within it interact, and how does this interaction influence albedo, melting and runoff?

We investigated the distribution of microbes in the weathering crust and feedbacks between the weathering crust, microbes and melting in Chapter 4.

We found that the conditions that favour weathering crust growth and removal also favour microbial growth and removal. Time-dependent solutions have demonstrated a lag between the growth of the weathering crust and microbial growth at the start of the melt season. This suggests that the timescale over which a weathering crust is grown and removed could influence the longer-term microbial growth. Exploring this behaviour further, using periodic or real-world forcings, is an area for future work. In particular, it would be interesting to investigate the response of microbes in the weathering crust to short-term (e.g. hourly to daily) melt–freeze cycles, as previously studied by Bradley et al. [2023] for microbes on the ice surface.

The coupled microbes and weathering crust model has enabled us to explore the potential positive feedback between microbes and the weathering crust, whereby enhance melting leads to enhanced algal growth, which lowers the albedo and leads

to even more melting [McCutcheon et al., 2021, Tedstone et al., 2020]. We have explored this feedback — and the similar melt–albedo feedback — by making the radiation absorption be a function of the microbial abundance and porosity, respectively. We have seen that these feedbacks do lead to enhanced melting, but our results suggest that the positive feedbacks are self-limiting — the increase in surface melting and thinning of the weathering crust also increases the removal of the albedo-reducing microbes and meltwater in runoff.

7.2 Future work

7.2.1 Higher dimensions

An important area not addressed by the one-dimensional model in this thesis is the spatio-temporal variability of the weathering crust and microbes over an ice–sheet surface. Therefore, a primary area for future work is to extend the model to higher dimensions. This would allow us to answer questions about how a weathering crust and microbes spread over the surface throughout a melt season, and how the extent of the weathering crust region will change with changing climate conditions. It would also enable the resulting spatio-temporal variability of the albedo to be studied, allowing for better predictions of melting across the south-western Greenland ice sheet, for example. The albedo schemes used in major climate models are often very simple and do not compare well with in-situ observations [e.g. Fettweis et al., 2017], so an improved physical approach like this would be beneficial. Such a model would also enable the transport of meltwater, microbes and nutrients through the weathering crust to be better quantified.

The work in this thesis has suggested that lateral drainage does not have a significant impact on the structure of the ice. This suggests that a reasonable method for studying the spatial variability of the weathering crust structure is to simply apply our one-dimensional model to each point in two-dimensional space. However, a genuinely higher-dimensional model would be necessary for capturing effects such as lateral diffusion of microbes, which could prove to be important. We have neglected diffusion of microbes from our one-dimensional model, but this can easily be incorporated.

To explore the transport of meltwater and microbes, we propose using a depth-integrated model (similar to the Dupuit approximation commonly used for modelling groundwater flow [Fowler, 2011]), making use of the small aspect ratio of the weathering crust. A depth-integrated model would be less computationally costly than a full two- or three-dimensional model [e.g. Leroux and Pomeroy, 2017, Moure et al., 2023, for snow], but could still capture the key behaviour. A similar, simplified approach (although not depth-integrated) has been used by Miller et al. [2020, 2023] to model firn aquifers.

7.2.2 Surface microbes

We have focussed on microbes that live within the water *in* the weathering crust, and which get advected with the meltwater flow. However, as demonstrated in Figure 1.3, there are also microbes (namely 'glacier ice algae') that exist 'stuck' to the ice surface, and these are thought to have an even more significant impact on the albedo. Therefore, an area for future work is to extend our model to include a population of surface microbes that can persist in the presence of meltwater runoff, necessitating a removal of our assumption that all microbes get washed away in runoff. This would enable more to be said about the total microbial abundance of the weathering crust, including that stored on the surface. Moreover, extending our modified surface ice algae model to higher dimensions (as discussed in Section 7.2.1) would enable an investigation of the spatio-temporal dynamics of algal blooms, such as have been observed on the south-western Greenland ice sheet. However, it remains unknown what controls when microbes are retained at the surface and when they are carried in the weathering crust water [Halbach et al., 2022], so this provides a modelling challenge.

7.2.3 Accumulation of snow

A deficiency of our current model is that it does not account for the accumulation of snowfall. We suggest that this could explain why our model slightly underestimates the ice temperature during the winter. In reality, snowfall will build up on the ice surface in the winter and subsequently melt away at the start of the summer, impacting the ice temperature, surface lowering and mass loss, as discussed further in Section 6.5.

Some modifications to our model and numerical method will be required to allow for accumulation. In particular, the boundary conditions will need to be updated [e.g. Meyer and Hewitt, 2017]. In addition, a compaction law [e.g. Herron and Langway, 1980, Li and Zwally, 2004, Arthern et al., 2010, Morris and Wingham, 2014] could be incorporated to account for the fact that snow compacts under its own weight, causing the density (porosity) to evolve even in the absence of melting and freezing. However, we expect that it could be reasonable to neglect compaction in surface snow that only persists for one season.

7.2.4 Liquid water on Mars

The work in this thesis can also be applied to identifying the presence of liquid water on Mars. Throughout stages of Mars's history, there have been water ice caps, glaciers and snow deposits present on Mars, with intermittent spells of liquid water present [Wordsworth, 2016]. It is thought that the penetration of shortwave radiation beneath the surface of the ice could provide a mechanism by which (subsurface) liquid water could be present in conditions under which that was previously thought to be impossible. In this context, the subsurface warming is referred to as the *solid-state greenhouse effect* [Matson and Brown, 1989], and can potentially result in subsurface melting. We have seen this effect in our model (e.g. in Figure 6.12(b)), and the model could plausibly be applied to a Martian setting to assess the conditions under which liquid water could be present.

7.3 Concluding remark

To conclude, the mathematical model presented in this thesis has proved a valuable tool for advancing our physical understanding of the weathering crust, the microbes within it, and their effect on the albedo, melting and runoff. We hope that it will enable improved quantitative predictions of ice–sheet surface mass loss in a changing climate.

Appendix A

Non-dimensionalisation

In this appendix, I present the non-dimensional version of the one-dimensional model used in this thesis. It is the non-dimensional model that is solved numerically. The model from Chapter 5 with lateral drainage and meltwater flow is already presented in non-dimensional form in Section 5.2.5, and so is not repeated here.

A.1 Weathering crust

A.1.1 Non-dimensionalisation

We non-dimensionalise using the scalings presented in Chapter 5 and repeated here for convenience. We non-dimensionalise by scaling $T = T_\mathrm{m} + [T]\hat{T}$ and scaling all other variables about zero with

$$\begin{gathered}[T] = \frac{[t][F]}{\rho c[Z]}, \quad [m_\mathrm{int}] = \frac{\rho}{[t]}, \quad [m_\mathrm{surf}] = [R_\mathrm{s}] = [R_\mathrm{r}] = [r_\mathrm{off}] = \frac{[Z]}{[t]}, \\ [H] = \rho c[T], \quad [q] = \frac{[Z]}{[t]}, \quad [p_\mathrm{w}] = \rho g[Z], \quad [h] = [Z],\end{gathered} \tag{A.1}$$

with $[Z]$, $[t]$ and $[F]$ prescribed. Typically, we use $[Z] = 1$ m, $[F] = 200$ W m^{-2}, and $[t] = 1$ day or 1 year. Typical values of the other scalings, calculated from the parameter values in Table 2.2, are shown in Table 5.1.

The following dimensionless parameters are introduced:

$$\begin{gathered}\hat{k}=\frac{k[t]}{\rho c[Z]^2},\quad \mathcal{S}=\frac{\mathcal{L}}{c[T]},\quad \hat{\alpha}=\alpha[Z],\quad \hat{r}=r[Z],\quad \hat{\kappa}=\kappa[Z]\\ \mathcal{K}=\frac{k_0\rho g[t]}{\mu[Z]},\quad \mathcal{B}=\frac{\rho g[Z]d_p}{\gamma},\quad \mathcal{K}_\mathrm{d}=\frac{\sin(\theta)\beta_\mathrm{h}[Z]}{L_\mathrm{d}},\end{gathered} \tag{A.2}$$

as described in Section 5.2.5. The dimensionless forcings are

$$\mathcal{Q}_\mathrm{si}=\frac{Q_\mathrm{si}}{[F]},\quad \mathcal{Q}_0=\frac{Q_0}{[F]},\quad \hat{\upsilon}=\frac{\upsilon[T]}{[F]},\quad \mathcal{T}_\infty=\frac{T_\infty-T_\mathrm{m}}{[T]}. \tag{A.3}$$

Typical values of the dimensionless parameters and forcings are shown in Table 5.3.

A.1.2 Saturated model

The dimensionless versions of the time-dependent, one-dimensional, saturated weathering crust model equations from Chapter 3 are

$$\frac{\partial\phi}{\partial t}+\dot{h}\frac{\partial\phi}{\partial Z}=m_\mathrm{int}, \tag{A.4}$$

$$\frac{\partial T}{\partial t}+\dot{h}\frac{\partial T}{\partial Z}=\hat{k}\frac{\partial^2 T}{\partial Z^2}-\frac{\partial F}{\partial Z}-\mathcal{S}m_\mathrm{int}, \tag{A.5}$$

$$F=(1-\chi)(1-a)\mathcal{Q}_\mathrm{si}e^{-\hat{\kappa}Z}, \tag{A.6}$$

$$-(1-\phi)\dot{h}=m_\mathrm{surf}\quad\text{at}\quad Z=0, \tag{A.7}$$

$$\hat{k}\frac{\partial T}{\partial Z}+\chi(1-a)\mathcal{Q}_\mathrm{si}+\mathcal{Q}_0-\hat{\upsilon}T=\mathcal{S}m_\mathrm{surf}\quad\text{at}\quad Z=0, \tag{A.8}$$

$$T\to\mathcal{T}_\infty\quad\text{as}\quad Z\to\infty. \tag{A.9}$$

The enthalpy formulation is

$$H=T+\mathcal{S}\phi, \tag{A.10}$$

$$\begin{aligned}\phi&=\begin{cases}0, & H\le 0,\\ \frac{H}{\mathcal{S}}, & 0<H<\mathcal{S},\\ 1, & H\ge\rho\mathcal{L},\end{cases}\\ T&=\begin{cases}H, & H\le 0,\\ 0, & 0<H<\mathcal{S},\\ H-\mathcal{S}, & H\ge\mathcal{S},\end{cases}\end{aligned} \tag{A.11}$$

$$\frac{\partial H}{\partial t} + \dot{h}\frac{\partial H}{\partial Z} = \hat{k}\frac{\partial^2 T}{\partial Z^2} - \frac{\partial F}{\partial Z}. \tag{A.12}$$

The Stefan condition is

$$-\hat{k}\frac{\partial T}{\partial z} = -\mathcal{S}\phi\dot{z}_{\mathrm{m}} \quad \text{at} \quad z = z_{\mathrm{m}}. \tag{A.13}$$

A.1.3 Steadily melting solutions

The dimensionless versions of the steadily melting equations from Chapter 2 are given by setting $\frac{\partial}{\partial t} = 0$ in the dimensionless equations in Section A.1.2, along with

$$\phi = 0, \quad T = 0, \quad \frac{\mathrm{d}T}{\mathrm{d}Z} = 0 \quad \text{at} \quad Z = Z_{\mathrm{m}}. \tag{A.14}$$

The dimensionless steadily melting solutions are

$$m_{\mathrm{surf}} = \frac{\chi(1-a)\mathcal{Q}_{\mathrm{si}} + \mathcal{Q}_0}{\mathcal{S}}, \tag{A.15}$$

$$Z_{\mathrm{m}} = -\frac{1}{\hat{\kappa}}\log\left(\frac{\dot{h}\mathcal{T}_\infty}{(1-\chi)(1-a)\mathcal{Q}_{\mathrm{si}}}\right), \tag{A.16}$$

$$T = \begin{cases} 0, & 0 < Z < Z_{\mathrm{m}}, \\ -\frac{(1-\chi)(1-a)\mathcal{Q}_{\mathrm{si}}}{\hat{k}\hat{\kappa}+\dot{h}}\left(e^{-\kappa Z} - e^{-\kappa Z_{\mathrm{m}}}e^{\frac{\dot{h}}{\hat{k}}(Z-Z_{\mathrm{m}})}\right) + \mathcal{T}_\infty\left(1 - e^{\frac{\dot{h}}{\hat{k}}(Z-Z_{\mathrm{m}})}\right), & Z > Z_{\mathrm{m}}, \end{cases} \tag{A.17}$$

$$m_{\mathrm{int}} = \begin{cases} \frac{\hat{\kappa}(1-\chi)(1-a)\mathcal{Q}_{\mathrm{si}}}{\mathcal{S}}e^{-\hat{\kappa}Z}, & 0 < Z < Z_{\mathrm{m}}, \\ 0, & Z > Z_{\mathrm{m}}, \end{cases} \tag{A.18}$$

$$\phi = \begin{cases} -\frac{(1-\chi)(1-a)\mathcal{Q}_{\mathrm{si}}}{\dot{h}\mathcal{S}}\left(e^{-\hat{\kappa}Z} - e^{-\hat{\kappa}Z_{\mathrm{m}}}\right), & 0 < Z < Z_{\mathrm{m}}, \\ 0, & Z > Z_{\mathrm{m}}, \end{cases} \tag{A.19}$$

$$\dot{h} = -\frac{(1-a)\mathcal{Q}_{\mathrm{si}} + \mathcal{Q}_0}{\mathcal{S} - \mathcal{T}_\infty}, \tag{A.20}$$

$$Z_{\mathrm{m}} = \frac{1}{\hat{\kappa}}\log\left(\left(\frac{(1-a)(1-\chi)\mathcal{Q}_{\mathrm{si}}}{-\mathcal{T}_\infty}\right)\Big/\left(\frac{(1-a)\mathcal{Q}_{\mathrm{si}} + \mathcal{Q}_0}{\mathcal{S} - \mathcal{T}_\infty}\right)\right), \tag{A.21}$$

where

$$\chi(1-a)\mathcal{Q}_{\mathrm{si}} + \mathcal{Q}_0 > 0, \tag{A.22}$$

$$\frac{(1-a)(1-\chi)\mathcal{Q}_{\mathrm{si}}}{-\mathcal{T}_\infty} > \frac{(1-a)\mathcal{Q}_{\mathrm{si}}+\mathcal{Q}_0}{\mathcal{S}-\mathcal{T}_\infty}, \tag{A.23}$$

for non-trivial steadily melting solutions to exist.

A.2 Microbes and nutrients

A.2.1 Non-dimensionalisation

The model for microbes and nutrients is non-dimensionalised with the following scalings, in addition to the scalings (A.1) for the weathering crust model:

$$[A_{\mathrm{w}}] = [A_{\mathrm{i}}] = A_{\max}, \quad [C_{\mathrm{w}}] = [C_{\mathrm{i}}] = C_{\mathrm{i},\infty}. \tag{A.24}$$

Scaling	Typical value
$[A_{\mathrm{w}}] = [A_{\mathrm{i}}]$	10^2 cells mL^{-1}
$[C_{\mathrm{w}}] = [C_{\mathrm{i}}]$	1 μmol L^{-1}

Table A.1: Scalings used to non-dimensionalise the microbes and nutrients model. The typical values are calculated from the values shown in Table 4.2, which are used throughout this thesis unless otherwise specified.

We introduce the dimensionless parameters,

$$\begin{gathered}\mathcal{G}_A = \beta_A[t], \quad \mathcal{G}_C = \frac{\beta_C[A_{\mathrm{w}}][t]}{[C_{\mathrm{w}}]}, \quad \kappa_F = \frac{k_{\mathrm{PAR}}}{\alpha_{\mathrm{PAR}}[F]}, \quad \kappa_C = \frac{k_C}{[C_{\mathrm{w}}]}, \\ \delta_{\mathrm{w}} = d_{\mathrm{w}}[t], \quad \delta_{\mathrm{i}} = d_{\mathrm{i}}[t],\end{gathered} \tag{A.25}$$

and the dimensionless deep-ice concentrations

$$\mathcal{A}_\infty = \frac{A_\infty}{[A_{\mathrm{i}}]}, \quad \mathcal{C}_\infty = \frac{C_\infty}{[C_{\mathrm{i}}]}. \tag{A.26}$$

A.2.2 Model

The dimensionless version of the one-dimensional microbes and nutrients model from Chapter 4, extended to include lateral drainage and meltwater flow (as in Chapter 5),

Symbol	Typical value	Dimensionless parameter
$\mathcal{G}_A$	20	Maximum microbial growth rate
$\mathcal{G}_C$	10	Maximum nutrient uptake rate
κ_{PAR}	0.89	Measure of radiation limitation
κ_C	1	Measure of nutrient limitation
δ_{w}	0	Death rate of microbes in water
δ_{i}	0	Death rate of microbes in ice
$\mathcal{A}_\infty$	0.01	Microbial abundance in deep ice
$\mathcal{C}_\infty$	1	Nutrient concentration in deep ice

Table A.2: Dimensionless parameters and forcings in the microbes and nutrients model. Typical values are calculated using the parameters values and scalings shown in Table 4.2, Table 5.1 and Table A.1.

is

$$\begin{aligned}\frac{\partial}{\partial t}\Big(\phi S A_{\mathrm{w}}\Big) + \dot{h}\frac{\partial}{\partial Z}\Big(\phi S A_{\mathrm{w}}\Big) + \frac{\partial}{\partial Z}\Big(A_{\mathrm{w}} q\Big) \\ = \mathcal{G}_A\left(\frac{F}{\kappa_F + F}\right)\left(\frac{\phi S C_{\mathrm{w}}}{\kappa_C + \phi S C_{\mathrm{w}}}\right)\phi A_{\mathrm{w}}(1 - A_{\mathrm{w}}) \\ - \delta_{\mathrm{w}}\phi S A_{\mathrm{w}} + A_{\mathrm{i}}\max(m_{\mathrm{int}}, 0) + A_{\mathrm{w}}\min(m_{\mathrm{int}}, 0) - q_{\mathrm{d}} A_{\mathrm{w}},\end{aligned} \tag{A.27}$$

$$\frac{\partial}{\partial t}\Big((1-\phi)A_{\mathrm{i}}\Big) + \dot{h}\frac{\partial}{\partial Z}\Big((1-\phi)A_{\mathrm{i}}\Big) = -d_{\mathrm{i}}(1-\phi)A_{\mathrm{i}} - A_{\mathrm{i}}\max(m_{\mathrm{int}}, 0) - A_{\mathrm{w}}\min(m_{\mathrm{int}}, 0). \tag{A.28}$$

$$\begin{aligned}\frac{\partial}{\partial t}(\phi S C_{\mathrm{w}}) + \dot{h}\frac{\partial}{\partial Z}(\phi S C_{\mathrm{w}}) + \frac{\partial}{\partial Z}(C_{\mathrm{w}} q) = -\mathcal{G}_C \phi A_{\mathrm{w}}\left(\frac{F}{\kappa_F + F}\right)\left(\frac{\phi S C_{\mathrm{w}}}{\kappa_C + \phi S C_{\mathrm{w}}}\right) \\ + C_{\mathrm{i}}\max(m_{\mathrm{int}}, 0) + C_{\mathrm{w}}\min(m_{\mathrm{int}}, 0) - q_{\mathrm{d}} C_{\mathrm{w}},\end{aligned} \tag{A.29}$$

$$\frac{\partial}{\partial t}\Big((1-\phi)C_{\mathrm{i}}\Big) + \dot{h}\frac{\partial}{\partial Z}\Big((1-\phi)C_{\mathrm{i}}\Big) = -C_{\mathrm{i}}\max(m_{\mathrm{int}}, 0) - C_{\mathrm{w}}\min(m_{\mathrm{int}}, 0), \tag{A.30}$$

$$A_{\mathrm{i}} \to \mathcal{A}_\infty \quad \text{as} \quad Z \to \infty, \tag{A.31}$$

$$C_{\mathrm{i}} \to \mathcal{C}_\infty \quad \text{as} \quad Z \to \infty. \tag{A.32}$$

The saturated, no-flow version of the model used in Chapter 4 is recovered by setting $S = 1$, $q = q_{\mathrm{d}} = 0$.

Appendix B

Details of numerical method

In this appendix, we present details of the numerical method used to solve the one-dimensional time-dependent weathering crust models presented in this thesis. In Section B.1, we describe the method used for the saturated problem with no water flow presented in Chapter 3. In Section B.2, we describe the extension of this method used from the unsaturated problem with water flow presented in Chapter 5.

In both cases, we use a finite volume scheme with semi-implicit timestepping, implemented in MATLAB, with a fixed timestep Δt (typically $\Delta t = 1$ hour for the saturated problem and $\Delta t = 5 \times 10^{-3}$ hours (18 seconds) for the unsaturated problem). We use a finite volume grid formed of N cells. The cell centres are at Z_j with $j = 1, 2, 3, ..., N$, the cell edges are at $Z_{j+1/2}$ with $j = 0, 1, 2, ..., N$. The ice surface $Z = 0$ lies at the first edge, $Z_{1/2} = 0$. The cell widths are $\Delta Z_j = \Delta Z_{j+1/2} - \Delta Z_{j-1/2}$ for $j = 1, 2, ..., N$, and the distances between the cell centres are $\Delta Z_{j+1/2} = \Delta Z_{j+1} - \Delta Z_j$ for $j = 1, 2, ..., N-1$. Variables with subscript j represent the numerical approximation to the solution at Z_j.

The interesting behaviour in our problems occurs in and just below the weathering crust, at the top of the domain. Deeper down, variations are less significant and occur over longer timescales. Therefore, we use a grid that is uniformly fine at the top (with $\Delta Z_j = \Delta Z_{\text{fine}}$) and uniformly coarse at the bottom (with $\Delta Z_j = \Delta Z_{\text{coarse}} > \Delta Z_{\text{fine}}$). Between the fine and coarse region, the grid size increases linearly over N_t cells. The fine mesh is used down to a depth Z_{fine}, chosen to be large enough such that the weathering crust is always contained within the fine region. Typical values used are $\Delta Z_{\text{fine}} = 0.01$, $\Delta Z_{\text{coarse}} = 0.1$, $Z_{\text{fine}} = 4$, $N_{\text{t}} = 10$, with the end of the domain being at $Z_{N+1/2} = Z_{\text{end}} = 100$.

B.1 Saturated problem without flow (Chapter 3)

We solve the enthalpy equation (A.12) using a semi-implicit finite volume scheme in MATLAB. The flux F is evaluated on cell edges, and the enthalpy H is evaluated on cell centres. We include $\dot{h}$ explicitly, H in the advection term implicitly, and T in the diffusion term semi-implictly, by carrying out iterations within each timestep (detailed below). The discretised dimensionless enthalpy equation is

$$\frac{H_j^{m+1} - H_j^{\text{old}}}{\Delta t} + \frac{f_{j+1/2} - f_{j-1/2}}{\Delta Z_j} = 0, \tag{B.1}$$

with

$$f_{j+1/2} = \dot{h}^{\text{old}} H_{j+1/2}^{m+1} - \hat{k}\left(\frac{T_H^m(H_{j+1}^{m+1}) - T_H^m(H_j^{m+1})}{\Delta Z_{j+1/2}}\right) + F_{j+1/2}^{m+1}, \tag{B.2}$$

where the superscripts 'old' represents the solution from the previous timestep, and superscripts m and $m+1$ represent solutions at the current and next iteration within the current timestep. T_H is a function that we use to express T in terms of H, based on the transformation (A.11) (discussed below). We approximate

$$\dot{h}^{\text{old}} H_{j+1/2}^{m+1} \approx \min(\dot{h}^{\text{old}}, 0) H_{j+1}^{m+1} + \max(\dot{h}^{\text{old}}, 0) H_j^{m+1} \tag{B.3}$$

using upwinding. Note that, in all the cases considered in this thesis, $\dot{h} \leq 0$ since we do not include accumulation in the model. In the method presented in this section (and used in Chapter 3), we use the analytical solution for F that holds when the absorption and scattering coefficients are uniform. A method for numerically solving the two-stream equations for F is presented in Section B.2

We want to include H in the diffusion term implicitly, but how T is expressed in terms of H depends on whether there is only ice, both ice and water, or only water (the three cases in (A.11)), which we do not know until we know the value of H. Similarly, the implementation of the surface boundary condition is different depending on whether or not there is surface melting, which, again, we do not know *a priori*. We tackle these issues by using an 'enthalpy flag' and a 'melt flag', and iterating within each timestep to determine the appropriate values of these.

B.1.1 Enthalpy flag

At each timestep, each point in the domain can be in one of the three states in (A.11). We label these using a flag $\mathbf{f}_H$, referred to as the enthalpy flag:

$$\mathbf{f}_H = \begin{cases} 1, & \text{if there is only ice} \quad (\phi = 0,\ T \leq T_\mathrm{m},\ H \leq 0), \\ 2, & \text{if there is both ice and water} \quad (0 < \phi < 1,\ T = T_\mathrm{m},\ 0 < H < \rho\mathcal{L}), \\ 3, & \text{if there is only water} \quad (\phi = 1,\ T \geq T_\mathrm{m},\ H \geq \rho\mathcal{L}). \end{cases} \tag{B.4}$$

Note that $\mathbf{f}_H$ is a vector with its size equal to the number of grid cells.

To ensure we use the correct conversion from T to H, we iterate the enthalpy flag $\mathbf{f}_H$ as follows, inspired by the method presented by Wetton [2023] [for problems such as Bridge and Wetton, 2007, Cheng et al., 2023]. Within each timestep, we carry out a set of iterations (up to a maximum of 10), updating the enthalpy flag each iteration. For the first iteration, we assume that $\mathbf{f}_H$ takes the value from the previous timestep. Within each iteration, we

1. Solve for H^{m+1} using the value of $\mathbf{f}_H$ from the previous iteration. The value of $\mathbf{f}_H$ tells us how to express T in the discrete enthalpy equation (B.1) in terms of H, following (A.11).

2. Update the enthalpy flag $\mathbf{f}_H$ if T and ϕ in the solution contradict the assumed enthalpy flag.

   - If we assumed only ice ($f_{H,j} = 1$) but found $T_j > T_\mathrm{m}$ ($H_j > 0$), set $f_{H,j} = 2$ (try assuming there is both ice and water).
   - If we assumed there is both ice and water ($f_{H,j} = 2$) but found $\phi_j < 0$ ($H_j < 0$), set $f_{H,j} = 1$ (try assuming there is only ice).
   - If we assumed there is both ice and water ($f_{H,j} = 2$) but found $\phi_j > 1$ ($H_j > \rho\mathcal{L}$), set $f_{H,j} = 3$ (try assuming there is only water).
   - If we assumed only water ($f_{H,j} = 3$) but found $T_j < T_\mathrm{m}$ ($H_j < 0$), set $f_{H,j} = 2$ (try assuming there is both ice and water).

3. If the assumed enthalpy flag was correct at all points in the domain, we stop iterating.

B.1.2 Melt flag

Solving the enthalpy equation implicitly also leads to difficulty implementing the surface boundary condition. Which boundary condition we use depends on whether or not the surface is melting, which we do not know until we have carried out the timestep. In the melt case, the surface is at the melting temperature, so $T = 0$ at $Z = 0$ is our boundary condition, and the surface energy balance (A.8) tells us the surface melt rate $m_{\text{surf}} > 0$. In the no-melt case, there is no surface melting ($m_{\text{surf}} = 0$), $T \leq 0$ at the surface, and the surface energy balance (A.8) is the boundary condition. Note that the surface temperature is evaluated on the top cell edge $Z_{1/2}$, whereas the temperature is in general evaluated on cell edges. We therefore approximate $T_{\text{surf}} = T_{1/2} \approx \frac{3}{2}T_1 - \frac{1}{2}T_2$ in terms of the cell centre values using linear extrapolation.

We label these two cases using the 'melt flag' f_{melt}, which determines which boundary condition we use. If $f_{\text{melt}} = 1$, $T = 0$ is used as the surface boundary condition (the melt case). If $f_{\text{melt}} = 0$, the surface energy balance (A.8) is used with $m_{\text{surf}} = 0$ (the no-melt case). To ensure we use the correct form of the surface boundary condition, we iterate the melt flag f_{melt} as follows.

1. First, we carry out the timestep (a set of iterations as described in Section B.1.1) using the melt flag f_{melt} from the *previous timestep*. That is, if the surface was (not) melting in the previous timestep then we assume it is (not) melting in the current timestep too.

2. If this assumption results in a non-positive melt rate $m_{\text{surf}} \leq 0$ or non-negative surface temperature $T_{\text{surf}} \geq 0$, we recompute the solution for the current timestep with the other melt flag.

3. If using the updated melt flag leads to an unphysical solution ($m_{\text{surf}} < 0$ or $T_{\text{surf}} > 0$), we revert to the solution found in step 1 (using the original melt flag).

It is important that the inequalities in step 2 are weak. This is to prevent the surface from getting 'stuck' in a no-melt state or vice versa. Having a solution with $m_{\text{surf}} = 0$ and $T_{\text{surf}} = 0$ is possible in both states, so having equality is not a contradiction. However, if $m_{\text{surf}} = 0$ is achieved having previously been in a state with $m_{\text{surf}} > 0$, it suggests that the surface is about to transition from melting to frozen in the next timestep. Not allowing this transition can cause numerical issues.

B.1.3 Implementing boundary conditions

Far-field temperature The far-field temperature boundary condition (A.9) is discretised as

$$T_{N+1/2} = \mathcal{T}_\infty. \tag{B.5}$$

Using this, we approximate

$$\left(\frac{\partial T}{\partial Z}\right)_{N+1/2} \approx \frac{T_{N+1/2} - T_N}{\frac{1}{2}\Delta Z_N}, \tag{B.6}$$

hence modifying

$$f_{N+1/2} = \dot{h}^{\text{old}}\mathcal{T}_\infty - \hat{k}\left(\frac{T_\infty - T_H^m(H_N^{m+1})}{\frac{1}{2}\Delta Z_N}\right), \tag{B.7}$$

where we have also used that $F \to 0$ as $Z \to \infty$, so $F_{N+1/2} = 0$.

Surface boundary condition In the melt case, the surface is at the melting temperature, and so $T = 0$ at $Z = 0$ is our boundary condition. The discretised condition is

$$T_{1/2} = 0, \tag{B.8}$$

from which we can approximate

$$\left(\frac{\partial T}{\partial Z}\right)_{1/2} \approx \frac{T_1}{\frac{1}{2}\Delta Z_1}, \tag{B.9}$$

and hence

$$f_{1/2} = -\hat{k}\left(\frac{2T_H^m(H_1^{m+1})}{\Delta Z_1}\right) + (1-\chi)(1-a)\mathcal{Q}_{\text{si}}, \tag{B.10}$$

where we have also used that $F = (1-\chi)(1-a)\mathcal{Q}_{\text{si}}$ at $Z = 0$, so

$$F_{N+1/2} = (1-\chi)(1-a)\mathcal{Q}_{\text{si}}. \tag{B.11}$$

In the no-melt case, the surface energy balance (A.8) is the boundary condition, with $m_{\text{surf}} = 0$. This is discretised as

$$\begin{aligned} -\hat{k}\left(W\frac{\partial T}{\partial Z}\right)_{1/2} &= (\chi(1-a)\mathcal{Q}_{\text{si}} + \mathcal{Q}_0) - (\hat{\upsilon} + R_{\text{s}} + R_{\text{r}})T_{1/2}, \\ &\approx (\chi(1-a)\mathcal{Q}_{\text{si}} + \mathcal{Q}_0) - (\hat{\upsilon} + R_{\text{s}} + R_{\text{r}})\left(\frac{3}{2}T_1 - \frac{1}{2}T_2\right), \end{aligned} \tag{B.12}$$

where we have used linear interpolation to express $T_{1/2}$ in terms of T_1 and T_2. (In the saturated case currently considered, $W = 1$, but the term is included here so that equation (B.12) also applies in the unsaturated case in Section B.2.) Using equations (B.12), (B.11), and the fact that $\dot{h} = 0$ when $m_{\text{surf}} = 0$,

$$f_{1/2} = (\chi(1-a)\mathcal{Q}_{\text{si}}+\mathcal{Q}_0)-(\hat{v}+R_{\text{s}}+R_{\text{r}})\left(\frac{3}{2}T_H^m(H_1^{m+1})-\frac{1}{2}T_H^m(H_2^{m+1})\right)+(1-\chi)(1-a)\mathcal{Q}_{\text{si}}. \tag{B.13}$$

B.2 Unsaturated problem with flow (Chapter 5)

The unsaturated flow problem is solved using an extension of the method presented in Section B.1. The enthalpy equation (5.35) and total water content equation (5.34) are solved using a finite volume scheme in MATLAB with semi-implicit timestepping. In addition to this, we must solve for the water flux q, as discussed in Section 5.3.1. The method presented here also solves the two-stream equations (5.32), (5.33) for the internal radiation F, allowing for the absorption and scattering coefficients $\hat{\alpha}$, $\hat{r}$ to be functions of, for example, ϕ and S. The fluxes q and F are evaluated on the cell edges, and the other variables H, W, T, ϕ, S are evaluated on the cell centres.

Note that the numerical method presented here does not apply to regions of pure water; we set the qT term in the enthalpy equation to zero.

B.2.1 Internal radiation

We solve the two-stream equations (5.32), (5.33) for the internal radiation F_-, F_+ using a second-order finite difference scheme. F_- and F_+ are evaluated on the cell edges $Z_{j+1/2}$, $j = 0, 1, 2, ..., N$, with their discretised values denoted by $F_{-,j+1/2}$, $F_{+,j+1/2}$.

The two-stream equations (5.32), (5.33) are discretised as

$$\left(\frac{\partial F_-}{\partial Z}\right)_{j+1/2} = -(\hat{\alpha}_{j+1/2} + \hat{r}_{j+1/2})F_{-,j+1/2} + \hat{r}_{j+1/2}F_{+,j+1/2}, \tag{B.14}$$

$$\left(\frac{\partial F_+}{\partial Z}\right)_{j+1/2} = (\hat{\alpha}_{j+1/2} + \hat{r}_{j+1/2})F_{+,j+1/2} - \hat{r}_{j+1/2}F_{-,j+1/2}. \tag{B.15}$$

The derivatives are approximated using a second-order accurate centred scheme,

$$\left(\frac{\partial F_{\pm}}{\partial Z}\right)_{j+1/2} \approx \frac{F_{\pm,j+3/2} - F_{\pm,j-1/2}}{\Delta Z_1 + \Delta Z_2}, \tag{B.16}$$

for $j = 1, 2, ..., N-1$, and the one-sided scheme

$$\left(\frac{\partial F_{\pm}}{\partial Z}\right)_{1/2} \approx \frac{-3F_{1/2} + 4F_{3/2} - F_{5/2}}{3\Delta Z_1 - \Delta Z_2}, \tag{B.17}$$

$$\left(\frac{\partial F_{\pm}}{\partial Z}\right)_{N+1/2} \approx \frac{F_{N-3/2} - 4F_{N-1/2} + 3F_{N+1/2}}{3\Delta Z_N - \Delta Z_{N-1}} \tag{B.18}$$

at the boundaries.

The boundary conditions are

$$F_{1,1/2} = (1 - \chi(1-a))\mathcal{Q}_{\mathrm{si}}, \tag{B.19}$$

$$F_{+,N+1/2} = 0, \tag{B.20}$$

and the albedo a is determined from the solution as

$$a = \frac{F_{+,1/2}}{\mathcal{Q}_{\mathrm{si}}}. \tag{B.21}$$

B.2.2 Solving for q and p_{w}

We consider the following different types of cells when calculating the water pressure p_{w} and water flux q:

- dry ($S \leq \mathrm{tol}_{S0}$, $\phi > \mathrm{tol}_{\phi 0}$)
- solid ($\phi \leq \mathrm{tol}_{\phi 0}$),
- unsaturated ($\mathrm{tol}_{S0} < S < 1 - \mathrm{tol}_{S1}$, $\phi > \mathrm{tol}_{\phi 0}$),
- saturated ($S \geq 1 - \mathrm{tol}_{S1}$, $\phi > \mathrm{tol}_{\phi 0}$),

where tol_{S0}, tol_{S1}, $\mathrm{tol}_{\phi 0}$ are tolerances used to define dry, saturated and solid regions so that, for example, S dropping slightly below 1 because of numerical error still results in the cell being treated as saturated. Typical values are $\mathrm{tol}_{S0} = 0$, $\mathrm{tol}_{S1} = 10^{-6}$, $\mathrm{tol}_{\phi 0} = 10^{-5}$.

Given a solution for the water pressure p_{w}, porosity ϕ and saturation S on the cell centres, we calculate q on the cell edges. We set $q = 0$ on any edge neighbouring a solid cell. We calculate q on the edges between two unsaturated cells, two dry cells, or one unsaturated and one dry cell as

$$q_{j+1/2} = \mathcal{K}k(\mathrm{hm}(\phi_{j+1}, \phi_j))\left(S_j^3 - \frac{2}{\mathcal{B}}\frac{S_{j+1} - S_j}{\Delta Z_{j+1/2}}\right), \tag{B.22}$$

and on edges between two saturated cells as

$$q_{j+1/2} = \mathcal{K}k(\mathrm{hm}(\phi_{j+1}, \phi_j))\left(1 - \frac{p_{\mathrm{w},j+1} - p_{\mathrm{w},j}}{\Delta Z_{j+1/2}}\right), \tag{B.23}$$

where we approximate the value of ϕ on the cell edges by the harmonic mean on the neighbouring cell centres,

$$\phi_{j+1/2} \approx \mathrm{hm}(\phi_{j+1}, \phi_j) = \frac{2\phi_{j+1}\phi_j}{\phi_{j+1} + \phi_j}, \tag{B.24}$$

and the value of S on the cell edges by the value on the cell above,

$$S_{j+1/2} \approx S_j, \tag{B.25}$$

since we expect the water to usually flow downwards. The water pressure p_{w} on saturated cells is found by solving the discretised equation

$$\begin{aligned} &\mathcal{K}\left(\left(k(\phi)\frac{\partial p_{\mathrm{w}}}{\partial Z}\right)_{j+1/2} - \left(k(\phi)\frac{\partial p_{\mathrm{w}}}{\partial Z}\right)_{j-1/2}\right)\Big/\Delta Z_j \\ &= \mathcal{K}\frac{k(\mathrm{hm}(\phi_{j+1}, \phi_j)) - k(\mathrm{hm}(\phi_j, \phi_{j-1}))}{\Delta Z_j} + \mathcal{K}_{\mathrm{d}}\mathcal{K}_d k(\phi_j), \end{aligned} \tag{B.26}$$

where we approximate

$$\left(k(\phi)\frac{\partial p_{\mathrm{w}}}{\partial Z}\right)_{j+1/2} \approx k(\mathrm{hm}(\phi_{j+1}, \phi_j))\frac{p_{\mathrm{w},j+1} - p_{\mathrm{w},j}}{\Delta Z_{j+1/2}}. \tag{B.27}$$

The boundary conditions for this system are continuity with atmospheric pressure at the surface and at interfaces between saturated and unsaturated regions, and no flux at solid boundaries. We apply $p_{\mathrm{w}} = p_{\mathrm{a}}$ at saturated–unsaturated interfaces, instead of continuity with the unsaturated pressure $p_{\mathrm{w}} = p_{\mathrm{a}} - \frac{1}{\mathcal{B}}S^{-2}$, to avoid numerical issues when there are large unresolved gradients in S at these interfaces. The two conditions are equivalent when $\mathcal{B} \to \infty$. Since the pressure is defined up to a constant, and p_{a} is constant, we set $p_{\mathrm{w}} = 0$ between saturated and unsaturated

regions, without loss of generality. We apply this on the first unsaturated cell centre outside of the saturated region, and on the surface edge $Z_{1/2}$ when the saturated region extends to the surface. The no flux condition is automatically satisfied at saturated–solid interfaces because $k(\phi) = 0$ when $\phi = 0$, and the harmonic mean on an edge is zero whenever the value on one of the neighbouring cells is zero.

As discussed in Section 5.3.1, in saturated regions bounded on both sides by solid ice, we can instead solve for the flux q directly without solving for p_w, which we do whenever there is a saturated region bounded on both sides by solid regions. We do this by solving equation (5.51) using `ode15s`. Note that solving for the pressure in such regions does not work because the elliptical equation (B.26) for p_w is ill-posed when $q = 0$ is prescribed on both boundaries; the solution p_w is only defined up to a constant.

On edges between a saturated and an unsaturated cell, we use whichever of the saturated flux or unsaturated flux gives the greatest flux out of the saturated region. This is necessary to conserve mass.

B.2.3 Discretised equations

The discrete enthalpy and total water content equations are (ignoring the qT term from the enthalpy equation)

$$\frac{H_j^{m+1} - H_j^{\mathrm{old}}}{\Delta t} + \frac{f_{j+1/2} - f_{j-1/2}}{\Delta Z_j} = -q_{\mathrm{d},j}, \tag{B.28}$$

$$\frac{W_j^{m+1} - W_j^{\mathrm{old}}}{\Delta t} + \frac{\tilde{f}_{j+1/2} - \tilde{f}_{j-1/2}}{\Delta Z_j} = -q_{\mathrm{d},j}, \tag{B.29}$$

where

$$f_{j+1/2} = \dot{h}^{\mathrm{old}} H_{j+1/2}^{m+1} - \hat{k} W_{j+1/2}^{m+1} \left(\frac{T_H^m(H_{j+1}^{m+1}) - T_H^m(H_j^{m+1})}{\Delta Z_{j+1/2}} \right) + F_{j+1/2}^{\mathrm{old}} + \mathcal{S} q_{j+1/2}, \tag{B.30}$$

$$\tilde{f}_{j+1/2} = \dot{h}^{\mathrm{old}} W_{j+1/2}^{m+1} + q_{j+1/2}, \tag{B.31}$$

and we approximate $\dot{h}^{\mathrm{old}} H_{j+1/2}^{m+1}$ and $\dot{h}^{\mathrm{old}} W_{j+1/2}^{m+1}$ by upwinding as in (B.3), and approximate $W_{j+1/2} \approx \mathrm{hm}(W_{j+1}, W_j)$ by the harmonic mean (B.24). The lateral drainage $q_{\mathrm{d},j}$ is approximated by

$$q_{\mathrm{d},j} = \mathcal{K}_\mathrm{d} \mathcal{K} (\phi_j^{\mathrm{old}})^3 (S_j^{\mathrm{old}})^3, \tag{B.32}$$

and the form used for flux $q_{j+1/2}$ depends on whether the edge is in a saturated or unsaturated region, which we do not know before carrying out the timestep. Therefore, similarly to the enthalpy and melt flags, we introduce an 'unsaturated flag' $\delta^{\text{unsatedge}}$.

B.2.4 Unsaturated flag

The unsaturated flag $\delta^{\text{unsatedge}}$ is used to decide on which edges to use the unsaturated form of the water flux (B.22) and on which to use the saturated form (B.23), and is defined as

$$\delta^{\text{unsatedge}} = \begin{cases} 1, & \text{if between two unsaturated cells in the previous iteration,} \\ 0, & \text{otherwise.} \end{cases} \tag{B.33}$$

The flux $q_{j+1/2}$ used in the H and W equations (B.28), (B.29) is then approximated by

$$q_{j+1/2} = \mathcal{K}(\phi^{\text{old}}_{j+1/2})^3 \left((S^{\text{old}}_j)^3 - \frac{2}{\mathcal{B}\Delta Z_j} \left(\frac{H^{m+1}_{j+1}}{\phi^{\text{old}}_{j+1}\mathcal{S}} - \frac{H^{m+1}_{j}}{\phi^{\text{old}}_{j}\mathcal{S}} \right) \right) \delta^{\text{unsatedge}} + q^{\text{old}}_{j+1/2}(1-\delta^{\text{unsatedge}}), \tag{B.34}$$

where once again we have approximated $S_{j+1/2} \approx S_j$. On edges that were between two unsaturated cells in the previous iteration, we use a discretisation of the unsaturated flux. We express S in the discretisation (B.22) in terms of the enthalpy H as $S = H/(\phi\mathcal{S})$ to enable us to include the $\frac{\partial S}{\partial Z}$ term in the flux (and, in particular, the diffusion terms it creates in the H and W equations) implicitly. We do this to prevent the diffusion terms from causing a timestep restriction. On other edges, we use the value of the q from the previous iteration, calculated as in Section B.2.2. Note that the $1/\phi^{\text{old}}_j$ is only ever included on unsaturated cells where $\phi > \text{tol}_{\phi,0}$, so we never end up dividing by 0.

B.2.5 Implementing boundary conditions

The far-field temperature condition (B.5) and surface condition (B.8) (melt case) or (B.12) (no melt case) still apply in the unsaturated model. In addition to those, we have the following conditions.

Far-field condition The far-field condition (5.46) is discretised as

$$W_{N+1/2} = 1. \tag{B.35}$$

Using this, we can include $\dot{h}W_{N+1/2} = \dot{h}$ exactly, without having to upwind like we do for the other edges. This modification, along with the far-field temperature and radiation conditions (B.5), (B.11), give

$$f_{N+1/2} = \dot{h}^{\text{old}}\mathcal{T}_\infty - \hat{k}\left(\frac{\mathcal{T}_\infty - T_H^m(H_N^{m+1})}{\frac{1}{2}\Delta Z_N}\right), \tag{B.36}$$

$$\tilde{f}_{N+1/2} = \dot{h}^{\text{old}}, \tag{B.37}$$

noting that $q_{1/2} = 0$ since there is no water present at depth (where the ice is cold and solid).

Kinematic condition The kinematic condition (5.42) (in the unsaturated case) is discretised it as

$$q_{1/2} + \dot{h}W_{1/2} = R_{\text{r}} + R_{\text{s}}, \tag{B.38}$$

where we approximate $\dot{h}W_{1/2} \approx \dot{h}W_1$ by upwinding. Note that we only need to worry about implementing this boundary condition directly in the W and H equations when the surface is unsaturated. When the surface is saturated, we use the saturated flux q from the previous timestep which was calculated to satisfy the boundary conditions (using $p_{\text{w}} = 0$ at $Z = 0$ as the boundary condition). Combined with the surface condition (B.8) (melt case) or (B.12) (no melt case), this gives

$$f_{1/2} = -\hat{k}W_1^{m+1}\left(\frac{2T_H^m(H_1^{m+1})}{\Delta Z_1}\right) + (1-\chi)(1-a)\mathcal{Q}_{\text{si}} + \mathcal{S}(R_{\text{r}} + R_{\text{s}} - \dot{h}W_1) \tag{B.39}$$

in the melt case,

$$\begin{aligned} f_{1/2} &= (\chi(1-a)\mathcal{Q}_{\text{si}} + \mathcal{Q}_0) - (\hat{v} + R_{\text{s}} + R_{\text{r}})\left(\frac{3}{2}T_H^m(H_1^{m+1}) - \frac{1}{2}T_H^m(H_2^{m+1})\right) \\ &+(1-\chi)(1-a)\mathcal{Q}_{\text{si}} + \mathcal{S}(R_{\text{r}} + R_{\text{s}} - \dot{h}W_1)\delta^{\text{unsatedge}} + \mathcal{S}q_{j+1/2}^{\text{old}}(1-\delta^{\text{unsatedge}}) \end{aligned} \tag{B.40}$$

in the no melt case, and

$$\tilde{f}_{1/2} = \dot{h}^{\text{old}}W_1^{m+1} + (R_{\text{r}} + R_{\text{s}} - \dot{h}W_1)\delta^{\text{unsatedge}} + q_{j+1/2}^{\text{old}}(1-\delta^{\text{unsatedge}}) \tag{B.41}$$

in both cases. Recall that, in general, we approximate $W_{j+1/2}$ by the harmonic mean of its neighbouring cells. The top edge only has one neighbour (the top cell), so we approximate $W_{1/2} \approx W_1$.

B.2.6 Iterations

In each timestep, we carry out at set of iterations until the enthalpy and unsaturated flags are correct (up to a maximum of 3 iterations). We do not update any other variables within the iterations, using values from the previous timestep instead.

At the start of each timestep, we calculate F. If we are prescribing the absorption and scattering coefficients as functions of model variables such as ϕ or S, we use a discretisation of the two-stream approximation (as described in Section B.2.1), using the values of the variables from the previous timestep. If we are prescribing $\hat{\alpha}$ and $\hat{r}$ to be uniform with depth (but possibly varying in time), we instead use the analytical solution for F, presented in Chapter 2.

Within each iteration, using values from the previous iteration and timestep as detailed in the discrete equations (B.28), (B.29), we

1. Solve the H equation (B.28) (which is independent of $\mathbf{W}^{m+1}$) to find $\mathbf{H}^{m+1}$.
2. Solve the W equation (B.29) (which depends on $\mathbf{H}^{m+1}$ just calculated) to find $\mathbf{W}^{m+1}$.
3. Recover ϕ, S, T from H, W using (5.26), (5.27), (5.28). We set $S = 1$ if $S \geq 1 - \mathrm{tol}_{S0}$, $S = 0$ if $S \leq \mathrm{tol}_{S0}$, and $\phi = 0$ if $\phi \leq \mathrm{tol}_{\phi 0}$, but do not adjust W or H, allowing W to slightly exceed 1.
4. Solve for p_w and q based on the new S, ϕ solution. Also update $\delta^{\mathrm{unsatedge}}$ based on this (as described in Section B.2.4).
5. Update the enthalpy flag based on the new solution (as described in Section B.1.1).
6. If the assumed enthalpy flag and unsaturated flags were correct at all points in the domain, we stop iterating.

The timestep is first carried out using the value of the melt flag from the previous timestep, then the procedure in Section B.1.2 is used to recompute the solution for the current timestep with a corrected melt flag if necessary.

Appendix C

Approximating the microbial growth rate

Here, we describe the method used to approximate the microbial growth rate β_A based on observations of doubling times for glacier ice algae on Greenland [Stibal et al., 2017, Williamson et al., 2018]. The approximation is crude, but is nonetheless useful for providing a rough indication of suitable values for β_A.

We consider the growth of microbes in a steadily melting crust, from a small initial microbial abundance $A_\mathrm{w} = A_\infty$ and nutrient concentration $C_\mathrm{w} = C_\infty$, as studied in Section 4.4.2.1.

We assume that growth dominates the dynamics such that the evolution equation (4.1) for the microbes in the water is approximately

$$\frac{\partial}{\partial t}\Big(\phi A_\mathrm{w}\Big) \approx \beta_A \tilde{g}(F, \phi C_\mathrm{w}, A_\mathrm{w})\phi A_\mathrm{w}. \tag{C.1}$$

In our model, the scaled growth rate is given by

$$\tilde{g}(F, \phi C_\mathrm{w}, A_\mathrm{w}) = \left(\frac{\alpha_\mathrm{PAR} F}{k_F + \alpha_\mathrm{PAR} F}\right)\left(\frac{\phi C_\mathrm{w}}{k_C + \phi C_\mathrm{w}}\right)\left(1 - \frac{A_\mathrm{w}}{A_\mathrm{max}}\right), \tag{C.2}$$

but for the purpose of this estimation of β_A, we replace this with a constant value,

$$\tilde{g}_0 = \tilde{g}(\bar{F}, \bar{\phi} C_\infty, A_\infty), \tag{C.3}$$

using depth-averaged values for the radiation and porosity,

$$\bar{F} = \frac{1}{Z_\mathrm{m}} \int_0^{Z_\mathrm{m}} F \, \mathrm{d}Z, \quad \bar{\phi} = \frac{1}{Z_\mathrm{m}} \int_0^{Z_\mathrm{m}} \phi \, \mathrm{d}Z. \tag{C.4}$$

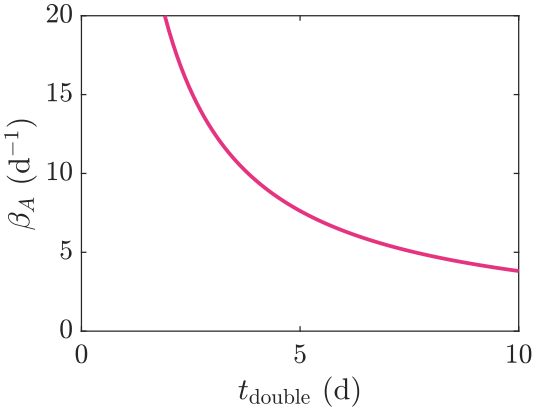


Figure C.1: The relationship (C.6) used to infer the microbial growth rate β_A from observed doubling times t_{double}.

The solution to equation (C.1) is then approximately exponential growth,

$$\phi A_{\mathrm{w}} \sim e^{\beta_A \tilde{g}_0 t}, \tag{C.5}$$

for which the doubling time t_{double} is

$$t_{\mathrm{double}} = \frac{\log(2)}{\beta_A \tilde{g}_0}. \tag{C.6}$$

This relationship is used to infer β_A from observed doubling times.

To apply the relationship (C.6), we must calculate a value for $\tilde{g}_0$. We use the 'default' steadily melting weathering crust solution from Chapter 2 (i.e. using the parameter values in Table 2.2) to calculate $\bar{\phi} = 0.25$ and $\bar{F} = 17.8$ W m^{-2}. Combining these values with the microbe and nutrient parameters in Table 4.2, we find that $\tilde{g}_0 = 0.018$. The resulting relationship (C.6) between t_{double} and β_A is shown in Figure C.1. The observed doubling times of 5.5 ± 1.7 days by Stibal et al. [2017] and 3.75 ± 0.36 days by Williamson et al. [2018] hence suggest that a value of $\beta_A \approx$ 5–10 is reasonable.

References

V. Alexiades and A. D. Solomon. *Mathematical Modeling of Melting and Freezing Processes*. Hemisphere Publishing Corporation, Washington; London, 1993.

M. Andersen, L. Stenseng, H. Skourup, W. Colgan, S. A. Khan, S. S. Kristensen, S. Andersen, J. Box, A. Ahlstrøm, X. Fettweis, et al. Basin-scale partitioning of Greenland ice sheet mass balance components (2007–2011). *Earth and Planetary Science Letters*, 409:89–95, 2015.

R. J. Arthern, D. G. Vaughan, A. M. Rankin, R. Mulvaney, and E. R. Thomas. In situ measurements of Antarctic snow compaction compared with predictions of models. *Journal of Geophysical Research: Earth Surface*, 115(3), 2010.

A. Aschwanden, E. Bueler, C. Khroulev, and H. Blatter. An enthalpy formulation for glaciers and ice sheets. *Journal of Glaciology*, 58(209):441–457, 2012.

E. A. Bagshaw, M. Tranter, A. G. Fountain, K. Welch, H. J. Basagic, and W. B. Lyons. Do cryoconite holes have the potential to be significant sources of C, N, and P to downstream depauperate ecosystems of Taylor Valley, Antarctica? *Arctic, Antarctic, and Alpine Research*, 45(4):440–454, 2013.

A. F. Banwell, N. S. Arnold, I. C. Willis, M. Tedesco, and A. P. Ahlstrøm. Modeling supraglacial water routing and lake filling on the Greenland Ice Sheet. *Journal of Geophysical Research: Earth Surface*, 117(4), 2012.

J. Bear. *Modeling phenomena of flow and transport in porous media*. Cham: Springer, 1st edition, 2018.

R. E. Bell. The role of subglacial water in ice-sheet mass balance. *Nature Geoscience*, 1(5):297–304, 2008.

L. G. Benning, A. M. Anesio, S. Lutz, and M. Tranter. Biological impact on Greenland's albedo. *Nature Geoscience*, 7(10):691, 2014.

R. Bintanja and M. R. Van Den Broeke. The surface energy balance of Antarctic snow and blue ice. *Journal of Applied Meteorology and Climatology*, 34(4):902–926, 1995.

J. Box, X. Fettweis, J. Stroeve, M. Tedesco, D. Hall, and K. Steffen. Greenland ice sheet albedo feedback: thermodynamics and atmospheric drivers. *The Cryosphere*, 6(4):821–839, 2012.

J. A. Bradley, C. B. Trivedi, M. Winkel, R. Mourot, S. Lutz, C. Larose, C. Keuschnig, E. Doting, L. Halbach, A. Zervas, et al. Active and dormant microorganisms on glacier surfaces. *Geobiology*, 21(2):244–261, 2023.

R. E. Brandt and S. G. Warren. Solar-heating rates and temperature profiles in Antarctic snow and ice. *Journal of Glaciology*, 39(131):99–110, 1993.

L. Bridge and B. Wetton. A mixture formulation for numerical capturing of a two-phase/vapour interface in a porous medium. *Journal of Computational Physics*, 225(2):2043–2068, 2007.

S. Buzzard, D. Feltham, and D. Flocco. A mathematical model of melt lake development on an ice shelf. *Journal of Advances in Modeling Earth Systems*, 10(2): 262–283, 2018.

P. C. Carman. Fluid flow through granular beds. *Trans. Inst. Chem. Eng. London*, 15:150–156, 1937.

D. M. Chandler, J. Alcock, J. Wadham, S. Mackie, and J. Telling. Seasonal changes of ice surface characteristics and productivity in the ablation zone of the Greenland Ice Sheet. *The Cryosphere*, 9(2):487–504, 2015.

X. Cheng, Z. Fu, and B. Wetton. Equivalent formulations of the oxygen depletion problem, other implicit moving boundary value problems, and implications for numerical approximation. *SIAM Journal on Applied Mathematics*, 83(1):52–78, 2023.

L.-A. Chevrollier, J. M. Cook, L. Halbach, H. Jakobsen, L. G. Benning, A. M. Anesio, and M. Tranter. Light absorption and albedo reduction by pigmented microalgae on snow and ice. *Journal of Glaciology*, 69(274):333–341, 2023.

B. C. Christner, H. F. Lavender, C. L. Davis, E. E. Oliver, S. U. Neuhaus, K. F. Myers, B. Hagedorn, S. M. Tulaczyk, P. T. Doran, and W. C. Stone. Microbial processes in the weathering crust aquifer of a temperate glacier. *The Cryosphere*, 12(11):3653–3669, 2018.

V. W. Chu. Greenland ice sheet hydrology: A review. *Progress in Physical Geography*, 38(1):19–54, 2014.

N. Clerx, H. Machguth, A. Tedstone, N. Jullien, N. Wever, R. Weingartner, and O. Roessler. In situ measurements of meltwater flow through snow and firn in the accumulation zone of the SW Greenland Ice Sheet. *The Cryosphere*, 16(10): 4379–4401, 2022.

S. Colbeck. A theory of water percolation in snow. *Journal of Glaciology*, 11(63): 369–385, 1972.

S. C. Colbeck. The capillary effects on water percolation in homogeneous snow. *Journal of Glaciology*, 13(67):85–97, 1974.

S. C. Colbeck. An analysis of water flow in dry snow. *Water Resources Research*, 12(3):523–527, 1976.

J. Cook, A. Hodson, A. Anesio, E. Hanna, M. Yallop, M. Stibal, J. Telling, and P. Huybrechts. An improved estimate of microbially mediated carbon fluxes from the Greenland ice sheet. *Journal of Glaciology*, 58(212):1098–1108, 2012.

J. Cook, M. Flanner, C. Williamson, and S. McKenzie Skiles. Bio-optical properties of terrestrial snow and ice. In A. Kokhanovsky, editor, *Springer Series in Light Scattering: Volume 4: Light Scattering and Radiative Transfer*, pages 129–163. Springer International Publishing, Cham, 2019.

J. M. Cook, A. J. Hodson, and T. D. Irvine-Fynn. Supraglacial weathering crust dynamics inferred from cryoconite hole hydrology. *Hydrological Processes*, 30(3): 433–446, 2016.

J. M. Cook, A. J. Hodson, A. S. Gardner, M. Flanner, A. J. Tedstone, C. Williamson, T. D. Irvine-Fynn, J. Nilsson, R. Bryant, and M. Tranter. Quantifying bioalbedo: a new physically based model and discussion of empirical methods for characterising biological influence on ice and snow albedo. *The Cryosphere*, 11(6):2611–2632, 2017.

J. M. Cook, A. J. Tedstone, C. Williamson, J. McCutcheon, A. J. Hodson, A. Dayal, M. Skiles, S. Hofer, R. Bryant, O. McAree, et al. Glacier algae accelerate melt rates on the south-western Greenland Ice Sheet. *The Cryosphere*, 14(1):309–330, 2020.

M. G. Cooper, L. C. Smith, A. K. Rennermalm, C. Miège, L. H. Pitcher, J. C. Ryan, K. Yang, and S. W. Cooley. Meltwater storage in low-density near-surface bare ice in the Greenland ice sheet ablation zone. *The Cryosphere*, 12(3):955–970, 2018.

M. G. Cooper, L. C. Smith, A. K. Rennermalm, M. Tedesco, R. Muthyala, S. Z. Leidman, S. E. Moustafa, and J. V. Fayne. Spectral attenuation coefficients from measurements of light transmission in bare ice on the Greenland Ice Sheet. *The Cryosphere*, 15(4):1931–1953, 2021.

J. Crank. *Free and Moving Boundary Problems*. Reprint, Oxford: Clarendon Press, [1984] 1987.

K. M. Cuffey and W. S. B. Paterson. *The Physics of Glaciers*. Burlington, MA: Butterworth-Heinemann, fourth edition, 2010.

R. Culberg, D. M. Schroeder, and W. Chu. Extreme melt season ice layers reduce firn permeability across Greenland. *Nature Communications*, 12(1):2336, 2021.

R. M. DeConto and D. Pollard. Contribution of Antarctica to past and future sea-level rise. *Nature*, 531(7596):591–597, 2016.

R. M. DeConto, D. Pollard, R. B. Alley, I. Velicogna, E. Gasson, N. Gomez, S. Sadai, A. Condron, D. M. Gilford, E. L. Ashe, et al. The Paris Climate Agreement and future sea-level rise from Antarctica. *Nature*, 593(7857):83–89, 2021.

T. L. Edwards, S. Nowicki, B. Marzeion, R. Hock, H. Goelzer, H. Seroussi, N. C. Jourdain, D. A. Slater, F. E. Turner, C. J. Smith, et al. Projected land ice contributions to twenty-first-century sea level rise. *Nature*, 593(7857):74–82, 2021.

E. M. Enderlin, I. M. Howat, S. Jeong, M.-J. Noh, J. H. Van Angelen, and M. R. Van Den Broeke. An improved mass budget for the Greenland ice sheet. *Geophysical Research Letters*, 41(3):866–872, 2014.

R. S. Fausto, D. van As, K. D. Mankoff, B. Vandecrux, M. Citterio, A. P. Ahlstrøm, S. B. Andersen, W. Colgan, N. B. Karlsson, K. K. Kjeldsen, et al. Programme for Monitoring of the Greenland Ice Sheet (PROMICE) automatic weather station data. *Earth System Science Data*, 13(8):3819–3845, 2021.

X. Fettweis, J. E. Box, C. Agosta, C. Amory, C. Kittel, C. Lang, D. van As, H. Machguth, and H. Gallée. Reconstructions of the 1900–2015 Greenland ice sheet surface mass balance using the regional climate MAR model. *The Cryosphere*, 11(2):1015–1033, 2017.

A. C. Fowler. *Mathematical Geoscience*. London: Springer, first edition, 2011.

P. Gantayat, A. F. Banwell, A. A. Leeson, J. M. Lea, D. Petersen, N. Gourmelen, and X. Fettweis. A new model for supraglacial hydrology evolution and drainage for the Greenland Ice Sheet (SHED v1. 0). *Geoscientific Model Development*, 16 (20):5803–5823, 2023.

H. Goelzer, S. Nowicki, A. Payne, E. Larour, H. Seroussi, W. H. Lipscomb, J. Gregory, A. Abe-Ouchi, A. Shepherd, E. Simon, et al. The future sea-level contribution of the Greenland ice sheet: a multi-model ensemble study of ISMIP6. *The Cryosphere*, 14(9):3071–3096, 2020.

J. M. Gray. Water movement in wet snow. *Philosophical Transactions of the Royal Society of London. Series A: Mathematical, Physical and Engineering Sciences*, 354(1707):465–500, 1996.

W. Greuell and J. Oerlemans. The evolution of the englacial temperature distribution in the superimposed ice zone of a polar ice cap during a summer season. In *Glacier Fluctuations and Climatic Change: Proceedings of the Symposium on Glacier Fluctuations and Climatic Change*, pages 289–303. Springer, 1989.

L. Halbach, L.-A. Chevrollier, J. M. Cook, I. T. Stevens, M. Hansen, A. M. Anesio, L. G. Benning, and M. Tranter. Dark ice in a warming world: advances and challenges in the study of Greenland Ice Sheet's biological darkening. *Annals of Glaciology*, 63(87-89):95–100, 2022.

J. Harper, N. Humphrey, W. T. Pfeffer, J. Brown, and X. Fettweis. Greenland ice-sheet contribution to sea-level rise buffered by meltwater storage in firn. *Nature*, 491(7423):240–243, 2012.

M. M. Herron and C. C. Langway. Firn densification: an empirical model. *Journal of Glaciology*, 25(93):373–385, 1980.

I. J. Hewitt and C. Schoof. Models for polythermal ice sheets and glaciers. *The Cryosphere*, 11(1):541–551, 2017.

M. J. Hoffman. *Spatial and temporal variability of glacier melt in the McMurdo Dry Valleys, Antarctica*. PhD thesis, Portland State University, 2011.

M. J. Hoffman, A. G. Fountain, and G. E. Liston. Surface energy balance and melt thresholds over 11 years at Taylor Glacier, Antarctica. *Journal of Geophysical Research: Earth Surface*, 113(4):F04014, 2008.

M. J. Hoffman, A. G. Fountain, and G. E. Liston. Near-surface internal melting: a substantial mass loss on Antarctic Dry Valley glaciers. *Journal of Glaciology*, 60 (220):361–374, 2014.

A. T. Holland, C. J. Williamson, F. Sgouridis, A. J. Tedstone, J. McCutcheon, J. M. Cook, E. Poniecka, M. L. Yallop, M. Tranter, and A. M. Anesio. Dissolved organic nutrients dominate melting surface ice of the Dark Zone (Greenland Ice Sheet). *Biogeosciences*, 16(16):3283–3296, 2019.

S. Hotaling, S. Lutz, R. J. Dial, A. M. Anesio, L. G. Benning, A. G. Fountain, J. L. Kelley, J. McCutcheon, S. M. Skiles, N. Takeuchi, et al. Biological albedo reduction on ice sheets, glaciers, and snowfields. *Earth-Science Reviews*, 220: 103728, 2021.

P. How, J. Abermann, A. Ahlstrøm, S. Andersen, J. E. Box, M. Citterio, W. Colgan, F. R.S., N. Karlsson, J. Jakobsen, K. Langley, S. Larsen, M. Lund, K. Mankoff, A. Pedersen, A. Rutishauser, C. Shield, A. Solgaard, D. van As, B. Vandecrux, and P. Wright. PROMICE and GC-Net automated weather station data in Greenland. GEUS Dataverse, 2022. URL `https://doi.org/10.22008/FK2/IW73UU`.

T. D. Irvine-Fynn and A. Edwards. A frozen asset: the potential of flow cytometry in constraining the glacial biome. *Cytometry part A*, 85(1):3–7, 2014.

T. D. Irvine-Fynn, A. Edwards, I. T. Stevens, A. Mitchell, P. Bunting, J. Box, K. A. Cameron, J. Cook, K. Naegeli, S. M. Rassner, et al. Storage and export of microbial biomass across the western Greenland Ice Sheet. *Nature Communications*, 12 (1):3960, 2021.

S. E. Jorgensen and G. Bendoricchio. *Fundamentals of Ecological Modelling*. Amsterdam: Elsevier, 3rd edition, 2001.

F. Kelliher, I. Owens, A. Sturman, J. Byers, J. Hunt, and T. McSeveny. Radiation and ablation on the névé of Franz Josef Glacier. *Journal of Hydrology (New Zealand)*, 35(1):131–150, 1996.

J. Kingslake, J. C. Ely, I. Das, and R. E. Bell. Widespread movement of meltwater onto and across Antarctic ice shelves. *Nature*, 544(7650):349–352, 2017.

J. Kozeny. Ueber kapillare leitung des wassers im boden. *Sitzungsberichte der Akademie der Wissenschaften in Wien*, 136:271, 1927.

R. Law, N. Arnold, C. Benedek, M. Tedesco, A. Banwell, and I. Willis. Over-winter persistence of supraglacial lakes on the Greenland Ice Sheet: Results and insights from a new model. *Journal of Glaciology*, 66(257):362–372, 2020.

A. Leeson, A. Shepherd, S. Palmer, A. Sundal, and X. Fettweis. Simulating the growth of supraglacial lakes at the western margin of the Greenland ice sheet. *The Cryosphere*, 6(5):1077–1086, 2012.

N. R. Leroux and J. W. Pomeroy. Modelling capillary hysteresis effects on preferential flow through melting and cold layered snowpacks. *Advances in Water Resources*, 107:250–264, 2017.

J. Li and H. J. Zwally. Modeling the density variation in the shallow firn layer. *Annals of Glaciology*, 38:309–313, 2004.

S. R. Ligtenberg, M. M. Helsen, and M. R. Van Den Broeke. An improved semi-empirical model for the densification of Antarctic firn. *The Cryosphere*, 5(4): 809–819, 2011.

G. E. Liston, J.-G. Winther, O. Bruland, H. Elvehøy, and K. Sand. Below-surface ice melt on the coastal Antarctic ice sheet. *Journal of Glaciology*, 45(150):273–285, 1999.

D. L. Matson and R. H. Brown. Solid-state greenhouse and their implications for icy satellites. *Icarus*, 77(1):67–81, 1989.

G. A. Maykut and N. Untersteiner. Some results from a time-dependent thermodynamic model of sea ice. *Journal of Geophysical Research*, 76(6):1550–1575, 1971.

J. McCutcheon, S. Lutz, C. Williamson, J. M. Cook, A. J. Tedstone, A. Vanderstraeten, S. Wilson, A. Stockdale, S. Bonneville, A. M. Anesio, et al. Mineral phosphorus drives glacier algal blooms on the Greenland Ice Sheet. *Nature Communications*, 12(1):570, 2021.

M. Meredith, M. Sommerkorn, S. Cassotta, C. Derksen, A. Ekaykin, A. Hollowed, G. Kofinas, A. Mackintosh, J. Melbourne-Thomas, M. Muelbert, et al. Polar regions. In *The Ocean and Cryosphere in a Changing Climate: Special Report of the Intergovernmental Panel on Climate Change*, pages 203–320. Cambridge University Press, 2019. ISBN 9781009157964.

S. H. Mernild, T. L. Mote, and G. E. Liston. Greenland ice sheet surface melt extent and trends: 1960–2010. *Journal of Glaciology*, 57(204):621–628, 2011.

C. R. Meyer and I. J. Hewitt. A continuum model for meltwater flow through compacting snow. *The Cryosphere*, 11(6):2799–2813, 2017.

A. B. Mikkelsen, A. Hubbard, M. MacFerrin, J. E. Box, S. H. Doyle, A. Fitzpatrick, B. Hasholt, H. L. Bailey, K. Lindbäck, and R. Pettersson. Extraordinary runoff from the Greenland ice sheet in 2012 amplified by hypsometry and depleted firn retention. *The Cryosphere*, 10(3):1147–1159, 2016.

O. Miller, D. K. Solomon, C. Miège, L. Koenig, R. Forster, N. Schmerr, S. R. Ligtenberg, A. Legchenko, C. I. Voss, L. Montgomery, et al. Hydrology of a perennial firn aquifer in Southeast Greenland: an overview driven by field data. *Water Resources Research*, 56(8):e2019WR026348, 2020.

O. Miller, C. I. Voss, D. K. Solomon, C. Miège, R. Forster, N. Schmerr, and L. Montgomery. Hydrologic modeling of a perennial firn aquifer in southeast Greenland. *Journal of Glaciology*, 69(275):607–622, 2023.

E. Morris and D. Wingham. Densification of polar snow: Measurements, modeling, and implications for altimetry. *Journal of Geophysical Research: Earth Surface*, 119(2):349–365, 2014.

A. Moure, N. Jones, J. Pawlak, C. Meyer, and X. Fu. A thermodynamic nonequilibrium model for preferential infiltration and refreezing of melt in snow. *Water Resources Research*, 59(5):e2022WR034035, 2023.

F. Müller and C. M. Keeler. Errors in short-term ablation measurements on melting ice surfaces. *Journal of Glaciology*, 8(52):91–105, 1969.

P. K. Munneke, S. M. Ligtenberg, M. Van Den Broeke, J. Van Angelen, and R. Forster. Explaining the presence of perennial liquid water bodies in the firn of the Greenland Ice Sheet. *Geophysical Research Letters*, 41(2):476–483, 2014.

P. K. Munneke, S. R. Ligtenberg, E. A. Suder, and M. R. Van den Broeke. A model study of the response of dry and wet firn to climate change. *Annals of Glaciology*, 56(70):1–8, 2015.

J. D. Murray. *Mathematical Biology*. Berlin: Springer-Verlag, second, corrected edition, 1993.

S. Nghiem, D. Hall, T. Mote, M. Tedesco, M. Albert, K. Keegan, C. Shuman, N. DiGirolamo, and G. Neumann. The extreme melt across the Greenland ice sheet in 2012. *Geophysical Research Letters*, 39(20), 2012.

B. Noël, W. J. van de Berg, S. Lhermitte, B. Wouters, H. Machguth, I. Howat, M. Citterio, G. Moholdt, J. T. Lenaerts, and M. R. van den Broeke. A tipping point in refreezing accelerates mass loss of Greenland's glaciers and ice caps. *Nature Communications*, 8(1):1–8, 2017.

J. R. Ockendon, S. Howison, A. Lacey, and A. B. Movchan. *Applied partial differential equations*. Oxford: Oxford University Press, revised edition, 2016.

D. K. Perovich. Theoretical estimates of light reflection and transmission by spatially complex and temporally varying sea ice covers. *Journal of Geophysical Research: Oceans*, 95(C6):9557–9567, 1990.

G. F. Pinder and W. G. Gray. *Essentials of multiphase flow and transport in porous media*. Hoboken, N.J. : Wiley, first edition, 2008.

J. C. Ryan, A. Hubbard, M. Stibal, T. D. Irvine-Fynn, J. Cook, L. C. Smith, K. Cameron, and J. Box. Dark zone of the Greenland Ice Sheet controlled by distributed biologically-active impurities. *Nature Communications*, 9(1):1065, 2018.

T. W. Schlatter. The local surface energy balance and subsurface temperature regime in Antarctica. *Journal of Applied Meteorology and Climatology*, 11(7):1048–1062, 1972.

C. J. Schuster. *Weathering crust processes on melting glacier ice (Alberta, Canada)*. PhD thesis, Wilfrid Laurier University, 2001.

S. Sellers. Theory of water transport in melting snow with a moving surface. *Cold Regions Science and Technology*, 31(1):47–57, 2000.

M. Shakeel, P. C. Matthews, R. S. Graham, and S. L. Waters. A continuum model of cell proliferation and nutrient transport in a perfusion bioreactor. *Mathematical medicine and biology: a journal of the IMA*, 30(1):21–44, 2013.

B. Smith, H. A. Fricker, A. S. Gardner, B. Medley, J. Nilsson, F. S. Paolo, N. Holschuh, S. Adusumilli, K. Brunt, B. Csatho, et al. Pervasive ice sheet mass loss reflects competing ocean and atmosphere processes. *Science*, 368(6496):1239–1242, 2020.

L. C. Smith, K. Yang, L. H. Pitcher, B. T. Overstreet, V. W. Chu, Å. K. Rennermalm, J. C. Ryan, M. G. Cooper, C. J. Gleason, M. Tedesco, et al. Direct measurements of meltwater runoff on the Greenland ice sheet surface. *Proceedings of the National Academy of Sciences*, 114(50):E10622–E10631, 2017.

I. T. Stevens, T. D. Irvine-Fynn, A. Edwards, A. C. Mitchell, J. M. Cook, P. R. Porter, T. O. Holt, M. Huss, X. Fettweis, B. J. Moorman, et al. Spatially consistent microbial biomass and future cellular carbon release from melting Northern Hemisphere glacier surfaces. *Communications Earth and Environment*, 3(1):275, 2022.

M. Stibal and M. Tranter. Laboratory investigation of inorganic carbon uptake by cryoconite debris from Werenskioldbreen, Svalbard. *Journal of Geophysical Research: Biogeosciences*, 112(4), 2007.

M. Stibal, M. Šabacká, and J. Žárskỳ. Biological processes on glacier and ice sheet surfaces. *Nature Geoscience*, 5(11):771–774, 2012.

M. Stibal, J. E. Box, K. A. Cameron, P. L. Langen, M. L. Yallop, R. H. Mottram, A. L. Khan, N. P. Molotch, N. A. Chrismas, F. Calì Quaglia, et al. Algae drive enhanced darkening of bare ice on the Greenland ice sheet. *Geophysical Research Letters*, 44(22):11–463, 2017.

P. Taylor and D. Feltham. Multiple stationary solutions of an irradiated slab. *Journal of Crystal Growth*, 276(3-4):688–697, 2005.

P. D. Taylor and D. L. Feltham. A model of melt pond evolution on sea ice. *Journal of Geophysical Research: Oceans*, 109(12):1–19, 2004.

M. Tedesco, S. Doherty, X. Fettweis, P. Alexander, J. Jeyaratnam, and J. Stroeve. The darkening of the Greenland ice sheet: trends, drivers, and projections (1981–2100). *The Cryosphere*, 10(2):477–496, 2016.

A. J. Tedstone, J. M. Cook, C. J. Williamson, S. Hofer, J. McCutcheon, T. Irvine-Fynn, T. Gribbin, and M. Tranter. Algal growth and weathering crust state drive variability in western Greenland Ice Sheet ice albedo. *The Cryosphere*, 14(2): 521–538, 2020.

J. Telling, M. Stibal, A. M. Anesio, M. Tranter, I. Nias, J. Cook, C. Bellas, G. Lis, J. L. Wadham, A. Sole, et al. Microbial nitrogen cycling on the Greenland Ice Sheet. *Biogeosciences*, 9(7):2431–2442, 2012.

The IMBIE Team. Mass balance of the Antarctic Ice Sheet from 1992 to 2017. *Nature*, 558(7709):219–222, 2018.

The IMBIE Team. Mass balance of the Greenland Ice Sheet from 1992 to 2018. *Nature*, 579(7798):233–239, 2020.

G. Traversa and B. Di Mauro. Weathering crust formation outpaces melt-albedo feedback on blue ice shelves of East Antarctica. *Communications Earth Environment*, 5:740, 2024.

L. D. Trusel, S. B. Das, M. B. Osman, M. J. Evans, B. E. Smith, X. Fettweis, J. R. McConnell, B. P. Noël, and M. R. van den Broeke. Nonlinear rise in Greenland runoff in response to post-industrial Arctic warming. *Nature*, 564(7734):104–108, 2018.

R. S. van de Wal, W. Boot, M. Van den Broeke, C. Smeets, C. Reijmer, J. Donker, and J. Oerlemans. Large and rapid melt-induced velocity changes in the ablation zone of the Greenland Ice Sheet. *Science*, 321(5885):111–113, 2008.

M. Van den Broeke, P. Smeets, J. Ettema, C. Van der Veen, R. Van de Wal, and J. Oerlemans. Partitioning of melt energy and meltwater fluxes in the ablation zone of the west Greenland ice sheet. *The Cryosphere*, 2(2):179–189, 2008.

M. Van den Broeke, C. Smeets, and R. Van de Wal. The seasonal cycle and interannual variability of surface energy balance and melt in the ablation zone of the west Greenland ice sheet. *The Cryosphere*, 5(2):377–390, 2011.

B. Vandecrux, R. Mottram, P. L. Langen, R. S. Fausto, M. Olesen, C. M. Stevens, V. Verjans, A. Leeson, S. Ligtenberg, P. Kuipers Munneke, et al. The firn meltwater Retention Model Intercomparison Project (RetMIP): evaluation of nine firn models at four weather station sites on the Greenland ice sheet. *The Cryosphere*, 14(11):3785–3810, 2020.

V. Voller and M. Cross. Accurate solutions of moving boundary problems using the enthalpy method. *International Journal of Heat and Mass Transfer*, 24(3): 545–556, 1981.

WCRP Global Sea Level Budget Group. Global sea-level budget 1993-present ETH Library Global sea-level budget 1993-present. *Earth Syst. Sci. Data*, 10:1551–1590, 2018.

B. Wetton. Enthalpy methods for moving boundary problems. British Applied Mathematics Colloquium 2023, Bristol, 3–5 Apr 2023, 2023.

R. A. Wharton Jr., C. P. McKay, G. M. Simmons Jr., and B. C. Parker. Cryoconite holes on glaciers. *Bioscience*, 35(8):499–503, 1985.

I. Wientjes and J. Oerlemans. An explanation for the dark region in the western melt zone of the Greenland ice sheet. *The Cryosphere*, 4(3):261–268, 2010.

C. Williamson, A. Anesio, J. Cook, A. Tedstone, E. Poniecka, A. Holland, D. Fagan, M. Tranter, and M. Yallop. Ice algal bloom development on the surface of the Greenland Ice Sheet. *FEMS Microbiology Ecology*, 94(3):fiy025, 2018.

C. J. Williamson, K. A. Cameron, J. M. Cook, J. D. Zarsky, M. Stibal, and A. Edwards. Glacier algae: a dark past and a darker future. *Frontiers in Microbiology*, 10(APR):524, 2019.

C. J. Williamson, J. Cook, A. Tedstone, M. Yallop, J. McCutcheon, E. Poniecka, D. Campbell, T. Irvine-Fynn, J. McQuaid, M. Tranter, et al. Algal photophysiology drives darkening and melt of the Greenland Ice Sheet. *Proceedings of the National Academy of Sciences*, 117(11):5694–5705, 2020.

T. Woods and I. J. Hewitt. A model of the weathering crust and microbial activity on an ice-sheet surface. *The Cryosphere*, 17(5):1967–1987, 2023.

T. Woods and I. J. Hewitt. Modelling the evolution of an ice sheet's weathering crust. *IMA Journal of Applied Mathematics*, page hxae031, 2024.

R. D. Wordsworth. The Climate of Early Mars. *Annual Review of Earth and Planetary Sciences*, 44:381–408, 2016.